



Thèse

2021

Open Access

This version of the publication is provided by the author(s) and made available in accordance with the copyright holder(s).

---

## Spatial navigation of a primate in three dimensions

---

Zimmermann, Robert

### How to cite

ZIMMERMANN, Robert. Spatial navigation of a primate in three dimensions. Doctoral Thesis, 2021. doi: 10.13097/archive-ouverte/unige:169648

This publication URL: <https://archive-ouverte.unige.ch/unige:169648>

Publication DOI: [10.13097/archive-ouverte/unige:169648](https://doi.org/10.13097/archive-ouverte/unige:169648)

UNIVERSITÉ DE GENÈVE

FACULTÉ DES SCIENCES

Professeur Daniel Huber, directeur de thèse

**TITRE DE LA THÈSE**

**Spatial navigation of a primate in three dimensions**

THÈSE  
Présentée à la  
Faculté des Sciences  
de l'Université de Genève

pour obtenir le grade de  
Docteur en Neurosciences

Par

**Róbert Zimmermann**

de Slovaquie

Thèse N° 312

Genève

Éditeur ou imprimeur : Université de Genève

2021

## Table of Contents

<b>Introduction</b>	<b>3</b>
History of research in spatial navigation across animal species	4
Understanding variables of orientation and navigation	5
Navigating to the unknown	6
Homing: when you know where to go	7
True navigators take shortcuts	8
The mouse lemur as a navigator	10
<b>Hippocampal Formation</b>	<b>12</b>
Hippocampus	13
Place cells	15
Entorhinal cortex	17
Grid cells	18
Grid cell characteristics	18
Head direction cells	19
Border cells	20
Speed cells	21
The oscillatory activity	<b>22</b>
Place cells and theta oscillations	22
Evidence from non-rodent animal models	<b>25</b>
Place cells in bats	25
Place cells in primates	25
Place cells in humans	29
In the search for the third dimension	<b>30</b>
Mouse lemur ( <i>Microcebus murinus</i> )	34
<b>Methods</b>	<b>38</b>
Handling procedures	38
Handling of the newborns	38
Food and food restriction	38
Surgery	39
Recording setup	40
Head-drive	40
Recording setup	46
Behavioural room	47
Behavioural priming	48
Tracking	48
Processing and spike sorting	50

<b>Results</b>	<b>51</b>
Single cell activity	51
Theta activity	53
<b>Discussion</b>	<b>56</b>
Maze and Thickness of the Branches	58
Experimental setup	59
Results	60
Quality and limitations of the results.	61
Conclusions and Future Perspectives	62
Additional work	<b>65</b>
Acknowledgements	69
References	71
Article 1	84
Article 2	111
Article 3	124
Annex 1	141

# Introduction

During my PhD studies, I worked on establishing tiny malagasy primate as a new systems neuroscience animal model. Transferring experimental techniques from rodents to primates, developing behavioural paradigms, establishing surgeries and exploring capabilities of the mouse lemur led me to be involved in several research projects. As for the topic of my thesis, I chose to focus on spatial navigation and orientation.

Self-perception in space is a long-debated topic and has been scientifically studied since the invention of analytic philosophy in the late 19th century. Orientation and navigation in space are among the main features characterizing animal behavior. Indeed, most animals spend a substantial part of their awake time trying to reach a specific location. Changing location increases the chance of finding mates, food, seeking better environmental conditions, or escaping predators and within-species competition.

How does an organism know where it is going? How will it come back? And why is it lost now and then? These questions have been extensively studied in various animal species and have led to fundamental insights into the computational processes that underlie spatial navigation.

This research project attempts to tackle a new aspect of navigation, namely the third dimension of space. Exploring arboreal environments has probably been a main driver behind primate evolution, thus understanding how three dimensional space is represented in the primate brain seems to be a pertinent question.

At the heart of this study is a small and arboreal mammal, which has retained many of the hallmarks of early primates: the gray mouse lemur (*Microcebus murinus*). This malagasy prosimian weighs only 60gr and thus facilitates the holding and handling compared to other, larger primates. In addition, it allows the direct transfer of many experimental tools initially designed for rodents.



**Figure 1: Mouse lemur**  
Mouse lemur (*Microcebus murinus*) during a typical jump from branch to branch.

# History of research in spatial navigation across animal species

The remarkable homing capacity of pigeons was noticed by humans as early as 3000 years BC when the first pigeon post was established in Egypt. Later on, their use as messengers grew in popularity and even established the organizing of pigeon competitions. They saw their utility increase exponentially in the 19th century, for their value in military communication during wars. The interest in understanding the homing ability of pigeons led the researchers in early postwar days to perform the first experiments in the field of spatial navigation and orientation (Kramer., 2008).

The first bird experiments opened a strong scientific discussion revolving around the use of magnetoreception, olfaction, landmarks or sun for navigation. However, most of the definitive answers came only decades after. The early day's bird experiments were soon accompanied by experiments on insects.

In the 1950s, Hughes was observing walking cockroaches (Hughes, 1957). Firstly, he let them walk with all their legs, and subsequently amputating them one after another. He noticed the cockroaches immediately adapted. This phenomenon, named "*correcting behaviour*", serves to maintain a stable heading direction. Regardless of the damages, when the animal was still capable of movement, it moved along a straight line. This brought an important understanding: even an animal as "simple" as a bug, is not just stochastically roaming around but performs the goal-directed movement. He then hypothesized that the inflow from proprioception and sensory organs into the central nervous system could drive coordinated insects goal-directed movement.

In 1965, Hugh Dingle forced a boxelder bug to make 90° turns whilst walking on the causeway. He observed that bugs being forced to turn along the causeway would take a second turn in the opposite direction as soon as it was possible. He speculated that the enforced turn acted against the tendency to follow a straight line trajectory, and therefore the bugs took the opposite turn to compensate for the deviation (Dingle, 1965). Based on these results, he suggested changing the term "*correcting behaviour*" for "*delayed compensatory response*". Trying to understand which sensory modality drove this behaviour, he occluded the bug's eyes and noticed that blinded bugs turned only approximately a third of a usual counter turn, elevating the significance of vision in navigation. The necessity of a visual system for the navigation process was further confirmed by many other researchers using a variety of different methods tackling this question. Among the examples, we can find observational studies of spiders jumping during prey hunt (Hill, 1979), or using light as a cue to confuse an orb-weaving spider by rotating clockwise his vertically oriented net (Crawford, 1984).

Meanwhile, evidence for the use of idiothetic cues (self-motion cues) -at first suggested by Darwin in 1873 (Darwin, 1873)- started to accumulate. For example, wandering spiders were found to be lost after ablation of their lyriform slit sense organs (Seyfarth et al., 1982), and experiments such as passively relocating a golden hamster, showed their ability to assess angular but not linear components of their journey, thus pointing towards the path integration direction (Etienne et al., 1986).

Further on, a wide spectrum of approaches was developed and a great variety of animals were used to shine light on this process. Spatial research in the early days was primarily characterized by its ethological and ecological approach. The focus used to be mainly on the investigation of the navigational strategies and sensory cues used during the navigation process. In the early '70s, advances in electrophysiology allowed psychologists and neuroscientists to look at the neuronal mechanisms underlying spatial navigation from a new perspective. This new branch of research focused mainly on the recording from the hippocampus and its related areas. It has been dominated by work done on rodents in laboratory conditions. Decades of research revealed a plethora of evidence which helped the scientific community to find a unified consensus in the understanding of mechanisms behind spatial navigation and orientation.

## Understanding variables of orientation and navigation

Orientation and navigation are processes during which an organism moves from a location A to a location B in the environment. Orientation is the process of understanding one's location, and navigation is a way to get to the desired location. In an ideal environment without obstacles, this would be successfully achieved by steering the current direction towards a specific goal and advancing until reaching the target. However, this is only rarely the case in the real world. Therefore, the continuous comparison between current and desired heading translates into compensatory steering commands.

Organisms, locations, and environment, all possess certain variables which can be almost freely combined. Locations or coordinates can either be known or unknown, with a known or unknown distance between them. Distance is usually categorized as immediate, short, medium or large. Depending on the species these terms can obviously have very different scales. Variables of the environment that can be used for orientation and navigation, are called environmental cues. Cues can be either external (environmental) or idiothetic. The external cues depending on their spatial availability differ between global (available almost everywhere on the planet), local (available in the broader environmental area) or immediate (not much larger than organism).

Idiothetic cues differ based on the sense that enregisters them. So far, optic flow (enregistered by vision) and step count (by proprioception) were identified. Global external cues can be further subdivided into celestial bodies (sun, milky-way, stars), skylight gradient (spectral or intensity), polarized light, magnetic field, and time. Local and immediate cues can be either visual, olfactory or auditory landmarks.

To minimize errors, organisms are usually integrating several available cues (using information from multiple sensory modalities) with different reliability values based on momentary signal to noise ratio. Such as vision, olfaction, audition, proprioception, magnetosensation etc. with the addition of integrative higher-order neuronal systems like the memory, compass or cognitive maps. For orientation global external cues are usually used, because their stability makes them more reliable. Navigational strategies depend on available cues and desired precision of navigation. It is common that along the trajectory, navigational strategies change with varying availability of environmental cues and immediate necessity for precision.

## Navigating to the unknown

Most of the time, animals know the direction of their desired location. But sometimes they don't. In that case, they can either forage without following any specific cues or they follow cues towards unknown locations. In the latter case we can observe various behavioural strategies. One example is the "straight-line orientation" during the escape reflex found in the dung beetle (Figure 2) (Dacke et al., 2003; J. J. Foster et al., 2017).

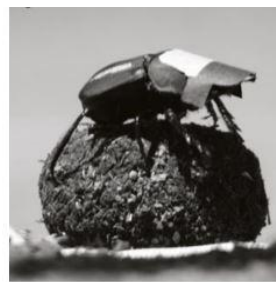
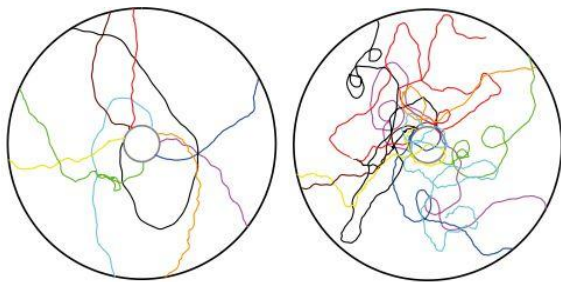


**Figure 2: Escaping Scarabaeus**  
Trajectories during straight-line escape reflex. Left, normal escapes. Middle, escapes while wearing a little hat preventing the bug from seeing the sky. Right, dung beetle with the hat on the top of his dung ball (Dacke et al., 2013).

Another navigation strategy towards unknown locations is olfactory or visual beaconing. Insects like moths follow the steepest slope of the odours concentration gradient (Grünbaum & Willis, 2015), as well as many other animals which follow their prey or search for the food sources -even across medium or long distances- according to the same process. Visual beaconing is mainly used during predation. Video footage analysis of dragonflies hunting drosophila's (Combes et al., 2012) or raptors' prey pursuit (Kane et al., 2015; Kane & Zamani, 2014), revealed an unusual strategy of predators approaching a predicted future prey location (Figure 3). Besides the usual straight-line trajectory towards the goal (tail hunt), aerial predators often take detours on their way to their prey.

Nonetheless, navigation to unknown places represents only a small fraction of all movements. The majority of navigation strategies are directed towards specific goals with a known spatial location. One of the impressive strategies where goal directed navigation becomes obvious is homing. Despite its name, homing strategies don't need to be used for the sole purpose to get home but can also be used to get to any known location.

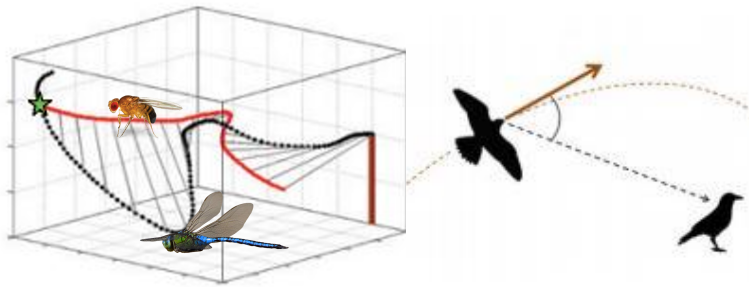


**Figure 3: Aerial predation**

Left, trajectory of a fly hunted by a dragonfly. After the first unsuccessful attempt (at the vicinity of the shortest distance between their trajectories) dragonfly strikes again. Now successfully at the green star. Right, the trajectory of a raptor during a hunt. (Combes et al., 2012; Kane et al., 2015)

## Homing: when you know where to go

Most of the time, when animals navigate towards their goal, they know where the location is. Strategies used while navigating towards the known location depends on the cues used. They can be either idiothetic or external. Idiothetic cues are used during path integration. Path integration is the process of accumulating self-motion evidence. Self-motion cues are either locomotion, vestibular activation or optic flow. For example, the odometer is a homing strategy used by honeybees and desert ants. Both are using global external cues such as celestial compass (Dickinson, 1994; Sommer & Wehner, 2005) or polarized light (Kraft et al., 2011; Leibold et al., 2012) for heading orientation. To estimate travel distances, honeybees use optic-flow based path integrator (Esch & Burns, 1995), while ants living in environments without any proximate visual cues use a step count to measure distances from the nest. Wittlinger's team let ants freely roam from their nest. Once they ventured to a radial distance of 10 meters, they captured them and shortened or prolonged (by cutting or attaching a tiny stilt) (Figure 4) their legs before returning them to the place where they were initially captured. As predicted, ants with shortened steps were looking for their nest in around a half of the distance between the release point and their nest. Contrarily, ants walking on stilts, making large steps, over-shooted the nest of about 5 meters. As a neat confirmation of strategy was the observation that once these ants were placed in the nest, they had no problem finding it again during their future homing (Müller & Wehner, 1988; Wittlinger et al., 2006).



**Figure 4: Ant odometer**

Ants walking on the shortened legs, on stilts or naturally (Wolf, 2011).

In different circumstances, if desert ants are walking in between two well-known locations (e.g. food, nest), in an environment with sufficient visual landmarks, they rather use the image matching based route following strategy (Figure 5). In this case, a current visual input is continuously compared to memorized sequences of visual "snapshots" that define a route for navigation (Kohler & Wehner, 2005).

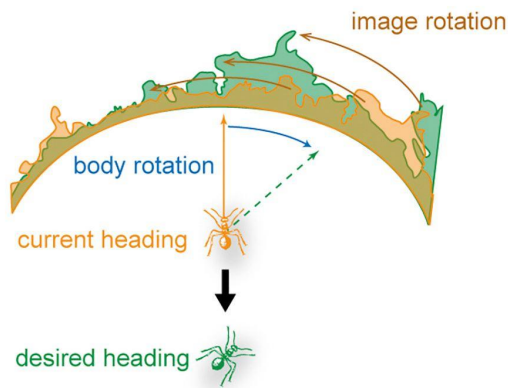


**Figure 5: Image matching**

Schematic of a snapshot strategy based on image matching. In visually rich environments ants use on their routine paths comparison between series of snapshots and current visual input. By performing body rotations they try to optimize compared images for the best match (Heinze, 2017).

Visual landmarks are most often used as a primary local or immediate external cues, even for animals operating in extremely low light conditions. One impressive example of visual cue use is the nest entrance identification in the dense tropical forest at night, conducted by sweat bees. The special anatomy of their compound eyes in combination with spatial and temporal binning during image post-processing leads to 30 times greater light sensitivity than in their cousin the honeybee (Warrant et al., 2004). Studies on countless homing insects, revealed many mechanisms of orientation thanks to their easy handling and manipulation, as well as their relative simplicity as model organisms. Throughout those studies, we learned that almost everyone who has a home is (not surprisingly) able to return home. On the other hand, we understood as well, that not every homing is equal. Some animals, once they get lost, are lost forever. Others get lost every day, but each time they find their way. Nonetheless, we recognise animals with the ability to use a cognitive map as “true navigators” (Kenneth P. Able, 2001; K. P. Able et al., 1980; Emlen, 1975; Keeton, 1974; Phillips, 1996; Wikelski et al., 2015), yet there is no evidence supporting insects being “true navigators”.

### True navigators take shortcuts

The hallmark of true navigation is a shortcut, it refers to the ability of an animal to move freely between places using novel trajectories. This type of behaviour necessitates, besides a compass, the use of cognitive maps of an environment. The use of cognitive maps by rats and man was first predicted in 1948 when Tolman observed flexible inferences of rats navigating in complex mazes (Tolman, 1948). Today, the use of cognitive maps is still perhaps the most sophisticated type of navigation observed in the animal kingdom. The main advantage of this system, in comparison to other navigational strategies lies in its versatility.

True navigation was previously experimentally approached by displacement of animals into an unfamiliar location with no familial landmarks or information about displacement route. Observation of shortcuts used in natural conditions was until now troubled by the uncertainty of their previous use, which would discredit their novelty. However, recent recordings from lab-raised bats showing a whole life-long history of their flight trajectory proved their use of the cognitive map (Figure 6) (Harten et al., 2020).

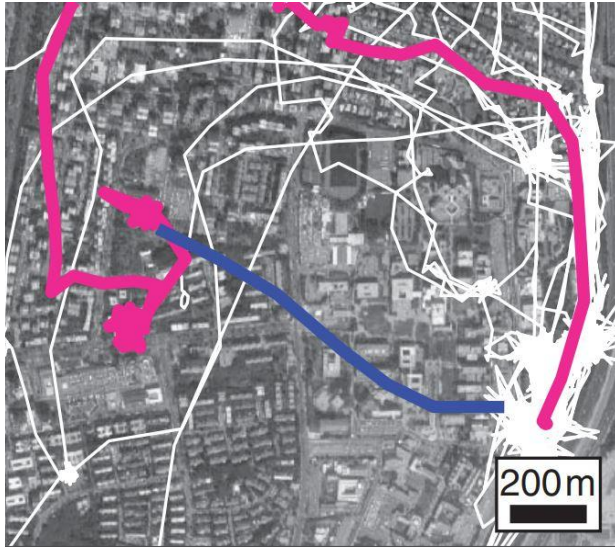


**Figure 6: Shortcut**

The trajectory of a novel shortcut taken by a flying bat is visualized by the blue line. The magenta line shows the same night previous path and the thin white line represents flight trajectories from previous nights (Harten et al., 2020).

So far, only vertebrates (Rodda & Phillips, 1992), and one crustacean (Boles & Lohmann, 2003), were shown to be capable of this form of navigation. Perhaps, the most famous “true navigator” is the previously mentioned homing pigeon (Gagliardo et al., 2005), which seems to use an olfactory gradient map (Figure 7) as suggested by (Wallraff, 2004). While birds were studied for navigation since the beginning, the field of navigation in non-human primates is only poorly developed.

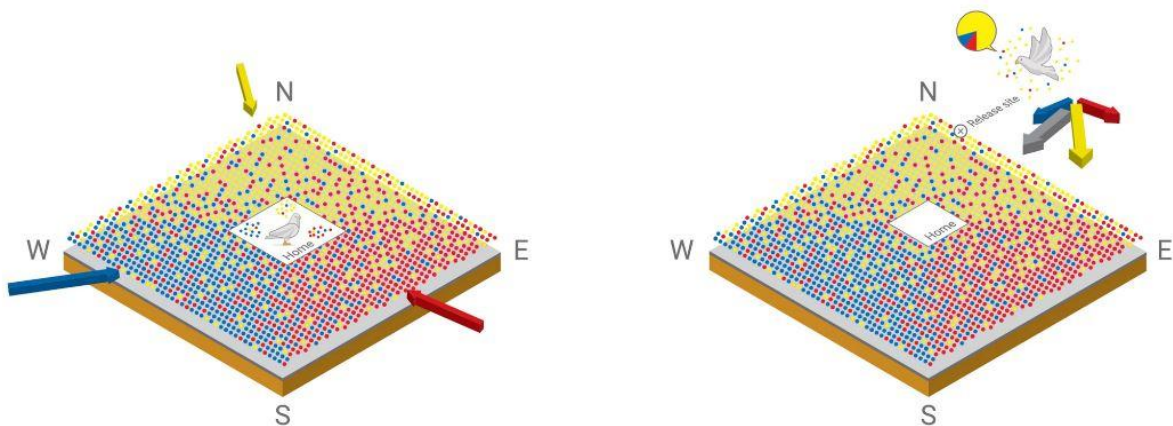


**Figure 7: Cognitive map**

Left, colourful arrows and dots represent the schematic of the odour gradient map of the horizontal plane of the environment with the pigeons home located in the middle. Coloured dots inside the home represent directional exposure of odours from the environment. On the right colourful arrows visualize pigeons perceived odour at the unknown location after the relocation. From (Zannoni et al., 2020).

## The mouse lemur as a navigator

*Microcebus murinus* is a small nocturnal Malagasy prosimian from the genus Lemuriformes. Mouse lemurs can be found in the forests of southern and western Madagascar (Atsalis, 2015). With a body weight of around 60 grams they are among the world's smallest primates (J. Schmid & Speakman, 2000). During the night, they move as solitary foragers, but during the day they sleep in stable social groups (Radespiel, 2000). Babies and adolescent mouse lemurs live with the group they were born in. Both, females and males, forage in around 120m<sup>2</sup> area (Radespiel, 2000). After a year, when males reach adulthood, they leave the home nest to venture into the unknown. Long range dispersal of young adult males during the search for their new territory is the only known long range travel they do in their lifetime. During dispersal, they seemingly choose a random direction (Figure 8). Following a straight line trajectory, they distance themselves from their home territory by a length of one to seven times the home range diameter (up to 960 meters) (Schliehe-Diecks et al., 2012).

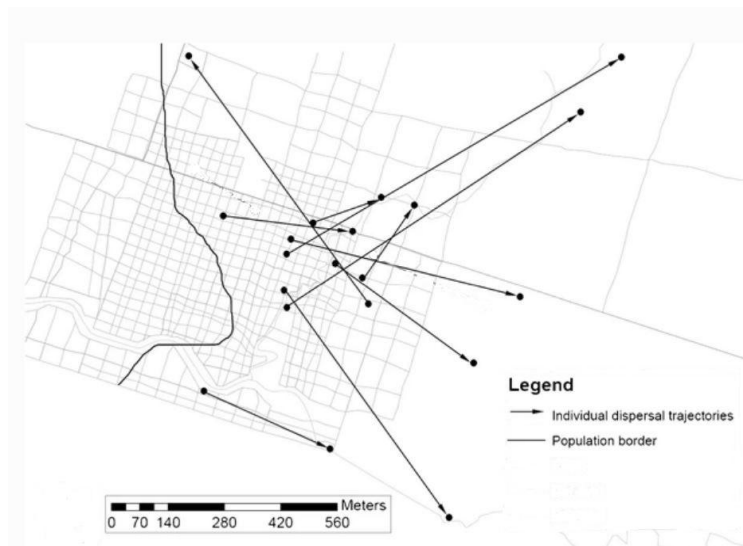


**Figure 8: Random direction dispersal**  
Map of individual dispersal trajectories of 10 male Mouse lemurs. Black dots represent the centre of their territories. Arrow points in the direction of dispersals towards the target territory. Adapted from (Schliehe-Diecks et al., 2012).

The way how mouse lemurs keep a straight line (Figure 9) during dispersals still needs to be discovered. Yet, it is reminiscent of the straight line escape reflex of the dung beetle (see page 5). Once young mouse lemur males establish themselves in a new social group, they are ready for the first mating season. During this time, they frantically search for the receptive females. To succeed in evolutionary competition with their mates they need to reproduce with as many females as they can (Andrès et al., 2003). Though, female lemurs don't make it easy for anyone. Ovulating only one day a year and additionally, in high synchronicity triggered by photoperiod change, female mouse lemurs are usually picky. Female mouse lemurs copulate with up to seven males, thus exerting a high reproductive pressure. As a coping mechanism, males increase the size of their testicles as well as the territory they occupy. Both, testes and territory in this period double their average size (Radespiel, 2000; Jutta Schmid & Kappeler, 1998). Volumetric increase of testes is driven by intense scrambled competition, and the larger the territorial area is, the higher the chance to find a receptive female.

Scanning a large forest area in search of mates, and the ability to navigate from one mate to another seems inevitable. Ultimately, it comes with heaps of homing. Even though evidence for the use of cognitive maps is still missing, its absence would be rather surprising.

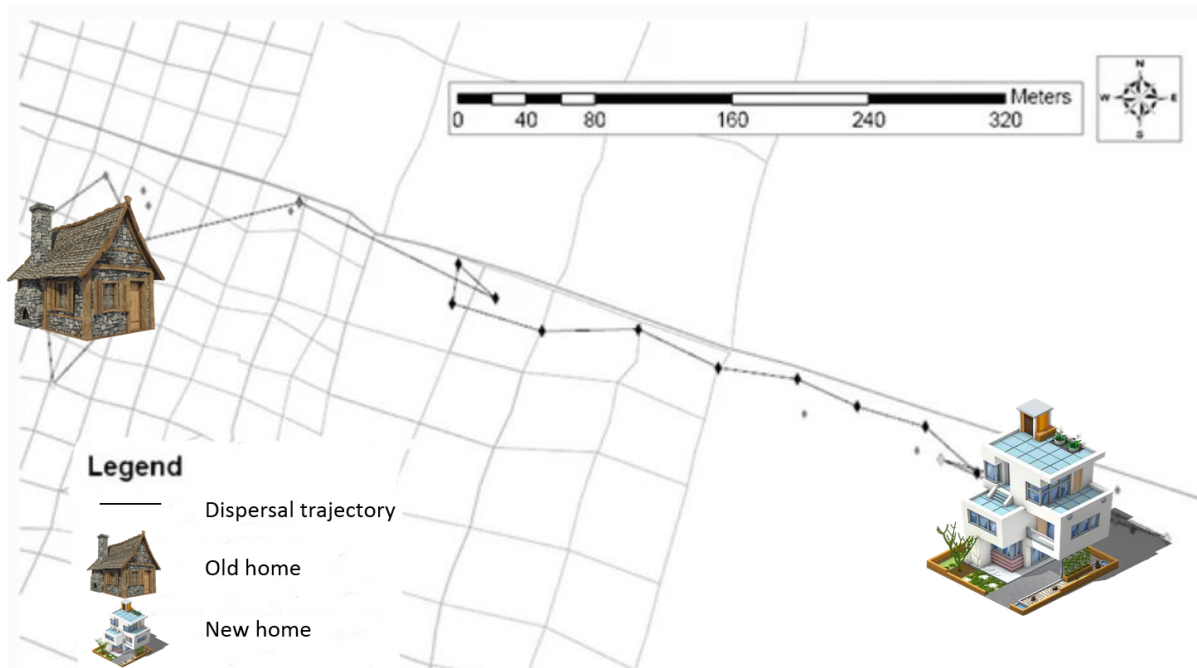


**Figure 9: Dispersal**

Example of mouse lemur dispersal. The old shaded area represents the old home range and the new shaded area is the new home range. The black line with black dots represents the trajectory of dispersal. Adapted from (Schliehe-Diecks et al., 2012).

Nocturnal foraging and navigation in the dense forest vegetation during the night requires excellent vision. The eyes of mouse lemurs are therefore equipped with tapetum lucidum, which acts as a mirror on the back of the retina. Reflecting photons back towards the photosensitive cells increases the chance of photons getting absorbed by the photoreceptors (Garbutt, 1999). Besides the big eyes, mouse lemurs also have big ears and an exquisite chemosensory system (Braune et al., 2005; Kappel et al., 2011; Perret & Schilling, 1993; Sündermann et al., 2008). Nonetheless, the use of its sensory modalities during navigation is largely unknown. This and similar questions are now possible to answer thanks to the mouse lemur colony in Brunoy, France.

The question of how “true navigators” mentally represent the surrounding environment guided the tips of the recording electrodes into the hippocampal area of a rat. This new era, defined by a better understanding of maps used for spatial navigation, began nearly half a century ago when O’Keefe & Dostrovsky recorded neurons in rats’ dorsal CA1 of the hippocampus. Subsequently, spatial research expanded to encompass the whole hippocampal formation revealing a legion of functionally important cells involved in spatial navigation and orientation. Unfortunately, the technical requirements and the necessity for laboratory conditions come at the cost of narrowing the great variety of animal models used in previous spatial research down to three, under the hegemonial domination of rodents. Recent technological advances now present an opportunity to start working with other species again.

# Hippocampal Formation

The hippocampal formation is a compound structure of the medial temporal lobe (Squire et al., 2004). This set of functionally and anatomically closely related brain areas consists of the hippocampus, with several “associated areas” (such as the parahippocampal gyrus, the parasubiculum, the presubiculum and the subiculum) and the entorhinal cortex (Figure 10) (Amaral & Lavenex, 2007). This structure and its internal connectivity pattern are well preserved across mammals (Andersen et al., 2007; Bingman et al., 2009). The internal hippocampal connectivity on the transverse axis is preserved across the whole hippocampus on its longitudinal axis. Nevertheless, dorsal hippocampal formation differs from the ventral hippocampal formation in many aspects, such as gene expression, network dynamics and activation patterns (Strange et al., 2014). In terms of its anatomical division, differences between the dorsal and ventral hippocampal formation lie in the extrinsic connectivity with the rest of the brain. The vast majority of inputs to the hippocampal formation can be best divided into those descending from cortical areas to the entorhinal cortex and the subiculum (Witter, 2010) and those which hippocampal formation receives as innervation from the subcortical regions such as medial septum or supramammillary nucleus. The topological organization between the entorhinal cortex and other cortices is extended to the hippocampus due to direct entorhinal-hippocampal connectivity. This topology is often smooth, continuous and gradual (Strange et al., 2014). Perhaps, the most important and well-known structure of the hippocampal formation is the hippocampus itself.

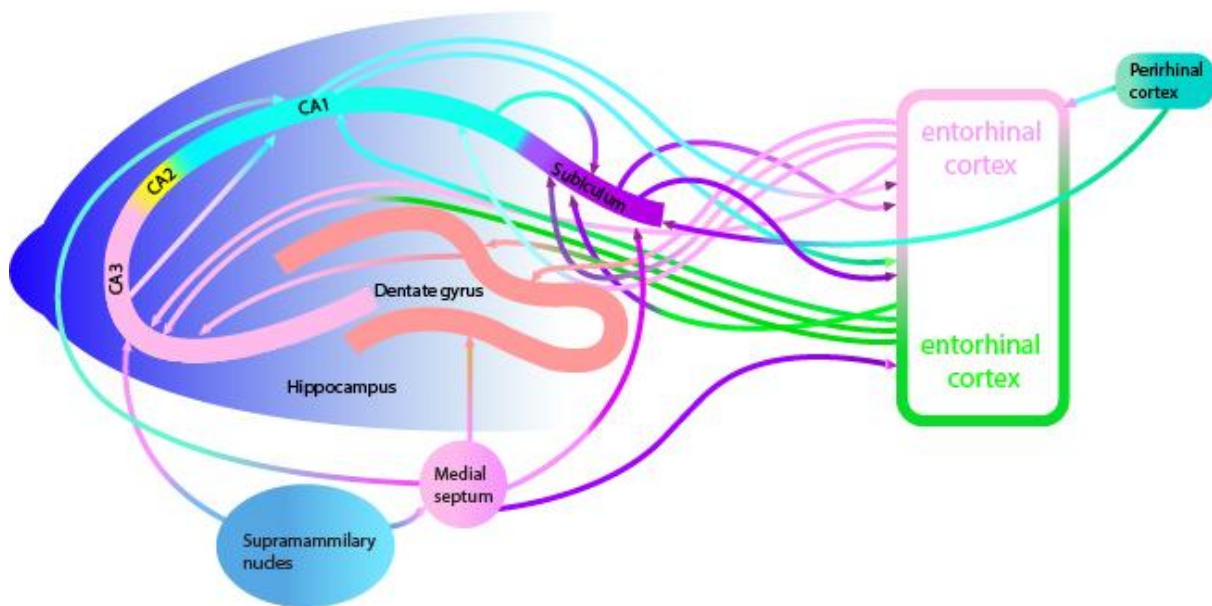


**Figure 10: Hippocampal formation**

Simplified schematic diagram of hippocampal connectivity. Connections with the entorhinal cortex are divided into purple, representing connections with the posterior hippocampus and green, connections with the anterior hippocampus. Adapted from (Kleinfeld et al., 2016).

## Hippocampus

The hippocampus is a "C" shaped (Figure 11) brain structure (Schultz & Engelhardt, 2014) that is a part of the limbic system (Gloor, 1997). If we would section the hippocampus across its transverse axis (Skrede & Westgaard, 1971), we could recognize the unveiled structures, as the hippocampus continues from the cortex: Ammon's horn (*Cornu Ammonis*) fields CA1, CA2, CA3 and the Dentate gyrus (Figure 10) (Amaral & Lavenex, 2007). Internal hippocampal connectivity across this transverse plane is very well maintained along the hippocampal length (Cappaert et al., 2015). The Hippocampus, along its longitudinal axis, is often subdivided into two sections named dorsal and ventral (or anterior and posterior, or septal and temporal) (Fanselow & Dong, 2010). This difference in the nomenclature comes from the relative orientation of the hippocampus ("C"), versus the rest of the brain/body. In rodents dorsal and ventral is most often used, while in primates it is anterior and posterior. Therefore, dorsal or posterior and ventral or anterior terminology will be used interchangeably.

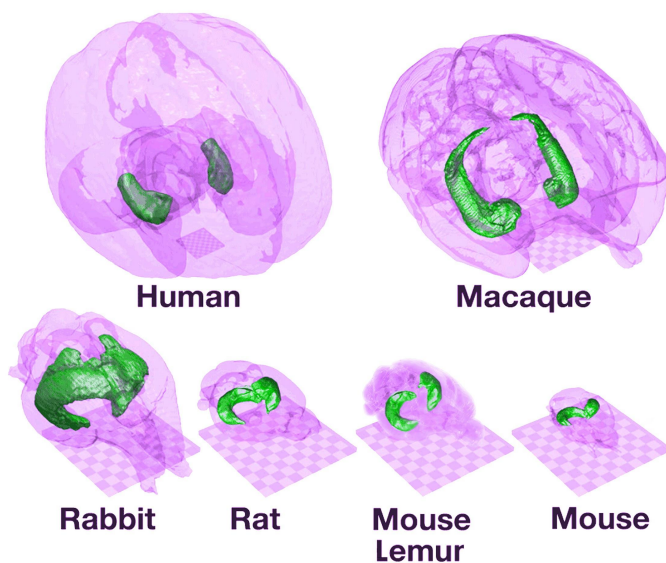


**Figure 11: Hippocampus in the brain**  
Comparison of a brain and hippocampal size and orientation. Purple, outlines of a brain of different animal species with visualization of the hippocampus in green. Adjusted from (Madan, 2015; NITRC, n.d.).

More importantly, this dorsal (posterior) and ventral (anterior) division of the hippocampus is historically based on its observed functions, rather than on clear physiological or cytoarchitectural distinctions. These functional differences between anterior and posterior hippocampus fueled several decades-long hippocampal dichotomy represented by memory vs navigation research camps. However, recent trends point in the direction of a smooth and continuous transition between several functions (Strange et al., 2014).

Rodent research identified expression of over 4000 genes in the hippocampal region, regardless of the neuronal type (Lein et al., 2007). Based on the expression level, the expression density, and the gene clustering, hundreds of selected genes were subjected to further investigation by microarray analysis (RNA-seq), or manual screening of expression patterns (Cembrowski et al., 2016; Dong et al., 2009; Leonardo et al., 2006). Results have shown that the molecular profile of the hippocampal CA1 region, across its longitudinal axis, is very homogeneous. More than 90% of all genes have less than 20% variation in their expression levels, and less than 0.1% (23 genes) showed expression levels differing more than threefold.

The majority of genes with the greatest ratio between expression levels in dorsal vs ventral hippocampus are genes participating in adhesion molecules, ion channels and in general neurotransmitter receptor expression. Changes in expression levels of some of these genes are gradual along the hippocampus, while in others it is strictly discrete at its dorso-ventral regions. In any case, they are primarily bound to the connectivity differences (Leonardo et al., 2006; Yu et al., 2020). This genetic analysis and the resulting distinct molecular profiling across longitudinal axes of the hippocampus could also underpin its functional differentiation.

Because of the circumscribed localisation of these genes in certain areas along the dorso-ventral axis, they have been used as molecular spatial markers. The hippocampal division into gene expression domains matches the functional dichotomy of the hippocampus. The gene expression profile of hippocampus correlates primarily with the regions they directly or indirectly project to or have a reciprocal connection. Therefore the highest correlation of gene expression in dorsal hippocampus can be found in the regions involved in theta rhythm modulation or spatial representation, such as mammillary bodies or anterior thalamic nuclei, both involved in sensory-motor integration of head direction (Cenquizca & Swanson, 2007; Hunsaker et al., 2008; M. B. Moser & Moser, 1998; Jeffrey S. Taube, 2007). On the other end, the gene expression profile of domains located at the ventral part of hippocampus matches with regions regulating autonomic and endocrine systems, as well as emotional or primal goal-directed behaviour involved in reproduction, defence or food searching (Cenquizca & Swanson, 2007; Petrovich et al., 2001; Risold et al., 1997).

Certain differences between the dorsal and ventral hippocampus were also found in the dynamics of its inner circuitry. Dorsal hippocampus seems to have lower intrinsic neuronal excitability and stronger inner inhibition (Dougherty et al., 2012; Malik et al., 2016; Costas Papatheodoropoulos, 2015). Additionally, dorsal CA1 operates on a higher dynamic range of frequency-dependent modulation of both input and output (Koutsoumpa & Papatheodoropoulos, 2019). The input-output relation is strongly influenced by timing and frequency of presynaptic activation of dorsal CA1. Whereas ventral CA1 has shown more monotonous input-output relationships over time and frequency domains and exhibits mostly depression responses to presynaptic activation (Koutsoumpa & Papatheodoropoulos, 2019). These changes in inner circuitry dynamics are gradual along the hippocampus (Malik et al., 2016) and are reflected in the vulnerability to long term potentiation (LTP) induction differences (Maggio & Segal, 2007). The dorsal region of the hippocampus is more prone for LTP induction than the ventral region (Dubovyk & Manahan-Vaughan, 2018; Kouvaros & Papatheodoropoulos, 2016; Maruki et al., 2001; Milior et al., 2016; C. Papatheodoropoulos & Kostopoulos, 2000).

Taken all together, the hippocampus (even though seemingly uniform in structure) performs various types of computations which are mainly dictated by the extrinsic connectivity with the rest of the brain. Additionally, the dorsal part seems to be more promptly reactive to sudden environmental changes. This is in accordance with its functional connections. The dorsal part of the hippocampus is primarily involved in navigation which is a process often involving taking sharp turns.

## Place cells

In 1971, O'Keefe and Dostrovsky recorded single-unit activity in the hippocampus and discovered place cells. The activity of place cells stands out for being solely bound to the rat's position when placed in a recording arena (O'Keefe & Dostrovsky, 1971). The environmental location which activates certain cells is understood as a cell's place field. Research showed that the entire environment is fully covered with such place fields (O'Keefe, 1976; Wilson & McNaughton, 1993) (Figure 12 and 13). Place cells show strong directional sensitivity if recordings take place on a linear track (McNaughton et al., 1983). However, neural responses in open arenas are insensitive to the direction by which an animal approaches the place (Muller et al., 1994). No topological organization was found between place cells and their corresponding place-fields. Even cells in close proximity have unrelated place-fields in different environments (O'Keefe & Conway, 1978).



**Figure 12: Place cells**

Schematic example of visualised place cell activity along a curved linear track (green) on which the mouse walks. Each colourful dot represents a neuronal spike. Dots of the same colour belong to the same neuron.

The activity of place cells is defined by two complementary mechanisms. The environment, which usually contains multiple features and can be perceived by different sensory modalities, and path-integration (self-motion). This division into cues from sensory input and cues from self-motion was predicted by Darwin in 1873 and O'Keefe in 1976 and further substantiated by other scientific findings (Darwin, 1873; O'Keefe, 1976).

Evidence for the impact of environmental sensory input onto place cells activity was documented by (G. Chen et al., 2013; Muller & Kubie, 1987; O'Keefe & Burgess, 1996; O'Keefe & Conway, 1978; Ravassard et al., 2013) who showed how changes of environmental landmarks initiate place fields remapping.

Evidence for path integration was brought by (Aghajan et al., 2015; G. Chen et al., 2013; Gothard et al., 1996; Pastalkova et al., 2008; Quirk et al., 1990; Ravassard et al., 2013; Terrazas et al., 2005; Villette et al., 2015) who demonstrated that the activity of place cells persisted even when the subject was moving in complete darkness, or responded to travelled distance regardless of environmental stimuli. Despite the behavioural evidence, the direct input information channels and their anatomical counterpart has not been straightforward.

The most often investigated environmental cues for spatial navigation are visual landmarks. Other aids for self-localization can be nonvisual cues such as scent, a sound source, a texture, vibrations, etc. In wildlife, animals use a wealth of sensory modalities such as olfaction, acoustic echolocation, light polarization, magnetoreception and many others. In order to maintain the most accurate mental map, cues are differentially weighted based on their importance and reliability. Animals continuously evaluate these cues, thereby building an internal representation of the environment and their location in it. If the cues are insufficient or incoherent with each other, the internal model of the environment becomes inaccurate and the animal is prone to make navigational errors. In that case, certain place cells might exhibit activity not only at their place field but also at a location at which the animal arrives by mistake (O'Keefe & Speakman, 1987).

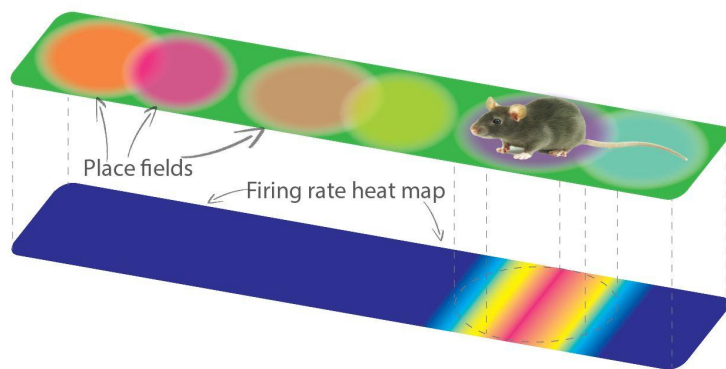


**Figure 13: Place fields**

Mouse on the linear track (green) with visualized place fields (coloured circles). Below, visualized firing rate heat map. Dark blue = no firing, red = maximum firing rate.

If the environment changes drastically and its representation based on previous cues can no longer serve as a reliable map, remapping takes place. Based on the severity of the changes, remapping can take place partially or totally. In general, only a small fraction of hippocampal CA1 cells participates with its activity in the encoding of one location; when total remapping occurs a whole new set of neurons ends up coding for the same location (Alme et al., 2014; Leutgeb et al., 2005; Thompson & Best, 1989). Since the physical space is fully covered by place fields and the borders of place fields are not strictly defined, they often tend to overlap; as a consequence, clusters of cells from neighbouring place-fields often fire together, a phenomenon called “cell ensemble”. These environment-specific ensembles are thought to encode for the location and also for a specific environmental identity (Kubie & Muller, 1991). During total/global remapping, old ensembles vanish and a full set of brand new ensembles emerges.

This new ensemble is then orthogonal to the previous (original) one (Anderson & Jeffery, 2003; Latuske et al., 2017; Vazdarjanova & Guzowski, 2004). During partial remapping most of the cells keep their initial place-field and therefore the new ensembles differ only by a subgroup of cells. Moreover, individual place cells are inherently unstable. While some place cells change their place fields in the course of minutes (Mau et al., 2018), some persist longer and only 15% of place cells show stability across days (Ziv et al., 2013). The record in stability holds Best documented place cell with persistent activity for 153 consecutive days (Thompson & Best, 1989).

## Entorhinal cortex

Through the first 30 years of spatial research, the scientific community focused primarily on the hippocampus and its place cells. Well-defined rodent-like place cells were, to some extent, successfully found in bats. In primates, spatial view cells were accepted to be analogous to rodent place cells, as it was attributed to species' specific use of different spatial reference frames and cognitive ability of self perception in space. Additionally, recent evidence suggests that the initially discovered spatial view cells might reflect a rather conceptual representation (Baraduc et al., 2019). Later, other brain areas were also shown to play an important role in spatial navigation, such as the entorhinal cortex (EC), which represents a major anatomical input into the hippocampal formation. The rest of the hippocampal formation is often considered a direct morphological extension of the entorhinal cortex. The medial part of the entorhinal cortex plays a major role in the complex process of spatial computation. The EC belongs to a group of associative cortices whose functional properties are usually hard to interpret. Contrarily, somatosensory, motor, visual or any other primary cortex have the advantage of relatively clear relations between neuronal firing rate and the stimulus properties. Matching the neuronal correlates of the associative cortices with behavioural variables is more than difficult. This is due to the mixture of multiple inputs from areas which already heavily process input signals. The entorhinal cortex represents the only known exception to this rule.

The entorhinal cortex gained the spotlight of the spatial navigation research community in 2005. If this structure did not garner its deserved attention previously, it is mainly due to the misleading interpretation of EC cells coding only for weakly tuned place fields (Quirk et al. 1990). As a result, for a long time it was outside the considerations for a computationally important input to the hippocampus. Subsequently, many theories and models predicted that place cell activity emerges strictly from internal hippocampal circuitry. They predicted that the spatial tuning of CA1 neurons would be decimated by ablating CA1 from the rest of the hippocampal formation. In the first place, McNaughton and colleagues destroyed the CA1 inputs from the Dentate gyrus (McNaughton et al. 1989), to which no effect ensued on place cell activity. In further research, Mizumori and colleagues abolished the medial septal inputs (Mizumori et al. 1989), and likewise the place cell formation remained unaffected. Lastly, Brun and colleagues lesioned the connection between CA3 and CA1 (Brun et al. 2002), and concluded once again, a neglectable effect on place cell activity.

After the exhaustive sequential dissection of the inner hippocampal inputs into the CA1 proved ineffective, the input from the EC has been reexamined. This reexamination was inspired by Menno Witter's review of the entorhinal-hippocampal systems, and his suggestion during direct consultations with Mosers (Moser et al. 2017). In light of this reconsideration, functionally-distinct types of neurons were found in the medial entorhinal cortex. Similar to the primary sensory cortices these cells displayed firing correlates with behaviour that were easily observed and well defined. Moreover, the fact that these cells never changed their roles makes them alluring for investigation. Most of the functionally different cells can be found in the entorhinal cortex, and perhaps the most computationally interesting are the grid cells.

## Grid cells

After almost 30 years since the first discovery of place-tuned neurons in the entorhinal cortex, electrodes were inserted into this area once again. Fyhn and colleagues observed that the medial entorhinal cortex (MEC) cells had place cell-like characteristics, although with the difference of sensitivity at multiple place-fields distributed over the environment in a more regular manner than expected by chance (Fyhn et al., 2004). Following enlargement of the recording arena diameter to 2m allowed them to spot a clear hexagonal pattern (Hafting et al., 2005) (Figure 14). Shortly after, grid cells were observed in many other species such as mice (Fyhn et al., 2008), bats (Yartsev et al., 2011), monkeys (Killian et al., 2012) and humans (Doeller et al., 2010; Jacobs et al., 2013).

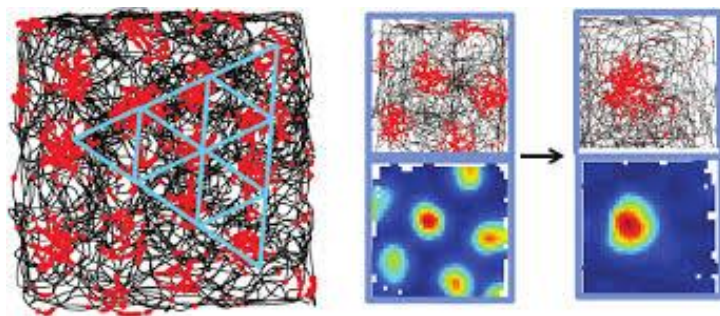


**Figure 14: Grid cells**

Example of grid cell activity. Left, squared recording arena with a trace of the trajectory (black line) and single neuron spiking activity (red dots). In the middle and right top, same visualization and below heat-map representing firing rate, from blue = no firing to red = maximum firing rate (M.-B. Moser et al., 2015).

### Grid cell characteristics

In 2005, Hafting and colleagues noticed populations of cells representing grids with different lengths between receptive fields. Subsequently, he noticed that individual cells can have different firing rates, and that cells belonging to the population with the same size grid tend to be oriented the same way, but with a certain phase shift (Hafting et al., 2005). Hence, only a few cells are sufficient to cover the whole environmental area with their receptive fields.

In addition, Barry and colleagues noticed that the distribution of grid cells across the medial-entorhinal cortex, from dorsal to ventral, correlates with an increased distance between receptive fields (Barry et al., 2007). This increase along the dorso-ventral axis mirrors the increase of the place cell receptive field in the hippocampal formation (Jung et al., 1994; Kjelstrup et al., 2008) (Figure 15).

What is more, the growth of the grid is not smooth, but falls into discrete modules in a stepwise fashion. The presence of grid cells along the whole medial-entorhinal cortex was proven in 2008 (Brun et al., 2008). Later on, Stensola and colleagues documented the presence of at least five different sizes of the grid encoded by the cells in the medial entorhinal cortex (H. Stensola et al., 2012). The difference in size between grids is a constant ratio of around 1.421. This ratio seems to be an ideal ratio, for a set of frequencies to span space for efficient coding (Vágó & Ujfalussy, 2018).

An additional feature of grids is shearing-induced asymmetry (T. Stensola et al., 2015). Shearing, as an elliptic distortion of a grid, creates an angular misalignment in relation to the walls of the squared, rectangular or triangular etc. environment. This misalignment reduces the symmetry of the environment in order not to mistake the corner of a square room in which one is located (T. Stensola et al., 2015). This misalignment in squared arenas is usually  $7.5^\circ$ .

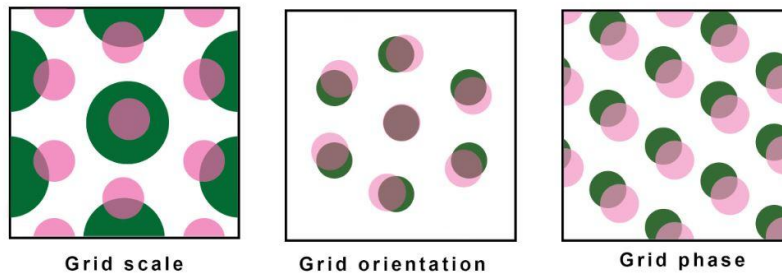


**Figure 15: Grid**

Schematic representation of grid characteristics. Left, grid-scale, grids of different sizes. Middle, grid orientation in the squared arena is usually rotated to minimize uncertainty level. Right, phase shift of two different grid cells. Adjusted from (E. I. Moser et al., 2014).

There are different types of grid cells. Either they are pure grid cells or they can be conjunctive with the head direction. Pure grid cells are thought to be omnidirectional while conjunctive grid cells are firing in their place fields only if the animal's head direction agrees with the cell's preferred head direction. (Hardcastle et al., 2017; Sargolini et al., 2006). However, a recent study showed that individual place fields of pure grid cells might also be tuned. Tuned to multiple head directions with the preferred sets of directions that are differing between fields (Gerlei et al., 2020). The fact that these grids keep their orientation and size in all environments, regardless of the speed of movement or absence of any grid-like structure, suggests that the grid is created purely by the brain itself. Similarly to place cells, grid cells do not hold any obvious topological organization with their environment (Hafting et al., 2005).

## Head direction cells

Head direction cells are responsive to the azimuth of head direction and thus essential in navigation. They were recorded for the first time in the postsubiculum (J. S. Taube et al., 1990) and later abundantly found in several brain areas such as anterior thalamic nuclei (J. S. Taube, 1995), lateral dorsal thalamus (Mizumori & Williams, 1993), retrosplenial cortex (L. L. Chen et al., 1994), striatum (Wiener, 1993) and the lateral mammillary nuclei (Leonhard et al., 1996). Nowadays, most attention is paid to head direction (HD) cells from Medial Entorhinal Cortex (MEC).

Head direction cells seem to have extraordinary stability. The activity of these cells is irrespective of the proximate environment, they are unaffected by substantial environmental changes, as for example the presence (or absence) of a home cage, or the introduction of a new boundary in the recording area. Their activity is often persistent even after sleep. This makes them one of the most stable functionally specific cells used in spatial navigation systems, contrasting the place cells or grid cells, which both exhibit a certain amount of remapping or distortion after environmental changes (Barry et al., 2006; Sanguinetti-Scheck & Brecht, 2020).

Shortly after the initial discovery of HD cells, Skaggs proposed an attractor model mechanism (Skaggs et al., 1995) (Figure 16) based on connectivity between cells organized into a physical ring. A persistent activity bump created from a mixture of vestibular path-integration information and landmark-based visual information input travels along the circle as the animal turns its head.

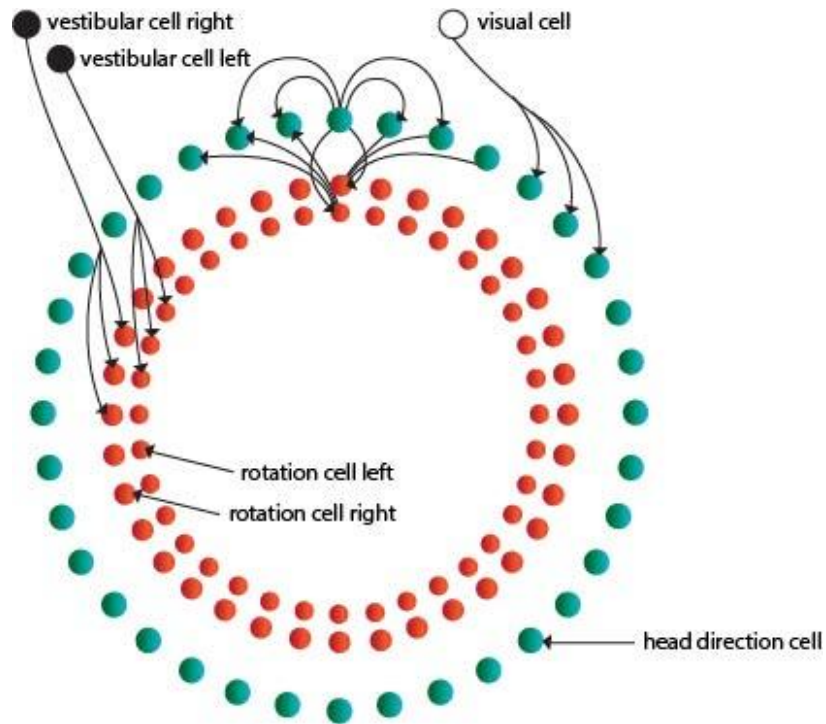


**Figure 16: Head direction model**

The architecture of the head direction cell model adapted from (Skaggs et al., 1995).

Head direction cells seem to be functionally independent of the medial-entorhinal cortex and other cells in the hippocampal formation. Behavioural evidence indicates the necessity of the nucleus prepositus for their function. The nucleus prepositus is a small structure located at the caudal pons which is known to be a part of the horizontal gaze holding system that acts as a neural integrator. The unimodal function, early development and independence of these cells, qualifies them as the foundation for the internal compass used in orientation. Also, optogenetically induced functional disruption of this structure in rodents lead to an error in homing direction (Butler et al., 2017).

Evidence for head-direction (HD) cells was afterwards found also in other species than rodents. But the idea that a persistent activity bump travels in compensatory direction to angular head movement on the physical ring, was only confirmed when the group of Vivek Jayaraman published in 2017 a paper about ring attractor dynamics in the fruit fly. They found cells organized in the actual ring, in the ellipsoid body of a drosophila using calcium imaging during head-fixed flight (S. S. Kim et al., 2017).

## Border cells

Another functionally distinct cell type is the so-called boundary-vector/boundary/border cells. The existence of these cells was predicted and modelled by Burgess et al. in 2006, two years prior to their discovery (Barry et al., 2006). In 2008, Moser's group presented for the first time evidence of these cells in the entorhinal cortex and parasubiculum. Their presence has been reported in all layers of the medial entorhinal cortex, representing approximately 10% of the local population count (Bjerknes et al., 2014; Savelli et al., 2008; Solstad et al., 2008).

Afterwards they were also found more abundantly in the subiculum (Lever et al., 2009). Their activity is orientation-specific and edge-opposing. They possess firing properties similar to those found in place cells. More specifically, these cells fire in the close vicinity of the physical boundary, which could either be a wall or an edge of the platform. Their activity persists even after an environmental alteration (e.g. stretching of the recording area, changing the experimental room or after the introduction of new boundaries in the recording area) (Figure 23). Experimental evidence confirms the predicted stability of the border cells. For example in 2008, Savelli conducted an experiment which consisted of the sudden and complete removal of the walls installed in a squared recording arena occupied by mice, causing the mice's boundary vector cells to turn off, and only to reactivate once in the proximate vicinity of the new corresponding walls (Savelli et al., 2008). Due to the stability of these cells, it has been suggested that they would play a role in the matter of planning and anchoring the entorhinal grids and the hippocampal place fields to a geometric reference frame (Solstad et al., 2008).

## Speed cells

The last from the arsenal of functionally specific cells I will mention is the speed cell. These velocity modulated cells were mentioned for the first time in 2006, in an article written by Sargolini and colleagues explaining that grid cells, head direction cells and conjunctive cells were all modulated by running speed (Sargolini et al., 2006). These results inspired the Mosers group, which investigated this new idea and published an article in 2015 dedicated to speed cells. They were recording from all layers of the MEC and the hippocampal formation using two different setups. In the first setup, a rat had to run along a four-meter linear track in the motorized bottomless and roofless box. The second assay was a free exploration of a squared recording arena. The results showed that speed cells are context invariant path integrators with linear positive response to the running speed. Their speed modulated activity is stable across time and space sharing a prospective bias of ~50-80 ms with the grid cells. They might represent an important element in the clockwork of dynamic representation of self-location (Kropff et al., 2015).

Single-cell recordings helped to identify numerous functionally different cells. Each having a specific purpose that they contribute with their activation patterns to neatly orchestrated global activity. As none without the rest would be able to provide the necessary computational complexity for the process of orientation and navigation. What are the observed correlations between their activation? In order to fully understand the information flow, the occurrence and disappearance of their activity or association with memory and context, it is important to scale up the investigation of this system from a single cell to a cell population level. Local field potentials are a measure of concurrent activity of large numbers of cells. Different frequencies of this activation often come with their behavioural correlates.

# The oscillatory activity

Considering all the functionally different cells, knowing their roles and relationships between them, we can henceforth partially explain the process of registering environmental cues, sense of orientation and path integration. The environmental cues act as a base for allocentric perception, whereas the registration of the self-motion is used for the egocentric understanding of one's position. Despite its complexity, this process does not appear to be sufficient for effective navigational behaviour. The necessity of post-processing and storage of spatial information into memory is inevitable if one has to deal with life-like situations in complex and large territories in an ever-changing environment. It is known that a single neuron has only a limited capacity for computational processes; therefore, the coordination of multiple neurons is necessary for memory formation. The basic principle of memory formation can be seen as a well-orchestrated consequential-reactivation of distributed neuronal ensembles. These neuronal ensembles, if successfully stored, are thought to represent basic memory units, a process long known as Hebbian learning (Hebb, 1949). In order to facilitate the transmission of the immediate information into memory, the brain is thought to employ different periodically fluctuating waves of synchronous neuronal activity. Large numbers of cells produce electric currents whose superposition is measurable as local field potential (LFP). This LFP signal is often strong enough to be detected through the intact human skull by a surface electrode, a recording method commonly known as an electroencephalogram (EEG). The hippocampal LFP is, due to the innate hippocampal cytoarchitecture, stronger than in any other region in the brain. This is especially valid for the CA1 region of the hippocampal formation, where dendrites of pyramidal neurons are collaterally and homogeneously aligned, resulting in the summation of aligned synaptic current flow and therefore in very large LFP. Unfortunately, the hippocampus is deeply embedded in the brain and so far, only invasive techniques could be used for recordings, limiting in vivo studies to animal models.

## Place cells and theta oscillations

Theta oscillations are relatively slow (4-10Hz) sinusoidal waves prominent in rodent hippocampal regions (Kahana et al., 2001). They are mostly present during REM sleep, during active exploration and locomotion or other voluntary behaviours (Bragin et al., 1995; Vanderwolf, 1969). Their presence is confirmed in many animal species such as mice, rats, cats, monkeys and humans (Green & Arduini, 1954; Jutras et al., 2013). Theta waves are thought to be driven by the medial septal-diagonal band of Broca which has a direct implication on the generation of hippocampal theta oscillation (Green & Arduini, 1954; Mitchell et al., 1982). Theta waves then travel across the whole hippocampal length in the dorso-ventral direction. Meanwhile they are progressively subjected to half a cycle phase shift, decrease in power, frequency and coherence (Patel et al., 2012). The medial septal inhibitory interneurons project to the hippocampal formation (Freund & Antal, 1988), where through oscillatory inhibition of the hippocampal interneurons disinhibit the pyramidal neurons resulting in theta oscillations (Hangya et al., 2009). More specifically, septal interneurons modulate several types of hippocampal interneurons (Freund & Antal, 1988) which are interlocked with precise phases of the theta oscillation cycle (Skaggs et al., 1996). Perisomatically targeting hippocampal interneurons are active at an early stage of the theta cycle with control over the theta phase of place cell spike, whereas dendrite targeting interneurons fire later in the theta cycle and gate the place cell bursting activity (Royer et al.,

2012). Besides the inhibitory mechanisms, theta oscillations are modulated also by excitatory connections from the entorhinal cortex. These postsynaptic excitatory currents are phase-locked with theta oscillations (Pernía-Andrade & Jonas, 2014) and are proven necessary for place cell activation (Dickson et al., 2000). A result of these excitatory and inhibitory activities is hippocampal place cell phase precession. Place cell activity onset - at the beginning of the place field - occurs around 360° of the theta wave and continuously moves towards the 0° as the animal advances across the place field (O'Keefe & Recce, 1993; Skaggs et al., 1996).

The behavioural importance of theta oscillation in the learning process and the memory formation was corroborated by two studies in the 1970s. In the first study carried out with rats, a positive correlation between learning aversive stimuli and theta oscillations was demonstrated (Landfield et al., 1972). In the second study carried out with rabbits, theta oscillations were employed as a strong predictor for estimating the learning rate in rabbits (Berry & Thompson, 1978). Later on, numerous pieces of evidence supported the theory that theta waves coordinate the activity of the neurons into specific sequences, and that these sequences are the necessary building blocks for memory formation (Wang et al., 2015). Thereafter, the neuronal ensembles organized by theta waves were defined and referred to as "theta sequences" (Figure 17) (Dragoi & Buzsáki, 2006; D. J. Foster & Wilson, 2007; Skaggs et al., 1996). Theta-sequences seem to integrate not only spatial but also experience-dependent multisensory information like olfaction (Macrides et al., 1982) or whisking (Komisaruk, 1970), and therefore create complex meaningful memory.

While theta is already present during the exploration of a novel environment, theta-sequences are developed with experience (Feng et al., 2015). They represent chunks of meaningful spacetime information (Gupta et al., 2012), that can further be used to reflect current goals in context-dependent environments (Wikenheiser & Redish, 2015).

Theta sequences can swiftly change, on a moment-by-moment basis, depending on the rat's current goal and therefore suggests that these sequences are dynamically linking different cell ensembles rather than representing hard-coded connections. Depending on the current needs, this process creates an integrated representation of complex concepts (Wikenheiser & Redish, 2015).

Additionally, the theta rhythm seems to be aligned with probing sensory input and uncoupled with the input of low informational value. When conducting the olfactory discrimination task in rats, if the theta is aligned with the sniffing and whisking rhythm, the performance is significantly higher than in a case of misalignment (Kepecs et al., 2007). If the animal is just aimlessly sniffing into the air, the theta conveys no correlation (Berg et al., 2006). In primates however, during a visual discrimination task, eye saccades were shown to reset theta oscillations (Jutras et al., 2013). It is, therefore, reasonable to think that attention directed towards sensory input of high value is priming the brain for encoding, in order to create a meaningful internal representation of reality. It seems plausible that theta cycles represent basic building blocks of episodic memory with the capability to encode meaningful information, happening in discrete space-time chunks as theta-sequences.

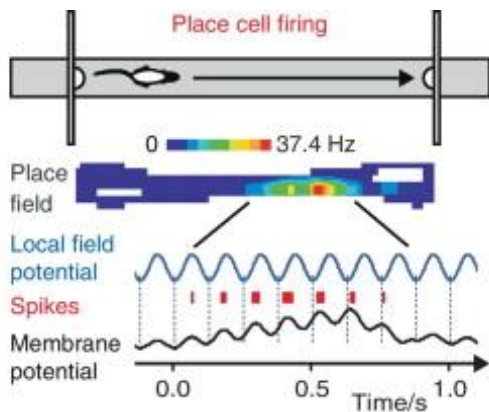


**Figure 17: Theta sequences**

Single place cell firing within the theta phase. On the left top trajectory of a mouse walking on a linear track while passing over the place cell placefield. Below, heat-map of firing activity of the place cell under which zoomed on the LFP during place field crossing. Red ticks represent spikes and their position within the LFP cycle. On the bottom left is shown the cell membrane potential and timeline (Burgess & O'Keefe, 2011).

Theta oscillations are widely thought to be substantial for place cell formation. In support of this mechanism, studies exhibit extremely fast flickering between place-cell maps on the scale of one theta cycle, in between two environments (Jezek et al., 2011).

Other findings indicate a re-learning process of the altered -same- environment, where largely segregated theta sequences were progressively interchanged with new ones, as the animal learned a new position of hidden food location. This evidence was concordant with place cell map formation (Dupret et al., 2013).

The segregation of the theta sequences has been documented in a study showing that head direction cells with similar preferred azimuthal orientation, tend to be part of the same theta sequence while cells tuned to different orientations are segregated into different theta cycles (Brandon et al., 2013).

The studies mentioned above signal the importance of theta oscillations for multisensory information integration and memory formation. However, several studies put a big question mark above these theories. They highlight how place cell formation occurs after blocking the theta, by ablating inputs from medial septum, suggesting that place cell activity could be independent of the theta activity (Brandon et al., 2014). In addition, recordings from Egyptian fruit bats show little to no theta activity in the hippocampal formation nor the entorhinal cortex (Eliav et al., 2018; Yartsev et al., 2011; Yartsev & Ulanovsky, 2013).

While behavioural effects of theta during waking states have been demonstrated (Bieri et al., 2014; Blair et al., 2007; Burgess et al., 2007; Colgin, 2016; Domnisoru et al., 2013; Hasselmo et al., 2007; Jutras et al., 2013; O'Keefe & Recce, 1993; Skaggs et al., 1996), theta oscillations are also prominent during REM sleep (Cantero et al., 2003; Del Rio-Bermudez et al., 2017; Gonzalez et al., 2018; B. Kim et al., 2017). There is also a plethora of evidence showing cell sequence replays during sleep. Theta might therefore also play a role in the memory consolidation process (Boyce et al., 2016; Headley & Paré, 2017; Klimesch, 2003; Langille, 2019; Ognjanovski et al., 2018). Besides rodents, there is only little evidence for theta activity regarding navigation in primates or bats. Nevertheless, the absence of theta does not seem to influence the presence of their spatially modulated cells.

# Evidence from non-rodent animal models

## Place cells in bats

A great effort towards the understanding of spatial navigation in the Egyptian fruit bat (*Rousettus aegyptiacus*) or the Big brown bat (*Eptesicus fuscus*) has been carried out by the group of Prof. Nachum Ulanovsky. Even though bats were last to join the menagerie of spatial navigation neuroscience, they caught up fast and entrenched themselves in the field. Place cells in bats were found in 2007, in a study involving two bats crawling and sleeping alternatively in a 0.5 m<sup>2</sup> arena while the activity of the pyramidal neurons in the septal part of hippocampal CA1 was recorded. Around 30% of recorded cells were classified as place cells with characteristics of those in rodents. However, the majority of them were active during sleeping periods (Ulanovsky & Moss, 2007).

Later, his lab reported spatial view cells as were known from the primate literature (see page 29 paragraph 3) (Ulanovsky & Moss, 2011), i.e. cells with activity bound to the view of a certain spatial area. Further, new species-specific characteristics of place cells were reported. They showed to have a dynamic relationship between the size of the place fields and the temporal distance of the spatial information availability. More concretely, echolocation-defined place-fields were diffusing with time. Further, his lab also reported spatial goal cells coding for vectorial representation of a reward location (Sarel et al., 2017) or social place-cells coding for location of conspecifics (Omer et al., 2018).

## Place cells in primates

Ensuing the discovery of place cells in rodents, scientists have wondered if these neurons exist also within the primate brain. Unfortunately, to this day, primate studies on the topic are somewhat limited. Primates, usually navigating in three dimensions, were initially subject to experiments focused on exploring their two-dimensional representation with hopes for the discovery of rodent-like place cells. The search for space representation in the primate hippocampus began in 1985 when Watanabe and Niki used a two-choice visual delayed response task to examine whether or not neurons in the hippocampus showed patterns of discharge related to some aspects of the task. They recorded nearly 2000 neurons in the macaque hippocampal area, finding dozens of neurons exhibiting an increased activity in response to specific events during the task or during the answering period (Watanabe & Niki, 1985).

Similar results have been reported by Miyashita and Niki in 1989. In their study, individual neurons located in hippocampal CA3 were activated by a differential position of target objects shown to the monkey on a touch screen. They concluded the necessity of associating objects and positions for a correct learning process (Miyashita et al., 1989). In 1990, Tamura and Nakamura head-fixed a stationary monkey, but with the ability to rotate by himself and thus visually inspect its environment. The study brought for the first time partial evidence for encoding egocentric and allocentric coordinates in the primate hippocampus. Besides allocentric and egocentric neurons, they found intermediate conjunctive neurons. The analysis of the activity from the hippocampal formation resulted in around 10% of neurons classified as responsive to space or auditory modulation (Tamura et al., 1990). Most importantly, this experiment set a new experimental standard for the following years.

In 1991 Ono et al. adopted a similar experimental setup. Although in this case, the monkey, despite being fixed in a restraining chair, was able to partially move by pressing a push-button on the chair (i.e. the “monkey in the cab” experiment)(Figure 18).

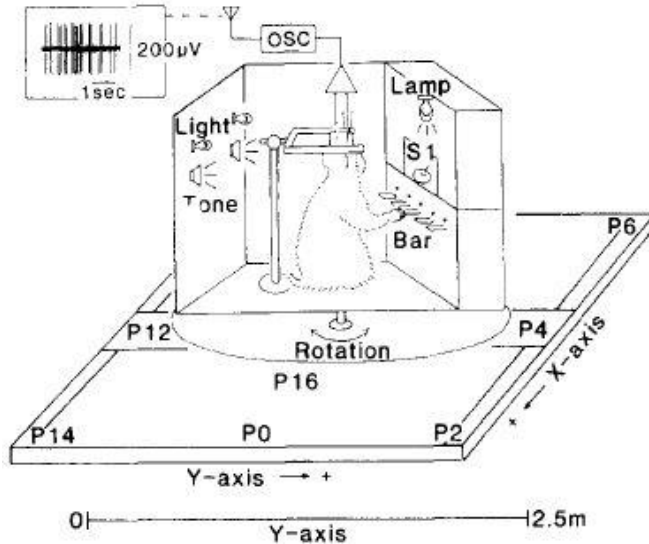


**Figure 18: Cab experiment**

Experimental setup referred to as “monkey in the cab” first time by Ono in 1991. The monkey is head-fixed in the cab and can rotate and move via pressing bars in front of him. The cab is equipped with several sensory stimuli such as loud speakers or light bulbs positioned around its head. The cab has a window in front of the monkey's face that allows observation of the environment in front of the cab (Ono et al., 1991).

The monkey was presented with various visual stimuli from different directions and locations. Approximately 10% of neurons were selective to the direction of the stimulus and around 25% showed activity related to location. Out of all the location-specific neurons, a quarter was correlated to location and stimulus at the same time. They concluded high proximity between egocentric and allocentric space representation of the primate hippocampus (Ono et al., 1991).

In 1992, Tamura et al. reported another experiment using stationary monkeys being presented with a visual and auditory stimulus. They analysed over one thousand neurons, and 10% of those neurons showed visual, auditory, mixed (visual and auditory) or directional stimulus-response. The responses recorded were further classified as selective or nonselective, and allocentric or egocentric. They concluded that the recorded neurons might be involved in the identification of the relationship between different sensory modalities (Tamura et al., 1992).

In 1993, Ono et al. reported the “monkey in the cab” experiment. More than a third of the recorded neurons were responsive to spatial location, another third to the cues in a spatial moving task, 17% were directionally selective and 14% were responsive to a combination of task and location. Relatedness of neuronal activity with the occurrence of significant events and monkeys' location was understood as a result of the hippocampal gating on incoming information. They suggested the episodic memory to be a linkage between spatial and non-spatial hippocampal memory (Ono et al., 1993).

In another cab experiment, Rolls showed that around 10% of neurons displayed a whole-body motion-related activity. In this experiment, the monkey could move and turn in a 2x2m arena and collect the reward, in the form of fruit pieces, by moving to the location where the food was hidden, under inverted cups.

The results suggested that the whole body motion and the spatial view is represented in the hippocampus, and therefore that the hippocampus plays a central part in spatial memory and navigation (O'Mara et al., 1994).

A year later, Rolls and his colleagues published an article where he established the nomenclature of “spatial view cell”. He found that around 6% of recorded cells in the monkey hippocampus showed view-related activity. They concluded that spatial view-responsive neurons are most probably useful for forming memories of environments. Additionally, when those neurons are combined with the whole-body motion neurons, it seems that they are proven useful in the process of remembering trajectories, which also plays a role in short-range spatial navigation (E. T. Rolls & O'Mara, 1995).

In 1997, two papers were published. In the first paper, Nishijo and colleagues suggested that the hippocampus accurately represents space, in situations where the animal is being particularly active in that space. Following this experiment, they claimed that almost half of the neurons are place-action related. In the second paper, Rolls and his colleagues described an experiment in which the monkeys in the cab were able to move in the 2.7x2.7m arena. It differed from previous experiments, as the monkeys were now able to walk by themselves, rather than using a manipulandum. Additionally, for the first time, they used the search coil technique with field coils attached to the chair to record eye position (horizontal and vertical). They reported spatial view cells which are strictly activated when the monkeys are looking at a particular place, independent of the animal's location or head-direction. (Figure 19) They concluded that the allocentric representation of “out there” is part of the primate memory system involved with memories of objects in space. That memory of the location as a spatial component of the event or episode provides part of the memory context (E. T. Rolls et al., 1997). In 1998, Rolls and colleagues described the hippocampal ensembles' information processing and their distributed encoding. By extracting information bit rate from activity in and out of the receptive fields, and calculating their neuronal contribution in population coding, they contributed to the theoretical framework of the pattern separation, and the exponential increase in stimulus encoding capacity theory (E. T. Rolls et al., 1998).

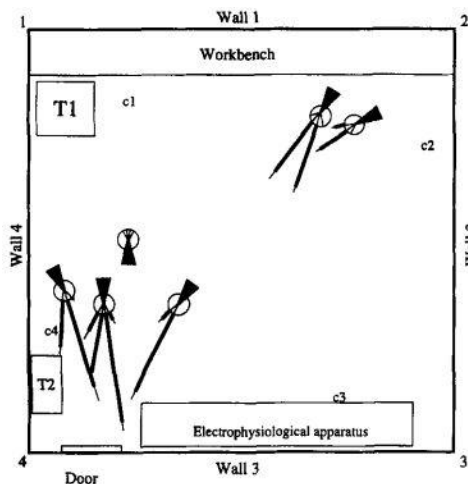


**Figure 19: Spatial view cells**

Results of the experiment where the monkey in the cab actively walked in the room. Position and head direction were tracked by video monitoring and for gaze estimation was used search coil technique. The black triangles represent the position and acute head direction of a monkey in the recording room. Lines inside the circle represent viewing directions and lines outside the circle represent the mean firing rate (and the SEM) in that direction. T1 - trolley, T2 - table, c1-4 - location of food cups. (E. T. Rolls et al., 1997).

Robertson and colleagues described the effects of the details' removal from the visual space of monkeys. They concluded that the CA1 region, parahippocampal gyrus and presubiculum, contain cells reflecting the operation of a memory system, while the CA3 neuronal activity requires direct visual input (Robertson et al., 1998).

In 1999, Matsumura and colleagues found 40% of recorded neurons to have spatial and/or task-dependent activity in virtually and/or physically translocated monkeys. They concluded that the hippocampal formation can encode different reference frames which are context or task-dependent (Matsumura et al., 1999).

Georges-Francios further analysed spatial view cells where he excluded the theory of activation by eye position, head direction or monkey location. He concluded and confirmed that these purely spatial view cells are allocentric (Georges-François et al., 1999).

During the same year, Robertson and colleagues reported five head-direction cells in pre-subiculum (Robertson et al., 1999). In both Robertson and Roll's cases, cells were reportedly able to keep their activity for several minutes in an obscured or dark environment.

In 2003, Hori and colleagues showed neurons with placefield in virtually and physically translocated monkeys, which strongly suggested that activity patterns of the hippocampal neurons represent spatial information and that they might provide a base for cognitive maps (Hori et al., 2003).

In 2005, Rolls et al. performed touchscreen reward place association task. They found characteristics of spatial-view cells in one-quarter of them. They concluded that the hippocampus is involved in object-place event memory and that it is an important part of association memory (Edmund T. Rolls & Xiang, 2005).

During the same year, Hori and colleagues reported that a third of neurons have place-related activity in monkeys navigating in a virtual environment. They concluded that hippocampal formation encodes for both, allocentric spatial representation and context, which together might be the base for episodic memory (Hori et al., 2005).

In 2004, previously unheard of, Ma and colleagues recorded neurons in a macaques posterior hippocampus. Cells they found were described with the following words: "Other neurons are active at random locations within the testing room, rather than to monkey actions around the dispenser, per se. Such responses resemble those of place-field neurons found in the rat hippocampus (O'Keefe, 1999)" (Ma et al., 2004). Therefore it is remarkable that these, perhaps first recorded primate place cells, were actually not at all the focus of the study but rather an accident which ended up being mentioned only in the last paragraph before acknowledgements. Unfortunately, they did not show convincing data regarding these cells.

A second study from the same year when Ludvig Nandor published data featuring six squirrel monkeys freely roaming in a square room, walking on the floor or climbing on the walls. He reported finding location-specific neurons, which he associated to rodent's place cells; yet this study hides an underwhelming twist, as he did not record the head direction. Regrettably, this exact piece of information is crucial to exclude the possibility of recorded cells being just the previously described spatial view cell (Ludvig et al., 2004).

A study published in 2017 examined macaques hippocampal processing during navigation in a virtual environment. Clever experimental design allowed for disentanglement between landmark position and reward location. Results confirmed previously suggested multidimensionality of primate hippocampal place cells with addition of direct characterisation of adjoint variables. The study showed that position, spatial view, head

direction etc. are accompanied by the internal state of the specific action during goal directed behaviour (Wirth et al., 2017).

To my knowledge, the most recent study with a focus on primate place cells recordings was performed in 2019. Freely moving marmosets were recorded from the hippocampal area. Authors of the article report hundreds mainly unidirectional place cells. Yet again we have to take into consideration several unfavourable experimental conditions. Even though marmosets were allowed to move freely, their movement was restricted to only two dimensions. The whole track was only around 4 meters long which is about 8 times the length of the marmoset. What is more, they were locked into a linear “L” shaped track practically forcing them to move only along the line.

## Place cells in humans

Alongside the experiments previously discussed, the primate literature includes the experiments performed on humans. However the relative sparsity of experimental subjects available for invasive electrophysiology restricts this area to very few studies. These studies are accompanied with additional indirect evidence acquired with fMRI. In both cases (direct or indirect measurements), humans were navigating in virtual or imagined environments.

The direct recordings were performed on patients with pharmacologically intractable epilepsy which were implanted (for several days) with intracranial electrodes in order to identify the focal seizure for potential surgical intervention. Multiple electrodes were usually implanted in the hippocampus, the parahippocampal gyrus, the entorhinal cortex and the amygdala. This provided a window of opportunity for conducting experiments in virtual navigation. The common concept of these experiments consists of playing a game in the role of a delivery person translocating objects from one place to another. In 2003, Ekstrom et al. showed evidence that the place and place-goal conjunctive cells are primarily inhabiting the hippocampus, and the spatial view cells are mainly located in the parahippocampal region (Ekstrom et al., 2003). Further evidence of place cells (primarily unidirectional) was substantiated by Miller et al. in 2013 when epilepsy patients, implanted in the entorhinal cortex, navigated and recalled navigation in a virtual environment (Miller et al., 2013). The same year, (Jacobs et al., 2013) brought direct evidence for grid-like neuronal activity during virtual navigation in humans.

Studies performed on healthy participants subjected to experiments in functional magnetic resonance imaging (fMRI) technique showed presence of grid in human memory network. Doeller et al. predicted that grid alignment of medial entorhinal cells (MEC) should cause a macroscopic signal detectable with fMRI. Indeed, their results showed an effect of 6-fold rotational symmetry, reflecting alignment or misalignment of running direction with the grid. Besides the classical pure grid cells they showed evidence also for conjunctive grid-directional cells (Doeller et al., 2010). Additional experiments showed that this grid-like activity is also present during mental simulation of virtual navigation. (Bellmund et al., 2016) Similarly to rodents, the grid in the human entorhinal cortex is boundary-anchored and offsetted  $7.5^\circ$  from the walls in a squared environment (Julian et al., 2018). In addition, rodent research is finding that in old human individuals grid-cell-like representation is compromised, which might explain the mechanism behind age-related navigational deficits (Stangl et al., 2018). Overall human experimentation, with their direct or indirect methods, brought results which are in alignment with the findings from rodent and non-human primate studies.

Non-human primates as well as humans naturally live and orient themselves in large territories where they often actively use all three spatial dimensions. Understanding the mental representation of one or two dimensions of space in an animal that uses three will always paint only a scant image of reality. We can conclude that we have to scale up our experimental design towards conditions resembling naturalistic behaviour. In our case, it is clear. We have to stop ignoring the third dimension.

## In the search for the third dimension

Throughout the years, various scientific studies in the field of spatial navigation brought a better understanding of the mechanisms and of the neuronal circuits involved. However, the vast majority of this research was performed on rodents in a two-dimensional environment. This environment is often planar and horizontal, which restricts movement from the tangential direction to the surface. However, the movement in the real world (even if locally planar) might not be horizontal, but is often three dimensional (3D), as for movements in water, air or dense vegetation of the rainforest. The navigation in 3D is computationally complicated because the represented space is much larger, since volume grows cubically while planes grow squarely, and because the order of rotations in orthogonal planes matters. The sequence of same rotations in different orders leads to different final positions. Considering the horizontal plane as a reference frame for the 3rd dimension and the 3rd dimension as the one against gravity, there are several differences between moving along horizontal and vertical planes. Vertical plane does not provide cues for navigation (such as celestial cues or magnetic field) but provide cues that are imperceivable while moving along a horizontal plane (such as light or thermal gradient, hydrostatic or air pressure). Movement along the vertical dimension is polarized by gravity. In case of elevation, the movement costs additional energy and therefore there is no confusion in orientation as it can be in the horizontal dimension. If the vertical dimension is encoded the same way as the horizontal dimension; or if these differences substantiate a difference in its neuronal representation, leading to a bicoded map where the third dimension is encoded in a separate coordinate system, remains a question for further investigation.

There are only a handful of studies which are exceptions, most of which are coming from Kate Jefferys lab (Grieves et al., 2020; Hayman et al., 2011; Page et al., 2018). They initially used a vertically elevated helical track or a pegboard (vertically oriented pegboard with horizontally oriented pegs used as a support for vertical movement of the rat) for place or grid cell recordings (Figure 20, top). Prior to the investigation of the vertical dimension via a pegboard, the rat's place/grid cells were recorded in the horizontal open field arena. Once the place/grid cell has been found and sufficiently recorded in a horizontal plane, the rats were then subjected to the pegboard for vertical dimension exploration.

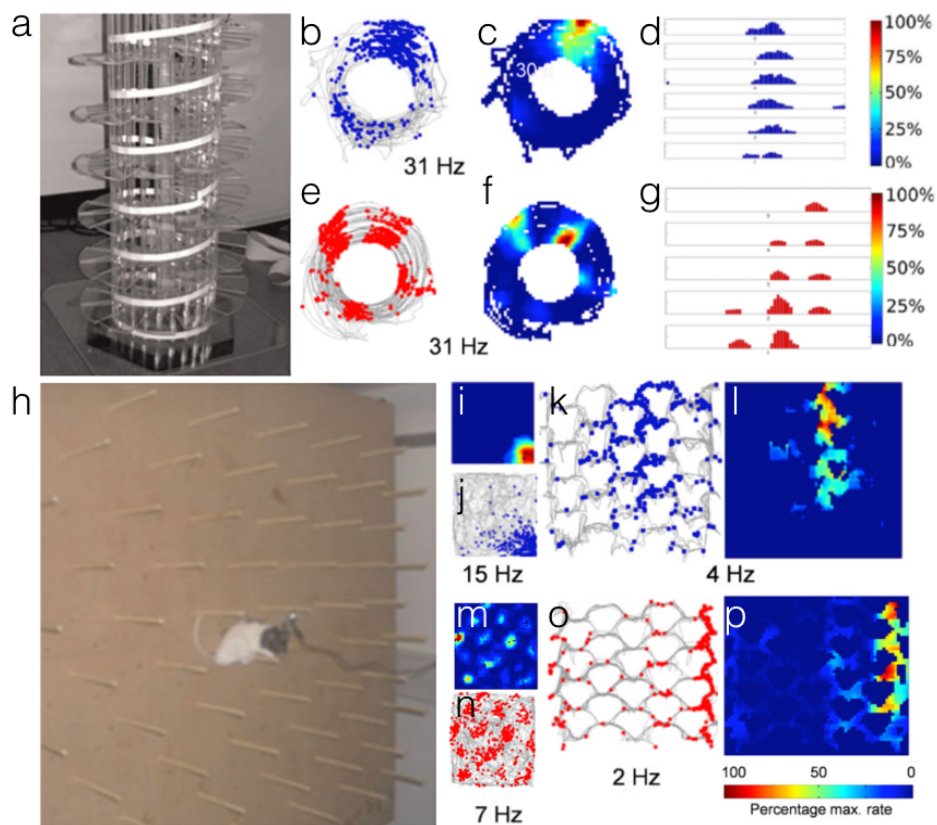


### Figure 20: First 3D experiments

Results from the experiment investigating the neuronal representation of the vertical dimension in the rat brain. (a) photo of the helical track; (b) gray lines -superimposed animal trajectory with blue -place cell spiking activity; (c) place cell firing activity heat-map; (d) decomposition of individual coils into the firing rate histogram; (e)-(g) same as (b)-(d) but recorded was a grid cell; (h) photo of the pegboard; (i) place cell firing heat-map in horizontal recording arena; (j) gray lines shows animal trajectory in horizontal recording arena with individual spikes as colored dots; (k) same as (j) but recorded on the pegboard; (l) place cell firing rate activity heat-map on pegboard; (m)-(p) same as (i)-(l) but recorded was grid cell; adapted from (Grieves et al., 2020; Hayman et al., 2011; Page et al., 2018).

This experiment yielded multiple results, here I will summarize the main four:

First, the place cell investigated during locomotion on the helical track showed activation in the same part of the turn on each of the vertical levels. Second, the grid cell on the helical track showed activity at the same horizontal coordinates across multiple levels. Third, the classic place cell (as shown on Figure 20-i&j) showed on the pegboard place field elongation in the vertical axis. Finally, the classic grid cells (as shown on Figure 20-m&n) showed place field elongation and a loss of periodicity while on the pegboard. Additionally, in experiments involving pegboard, neurons substantially decreased their firing rate while on pegboard (in comparison to firing rate in the horizontal recording arena). A subjective interpretation of these results, translated into theories of volumetric space perception, triggered controversy and became widely discussed (Jeffery et al. 2013).

In the following experiments, the use of the wireless recording system allowed Jefferys lab to use a 1m<sup>3</sup> lattice maze, initially developed in Lausanne Switzerland (Grobéty & Schenk, 1992). The lattice maze provided structural support for the free movement in all directions of 3D space for rats (Figure 21).



**Figure 21: 3D maze**

Three-dimensional maze used for recordings in rats in Kate Jefferys lab, from (Grieves et al., 2020; Hayman et al., 2011; Page et al., 2018).

The results of these experiments convincingly show that, usually, two-dimensional place cells of rats are also capable of representing the third dimension. On Figure 22. are visualized spherical rodent place fields with a somewhat elongated shape. Yet, it remains moot if this representation is the same as in the animals naturally navigating in 3D.

So what is the evidence from the real 3D navigating animals? So far not many species provided us with evidence. The one and only comes from bats.

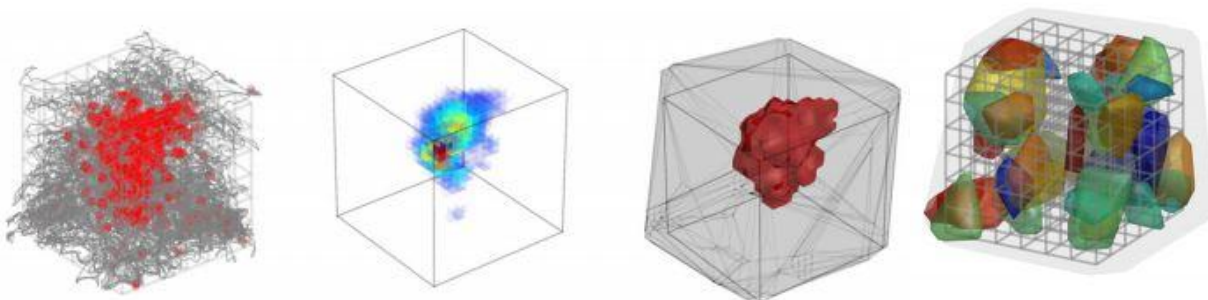


**Figure 22: Rodent 3D place cell**

From left to right cube 1-4. Cube 1, gray line represents trajectory of animal moving in the three-dimensional maze from Figure 27. Red points show individual spikes of recorded neuron. Cube 2, firing rate heat map. Cube 3, place field and cube 4, is an example of multiple place fields in the lattice maze (Grieves et al., 2020).

Shortly after the discovery of the first bat 2D place cells (Ulanovsky & Moss, 2007) and spatial view cells (Ulanovsky & Moss, 2011), the team of Nachum Ulanovsky mastered neural recordings also in flying bats, and found cells active during flight. The 3D place cells in flying bats were reported for the first time in a 2013 study (Yartsev & Ulanovsky, 2013). In this experiment, bats were allowed to freely fly in a 6x5x3 m room while single-neuron activity was

recorded from the dorsal CA1 of the hippocampus. Over the course of the experiment, bats covered the entire space with their flight trajectory and almost every place in the room was mapped by a certain place field (Yartsev & Ulanovsky, 2013). Over 30% of the recorded neurons showed place cell properties. In more than 90% of the cases, their place-fields were encoded in all three dimensions of the space with similar resolution (Figure 23).

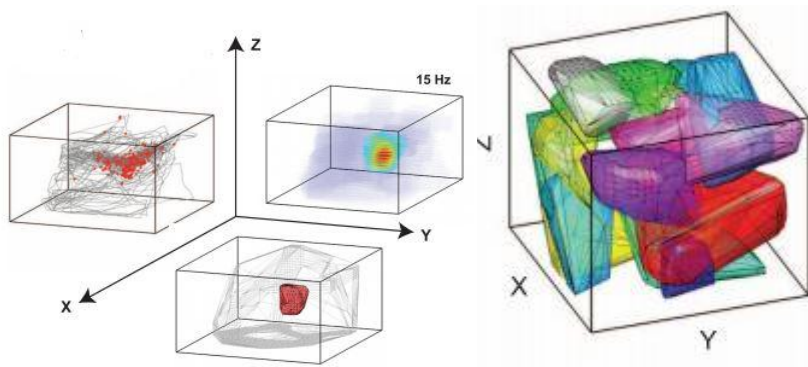


**Figure 23: Bat 3D place cell**  
 Left, between axis X and Z gray line represents flight trajectory. Between axis Z and Y is shown a firing heat-map and between X and Y the place field of the recorded neuron. On the right is an example of multiple place fields in the recording room. From (Yartsev & Ulanovsky, 2013).

The similarity between rodent and bat 3-dimensional place-cells is undeniable, reflecting probably shared evolution.

One could therefore argue against the use of other model organisms in order to look at the same question. Especially when understanding if the third dimension of rodent place cells is just a Z plane projection (or not) remains elusive. But let this be an excellent example of the opposite. Thanks to the use of animals which are naturally navigating in 3D -as bats do- we found new types of functionally specialized cells, helping us to understand how truly volumetric space orientation works.

After the initial discovery of the head-direction cells in the hippocampal CA1 of crawling bats, most of the cells showed also location sensitivity in addition, making them conjunctive place - head direction cells. It was argued that head-direction may represent the inner compass of the animal, while place sensitivity serves to build a map, hence suggesting that a single neuron conveys the function of both a map and a compass (Rubin et al., 2014).

Besides the azimuth, head-direction cells in bats can be also sensitive to pitch and/or roll. The preferred head-directions of the recorded neuronal population spread over, and cover the whole 360° of azimuth. In comparison with the CA1 cells, the presubicular HD cells showed only very little place tuning. In the article from 2015, they proposed a toroidal model for the head-direction, where the 3D head-direction is represented in azimuth x pitch toroidal coordinates (Figure 24)(Finkelstein et al., 2015).

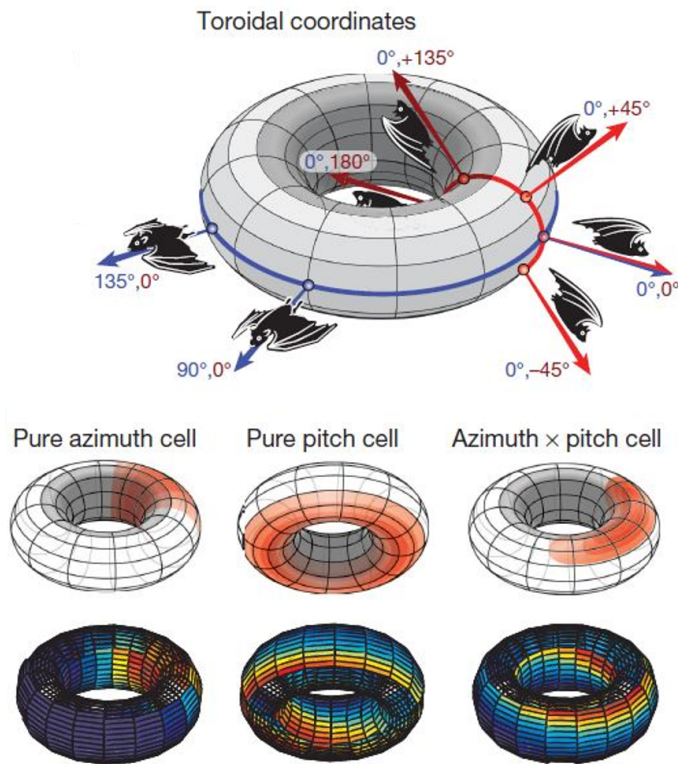


**Figure 24: Toroidal HD model**

Toroidal model for head direction of flying bats. Top toroid illustrates in blue animal heading towards different azimuth ( but same pitch) and in red orientation towards the different pitch (but same azimuth). Below schematic examples of firing rate heat map of pure azimuth, pure pitch or conjunctive (azimuth and pitch) cell (Finkelstein et al., 2015).

The literature on bat-experimentation provides valuable addition to the understanding of the mechanisms underlying spatial navigation and orientation, but species-specific differences remain. E.g. even though most of the primates navigate in 3D, they need a physical substrate as they can't fly. Therefore it would be more than surprising to find a population of cells devoted to rolling in a primate brain.

## Mouse lemur (*Microcebus murinus*)

There are advantages in the use of a much smaller primate such as the mouse lemur. Previous research in mouse lemurs, in wild or in laboratory conditions, suggests that this little primate has the potential to become a new model organism for systems neuroscience (Ezran et al., 2017; Hozer et al., 2019; F. Pifferi et al., 2019; Roberts, 2019; Yoder, 2013). Two popular model organisms in systems neuroscience are macaque monkey and mouse. Both of them have their strong and weak points at different levels. The mouse lemur possesses several attributes which give it an advantage over macaque or mouse, as listed in Table 1.

Currently mice are dominating the scientific world for applied as well as fundamental research. They are the most commonly used mammalian research model and are used for research in nearly all disciplines. Advantages of rodent research come from centuries of prior experimentations (thus facilitating the work of contemporary scientists), paired with a plethora of experimental tools which do not yet have an analogue for the other model organisms.

The outstandingly large variety of behavioural tasks, setups and analytical approaches is one of the main backbones of rodent research. Despite its obvious assets for research, over the past decade research has unveiled the mice's limitations as a model organism mainly in translational value. Fortunately, the mouse lemur is comparable in size so that most of the tools developed for mice are directly transferable to it (Ho et al., 2020).

One important category of tools used with mice is genetics. Primate neuroscience still has a long way to catch up in this regard. The mouse lemur genome has been fully sequenced and a library of genetic samples from phenotypic variations has already been built (Ezran et al., 2017). The rapid development of CRISPR techniques will likely advance genetic manipulation.

The size of the rodent animal models brings several other advantages. Firstly, the small body size of rodents requires a fairly simple training (Hurst & West, 2010), while primate handling is often very demanding (Clay et al., 2009). The mouse lemur, due to its small size, allows the training to be very similar to the mice handling procedure. Secondly, the body size of the model organism has an impact on the necessary financial resources for keeping a colony. Those are incomparably smaller than those necessary for macaque colonies. Here, mouse lemur is once again much closer to mice than to the other primates. Thirdly, rodents' small brains are considerably more stable in the skull than large primate brains (Griffiths et al., 2020; Li et al., 2017). The brain of a mouse lemur is about the size of a rat brain and is therefore probably as stable.

This quality is the main advantage during optical imaging techniques. Besides stability, the rodent brain has the advantage of being lissencephalic (Scholz et al., 2016). The entire surface of the rodent brain is easily accessible, contrary to primates which often come with strongly convoluted brains, where large portions of the cortex are hidden in the sulci (Reveley et al., 2017). Although being a primate, the mouse lemur has also a lissencephalic brain, with the Sylvian fissure as an exception (Clark, 1931) (Figure 25).

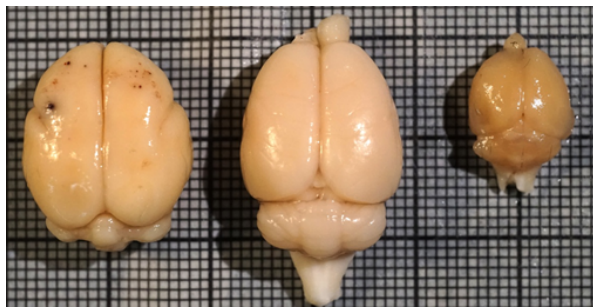


**Figure 25: Brains**

Left to right mouse lemur, rat and mouse brain on the millimetre paper. (The olfactory bulb of the mouse lemur brain is missing)

Another practical advantage of working with rodents is their relatively short lifespan in comparison with primates. Rodents live approximately a year whilst macaques can reach a lifespan of up to 25 years (Bercovitch & Berard, 1993; Fedigan, 1991). Indeed, a macaque can easily outlast 6 to 7 PhD students, which creates certain inevitable troubles. The mouse lemur, on the other hand, has a lifespan averaging around 4-5 years, which makes him a great compromise allowing longevity studies without becoming a liability in between different projects (Languille et al., 2012).

Another point to consider when comparing lemurs, rodents and macaques as model organisms in neuroscience is ethics. Mouse lemurs' ethical considerations are yet to be defined but the fact that prosimians are not classified as monkeys will probably result in less strict rules.

There are also advantages in work with primates. Most of them are a result of their closer-to-human distance on the phylogenetic tree. Macaques and humans diverged on the phylogenetic tree around 30 million years ago, making it the most pertinent model organisms available for research (Fa, 1989). Rodents and mouse lemur diverged respectively 90 million years ago, and 60 million years ago (Nei et al., 2001; Yoder & Yang, 2004).

Without having the evolutionary edge as macaques, the mouse lemur remains a considerably better choice than rodents. Macaques and more generally primates have excellent vision, comparable to humans' (Merigan, 1989). Unlike rodents, which are endowed with a much poorer vision. Functional organization of mouse lemurs' visual cortex and its cytoarchitecture is nearly the same as in other primates. Despite its size, the mouse lemur brain has a pinwheel organization and not a salt-and-pepper like similarly big rat brain (Ho et al., 2020). Besides vision macaques display highly precise dexterity while mice are limited to basic reach (Galiñanes et al., 2018). Mouse lemurs, even though unable of single-digit movements, exert natural abilities for manipulating objects with their hands (G. Boulinguez-Ambroise et al., 2019).

Another advantage of a macaque in comparison to a mouse is its overall greater cognitive capacity (Elston et al., 2006). Macaques being so far the only laboratory animals that are shown to have internal representation of abstract concepts same as those found in humans (Baraduc et al., 2019). Here the mouse lemur represents once again the "middle ground"; even though its full cognitive capacities are yet to be discovered. Lastly, macaques are excellent disease models. Despite the relentless efforts, mice are nowhere near as good for this type of research. The Mouse lemur as a disease model still hasn't been fully evaluated. Nevertheless naturally occurring Alzheimer-like pathology might be a sign of potentially high face value (F. Pifferi et al., 2019; Sarasa & Pesini, 2009). The caloric restriction-induced longevity predicts it to be a good model for aging studies (Languille et al., 2012; Nadkarni et al., 2019) as well as for psychological and neuropsychiatric symptoms of dementia (Fabien Pifferi et al., 2019).



Mouse



Mouse Lemur



Macaque

Scientific tools	Excellent	Excellent	Moderate
Genetics	Excellent	Reverse genetics	Moderate
Brain stability	Small movements	Small movements	Large movements
Cortical access	Excellent	Excellent	Moderate
Handling	Easy	Easy	Difficult
Costs	€	€	€€€
Life span	±1 year	±5 years	±25 years
Ethics	Acceptable	Acceptable	Very strict
Evolutionary distance	90 mya	60 mya	30 mya
Vision	Poor	Excellent	Excellent
Dexterities	Poor	Moderate	Excellent
Cognition	Moderate	To be determined	Excellent
Disease model	Poor	To be determined	Excellent

**Table 1: Macaque vs lemur vs mouse.**

Comparison of the “pros and cons” of mice, mouse lemurs and macaques as systems neuroscience animal models.

Hitherto I presented an argument suggesting that the mouse lemur might be suitable for systems neuroscience as an animal model. We hope to further strengthen its position within other animal models by our study.

Even though a great body of work about spatial navigation and orientation exists, several questions still need clarification. Here we argue that research with freely-moving mouse lemurs will be an important contribution to understanding spatial navigation.

# Methods

## Handling procedures

Mouse lemurs are larger than mice but they still easily fit into one's hand. They are substantially more agile compared to laboratory mice (Boettcher et al., 2020; Grégoire Boulinguez-Ambroise et al., 2020; Chazeau et al., 2013; Thomas et al., 2016). Lemurs are also very strong for their size (Boettcher et al., 2020; Chazeau et al., 2013). Therefore, one has to be very careful during handling so that the lemur does not escape from the hand. If someone is used to handling mice, manipulating a mouse lemur might feel unnatural (regarding force) with one having to hold the lemur in the hand firmly. Lemurs should be held by enveloping their whole body, with their head sticking out between the index finger and the thumb. Mouse lemurs should never be held solely by the limb nor by the tail.

## Handling of the newborns

Mouse lemurs are usually manipulated only in their adulthood, after one year. However, there is one special case when newborns are adopted by humans when three lemurs (instead of two) are born. Since the mother lemur has only two nipples, she can only feed two pups and the third one will get abandoned. Which one it is can be determined in about a week or two after birth by monitoring the weight of the pups. The one which stops gaining weight and becomes weaker will naturally die. Because of the high value of these animals, we prevent it by adopting it. The adopted animal is carried in the little cotton pouch on the neck of its adopted parent. It is necessary to maintain pups in bodily temperature. The little lemur has to be fed milk with honey every two hours of the day and the night during the first two weeks. Afterwards, it's followed by a gradual prolongation of time between meals. During the night, pups should be kept under the pillow, in the pouch, inside a glass jar to keep them warm and to prevent squishing them. The lid of the glass jar has to have holes to maintain airflow. The little lemurs need to be helped to urinate, by stimulating their genitals with soft paper tissue every time after the feeding occurs for the first month and a half. The little lemurs don't comply with circadian rhythm, so there is no necessity to maintain strict photoperiod (like with adult lemurs).

## Food and food restriction

The food for mouse lemurs consists usually of fruits, bouillie, and insects. Among the most preferred fruits are grapes, bananas, kiwi, melon, apple pear... Between insects fed to lemurs, we can count mealworms, crickets or locusts. Bouillie, which is a major part of the lemur's diet is made as a fluid mixture of 13 slices of spiced bread, 4 bottles de lait concentré non-sucré (410g), 400ml egg yolk, 400ml oil, 2kg of cottage cheese, 800g of porridge for babies, 300g of soja flower. Most of the time mouse lemurs are maintained on food ad libitum, food will be restricted only if they become overweight, or if we need to use food as motivation to perform in behavioural experiments.

Mouse lemurs used in experiments with the behavioural paradigm are often food restricted. Food restriction can be either partial/complementary or full. During partial food restriction, animals get food complement in the cage after the experiment, the amount of food is measured to maintain the animal's operational bodyweight. The fully food-restricted animal has food available only during the experiment.

## Surgery

All surgical procedures are performed under strict sterile conditions, and according to the Swiss national animal welfare regulations. Day prior to the surgery, the animal is administered with the antibiotic Ceftriaxone. Just before the surgery, anaesthesia is induced by subcutaneous Buprenorphine (1ul/1g) injection and ~5% Isoflurane in the Plexiglas box. One minute after the animal stops moving, the animal is removed from the box and is administered intramuscularly with Dexamethasone (0.8ul/1g), Carprofen (0.022mg/g) and Ceftriaxone (50mg/kg). The animal is then placed on the heated platform (add brand) and fixed in a stereotaxic frame (Kopf cat frame), with adjusted ear-bars and custom-built mouth holder (Picture 1). The eyes and tongue are protected with Lacryvisc and the whiskers with Vaseline. The standard air tubing with rubber facemask is placed in front of the animal's snout for continuous delivery of Isoflurane.



**Picture 1: Head-fixation apparatus.**

From bottom right diagonally ear-bars with dental acrylic moulded protection of sharp inserting points. Silver, mouth mounting piece. Red, tubing with rubber snout mask. Copper, water-heated platform.

The area of the surgical procedure is disinfected, and Lidocaine is administered subcutaneously in the skull area. During the surgery, the anaesthesia levels are maintained at 1-2% isoflurane, according to the breathing rate and reflexes. The skull is exposed and skull screws are attached. The Circular craniotomy is then drilled and the bone removed. The head-drive is attached to a holder and placed with tetrodes over the craniotomy, and the drive is slowly lowered until the tetrodes insert the brain. The craniotomy and the tetrodes are afterwards covered with a thin layer of vaseline and the whole area is then sealed with dental acrylic.

After surgery, the animal is placed into a heat controlled recovery cage where we let it recover for the next five days. We administer analgesics for a week, and antibiotics for 9 days following the surgery.

Drug	Dosage	Route	HalfLife	Notes
Buprenorphine	1ul / 1g	subcut.	4-24 (12)h	
Carprofen	0.022mg/g 25ul/60g	IM	~8h	Dilute 10% solution,
Ceftriaxone	50mg /kg	IM	24h	Dilute 1g of ceftriaxone powder in 5 ml of Lidocaine. (5ul of the solution will contain 1mg)
Dexamethasone	0.8ul / 1g	IM		
Metacam/Meloxicam	0,4ul/1g	subcut.	24h	Dilute 10% solution,
Benzodiazepine	2ul/1g	IM	20-50h	

**Table 2: Drugs.**

Indicates name, dosages, route of administration, drug's half-life, and notes of the drugs we used during surgery or experiment. (For the precise details of surgery attached surgery protocol annex 1.)

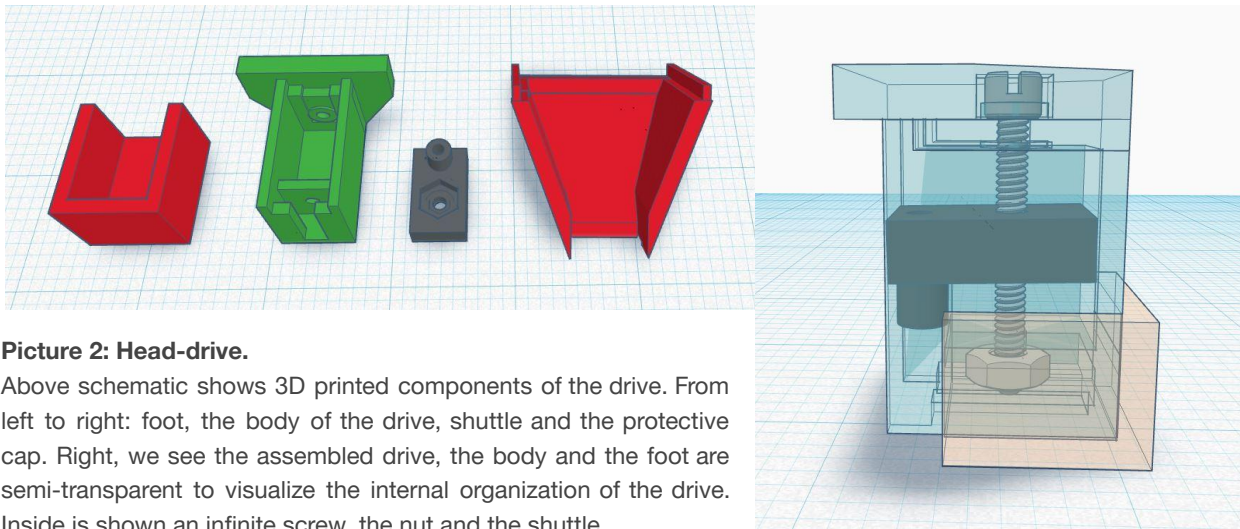
## Recording setup

The setup for neuronal recordings consists of several components: The head-drive, which is the main interface for connecting the neuronal data recording headstage; the wireless data logger (the headstage); the neuronal data acquisition system; the behavioural room where experiments take place; the tracking system used for correlation of the animals' position in space with the neuronal data; the data processing pipeline and the spike sorting process; and computer for data analysis.

### Head-drive

To facilitate neuronal signal recordings I used a custom 3D printed head drive adapted from (Naudé et al., 2018), with glued-on custom made electrode interface board (EIB) connected to eight tetrodes. The head-drive (approximately 1cm) printed with PVA (polyvinyl alcohol) on Ultimaker2 3D printer has two main parts: the static body and the shuttle. The shuttle can be moved 7mm vertically according to the body. The shuttle has an embedded M1 nut, with which it is screwed on the infinite screw; and in front, it has a hole equipped with a series of polyamide tubings. These tubings are used to organize, lead and fix the tetrodes to the shuttle. Shuttle after facilitates the lowering of the tetrodes into the desired depth.

The shuttle moves by turning an infinite M1 iso screw of the drive. The screw is held in the body of the drive at the top of the drive, and stabilized at its bottom with the glued on HEX nut. Head drive has two additional parts, a protective cover and a footer (Picture 2). The protective cover encapsulates tetrodes and the footer is used for mediation of contact with the skull. In the case that the head-drive would get damaged, it could be removed from the footer and a new head-drive could be used on the animal without the need for complicated surgery. To replace the head-drive, we can simply delineate the border of the footer with the dental drill and lift the head-drive. The new head-drive can be afterwards placed into the footer and secured with a few drops of superglue.



**Picture 2: Head-drive.**

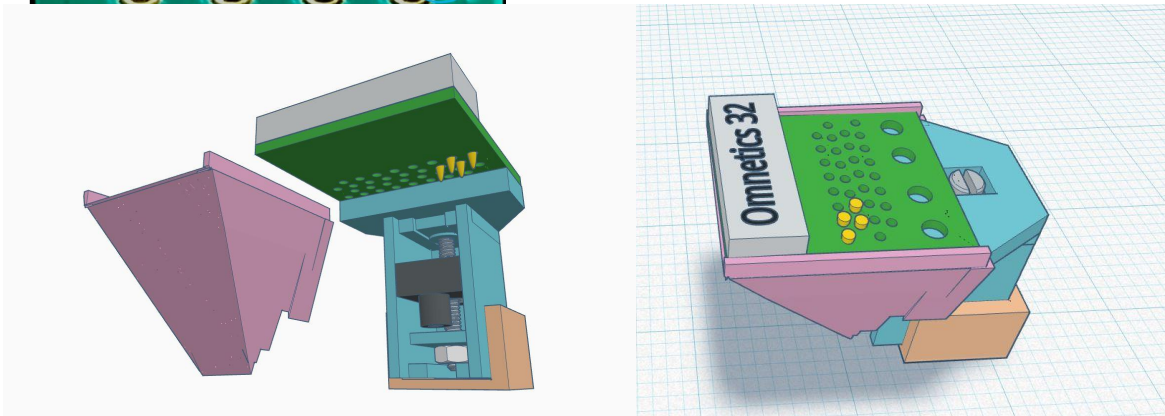
Above schematic shows 3D printed components of the drive. From left to right: foot, the body of the drive, shuttle and the protective cap. Right, we see the assembled drive, the body and the foot are semi-transparent to visualize the internal organization of the drive. Inside is shown an infinite screw, the nut and the shuttle.

In order for EIB to mediate the connection between the recording stage and the tetrode wires, the Omnetics A79026-001 32 channel connector has to be soldered onto the EIB board circuit (Picture 3). Then the EIB with the connector gets glued on the drive and individual loose ends of the tetrodes are led through the holes in the EIB. Subsequently, the tetrodes are fixed in the holes with gold pins (Picture 4). The handmade tetrodes (bundle of four electrodes) were produced by twisting (80x clockwise and 30x counterclockwise) four individual 7cm Kanthal NiChr Bond XTC 0.0127mm Ø wire heat-bound together with a heat gun. For the ground wire, A-M Systems 1.4mm Ø used. For twisting, I used an Arduino based tetrode twister from Open Ephys. The tetrodes free ends are led through the polyimide tubing and glued with two-component glue. Tetrodes are measured, for the required length + 5mm from the tubing, and cut. The protective cover is placed on the drive and the whole drive gets wrapped around by Parafilm, with the exception of a small space around the tetrodes. Shortly before the surgery, the tetrodes are gold plated by using NanoZ from Neuralynx. The electrode tips are gold-plated with Sifco 5355 (mixed 1:1 with PEG solution and carbon nanotubes, Neuralynx) in order to lower the impedance.



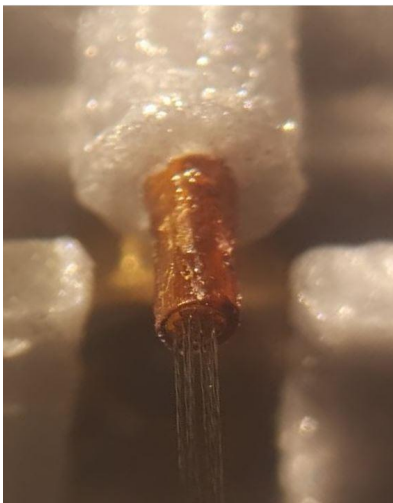
**Picture 3: Electrode interface board (EIB).**

Custom made EIB (without Omnetics connector), in yellow indicate the holes for individual cables of tetrodes leading to plates for connector attachments, red indicates ground and blue are coffee beans used for keeping the grounding circuit opened or closed after soldering.



**Picture 4.: Drive with EIB.**

Above two angles of view of the assembled microdrive. Below left, view from the bottom with an exploded protective cap and on the right view from the top, drive with the EIB and four gold pins.



**Picture 5: Tetrodes.**

Left, zoom on the polyimide tubing, big (250  $\mu\text{m}$ ) encapsulating 9 thin tubings (40  $\mu\text{m}$ ). Thin tubing is used to guide the tetrodes and the big tubing is holding them together. Right shows altogether once tetrodes are inserted and length is adjusted in the polyimide tubes, they are all glued with the shuttle using two-component glue.

In the following pictures (picture 6, 7 and 8) is shown a drive implanted on the head of the mouse lemur. Picture 6 shows top view of a mouse lemur head with the drive, on picture 7 is the frontal view of the headstage with battery connected to the drive and on picture 8 is side view of the head stage covered by the protective foam to decrease possible damage during recordings.



**Picture 6: Head with drive**

Left, Mouse lemur with implanted headstage hold in the hand.

**Picture 7: Head with drive and stage**

Bottom left, frontal view of the mouse lemur head with the drive and head stage connected.

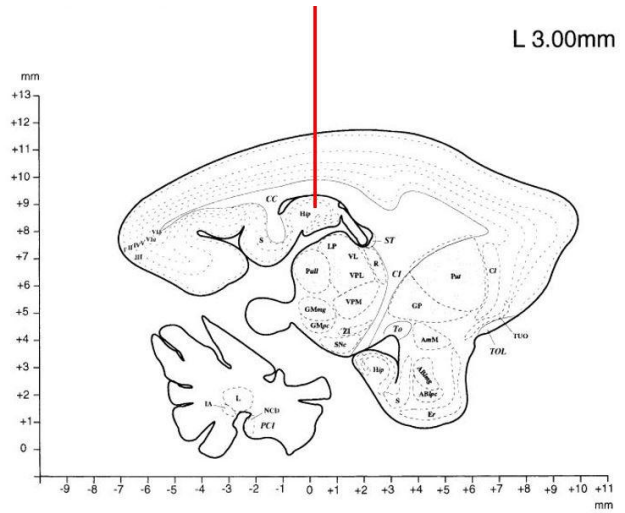
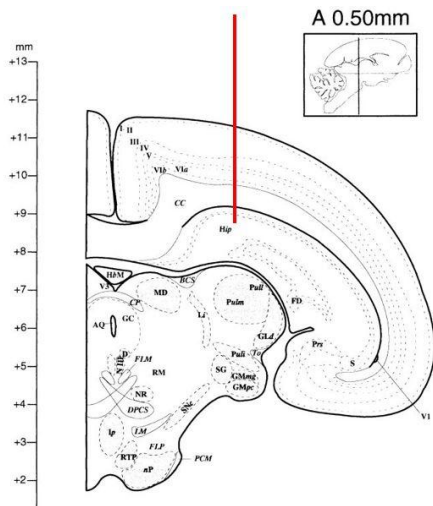
**Picture 8: Head with drive and stage protected**

Bottom right, side view of the mouse lemur head with the protective cover encapsulating recording apparatus



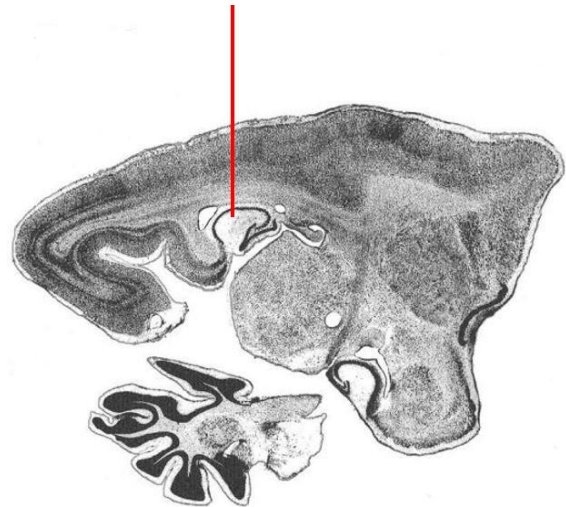
### Hippocampal targeting

To determine the best coordinates for the tetrode implantation into the dorsal CA1 of the hippocampus, I used a stereotaxic atlas of the grey lesser mouse lemur brain (Bons et al., 1998) (Picture 9a and 9b) in combination with a 3D atlas of mouse lemur brain (Picture 10) (Nadkarni et al., 2019)



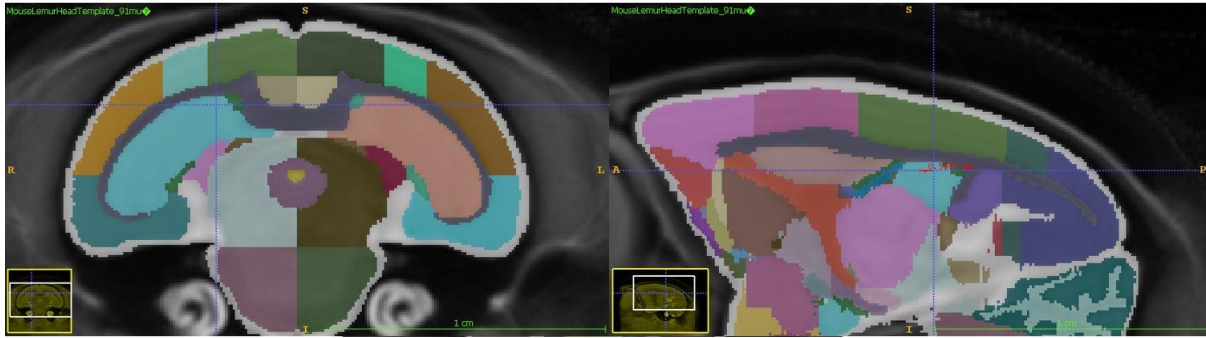
**Picture 9a: Coordinates schematic**

Schematic dorsal CA1 coordinates based on Bons atlas (Bons et al., 1998). Left, coronal section 0.5mm anterior from intraaural line. Right, sagittal section, 3mm lateral from midline. Red line represents the desired location for tetrodes implantation.



**Picture 9b: Histology sections**

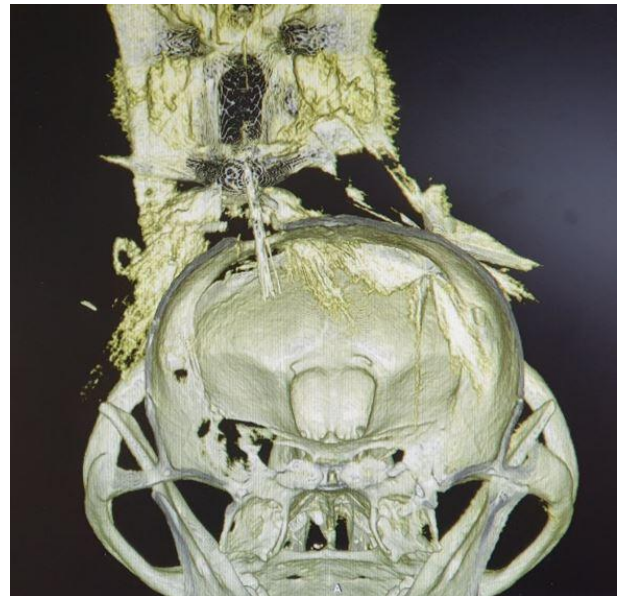
Histology sections of mouse lemur brain from Bons atlas (Bons et al., 1998). Left, coronal section 0.5mm anterior from intraaural line. Right, sagittal section, 3mm lateral from midline. Red line represents the desired location for tetrodes implantation.



**Picture 10: MRI of mouse lemur brain**

Coronal (left) and sagittal sections with labeled brain regions (Nadkarni et al., 2019). Hippocampus is in sky blue color. Crossing of thin blue lines represents desired location for tetrodes implantation. Left, coronal section 0.5mm anterior from intraaural line. Right, sagittal section, 3mm lateral from midline.

After the surgery, the position of the tetrodes is determined by the 3D reconstruction of in vivo computer tomography (CT) scans (Picture 11). We used the MicroCT platform of the University Paris Descartes where we briefly anaesthetized animals (isoflurane anaesthesia as detailed above) and proceeded to scan them (scan time = 3 min). Further, we estimated the tetrode position and overlaid our CT scan (visualizing the skull and the tetrodes) with the average mouse lemur brain (MRI scan averaged from 35 mouse lemurs) using the AMIRA (Thermo Fisher Scientific) (Picture 12).



**Picture 11: CT scan.**

Left, coronal section view from front/lateral side, taken after surgery. Right, coronal section view from the back of the head towards the rostrum, taken after recording sessions.

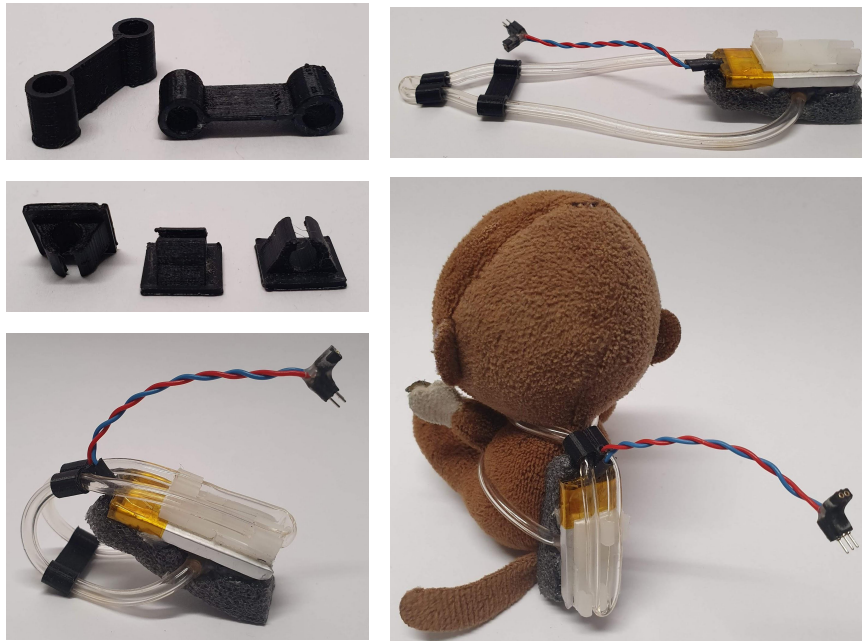


**Picture 12: CT + MRI.**

Overlaid CT scan with the MRI of the averaged mouse lemur brain. The yellow traces show the estimated position of the tetrodes in the brain.

### **Recording setup**

For wireless neuronal data acquisition, I used the SpikeGadgets wireless recording system. This system is built out of a wireless data logger which is mounted on the head of the animal via a head-drive, the main control unit (MCU) used as a central hub of the recording systems, and a computer with the SpikeGadgets software Trodes. The animal equipped with the head-drive is connected to the head-stage via Omnetics connector. The thirty-two channel wireless data logger powered by an external battery (Lipo 3.7 V, 140-800 mAh, LP451430) is storing data on the industrial-grade 32GB microSD card. The wireless data logger acquiring frequency is 20-30kHz with broadband filtering 0.1 - 10 kHz. The main control unit (MCU) is connected to two computers (acquisition computer and tracking computer) and to the radio frequency (RF) transceiver. The MCU sends synchronization time-to-live (TTL) pulses, every 10 seconds, to the acquisition computer via HDMI cable, to the tracking computer via wifi Arduino (MKR-1000) via the user datagram protocol (UDP), and to the head-stage via RF transceiver. The tracking computer is listening through wifi to a UDP from the Arduino, and the timing of this signal is recorded in the tracking software. The battery is carried on the back of the animal as a backpack, using the silicone Tygon tubing. The battery and the Tygon tubing are held together by on-battery glued on 3D printed holding loops (Picture 13). The battery also powered a tracking light-emitting diode (LED), which is attached to the connector at the same point as the head-stage. Since the battery is independent of the head-stage, I was able to use different types of batteries which varied from 40mAh to 800 mAh. While the 40 mAh battery lasted for around 20 minutes of recording, the longest recordings of 5 hours were acquired with the 800 mAh battery. Even though a recording of 6 hours is possible, we decided on shorter recording sessions of around 2-3 hours. The continued data format of 6h of recordings was very heavy for post-processing, even though in principle it is possible to acquire these lengthy sessions if there would be a reasonable question at stake.

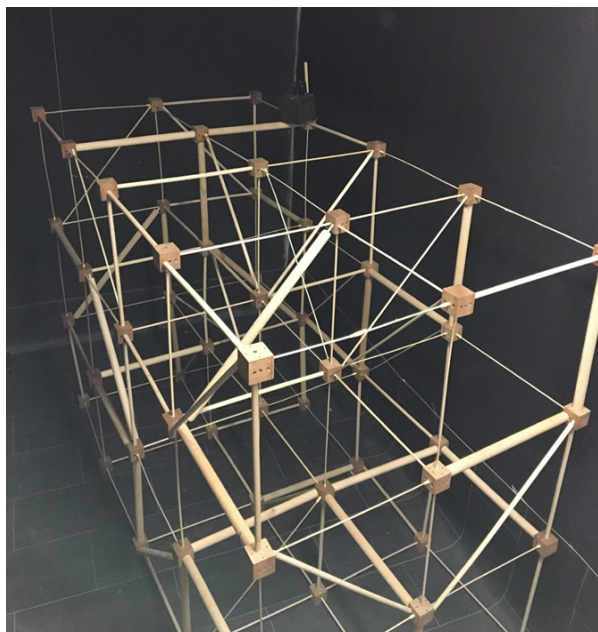


**Picture 13: Battery back-pack.**

Left top, adjustable straps. Left middle, tube holders. Left bottom and top right battery back-pack. Right bottom back-pack on toy monkey.

### **Behavioural room**

The behavioural room used for the recording is 4m x 2m x 2m, with two fake walls (a long one and a short one) in order to hide the necessary technical equipment. The walls are painted black mat, in order to minimize the reflection of the LED used for the tracking of the animal. The floor is covered with black lino for the same purpose. The white and red light is installed on the ceiling of the room, and the temperature is controlled by a heater behind one of the fake walls. Inside the room is a 2x3x4 lattice made of a wood stick of different thickness held together by wooden cubes inspired by (Grobéty & Schenk, 1992). The sticks are 30cm long with a thickness of 4 - 24mm, and the wooden cubes are 5x5cm (Picture 14).



**Picture 14: Lattice maze.**

Wooden sticks lattice maze built in the recording room. Wooden stick with length of 30cm and diameter 4/6/12/24 mm connected with 5x5cm wooden blocks.

## Behavioural priming

In order to prime animals moving across the lattice maze, we use RECO-boxes (Picture 15). The RECO-box is a battery-powered wirelessly controlled box that can emit: food, click, beep or light signal. The sequential activation of food delivery by these boxes positioned at the further edges of the maze provided motivation for animals to run through the maze. Each RECO-box can be operated either directly by an experimenter (they can follow a preprogrammed schedule) or they can be activated based on the behavioural pattern of the animal. For example, a certain position of the animal in the maze might act as a trigger for the RECO-box activation.



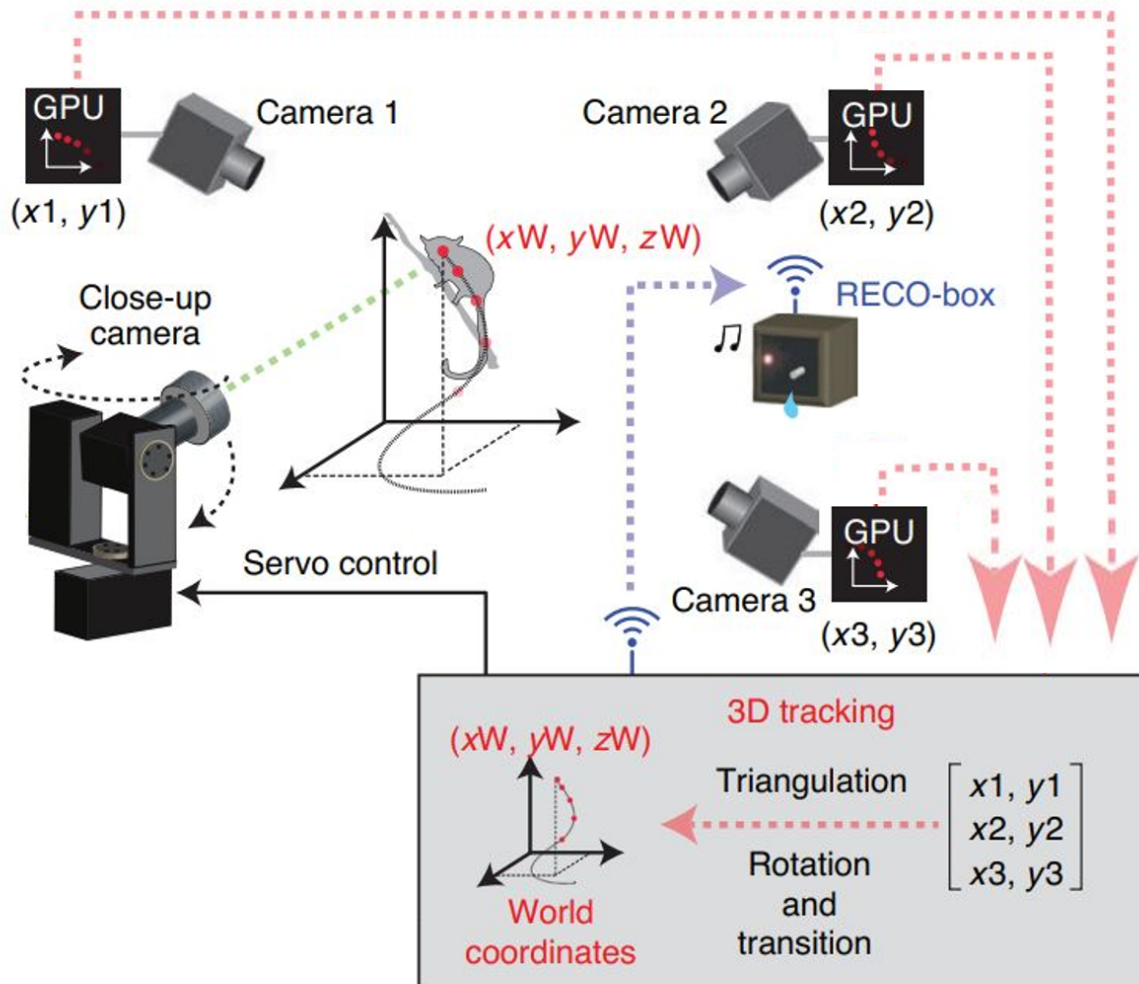
**Picture 15: RECO-box.**

Mouse lemur hinged over the RECO-box (black) placed in the branches.

## Tracking

The tracking of the animal is done by a custom-developed tracking system. Five high-speed USB3 cameras (MQ013CG-OC, XIMEA) are equipped with a wide-angle lens (NAVITAR, f4.5mm, 1.4) and an infrared band-pass filter (FGL 665, Thorlabs) to capture the infrared LED (SMC660) carried by the animal. Each camera connected to the GPU computer (Jetson TK1, NVIDIA, running Linux4Tegra) extracts XY coordinates in real-time and sends them via ethernet (TK1) to the host computer (Optiplex 9020 - Intel Core i7, DELL, running Linux Ubuntu 16.04 LTS). After receiving the coordinates from at least 3 Jetsons, the host computer performs triangulation and calculates the real-world coordinates of the LED. This is further used to control two servo motors (MX-64, Dynamixel) mounted on the two-axis custom-build gimbal holding the close-up near-infrared (NIR) enhanced CMOS camera (MQ013RG-E2,

XIMEA) to provide a zoomed image of the animal. The close-up camera carries a high-resolution lens (Xenon, 2.0/50 mm, Schneider) and an electrically tunable lens (EL-16-40-TC, Optotune). One additional camera (MQ013CG-OC, XIMEA) is used for capturing the “live view” video of the experimental room.



**Schematic 1: Tracking.**

The depiction and spatial arrangement of the different tracking system elements. Multiple infrared cameras (cameras 1–3) with dedicated GPUs process images from different viewing angles. The identity and positions of the detected markers are transmitted to a central host computer for 3D reconstruction (triangulation, followed by rotation and transition into real-world 3D coordinates). The 3D coordinates are forwarded to control the position and focus of a gimbal-mounted close-up camera.

## Processing and spike sorting

Before spike sorting, the data have to be extracted and pre-processed. After the experiment, the head-stage is removed from the animal and mounted on an SD card-like docking station from SpikeGadgets. The docking station is plugged in a standard computer SDcard slot and using DataLoggerGUI, from SpikeGadgets, data are extracted from the head-stage and saved as a .dat file. Using the same software and head-stage configuration file .trodesconf and extracted neuronal data .dat file is merged into the .rec file recorded by the acquisition computer. Once merged, .rec file is transferred into the spike sorting computer where it is reformatted into the .phy format, and the DIO signal is extracted using export functions from trodes bitbucket repository. Afterwards, SpyKing Circus (with the configuration .txt and the channel mapping .txt file) automatically detects spikes and pre-sorts them. SpyKing circus is a massively parallel code which performs semi-automatic spike sorting. It uses a smart clustering and a greedy template matching approach. The results are then visualized and further, manually sorted in the PHY GUI from Cortexplab. Once data spike sorted, individual spikes were saved as timestamps into .txt files using Matlab.

## Analysis

The spike data are plotted with the trajectory of the animal. When spikes have a spatial correlation, it is visible as the spikes are clustered around some particular area. For further more detailed analysis, Spike3D (custom-written program by Ali Zonos) was used to assess the animal's behaviour, with the spikes visualised during the recording session.

## Animals

Six adult grey mouse lemurs (*Microcebus murinus*) were used for this study so far. All mouse lemurs were born and raised in the "Mouse Lemur Platform" (authorization number E-91-114-1) of the Museum of Natural History in Brunoy, France. Some of the animals were in the care of the staff of the UMR CNRS-MNHN 7179-MECADEV until we requested them for the experiments, and some were born directly into our care. The procedures are in accordance with European animal welfare regulations, and were reviewed by the local ethics committee ("Comité d'éthique en expérimentation animale No. 68") in Brunoy, France, by the ethics committee of the University of Geneva, Switzerland, and authorized by the French "Ministère de l'éducation nationale de l'enseignement supérieur et de la recherche". Animals are kept on an inverted light-dark period so we could perform our experiments during their active time. Animals are housed socially (2 or 3 per cage) in cages (50 × 60 × 70 cm) with wooden branches, leaves and nest boxes until they underwent surgery. After surgery, they are housed individually to protect their head-drives. The temperature is kept between 24 and 26 °C, the relative humidity is approximately 55%, and the artificial light cycling on 14 hours ON per day (winter period, (Perret, 1997)). Animals have food available ad libitum, or if it is necessary under food restriction and always with unrestricted access to water.

# Results

## Single cell activity

By synchronizing the recorded neuronal activity with the 3D position of the mouse lemur we found neurons that were responsive to a large region (floor, Figure 26a,b) or a specific location (single branch, Figure 26c,d and Figure 27) of the lattice maze, or mainly when moving in one direction on branches with a given diameter (Figure 28e–i). With the EthoLoop tracking system we induced the specific foraging patterns and thus ensured that the animals either cover large parts of the lattice maze (Figure 26a,c) or create multiple reproducible paths across a given location (Figure 26e). These recordings are to our knowledge among the first examples of 3D place cell-like activity recorded in freely roaming primates.

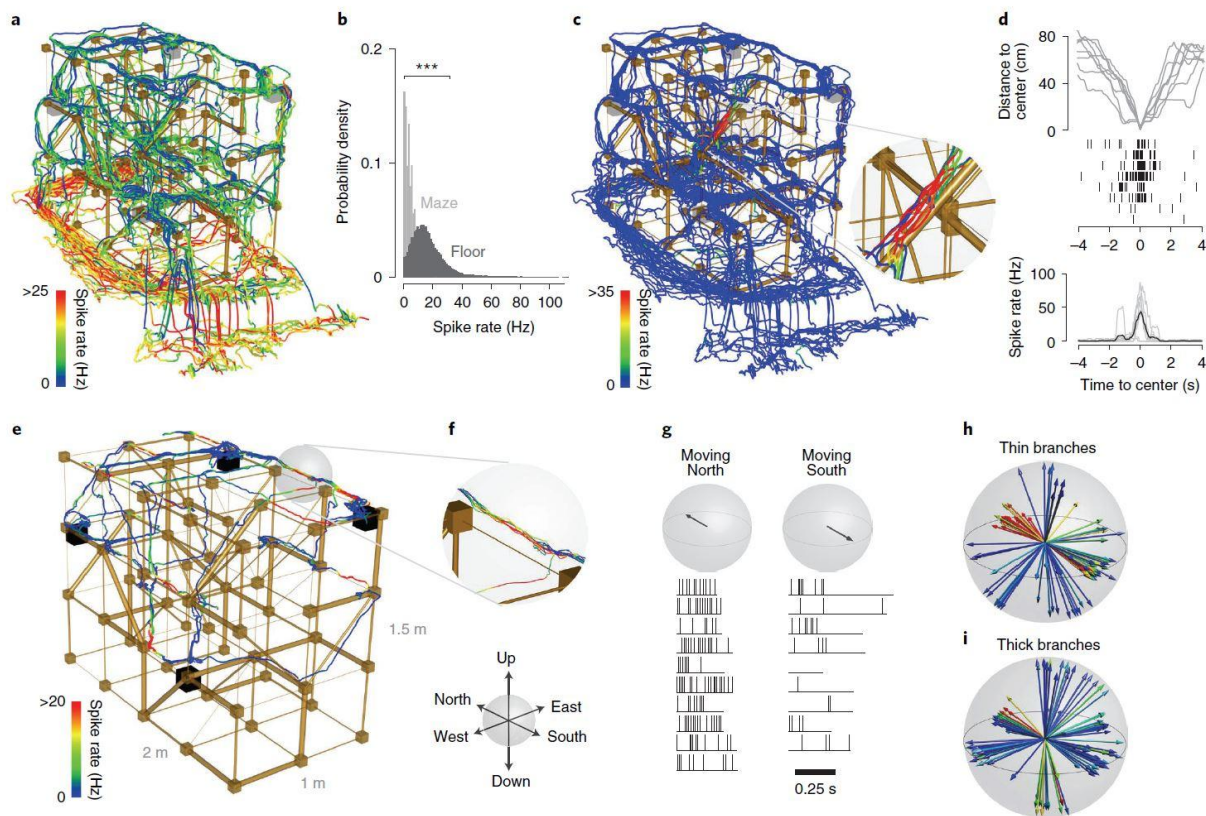


**Figure 26: Wireless recordings of neuronal activity in dorsal CA1 during navigation in a 3D lattice maze.** a, A neuron in mouse lemur CA1 during foraging in a lattice maze showing increased spike rate when on the floor. b, The neuronal activity (over segments of 13 cm) on the floor compared to the activity in the rest of the lattice maze ( $***P < 2.2 \times 10^{-16}$ , two-sample Kolmogorov–Smirnov test). c, Spike rates for a CA1 neuron showing increased activity preferentially on a single branch location (same recording session as in a. d, Distance of the animal to the location with highest average activity (top), action potentials of the recorded neuron (middle) and spike rate of the recorded neuron during individual passages (gray) and their average (black), in relation to the time to reach the center (highest average activity). e,f, Spike rates of a CA1 neuron showing increased activity on multiple locations in the maze. g–i, Additional analysis revealed that the neuronal activity was specific to one specific spatial direction (g) (north, neuronal data from the location in the gray sphere in e and higher when moving north on thin (h) compared to thick branches (i). The arrows in the sphere indicate the movement directions (13 cm segments), while the color indicates the level of activity. From (Nourizonoz et al., 2020).

Below we show some additional place cells. In Figure 27a we see a place cell with a maximum firing rate of 5Hz. In Figure 27b place cell activated when an animal in direct contact with one of the four feeders on the maze and cell shown on Figure 27c is responsive to two locations.

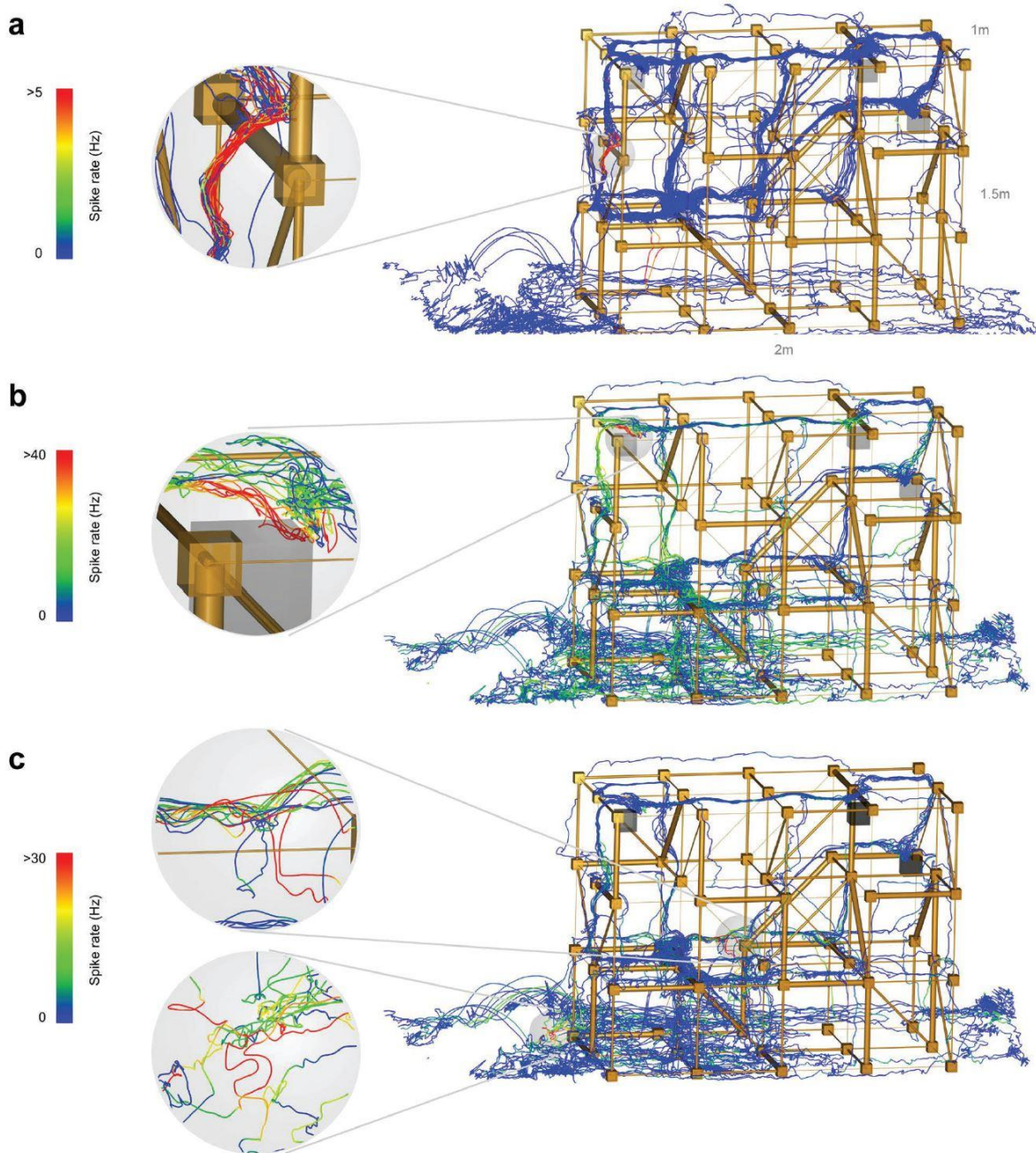


**Figure 27: Additional CA1 neurons with spatially restricted activity.**

a, CA1 neuron showing increased activity preferentially on a single branch. b, CA1 neuron from different sessions showing increased activity near a feeder (gray square). c, CA1 neuron from the same session as (b) but showing increased activity at two different locations. From (Nourizonoz et al., 2020).

## Theta activity

Power spectrogram of the local field potential from multiple recordings shown in Figures 28 and 29 revealed dominant oscillations. Experimental sessions of more than one and half hour were used to look for theta activity. Behavioural states during the whole experimental session are annotated and visualised in Figure 34 above the power spectral time series. The animal was at the beginning of the session held in the hand and moved in close vicinity of the maze around its outer edge. After the release in the maze, I chased the animal and the animal responded with an escape run. The experiment continued by letting animals behave alone in an experimental room which resulted in periods of free maze explorations or sleep. At the end of the session, I chased the animal again until I managed to catch it and at the very last step, I repeated the fly over the maze with the animal in the hand. This structure of the experiment was the same in both experiments. Figure 35 has instead of behavioural clustering visualized spike rate and speed of an animal. In both experiments during running of animals most prominent oscillations were between 2-4Hz and during sleeping 10-14Hz.

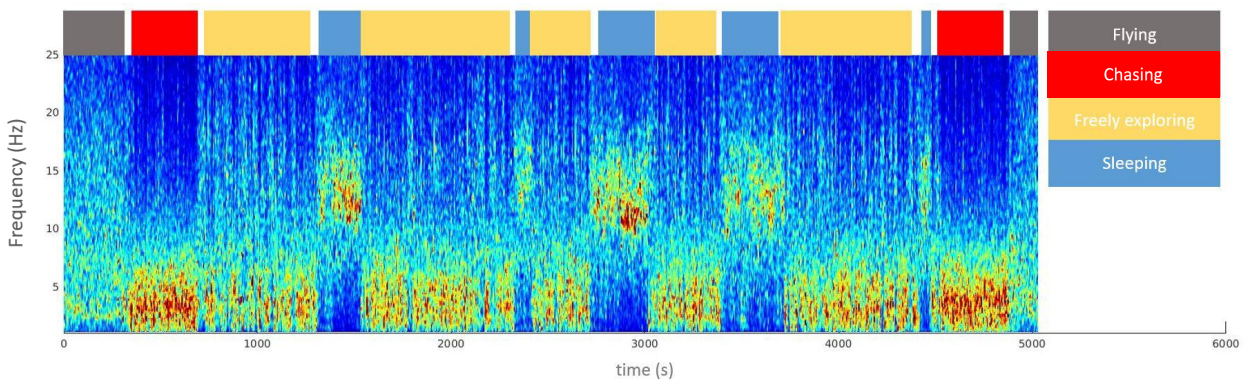


**Figure 28: Power spectrogram**

Power spectrum time series of the local field potential during a recording session. The colored bars above the plot indicate the behavioural state of the animal. The gray represents the times when an animal was held in the hand and moved around the maze. The red represents the periods where the experimenter actively followed the animal around the maze, yellow represents the time when animal freely explored the maze and blue are moments when animal was sleeping.

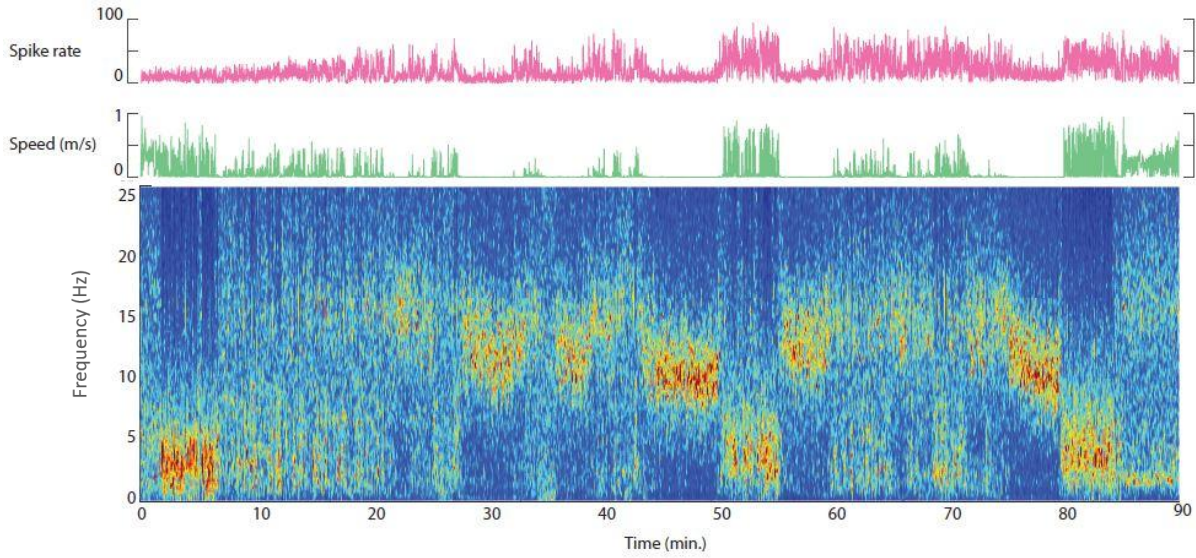


**Figure 29.: Power spectrogram.**

Time series of power spectrum from a 90 minute recording. Above in pink visualized spike rate of a cell from which local field potential was used for power spectrogram. Green represents the speed of the animal during the recording session.

Extraction of the power in different frequency bands from the session visualized in Figure 28 is presented in Figure 30. Data from the session are divided into three different oscillatory frequency bands representing below/above theta and theta oscillation. Even though there is no theta frequency (6-10 Hz) represented in the signal, there is a certain leakage from the frequencies below and above.

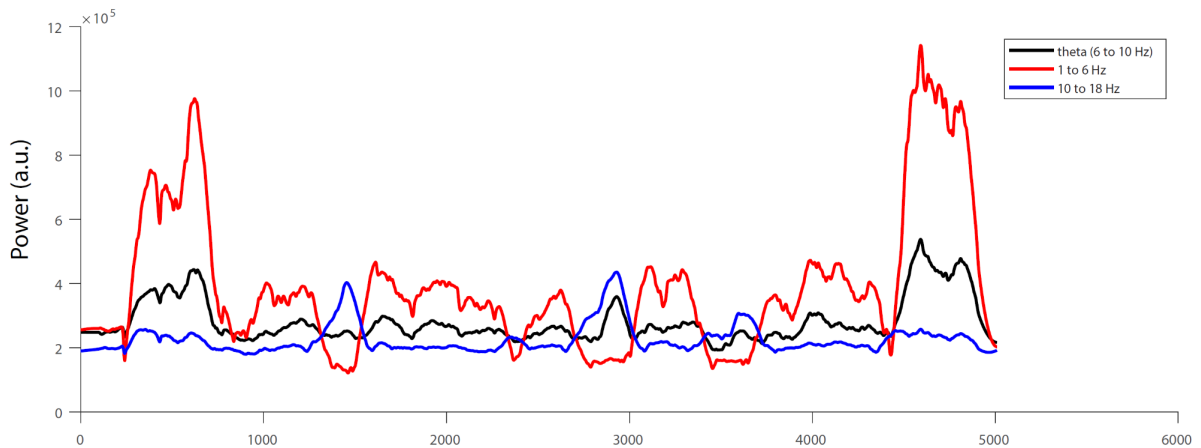


**Figure 30: Frequency bands**

Visualisation of the power spectral lines of different frequency bands from one recording session. Black line is theta frequency 6-10Hz, red is 1-6Hz and blue is 10-18Hz.

At no stage of the experiment were present significant bouts of theta activity as in rodents. Theta activity present in our data is usually restricted to around one to three seconds. On the other hand, this lack of theta is in coherence with data from other primates and bats ([Yartsev et al. 2011](#); [Yartsev and Ulanovsky 2013](#); [Eliav et al. 2018](#); [Courellis et al. 2019](#));

To facilitate our recordings in volumetric space we let the animals freely roam in the three dimensional maze built out of sticks of different thickness. We have quantified how many times animals ran over each thickness and we found no preference for branch thickness. On the figure 31 is shown the number of runs over different thickness in five experimental sessions. No preference towards the branch thickness was observed.

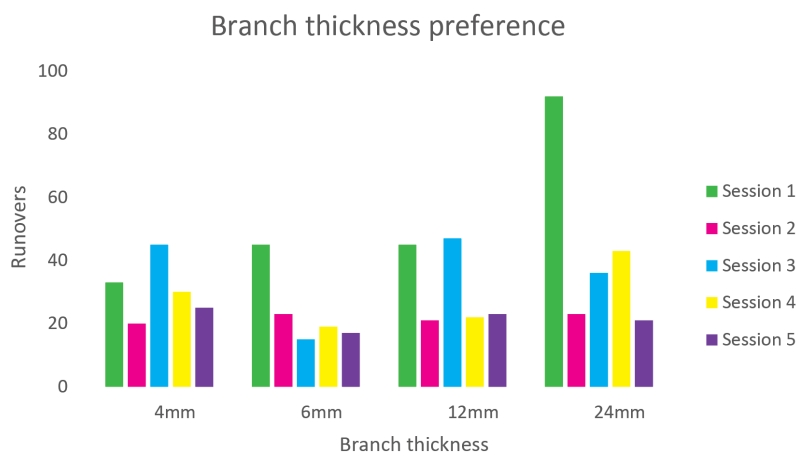


**Figure 31: Thickness preference.**

Five experimental sessions, each represented by specific color and divided into groups based on the thickness of the branch.

# Discussion

For almost a century, researchers have tried to understand the mechanisms underlying spatial navigation. The first twenty years of research were primarily characterized by ethological research. In the 1970s, with the development of electrophysiology, the ethological research on spatial navigation merged with neuroscience. Since then, both streams of scientific approaches produced a great body of work and contributed to the overall understanding of processes involved in navigation and orientation. Spatial navigation is by no means a simple behaviour.

The ethological approach focused primarily on the search for strategies, sensory modalities and use of cues, leading to the investigation of a plethora of animal models. This resulted in understanding the great diversity of this behaviour. While some animals use senses and cues similar to those used by humans, senses and cues used by other animals are unique to their species. Amongst the most peculiar are ultrasound sonar used by dolphins (Starkhammar et al., 2011), polarized light used by lizards (Beltrami et al., 2010), or smell in order to create an odour-gradient map as is observed in pigeons (Gagliardo, 2013). These findings, although not transferable to humans, contribute to our overall understanding of the principles of navigation and serve as a source of inspiration for further research.

Neuroscience research focuses on understanding the mechanisms behind neuronal processing that mediates navigation. Unfortunately, limitations of laboratory work and recording techniques narrowed this research almost exclusively to rodents. So far, it seems that, at least for the land-walking mammals, the principles guiding neuronal computations are, to a large extent, similar. Perhaps it is the consequence of a well preserved hippocampal formation that obeys similar cytoarchitecture and function across mammalian species: the entorhinal cortex, acting as a bridge between cortices and hippocampus, contains grid cells in humans as well as in rodents (Doeller et al., 2010; Jacobs et al., 2013; M. Kim & Maguire, 2018), (Hafting et al., 2005). The hippocampal place cells of rodents are analogous to those found in humans (Ekstrom et al., 2003; O'Keefe & Dostrovsky, 1971). Nevertheless, rodent research isn't without caveats. Several obstacles lie in the way of assuming a fully analogous system of rodent and human space perception. Perhaps the major hurdle is an uncertainty of the third dimension representation in rodents. In nature, rodents are thought to move on or in the ground, and therefore nearly all evidence from rodent research is only two dimensional. The lack of the third dimension makes the understanding of human fully volumetric space perception incomplete.

Another possible misalignment between the rodent and human navigation systems rests in the differing use of sensory modalities. Humans don't possess whiskers as rodents do, and instead rely mostly on vision for navigation. A consequence of this is that it leads to the arising of factors that make interpretations difficult. For example, understanding the utilization of egocentric or allocentric reference frames or the directionality of rodent place cells in linear

tracks (Battaglia et al., 2004). Closing the knowledge gap caused by these differences asks for the use of more suitable animal models. The former problem of addressing the third dimension was elegantly approached by investigation in bats. Indeed, it resulted in the finding of the spherical place cells (Ulanovsky & Moss, 2007). The continuous effort invested in this flying mammal has paid off and many other types of cells were documented.

Although the research with the Egyptian fruit bats revealed several riveting mechanisms of navigation, it is uncertain if these mechanisms translate to humans. We therefore wonder: Is the representation of space the same for non-flying-mammals and bats? Can land-walking animals have bat-like place cells, which are hanging in the air? In order to answer these questions, it is necessary to study land-walking animals that navigate in 3D.

To see the full picture, it seems that we cannot avoid looking at primates. Unfortunately, most of the previous primate evidence suffered from multiple issues, ranging from technical, through to experimental designs and the interpretation of results. Pioneering primate studies on macaques faced many technical challenges of ancient recording systems. Additionally, it is very difficult to record the dorsal Ca1 area. This is due to this area of the hippocampus only being a very thin layer that is difficult to target. Therefore, most of the recording electrodes were placed in the more medial part of the hippocampus. Additionally, the burden of rivalry between labs led to the repetition of results. On the other hand, more recent primate studies seem to suffer primarily by experimental design. Although the animals are moving “freely”, they are often restricted to movement in a two dimensional space, the conditions are not naturalistic, and recording sessions are only short time periods.

Overall, the outcome of these previous studies on spatial navigation in primates is that the presence of neurons is modulated by the locations and the tasks of the primates. The absence of “pure” rodent-like place cells in the primate brain suggests that, unlike rodents, primates have allocentric representation defined by spatial view cells. Nonetheless, it is important to stress a few pitfalls. Firstly, there are only two laboratories behind most of the primate work that has been presented so far (Rolls, Ono). In addition to this, the results presented in the aforementioned papers belong to a fairly small set of experiments. Indeed, only three experiments have been performed in the Rolls laboratory and four experiments in the Ono laboratory.

The authors of these studies have argued that there are multiple reasons why primate studies carried out to date have failed to show place cells with an activity pattern comparable to the one previously described in rodents (O’Keefe, 1976). In their opinion, the differences between the findings of primates and the rodents could be due to the development of the fovea, or differences in the eye movements of the two species (which would ultimately result in the allocentric perception of the space “out there”) (Rolls and Wirth 2018).

An alternative explanation as to why no classical place cells have been found in primates, might be due to the location of recording electrodes. Most of these studies report recording

sites from the anterior and medial hippocampus, which is homologous to the rodent ventral hippocampus. It should be stated that for rodents the vast majority of place cells with high spatial resolution are located in the dorsal hippocampus, whereas its primate homologous is located in the posterior hippocampus (Andersen et al., 2007; Jung et al., 1994; Kjelstrup et al., 2008; O'Keefe & Dostrovsky, 1971). Recent data recorded from the rodent ventral hippocampus indeed seems coherent with this interpretation and confirmed the presence of cells coding for task-related spatial information (Spellman et al., 2015), (Matsumura et al., 1999; Miyashita et al., 1989; Nishijo et al., 1997).

Recent technological advances now provide precise and practical solutions to measure body movement, head-direction and eye movement as well as neural activity and thus, allows us to revisit the question of how spatial parameters are represented in the primate brain with new methods. Additionally, the choice of a small primate species such as the mouse lemur allows probing naturalistic behaviours. It was therefore an ideal moment to combine classical ethology and neuroscience. Our novel tracking and recording methods presented here allowed us to closely monitor primates in a naturalistic habitat, while recording their neuronal activity and tracking their position with high precision. Altogether, we think that this is a promising tool for future discovery.

## Maze and Thickness of the Branches

In order to investigate how mouse lemurs' cells code for the third dimension of space, we built a three dimensional lattice maze. Our lattice maze allows them to roam freely in volumetric space while recording neuronal activity in the hippocampus. When designing the lattice maze we firstly considered a lattice with branches of the same thickness, as has previously been and currently is used with rodents (Grieves et al., 2020; Grob ty & Schenk, 1992). However, after discussion with Anthony Herrel, we decided to use a lattice with sticks of varying thicknesses. Initially, we hoped that mouse lemurs' evolutionary adaptation for arboreal locomotion would be observable in the animals' preference for movement along sticks of certain thicknesses.

However, in our experiments where animals foraged for the food reward, efficiency between rewards places seems to play a more important role, as animals usually chose the shortest connecting path between feeders and further followed a very stereotypical route. Nevertheless, our findings showed to be in concordance with the results from Toussaint et al. (2015), which concluded that mouse lemurs were rather opportunistic and not specialized in the use of a specific branch thickness (Toussaint et al. 2015). Our lattice served well for the purpose of animal navigating in 3D, but these experiments might not provide sufficient evidence for the preference towards a given branch thickness.

## Experimental setup

In order to record neuronal data while mouse lemurs swiftly move in all directions across the lattice maze, we had to use a wireless system. So far, neuronal recordings in freely roaming primate in 3D represented a major challenge. Since our main motivation was to look for evidence for 3D place cells, we had to correlate neuronal data to the animals' position.

In the attached paper, we are presenting proof of principle of our recent development, which integrates neuronal data and tracking systems (Nourizonoz et al. 2020). Thanks to the mouse lemurs as a favourable animal-model and recent technological advancements, we can record neuronal activity in the unrestrained, freely moving primate. Our animal is free to run along the 2m x 1.5m x 1m lattice where the two most distant points on the lattice are around thirty times the body length of the lemur. Additionally, our animals were allowed to explore the ground of the experimental room, which further expanded the area.

The only comparable spatial navigation studies reporting similar freedom of locomotion are the bats recordings carried out by Nachum Ulanovsky's group. Experimental bats in study concerning 3D place cells and goal-direction cells were flying in room of 5.8 x 4.6 x 2.7m (Yartsev & Ulanovsky, 2013), (Sarel et al., 2017), whereas those in the study concerning social place cells were in a 2.3 x 2.7 x 2.6 m room (Omer et al., 2018). The neuronal recordings from bats were obtained from one of four implanted tetrodes. Additionally, due to telemetric transmission limitations, their neuronal recorder had to be filtered with a 300Hz high pass filter, which prevented the collection of LFPs. In primate literature, only a handful of studies claim a combination of freely moving primate with electrophysiology. These include a study on marmosets from 2012 titled "Wireless multi-channel single-unit recording in freely moving and vocalizing primates" from (Roy & Wang, 2012), a similarly developed system for macaques (Chestek et al., 2009), and a study involving freely navigating marmosets along an "L" shaped track (Courellis et al., 2019). In these systems, the free movement of their animals was restricted to two dimensions, and the distances they can travel were quite restricted as well in that they are just turning around one spot. The recording area was less than four times their body size, which is small in comparison to the area in which our animals navigate. In comparison to the experimental setups in these studies, our system has several advantages. First, our animals are free to move in all directions and in orders of magnitude larger space. Second, our maze is simple and hence it allows online data transmission for neuronally triggered close loop experiments. Finally, the length of our recordings is more or less equivalent to theirs, limited just by the weight and size of the batteries.

In addition, in our experiments the behavior of animals can be directly conditioned with robotic stimulus and reward delivering RECO-boxes. This conditioning can be driven by real-time input from the tracking system, based on either the position of the animal in the space or driven by the animal body posture. The real-time body posture can be analysed from the close-up camera input by employing an adjusted DeepLabCut algorithm ([Mathis et al. 2018](#)). Our preliminary data shows the temporal stability of the recording with a high quality of signal represented by a great signal-to-noise ratio.

## Results

Spatial navigation research was shaped by the discovery of place cells in the dorsal part of the rodent hippocampus in 1971 by John O'Keefe and Dostrovsky (O'Keefe & Dostrovsky, 1971). The activity of these cells was defined solely by the spatial location of the animal. Following this initial discovery, rodent place cells were in the spotlight of spatial navigation research for the next 30 years, and this included scientists working on other animal species trying to identify them as well. First, similarly behaving cells were discovered in the crawling bats in 2007 (Ulanovsky & Moss, 2007), and afterwards, in 2013, 3D place cells were reported in bats (Yartsev & Ulanovsky, 2013). Contrarily, the results from primate research did not succeed in delivering evidence for place cells as we knew them from rodents, but instead revealed evidence for new types of cells: spatial view, task and body movement cells (Cahusac et al., 1993; Miyashita et al., 1989; O'Mara et al., 1994; Ono et al., 1991, 1993; E. T. Rolls et al., 1997, 1998; E. T. Rolls & O'Mara, 1995; Tamura et al., 1990, 1992). Spatial view cells are activated by certain visual scenery, most often defined by head/gaze towards a certain direction. The difference between the presence of place cells or spatial view cells was explained by different spatial reference frames.

Several studies claimed finding place cells in primates, but experimental design or lack of control for head/gaze direction made it impossible to differentiate them from spatial view cells (Ludvig et al., 2004; Ma et al., 2004). Therefore, we concluded that rodent-like place cells are yet to be confirmed in primates. Here, we present several cells that are activated when an animal passes through a certain location. Our animals pass through the place field multiple times, in different directions, and therefore have an inconsistent view of an environment at the cells' place fields.

Our data indicates the presence of several interesting cells. In Figure 26a, we present a cell with activation spatially restricted to the floor of the experimental room. The cells devoted to this representation might play an important role for the mouse lemurs, since they commute either on the floor or in the branches above. In nature, the mouse lemur uses floor-commutes solely over larger distances. This phenomenon is observed mainly during dispersal when mouse lemurs favor a straight and fast getaway (Schliehe-Diecks et al., 2012). However efficient, this commute renders the mouse lemur considerably more vulnerable to predators. They therefore prefer above-ground commutes, which are slower but safer.

In Figures 26c and 27a, we show a bi-directional place cell with a place field of no apparent importance. This cell field is located on the diagonal medium-thickness branch across which the animal often runs (in between the reward sides). This place field is relatively small, with a length of around 15cm. So far, out of the cells we observed, we think this cell might be the closest to the rodent-like place cell. Unfortunately, the place field shown in Figure 26c lies in between nodes of the lattice and the one shown in Figure 27a lies at the corner of the maze. Therefore the animal did not approach this place from more than two directions.

In Figure 26e, we present a cell that is activated when an animal runs over a specific (very) thin branch in a particular direction. This cell is conjunctive between the thin branch and the running direction. Presumably, the cell preference to thin branches might be substantiated by the evolutionary adaptation for movement along thin arboreal substrates.

In Figure 27b, we show a place cell with a place field at the location of one of four RECO-boxes. The neuronal representation of the location where the animal receives rewards is also important and therefore expected.

In Figure 27c we show a place cell with two place fields. Even though there were only few passages over these place fields, it shows that mouse lemurs can have more than one place field per place cell, as it is also often found in rodents ([Grieves et al. 2020](#)).

To our knowledge, we present here the first examples of classical spatial place cells in primates. Yet other parameters also seem to play important roles, and other relevant cell types are also observed. This includes unidirectional place cells, cells specific to certain branch thicknesses, cells activated solely on the ground, cells with a place field at the reward site or cells with two place fields.

These are, so far, novel examples reported in primates. Our preliminary data suggests the existence of cells with high contextual specificity and cells that are not only strictly position-related cells, but act in conjunction with other features of the environment. Our cells exhibit variability in the size of their place fields, as is also reported in rodents or bats ([Dabaghian et al., 2012](#); [Grieves et al., 2020](#); [Ulanovsky & Moss, 2011](#)). Our cells also exhibit a large variability in firing rates, with some cells firing at a maximum spike rate around 2Hz, and other cells firing up to 100Hz. The observed firing range is of a significantly larger distribution than has so far been found in rodents, and therefore this unusual phenomenon requires further investigation.

Our data also confirms the previous observation of the absence of theta oscillations during navigation in primates. Place cells in rodents are thought to be specifically time locked to theta oscillations ([Burgess & O'Keefe, 2011](#)). Therefore, their absence in bats was firstly surprising, and afterwards thought to perhaps be a bat-specific feature. However in 2019, [Courellis and colleagues](#) observed an absence of rodent-like long stretches of theta activity ([Courellis et al., 2019](#)). The data that we are presenting shows that mouse lemurs, same as marmosets, have only present short bouts of theta oscillations, which do not seem to be related to navigation.

## Quality and limitations of the results.

Following our recent data collection, we are confident in the quality of our recordings. Our recording system enables the recording from 32 channels (8 tetrodes). This is not impressive in comparison with current trends in electrophysiology. Neuropixel probes are capable of recording from hundreds of channels ([Jun et al. 2017](#)), but our research questions do not

require this amount of throughput. Regarding the analysis, there is still plenty of room for improvement. Specifically, through the adoption of analysis algorithms currently used in rodent studies, we could have a greater yield in place cell recognition. The overly strict criteria we implemented to determine the validity of a place cell, prevented us from considering place cells that have multiple place fields. As a result, we were limited to examining place cells that only have one, or at most two, place fields. This differs from rodent studies, where cells with up to six place fields are still regarded as place cells.

Additionally, we should implement an automated pipeline for basic analysis of our signal. Even though the recent study of the marmoset freely moving along the “L” shaped track (Courellis et al., 2019) didn’t bring much novelty, it represents a great example of comprehensive and neat signal analysis.

One of the persisting issues we need to solve is the ability to analyze data faster, which would allow us to avoid the remapping process between recording sessions. Currently, it takes around five hours from the moment we finish the experiment until we have the visualization of neuronal activity projected in the space which allows us to identify cells, their potential place field and their localisation. For now, the large time-scale prevents us from observing the same place field per cell across experiments. Since some of our preferred future experiments necessitate manipulation of the environment, we need to avoid remapping. We hope that keeping the animal awake in the experimental room, in combination with shorter analysis time, will grant us the opportunity to record place cells with same place fields from one session to another.

## Conclusions and Future Perspectives

Thanks to the recent advances in technology, we are able to conduct long neuronal recordings in freely roaming primates in naturalistic conditions. We already obtained proof of principle data, and we are now ready to invest time into verifying or disproving multiple hypotheses raised from the generalization of rodent or primate research findings.

We wish to use this opportunity to answer novel and original questions. For future experiments, we plan to use the Open Ephys shuttle drive with 64 channels (Voigts et al., 2019), to alternate the head-stage connection between one or the other 32 channel connector between recordings. This way we plan to double the information yield per animal.

For the future we are excited by several ideas that we would like to examine, and I will now discuss a few of them below.

First, we would like to repeat Quirk's experiment performed on rats in the Nineties (Quirk et al., 1990), and examine the stability of place cells in complete darkness. Shortly, we plan to alter light and dark periods during the experiment, starting either with a light or with a dark period. The alternating of environmental cues should help to understand the priority of sensory modality used for spatial mapping.

One particularly interesting option - which is in part inspired by the study based on sound mapping from David Tanks' lab (Aronov et al., 2017) - is to project a real-world lattice, on which an animal is running, onto a virtual one, where real  $x$ ,  $y$  and  $z$  coordinates would be represented by different sound properties. The virtual sound lattice could be projected onto our lattice built of wooden sticks, which has dimensions of 5 by 4 by 3 nodes. On the dimension consisting of five nodes (length) five notes of the musical scale (C, D, E, F, G, A, B) could be mapped, the dimension consisting of four nodes (height) could see a continuing increase in pitch, and the dimension consisting of three nodes (width) could be mapped with sounds of different instruments. A location-specific sound will then be played as the animal moves over the lattice in complete darkness. Additionally, masking the other sensory inputs could create an environment with audio landmarks, which could subsequently easily be manipulated or used for navigational purposes. Once an animal learns the sound landscape, the presence of an activated robotic food delivery box could be indicated by a specific sound that represents its position. Alternatively, this experiment could be set up so that the animal - after learning the sound landscape - will hear a tone of a certain location, to which it will have to move to in order to receive a reward from only one feeding location.

Secondly, we would like to examine if a place cell activity is bound to its active movement in space, or if an animal that is passively transported would also exhibit the same responses in place cell activity. We plan to hold the animal in the hand and fly over the lattice in the closest distance possible at the beginning and at the end of the experimental session. This could help us understand the importance of path integration in place field formation.

Thirdly, we would like to understand if place fields (during our 3D lattice exploration) are determined by the coordinates on the lattice or more distant cues such as walls of the room, light source, etc. To understand, we plan to rotate the maze across its cardinal axis by  $180^\circ$ . There are three different expected results in this scenario: either the animal will remap completely, or it will keep the place fields in relation to the lattice, or it will not remap and keep them in relation to the room. Additionally, we can expect a partial remapping, a change regarding only the firing frequency, or the maintenance of the place field's position.

Fourth, we would like to examine the character of the place cell activity. This includes investigating factors such as if their activation proceeds the animal's position, if they are in absolute real time synchrony with the animals position, or if they report where the animal is currently positioned. We want to run experiments where the animals will have to perform long jumps from one place to another. If we will be able to find a place cell for the place where the animal is supposed to land on, the onset of the cell activity could provide us with necessary

information. We are also considering the option that the place cell will be activated as early as the moment when the animal starts to prepare for the jump or during visual fixation of the landing spot. Alternatively, the cell could be activated once the animal is in the air, during the jump, or that the cell is activated only after the moment of the landing.

Additionally, there are two other ideas we believe are worth pursuing. We are interested in recording from the entorhinal cortex. However, accessing this area might be very challenging. We would also like to start using the 2-photon miniscope to increase the yield of our experiments.

Overall, we are very satisfied with the contributions we were able to make to further the understanding of spatial navigation in the third dimension, and look forward to applying our methods in future experiments.

# Additional work

## **Pupil Size Coupling to Cortical States Protects the Stability of Deep Sleep via Parasympathetic Modulation**

**Authors:** Yüzgeç O\*, Prsa M\*, **Zimmermann R\***, Huber D. ( \* equal contribution )

**Journal:** Current Biology 2018 DOI:<https://doi.org/10.1016/j.cub.2017.12.049>

### **Abstract:**

During wakefulness, pupil diameter can reflect changes in attention, vigilance, and cortical states. How pupil size relates to cortical activity during sleep, however, remains unknown. Pupillometry during natural sleep is inherently challenging since the eyelids are usually closed. Here, we present a novel head-fixed sleep paradigm in combination with infrared back-illumination pupillometry (iBip) allowing robust tracking of pupil diameter in sleeping mice. We found that pupil size can be used as a reliable indicator of sleep states and that cortical activity becomes tightly coupled to pupil size fluctuations during non-rapid eye movement (NREM) sleep. Pharmacological blocking experiments indicate that the observed pupil size changes during sleep are mediated via the parasympathetic system. We furthermore found that constrictions of the pupil during NREM episodes might play a protective role for stability of sleep depth. These findings reveal a fundamental relationship between cortical activity and pupil size, which has so far been hidden behind closed eyelids.

### **Contributions:**

My personal contribution in this study was in bringing the initial idea of a sleep project, establishing technique of electrocorticogram (ECoG) recordings in our laboratory; characterizing body posture during natural sleep of mice using x-ray imaging; adjusting of the head-restriction system parameters to approach natural like posture that allows mice to sleep; developing training paradigm for mice to sleep in head-fixed conditions; creating an algorithm for pupil diameter and movement tracking; observation and discovery of the negative correlation between pupil size fluctuation and the ECoG power; obtaining a proof or principle data; manual annotating and control of electrophysiology data and control and correction of pupil measurements as a part of analysis.

### **Contributed results:**

Discovery of inverse correlation between pupil diameter and broad band ECoG power. Visualization of the ECoG signal, pupil diameter, mental states and pupil movement during the experimental session is in figure 1.

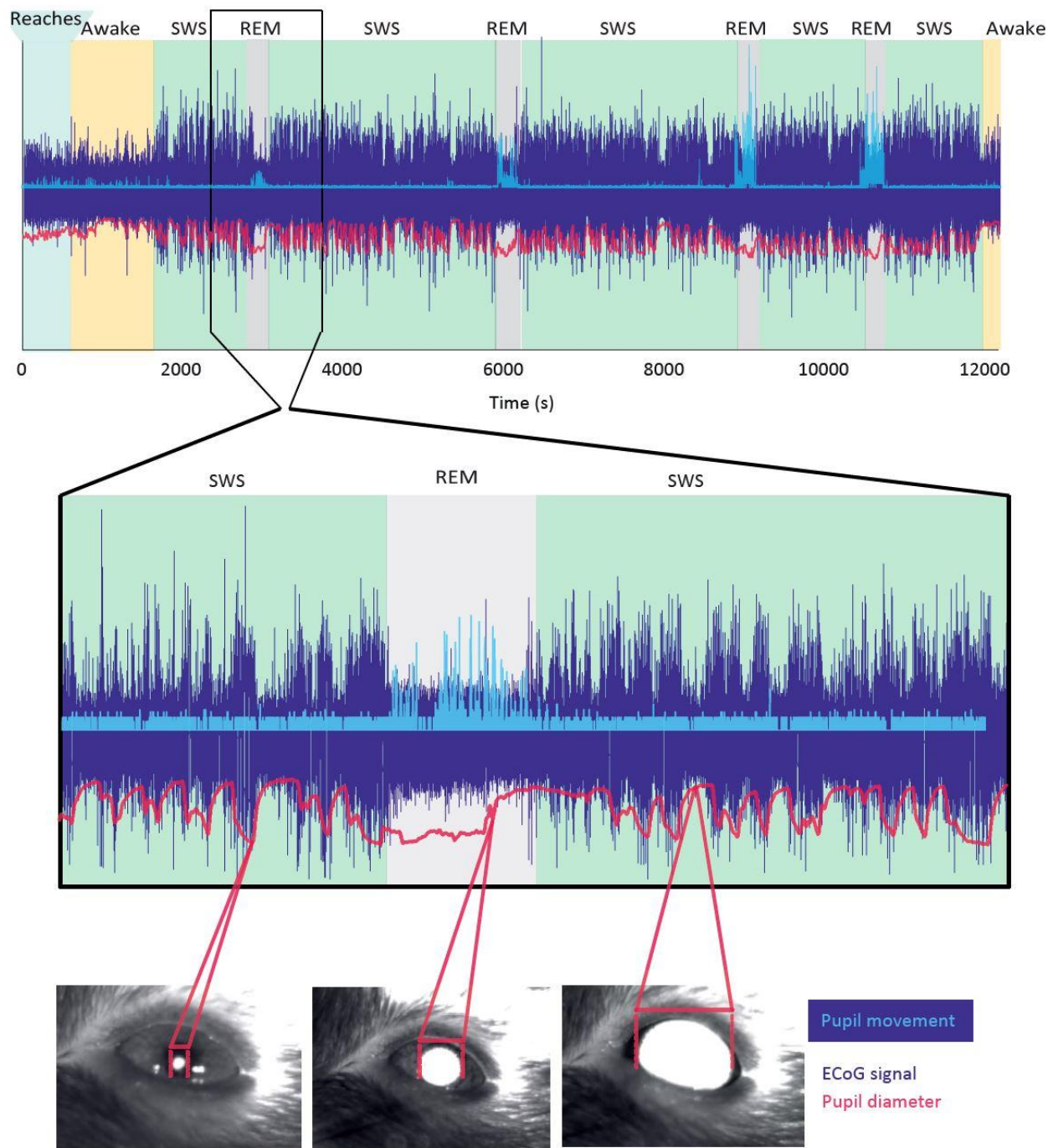


**Figure 1** Top: Dark blue, ECoG signal during experiment, brain states as background bars, yellow is awake, green is slow wave sleep, and rapid eye movement (REM). Sky blue represents movement of the pupil centroid. Red line is a pupil diameter. Second row: a close-up of the ECoG signals during awake, NREM, and REM states, pupil movement and diameter. Third row: example of differences in pupil diameter size.

## Orientation Preference Maps in *Microcebus murinus* Reveal Size-Invariant Design Principles in Primate Visual Cortex

**Authors:** Ho CLA\*, Zimmermann R\*, Florez Weidinger JD, Prsa M, Schottdorf M, Merlin S, Okamoto T, Ikezoe K, Pifferi F, Aujard F, Angelucci A, Wolf F & Huber D, (\* equal contribution)

**Journal:** Current Biology 2020 <https://doi.org/10.1016/j.cub.2020.11.027>

### Summary:

Orientation preference maps (OPMs) are a prominent feature of the primate primary visual cortex (V1) organization. In rodents, neurons are not organized in OPMs but are instead interspersed in a “salt and pepper” fashion, although clusters of orientation-selective neurons have been reported. As primates are typically larger than rodents in terms of brain and V1 size, does this fundamental difference reflect a lower size limit for orientation columns (OCs) below which they cannot be scaled down with decreasing V1 size? To address this question, we examined V1 of one of the smallest living primates, the 60-g prosimian mouse lemur (*Microcebus murinus*). Using chronic intrinsic signal imaging, we found that mouse lemur V1 contains robust OCs, which are arranged in a pinwheel-like fashion. OC size in mouse lemurs was found to be only marginally smaller compared to the macaque, suggesting that these circuit elements are nearly incompressible. The spatial arrangement of pinwheels is well described by a common mathematical design of primate V1 circuit organization. In order to accommodate OPMs, we found that the mouse lemur V1 covers one-fifth of the cortical surface, which is one of the largest V1-to-cortex ratios found in primates. These results indicate that the primate-type visual cortical circuit organization is constrained by a size limitation and raises the possibility that its emergence might have evolved by disruptive innovation rather than gradual change.

### Contributions:

My personal contribution to this study was in the development of the surgeries and further surgical procedures; fine tuning of drug composition and administration for anesthetized experiments; transformation of intrinsic signal imaging (ISI) setup used for mice into mouse lemur compatible setup; setting the experimental parameters and developing experimental procedure pipeline, running half of the ISI experiments and initial development and running experiments of the visual discrimination task.

### Contributed results:

Set of the ISI experiments during which the animal was presented with drifting black and white bars of different orientations resulted in the selective activation of the visual cortex. After color coding of selectively sensitive patches activated by different orientation stimuli, a pinwheel map as shown on figure 2 was revealed.

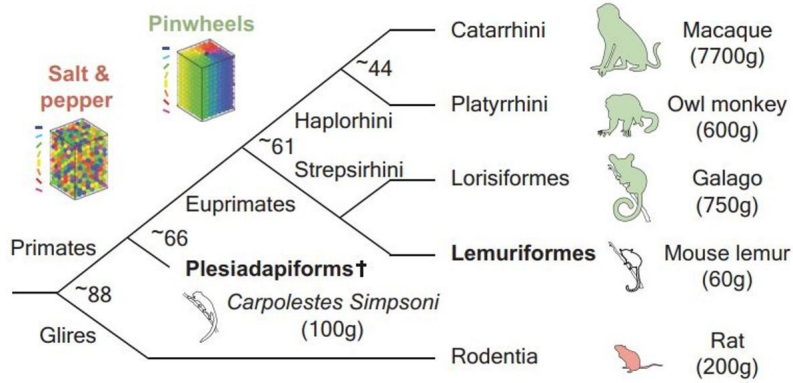


Figure 1.: Schematic tree of rodent and primate evolution. Species where V1 pinwheels have been reported are labeled in green; species with salt and pepper organization are in red. Numbers at the bifurcation points are approximate ages in millions of years.

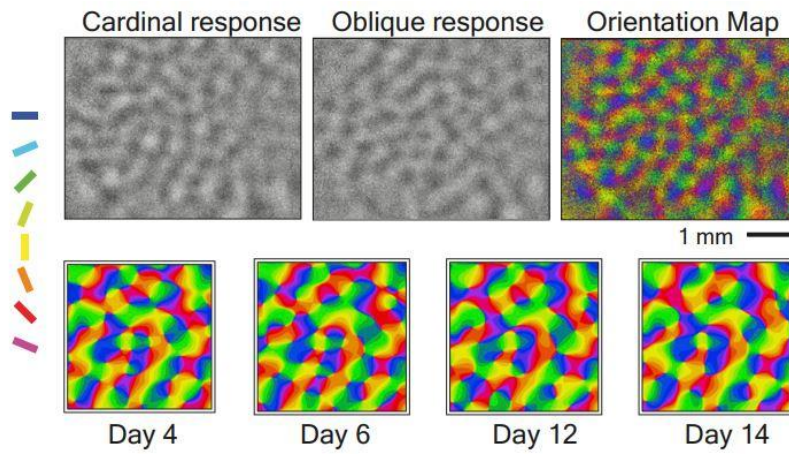


Figure 2.: Intrinsic signal imaging responses obtained by subtracting responses to the two cardinal and two oblique directions, respectively (top left and top center). Vector summation of responses to different orientation stimuli displayed as a color-coded orientation map (top right). The responses were stable for up to 14 days of chronic imaging.

# Acknowledgements

For the past six years during my doctoral studies, I walked with many those to whom I would like to thank. Without them this journey would certainly not be possible. Therefore I would like to say thanks: To Daniel aka Big Big Boss, for giving me a chance to pursue my studies in his lab, for mentoring and not giving up on me, for being always fair and direct, for teaching me some important lessons such as “if it works, record”, “if something can go wrong, it will go wrong”, “noone gives a fuck”, or “just do it” which after many repetitions transformed from initially annoying saying into the deeply meaningful phrase that is one of my favorite now. To Claudia and Karin, for providing inspiration and enthusiasm in the work place, company over long night shifts, long debates in realms of theoretical speculations, for place to hit the hay many more. Individually, to Karin for wild night bike rides and to Claudia for reminding of ever-present presence of creeping danger. To Mario and Gregorio, for their supervision and Matlab codes. To Andy for back2back production, Ali for keeping presence of those absent and to them both for keeping Brunoy crowded. To Antoine for being discrete, to Olga for her Chalet and also to the rest of the Geneva lab for being really nice colleagues. On the French site I would like to thank mainly to Anthony Herrel for making impossible possible and to Fab&Fab team for the same same but... I would like to thank as well to my parents for being very cool, to my little and big sister for their help and support and to my grandparents for great stories and staying alive. Special thanks to my companion Sacha, for appearing and sticking around, for making ordinary days remarkable, for providing better care and support than disabled puppies receive in YouTube videos. And cakes, ooh yess cakes. To graceful Niels, grande Mike and mastermind Nisheet, for being early intermediate and late companion in crime during my stays in Geneva. To Niels for discovering Geneva city and scene, to Michael for his hikes, reminding what is good/bad and for being first humanoid friend, to Nisheet for frequent sheltering while being a substitute girlfriend. To Slovak gang: Adams, Andy, Angelo, Danka, Drozdo, Oliver for their visits in Paris. To Roman for late night calls. To Dubak and Durko for being always welcomed. To Paris friends: Marine & Justine for before and after adoption, Steven & Stephane for inclusion, Oscar for Dimitri, Vlad & Nicolo for Tiquetonne experience. To Maylis, Lea, Laura for their good aura. To Koen, Artemis & Marina for keeping the Dutch flying. To Amira for trust and patience. To Slash, Dot, Hashtag, Asterisk and other brothers for everything. To Apolline, Vincent, Tiago, Armony, Alan, Patxi and all the others who were around. To those like Tom Mrsic Flögel, Vivek Jararaman and others whose meeting resonated as inspirational, motivational and charged with enthusiasm. Additional thanks to all of those without who's corrections this thesis wouldn't be readable. Their presence will remain signified by the difference between the rest and this very last paragraph of this thesis.

# References

- Able, K. P. (2001). The concepts and terminology of bird navigation. *Journal of Avian Biology*, 32(2), 174–183. <https://doi.org/10.1034/j.1600-048x.2001.320211.x>
- Able, K. P., Dingle, H., Gauthreaux, S. A., Blem, C. R., Meier, A. H., Fivizzani, A. J., & Kozlowski, T. T. (1980). *Animal migration, orientation and navigation*. Elsevier, New York.
- Aghajan, Z. M., Acharya, L., Moore, J. J., Cushman, J. D., Vuong, C., & Mehta, M. R. (2015). Impaired spatial selectivity and intact phase precession in two-dimensional virtual reality. *Nature Neuroscience*, 18(1), 121–128. <https://doi.org/10.1038/nn.3884>
- Alme, C. B., Miao, C., Jezek, K., Treves, A., Moser, E. I., & Moser, M.-B. (2014). Place cells in the hippocampus: eleven maps for eleven rooms. *Proceedings of the National Academy of Sciences of the United States of America*, 111(52), 18428–18435. <https://doi.org/10.1073/pnas.1421056111>
- Amaral, D., & Lavenex, P. (2007). Hippocampal neuroanatomy. *The Hippocampus Book*, 832, 37–114. <https://psycnet.apa.org/fulltext/2007-01023-003.pdf>
- Andersen, P., Morris, R., Amaral, D., O'Keefe, J., Division of Neurophysiology Tim Bliss, & Bliss, T. (2007). *The Hippocampus Book*. Oxford University Press, USA. <https://play.google.com/store/books/details?id=IQkTDAQAQBAJ>
- Anderson, M. I., & Jeffery, K. J. (2003). Heterogeneous modulation of place cell firing by changes in context. *The Journal of Neuroscience: The Official Journal of the Society for Neuroscience*, 23(26), 8827–8835. <https://www.ncbi.nlm.nih.gov/pubmed/14523083>
- Andrès, M., Solignac, M., & Perret, M. (2003). Mating system in mouse lemurs: theories and facts, using analysis of paternity. *Folia Primatologica; International Journal of Primatology*, 74(5-6), 355–366. <https://doi.org/10.1159/000073319>
- Aronov, D., Nevers, R., & Tank, D. W. (2017). Mapping of a non-spatial dimension by the hippocampal-entorhinal circuit. *Nature*, 543(7647), 719–722. <https://doi.org/10.1038/nature21692>
- Atsalis, S. (2015). *A Natural History of the Brown Mouse Lemur*. Routledge. <https://play.google.com/store/books/details?id=Al6kCgAAQBAJ>
- Baraduc, P., Duhamel, J.-R., & Wirth, S. (2019). Schema cells in the macaque hippocampus. *Science*, 363(6427), 635–639. <https://doi.org/10.1126/science.aav5404>
- Barry, C., Hayman, R., Burgess, N., & Jeffery, K. J. (2007). Experience-dependent rescaling of entorhinal grids. *Nature Neuroscience*, 10(6), 682–684. <https://doi.org/10.1038/nn1905>
- Barry, C., Lever, C., Hayman, R., Hartley, T., Burton, S., O'Keefe, J., Jeffery, K., & Burgess, N. (2006). The boundary vector cell model of place cell firing and spatial memory. *Reviews in the Neurosciences*, 17(1-2), 71–97. <https://doi.org/10.1515/revneuro.2006.17.1-2.71>
- Battaglia, F. P., Sutherland, G. R., & McNaughton, B. L. (2004). Local sensory cues and place cell directionality: additional evidence of prospective coding in the hippocampus. *The Journal of Neuroscience: The Official Journal of the Society for Neuroscience*, 24(19), 4541–4550. <https://doi.org/10.1523/JNEUROSCI.4896-03.2004>
- Bellmund, J. L., Deuker, L., Navarro Schröder, T., & Doeller, C. F. (2016). Grid-cell representations in mental simulation. *eLife*, 5. <https://doi.org/10.7554/eLife.17089>
- Beltrami, G., Bertolucci, C., Parretta, A., Petrucci, F., & Foà, A. (2010). A sky polarization compass in lizards: the central role of the parietal eye. *The Journal of Experimental Biology*, 213(Pt 12), 2048–2054. <https://doi.org/10.1242/jeb.040246>
- Bercovitch, F. B., & Berard, J. D. (1993). Life history costs and consequences of rapid reproductive maturation in female rhesus macaques. *Behavioral Ecology and Sociobiology*, 32(2), 103–109. <https://doi.org/10.1007/BF00164042>
- Berg, R. W., Whitmer, D., & Kleinfeld, D. (2006). Exploratory whisking by rat is not phase locked to the hippocampal theta rhythm. *The Journal of Neuroscience: The Official Journal of the Society for Neuroscience*, 26(24), 6518–6522. <https://doi.org/10.1523/JNEUROSCI.0190-06.2006>
- Berry, S. D., & Thompson, R. F. (1978). Prediction of learning rate from the hippocampal electroencephalogram. *Science*, 200(4347), 1298–1300. <https://doi.org/10.1126/science.663612>
- Bieri, K. W., Bobbitt, K. N., & Colgin, L. L. (2014). Slow and fast  $\gamma$  rhythms coordinate different spatial coding modes in hippocampal place cells. *Neuron*, 82(3), 670–681. <https://doi.org/10.1016/j.neuron.2014.03.013>
- Bingman, V. P., Salas, C., & Rodriguez, F. (2009). Evolution of the Hippocampus. In M. D. Binder, N. Hirokawa, & U. Windhorst (Eds.), *Encyclopedia of Neuroscience* (pp. 1356–1360). Springer Berlin Heidelberg. [https://doi.org/10.1007/978-3-540-29678-2\\_3158](https://doi.org/10.1007/978-3-540-29678-2_3158)
- Bjerknes, T. L., Moser, E. I., & Moser, M.-B. (2014). Representation of geometric borders in the developing rat. *Neuron*, 82(1), 71–78. <https://doi.org/10.1016/j.neuron.2014.02.014>
- Blair, H. T., Welday, A. C., & Zhang, K. (2007). Scale-invariant memory representations emerge from moiré interference between grid fields that produce theta oscillations: a computational model. *The Journal of*

- Neuroscience: The Official Journal of the Society for Neuroscience*, 27(12), 3211–3229.  
<https://doi.org/10.1523/JNEUROSCI.4724-06.2007>
- Boettcher, M. L., Leonard, K. C., Dickinson, E., Aujard, F., Herrel, A., & Hartstone-Rose, A. (2020). The Forearm Musculature of the Gray Mouse Lemur (*Microcebus murinus*): An Ontogenetic Study. *Anatomical Record*, 303(5), 1354–1363. <https://doi.org/10.1002/ar.24258>
- Boles, L. C., & Lohmann, K. J. (2003). True navigation and magnetic maps in spiny lobsters. *Nature*, 421(6918), 60–63. <https://doi.org/10.1038/nature01226>
- Bons, N., Silhol, S., Barbié, V., Mestre-Francés, N., & Albe-Fessard, D. (1998). A stereotaxic atlas of the grey lesser mouse lemur brain (*Microcebus murinus*). *Brain Research Bulletin*, 46(1-2), 1–173.  
[https://doi.org/10.1016/s0361-9230\(97\)00458-9](https://doi.org/10.1016/s0361-9230(97)00458-9)
- Boulinguez-Ambroise, G., Herrel, A., & Pouydebat, E. (2020). Ontogeny of locomotion in mouse lemurs: Implications for primate evolution. *Journal of Human Evolution*, 142, 102732.  
<https://doi.org/10.1016/j.jhevol.2019.102732>
- Boulinguez-Ambroise, G., Zablocki-Thomas, P., Aujard, F., Herrel, A., & Pouydebat, E. (2019). Ontogeny of food grasping in mouse lemurs: behavior, morphology and performance. *Journal of Zoology*, 308(1), 1–8.  
<https://doi.org/10.1111/jzo.12652>
- Boyce, R., Glasgow, S. D., Williams, S., & Adamantidis, A. (2016). Causal evidence for the role of REM sleep theta rhythm in contextual memory consolidation. *Science*, 352(6287), 812–816.  
<https://doi.org/10.1126/science.aad5252>
- Bragin, A., Jandó, G., Nádasdy, Z., Hetke, J., Wise, K., & Buzsáki, G. (1995). Gamma (40–100 Hz) oscillation in the hippocampus of the behaving rat. *The Journal of Neuroscience: The Official Journal of the Society for Neuroscience*, 15(1 Pt 1), 47–60. <https://www.ncbi.nlm.nih.gov/pubmed/7823151>
- Brandon, M. P., Bogaard, A. R., Schulteis, N. W., & Hasselmo, M. E. (2013). Segregation of cortical head direction cell assemblies on alternating  $\theta$  cycles. *Nature Neuroscience*, 16(6), 739–748.  
<https://doi.org/10.1038/nn.3383>
- Brandon, M. P., Koenig, J., Leutgeb, J. K., & Leutgeb, S. (2014). New and distinct hippocampal place codes are generated in a new environment during septal inactivation. *Neuron*, 82(4), 789–796.  
<https://doi.org/10.1016/j.neuron.2014.04.013>
- Braune, P., Schmidt, S., & Zimmermann, E. (2005). Spacing and group coordination in a nocturnal primate, the golden brown mouse lemur (*Microcebus ravelobensis*): the role of olfactory and acoustic signals. *Behavioral Ecology and Sociobiology*, 58(6), 587–596. <https://doi.org/10.1007/s00265-005-0944-4>
- Brun, V. H., Solstad, T., Kjelstrup, K. B., Fyhn, M., Witter, M. P., Moser, E. I., & Moser, M.-B. (2008). Progressive increase in grid scale from dorsal to ventral medial entorhinal cortex. *Hippocampus*, 18(12), 1200–1212.  
<https://doi.org/10.1002/hipo.20504>
- Burgess, N., Barry, C., & O'Keefe, J. (2007). An oscillatory interference model of grid cell firing. *Hippocampus*, 17(9), 801–812. <https://doi.org/10.1002/hipo.20327>
- Burgess, N., & O'Keefe, J. (2011). Models of place and grid cell firing and theta rhythmicity. *Current Opinion in Neurobiology*, 21(5), 734–744. <https://doi.org/10.1016/j.conb.2011.07.002>
- Butler, W. N., Smith, K. S., van der Meer, M. A. A., & Taube, J. S. (2017). The Head-Direction Signal Plays a Functional Role as a Neural Compass during Navigation. *Current Biology: CB*, 27(9), 1259–1267.  
<https://doi.org/10.1016/j.cub.2017.03.033>
- Cahusac, P. M., Rolls, E. T., Miyashita, Y., & Niki, H. (1993). Modification of the responses of hippocampal neurons in the monkey during the learning of a conditional spatial response task. *Hippocampus*, 3(1), 29–42.  
<https://doi.org/10.1002/hipo.450030104>
- Cantero, J. L., Atienza, M., Stickgold, R., Kahana, M. J., Madsen, J. R., & Kocsis, B. (2003). Sleep-dependent theta oscillations in the human hippocampus and neocortex. *The Journal of Neuroscience: The Official Journal of the Society for Neuroscience*, 23(34), 10897–10903.  
<https://www.ncbi.nlm.nih.gov/pubmed/14645485>
- Cappaert, N. L. M., Van Strien, N. M., & Witter, M. P. (2015). Chapter 20 - Hippocampal Formation. In G. Paxinos (Ed.), *The Rat Nervous System (Fourth Edition)* (pp. 511–573). Academic Press.  
<https://doi.org/10.1016/B978-0-12-374245-2.00020-6>
- Cembrowski, M. S., Wang, L., Sugino, K., Shields, B. C., & Spruston, N. (2016). Hipposeq: a comprehensive RNA-seq database of gene expression in hippocampal principal neurons. *eLife*, 5, e14997.  
<https://doi.org/10.7554/eLife.14997>
- Cenquizca, L. A., & Swanson, L. W. (2007). Spatial organization of direct hippocampal field CA1 axonal projections to the rest of the cerebral cortex. *Brain Research Reviews*, 56(1), 1–26.  
<https://doi.org/10.1016/j.brainresrev.2007.05.002>
- Chazeau, C., Marchal, J., Hackert, R., Perret, M., & Herrel, A. (2013). Proximate determinants of bite force capacity in the mouse lemur: Bite force in mouse lemurs. *Journal of Zoology*, 290(1), 42–48.  
<https://doi.org/10.1111/jzo.12011>
- Chen, G., King, J. A., Burgess, N., & O'Keefe, J. (2013). How vision and movement combine in the hippocampal

- place code. *Proceedings of the National Academy of Sciences of the United States of America*, 110(1), 378–383. <https://doi.org/10.1073/pnas.1215834110>
- Chen, L. L., Lin, L.-H., Green, E. J., Barnes, C. A., & McNaughton, B. L. (1994). Head-direction cells in the rat posterior cortex. *Experimental Brain Research. Experimentelle Hirnforschung. Experimentation Cerebrale*, 101(1), 8–23. <https://doi.org/10.1007/BF00243212>
- Chestek, C. A., Gilja, V., Nuyujukian, P., Kier, R. J., Solzbacher, F., Ryu, S. I., Harrison, R. R., & Shenoy, K. V. (2009). HermesC: low-power wireless neural recording system for freely moving primates. *IEEE Transactions on Neural Systems and Rehabilitation Engineering: A Publication of the IEEE Engineering in Medicine and Biology Society*, 17(4), 330–338. <https://doi.org/10.1109/TNSRE.2009.2023293>
- Clark, W. E. L. G. (1931). The Brain of *Microcebus murinus*. *Proceedings of the Zoological Society of London*, 101(2), 463–486. <https://doi.org/10.1111/j.1096-3642.1931.tb01023.x>
- Clay, A. W., Bloomsmith, M. A., Marr, M. J., & Maple, T. L. (2009). Habituation and desensitization as methods for reducing fearful behavior in singly housed rhesus macaques. *American Journal of Primatology*, 71(1), 30–39. <https://doi.org/10.1002/ajp.20622>
- Colgin, L. L. (2016). Rhythms of the hippocampal network. *Nature Reviews. Neuroscience*, 17(4), 239–249. <https://doi.org/10.1038/nrn.2016.21>
- Combes, S. A., Rundle, D. E., Iwasaki, J. M., & Crall, J. D. (2012). Linking biomechanics and ecology through predator-prey interactions: flight performance of dragonflies and their prey. *The Journal of Experimental Biology*, 215(Pt 6), 903–913. <https://doi.org/10.1242/jeb.059394>
- Courellis, H. S., Nummela, S. U., Metke, M., Diehl, G. W., Bussell, R., Cauwenberghs, G., & Miller, C. T. (2019). Spatial encoding in primate hippocampus during free navigation. *PLoS Biology*, 17(12), e3000546. <https://doi.org/10.1371/journal.pbio.3000546>
- Crawford, J. D. (1984). Orientation in a vertical plane: The use of light cues by an orb-weaving spider, *Araneus diadematus* clerk. *Animal Behaviour*, 32(1), 162–171. [https://doi.org/10.1016/S0003-3472\(84\)80334-6](https://doi.org/10.1016/S0003-3472(84)80334-6)
- Dabaghian, Y., Mémoli, F., Frank, L., & Carlsson, G. (2012). A topological paradigm for hippocampal spatial map formation using persistent homology. *PLoS Computational Biology*, 8(8), e1002581. <https://doi.org/10.1371/journal.pcbi.1002581>
- Dacke, M., Baird, E., Byrne, M., Scholtz, C. H., & Warrant, E. J. (2013). Dung beetles use the Milky Way for orientation. *Current Biology: CB*, 23(4), 298–300. <https://doi.org/10.1016/j.cub.2012.12.034>
- Dacke, M., Nilsson, D.-E., Scholtz, C. H., Byrne, M., & Warrant, E. J. (2003). Animal behaviour: insect orientation to polarized moonlight. *Nature*, 424(6944), 33. <https://doi.org/10.1038/424033a>
- Darwin, C. (1873). Origin of Certain Instincts. *Nature*, 7(179), 417–418. <https://doi.org/10.1038/007417a0>
- Del Rio-Bermudez, C., Kim, J., Sokoloff, G., & Blumberg, M. S. (2017). Theta Oscillations during Active Sleep Synchronize the Developing Rubro-Hippocampal Sensorimotor Network. *Current Biology: CB*, 27(10), 1413–1424.e4. <https://doi.org/10.1016/j.cub.2017.03.077>
- Dickinson, J. A. (1994). Bees link local landmarks with celestial compass cues. *Die Naturwissenschaften*, 81(10), 465–467. <https://doi.org/10.1007/BF01136652>
- Dickson, C. T., Magistretti, J., Shalinsky, M. H., Fransén, E., Hasselmo, M. E., & Alonso, A. (2000). Properties and role of I(h) in the pacing of subthreshold oscillations in entorhinal cortex layer II neurons. *Journal of Neurophysiology*, 83(5), 2562–2579. <https://doi.org/10.1152/jn.2000.83.5.2562>
- Dingle, H. (1965). Turn alternation by bugs on causeways as a delayed compensatory response and the effects of varying visual inputs and length of straight path. *Animal Behaviour*, 13(1), 171–177. [https://doi.org/10.1016/0003-3472\(65\)90088-6](https://doi.org/10.1016/0003-3472(65)90088-6)
- Doeller, C. F., Barry, C., & Burgess, N. (2010). Evidence for grid cells in a human memory network. *Nature*, 463(7281), 657–661. <https://doi.org/10.1038/nature08704>
- Domnisoru, C., Kinkhabwala, A. A., & Tank, D. W. (2013). Membrane potential dynamics of grid cells. *Nature*, 495(7440), 199–204. <https://doi.org/10.1038/nature11973>
- Dong, H.-W., Swanson, L. W., Chen, L., Fanselow, M. S., Toga, A. W., & Jones, E. G. (2009). Genomic—Anatomic Evidence for Distinct Functional Domains in Hippocampal Field CA1. *Proceedings of the National Academy of Sciences of the United States of America*, 106(28), 11794–11799. <http://www.jstor.org/stable/40484030>
- Dougherty, K. A., Islam, T., & Johnston, D. (2012). Intrinsic excitability of CA1 pyramidal neurones from the rat dorsal and ventral hippocampus. *The Journal of Physiology*, 590(22), 5707–5722. <https://doi.org/10.1113/jphysiol.2012.242693>
- Dragoi, G., & Buzsáki, G. (2006). Temporal encoding of place sequences by hippocampal cell assemblies. *Neuron*, 50(1), 145–157. <https://doi.org/10.1016/j.neuron.2006.02.023>
- Dubovik, V., & Manahan-Vaughan, D. (2018). Less means more: The magnitude of synaptic plasticity along the hippocampal dorso-ventral axis is inversely related to the expression levels of plasticity-related neurotransmitter receptors. *Hippocampus*, 28(2), 136–150. <https://doi.org/10.1002/hipo.22816>
- Dupret, D., O'Neill, J., & Csicsvari, J. (2013). Dynamic reconfiguration of hippocampal interneuron circuits during spatial learning. *Neuron*, 78(1), 166–180. <https://doi.org/10.1016/j.neuron.2013.01.033>
- Ekstrom, A. D., Kahana, M. J., Caplan, J. B., Fields, T. A., Isham, E. A., Newman, E. L., & Fried, I. (2003). Cellular

- networks underlying human spatial navigation. *Nature*, 425(6954), 184–188.  
<https://doi.org/10.1038/nature01964>
- Eliav, T., Geva-Sagiv, M., Yartsev, M. M., Finkelstein, A., Rubin, A., Las, L., & Ulanovsky, N. (2018). Nonoscillatory Phase Coding and Synchronization in the Bat Hippocampal Formation. *Cell*, 175(4), 1119–1130.e15.  
<https://doi.org/10.1016/j.cell.2018.09.017>
- Elston, G. N., Benavides-Piccione, R., Elston, A., Zietsch, B., Defelipe, J., Manger, P., Casagrande, V., & Kaas, J. H. (2006). Specializations of the granular prefrontal cortex of primates: implications for cognitive processing. *The Anatomical Record. Part A, Discoveries in Molecular, Cellular, and Evolutionary Biology*, 288(1), 26–35.  
<https://doi.org/10.1002/ar.a.20278>
- Emlen, S. T. (1975). Migration: orientation and navigation. In *Avian biology* (pp. 129–219). Elsevier.
- Esch, H. E., & Burns, J. E. (1995). Honeybees use optic flow to measure the distance of a food source. *Die Naturwissenschaften*, 82(1), 38–40. <https://doi.org/10.1007/BF01167870>
- Etienne, A. S., Maurer, R., Saucy, F., & Teroni, E. (1986). Short-distance homing in the golden hamster after a passive outward journey. *Animal Behaviour*, 34(3), 696–715. [https://doi.org/10.1016/S0003-3472\(86\)80054-9](https://doi.org/10.1016/S0003-3472(86)80054-9)
- Ezran, C., Karanewsky, C. J., Pendleton, J. L., Sholtz, A., Krasnow, M. R., Willick, J., Razafindrakoto, A., Zohdy, S., Albertelli, M. A., & Krasnow, M. A. (2017). The Mouse Lemur, a Genetic Model Organism for Primate Biology, Behavior, and Health. *Genetics*, 206(2), 651–664. <https://doi.org/10.1534/genetics.116.199448>
- Fa, J. E. (1989). The genus *Macaca*: a review of taxonomy and evolution. *Mammal Review*, 19(2), 45–81.  
<https://doi.org/10.1111/j.1365-2907.1989.tb00401.x>
- Fanselow, M. S., & Dong, H.-W. (2010). Are the dorsal and ventral hippocampus functionally distinct structures? *Neuron*, 65(1), 7–19. <https://doi.org/10.1016/j.neuron.2009.11.031>
- Fedigan, L. (1991). Life span and reproduction in Japanese macaque females. *The Monkeys of Arashiyama: Thirty-Five Years of Research in Japan and the West*, 140–154.  
<https://books.google.com/books?hl=en&lr=&id=9zwroOXx4WoC&oi=fnd&pg=PA140&dq=macaque+life+span&ots=q2IPkrxd6&sig=5lq4dRnHKF8AxJDWkDx4m9sKAP0>
- Feng, T., Silva, D., & Foster, D. J. (2015). Dissociation between the experience-dependent development of hippocampal theta sequences and single-trial phase precession. *The Journal of Neuroscience: The Official Journal of the Society for Neuroscience*, 35(12), 4890–4902.  
<https://doi.org/10.1523/JNEUROSCI.2614-14.2015>
- Finkelstein, A., Derdikman, D., Rubin, A., Foerster, J. N., Las, L., & Ulanovsky, N. (2015). Three-dimensional head-direction coding in the bat brain. *Nature*, 517(7533), 159–164. <https://doi.org/10.1038/nature14031>
- Foster, D. J., & Wilson, M. A. (2007). Hippocampal theta sequences. *Hippocampus*, 17(11), 1093–1099.  
<https://doi.org/10.1002/hipo.20345>
- Foster, J. J., El Jundi, B., Smolka, J., Khaldy, L., Nilsson, D.-E., Byrne, M. J., & Dacke, M. (2017). Stellar performance: mechanisms underlying Milky Way orientation in dung beetles. *Philosophical Transactions of the Royal Society of London. Series B, Biological Sciences*, 372(1717).  
<https://doi.org/10.1098/rstb.2016.0079>
- Freund, T. F., & Antal, M. (1988). GABA-containing neurons in the septum control inhibitory interneurons in the hippocampus. *Nature*, 336(6195), 170–173. <https://doi.org/10.1038/336170a0>
- Fyhn, M., Hafting, T., Witter, M. P., Moser, E. I., & Moser, M.-B. (2008). Grid cells in mice. *Hippocampus*, 18(12), 1230–1238. <https://doi.org/10.1002/hipo.20472>
- Fyhn, M., Molden, S., Witter, M. P., Moser, E. I., & Moser, M.-B. (2004). Spatial representation in the entorhinal cortex. *Science*, 305(5688), 1258–1264. <https://doi.org/10.1126/science.1099901>
- Gagliardo, A. (2013). Forty years of olfactory navigation in birds. *The Journal of Experimental Biology*, 216(12), 2165–2171. <https://doi.org/10.1242/jeb.070250>
- Gagliardo, A., Odetti, F., Ioalè, P., Pecchia, T., & Vallortigara, G. (2005). Functional asymmetry of left and right avian piriform cortex in homing pigeons' navigation. *The European Journal of Neuroscience*, 22(1), 189–194.  
<https://doi.org/10.1111/j.1460-9568.2005.04204.x>
- Galiñanes, G. L., Bonardi, C., & Huber, D. (2018). Directional Reaching for Water as a Cortex-Dependent Behavioral Framework for Mice. *Cell Reports*, 22(10), 2767–2783.  
<https://doi.org/10.1016/j.celrep.2018.02.042>
- Garbutt, N. (1999). *Mammals of Madagascar*. Pica Press.  
[https://play.google.com/store/books/details?id=NMR\\_QgAACAAJ](https://play.google.com/store/books/details?id=NMR_QgAACAAJ)
- Georges-François, P., Rolls, E. T., & Robertson, R. G. (1999). Spatial view cells in the primate hippocampus: allocentric view not head direction or eye position or place. *Cerebral Cortex*, 9(3), 197–212.  
<https://doi.org/10.1093/cercor/9.3.197>
- Gerlei, K., Passlack, J., Hawes, I., Vandrey, B., Stevens, H., Papastathopoulos, I., & Nolan, M. F. (2020). Grid cells encode local head direction. In *bioRxiv* (p. 681312). <https://doi.org/10.1101/681312>
- Gloor, P. G. (1997). Canadian Medical Association. *CMAJ; Ottawa*, 157(11), 1597–1598.  
<https://search.proquest.com/openview/acb4a25792b686cdf8c62167681a57bb/1?pq-origsite=gscholar&cbl=41339>

- Gonzalez, C. E., Mak-McCully, R. A., Rosen, B. Q., Cash, S. S., Chauvel, P. Y., Bastuji, H., Rey, M., & Halgren, E. (2018). Theta Bursts Precede, and Spindles Follow, Cortical and Thalamic Downstates in Human NREM Sleep. *The Journal of Neuroscience: The Official Journal of the Society for Neuroscience*, 38(46), 9989–10001. <https://doi.org/10.1523/JNEUROSCI.0476-18.2018>
- Gothard, K. M., Skaggs, W. E., Moore, K. M., & McNaughton, B. L. (1996). Binding of hippocampal CA1 neural activity to multiple reference frames in a landmark-based navigation task. *The Journal of Neuroscience: The Official Journal of the Society for Neuroscience*, 16(2), 823–835. <https://www.ncbi.nlm.nih.gov/pubmed/8551362>
- Green, J. D., & Arduini, A. A. (1954). Hippocampal electrical activity in arousal. *Journal of Neurophysiology*, 17(6), 533–557. <https://doi.org/10.1152/jn.1954.17.6.533>
- Grieves, R. M., Jedidi-Ayoub, S., Mishchanchuk, K., Liu, A., Renaudineau, S., & Jeffery, K. J. (2020). The place-cell representation of volumetric space in rats. *Nature Communications*, 11(1), 789. <https://doi.org/10.1038/s41467-020-14611-7>
- Griffiths, V. A., Valera, A. M., Lau, J. Y., Roš, H., Younts, T. J., Marin, B., Baragli, C., Coyle, D., Evans, G. J., Konstantinou, G., Koimtzis, T., Nadella, K. M. N. S., Punde, S. A., Kirkby, P. A., Bianco, I. H., & Silver, R. A. (2020). Real-time 3D movement correction for two-photon imaging in behaving animals. *Nature Methods*, 17(7), 741–748. <https://doi.org/10.1038/s41592-020-0851-7>
- Grobéty, M.-C., & Schenk, F. (1992). Spatial learning in a three-dimensional maze. *Animal Behaviour*, 43(6), 1011–1020. [https://doi.org/10.1016/S0003-3472\(06\)80014-X](https://doi.org/10.1016/S0003-3472(06)80014-X)
- Grünbaum, D., & Willis, M. A. (2015). Spatial memory-based behaviors for locating sources of odor plumes. *Movement Ecology*, 3(1), 11. <https://doi.org/10.1186/s40462-015-0037-6>
- Gupta, A. S., van der Meer, M. A. A., Touretzky, D. S., & Redish, A. D. (2012). Segmentation of spatial experience by hippocampal  $\theta$  sequences. *Nature Neuroscience*, 15(7), 1032–1039. <https://doi.org/10.1038/nn.3138>
- Hafting, T., Fyhn, M., Molden, S., Moser, M.-B., & Moser, E. I. (2005). Microstructure of a spatial map in the entorhinal cortex. *Nature*, 436(7052), 801–806. <https://doi.org/10.1038/nature03721>
- Hangya, B., Borhegyi, Z., Szilágyi, N., Freund, T. F., & Varga, V. (2009). GABAergic neurons of the medial septum lead the hippocampal network during theta activity. *The Journal of Neuroscience: The Official Journal of the Society for Neuroscience*, 29(25), 8094–8102. <https://doi.org/10.1523/JNEUROSCI.5665-08.2009>
- Hardcastle, K., Maheswaranathan, N., Ganguli, S., & Giocomo, L. M. (2017). A Multiplexed, Heterogeneous, and Adaptive Code for Navigation in Medial Entorhinal Cortex. *Neuron*, 94(2), 375–387.e7. <https://doi.org/10.1016/j.neuron.2017.03.025>
- Harten, L., Katz, A., Goldshtein, A., Handel, M., & Yovel, Y. (2020). The ontogeny of a mammalian cognitive map in the real world. *Science*, 369(6500), 194–197. <https://doi.org/10.1126/science.aay3354>
- Hasselmo, M. E., Giocomo, L. M., & Zilli, E. A. (2007). Grid cell firing may arise from interference of theta frequency membrane potential oscillations in single neurons. *Hippocampus*, 17(12), 1252–1271. <https://doi.org/10.1002/hipo.20374>
- Hayman, R., Verriotes, M. A., Jovalekic, A., Fenton, A. A., & Jeffery, K. J. (2011). Anisotropic encoding of three-dimensional space by place cells and grid cells. *Nature Neuroscience*, 14(9), 1182–1188. <https://doi.org/10.1038/nn.2892>
- Headley, D. B., & Paré, D. (2017). Common oscillatory mechanisms across multiple memory systems. *NPJ Science of Learning*, 2. <https://doi.org/10.1038/s41539-016-0001-2>
- Hebb, D. O. (1949). *The organization of behavior; a neuropsychological theory*. 335. <https://psycnet.apa.org/fulltext/1950-02200-000.pdf>
- Heinze, S. (2017). Unraveling the neural basis of insect navigation. *Current Opinion in Insect Science*, 24, 58–67. <https://doi.org/10.1016/j.cois.2017.09.001>
- Hill, D. E. (1979). Orientation by jumping spiders of the genus *Phidippus* (Araneae: Salticidae) during the pursuit of prey. *Behavioral Ecology and Sociobiology*, 5(3), 301–322. <https://doi.org/10.1007/BF00293678>
- Ho, C. L. A., Zimmermann, R., Flórez Weidinger, J. D., Prsa, M., Schottdorf, M., Merlin, S., Okamoto, T., Ikezoe, K., Pifferi, F., Aujard, F., Angelucci, A., Wolf, F., & Huber, D. (2020). Orientation Preference Maps in *Microcebus murinus* Reveal Size-Invariant Design Principles in Primate Visual Cortex. *Current Biology: CB*. <https://doi.org/10.1016/j.cub.2020.11.027>
- Hori, E., Nishio, Y., Kazui, K., Umeno, K., Tabuchi, E., Sasaki, K., Endo, S., Ono, T., & Nishijo, H. (2005). Place-related neural responses in the monkey hippocampal formation in a virtual space. *Hippocampus*, 15(8), 991–996. <https://doi.org/10.1002/hipo.20108>
- Hori, E., Tabuchi, E., Matsumura, N., Tamura, R., Eifuku, S., Endo, S., Nishijo, H., & Ono, T. (2003). Representation of place by monkey hippocampal neurons in real and virtual translocation. *Hippocampus*, 13(2), 190–196. <https://doi.org/10.1002/hipo.10062>
- Hozer, C., Pifferi, F., Aujard, F., & Perret, M. (2019). The biological clock in gray mouse lemur: Adaptive, evolutionary and aging considerations in an emerging non-human primate model. *Frontiers in Physiology*, 10, 1033. <https://doi.org/10.3389/fphys.2019.01033>
- Hughes, G. M. (1957). The Co-Ordination of Insect Movements. *The Journal of Experimental Biology*, 34(3),

- 306–333. <https://jeb.biologists.org/content/34/3/306>
- Hunsaker, M. R., Fieldsted, P. M., Rosenberg, J. S., & Kesner, R. P. (2008). Dissociating the roles of dorsal and ventral CA1 for the temporal processing of spatial locations, visual objects, and odors. *Behavioral Neuroscience*, *122*(3), 643–650. <https://doi.org/10.1037/0735-7044.122.3.643>
- Hurst, J. L., & West, R. S. (2010). Taming anxiety in laboratory mice. *Nature Methods*, *7*(10), 825–826. <https://doi.org/10.1038/nmeth.1500>
- Jacobs, J., Weidemann, C. T., Miller, J. F., Solway, A., Burke, J. F., Wei, X.-X., Suthana, N., Sperling, M. R., Sharan, A. D., Fried, I., & Kahana, M. J. (2013). Direct recordings of grid-like neuronal activity in human spatial navigation. *Nature Neuroscience*, *16*(9), 1188–1190. <https://doi.org/10.1038/nn.3466>
- Jezek, K., Henriksen, E. J., Treves, A., Moser, E. I., & Moser, M.-B. (2011). Theta-paced flickering between place-cell maps in the hippocampus. *Nature*, *478*(7368), 246–249. <https://doi.org/10.1038/nature10439>
- Julian, J. B., Keinath, A. T., Frazzetta, G., & Epstein, R. A. (2018). Human entorhinal cortex represents visual space using a boundary-anchored grid. *Nature Neuroscience*, *21*(2), 191–194. <https://doi.org/10.1038/s41593-017-0049-1>
- Jung, M. W., Wiener, S. I., & McNaughton, B. L. (1994). Comparison of spatial firing characteristics of units in dorsal and ventral hippocampus of the rat. *The Journal of Neuroscience: The Official Journal of the Society for Neuroscience*, *14*(12), 7347–7356. <https://www.ncbi.nlm.nih.gov/pubmed/7996180>
- Jutras, M. J., Fries, P., & Buffalo, E. A. (2013). Oscillatory activity in the monkey hippocampus during visual exploration and memory formation. *Proceedings of the National Academy of Sciences of the United States of America*, *110*(32), 13144–13149. <https://doi.org/10.1073/pnas.1302351110>
- Kahana, M. J., Seelig, D., & Madsen, J. R. (2001). Theta returns. *Current Opinion in Neurobiology*, *11*(6), 739–744. [https://doi.org/10.1016/S0959-4388\(01\)00278-1](https://doi.org/10.1016/S0959-4388(01)00278-1)
- Kane, S. A., Fulton, A. H., & Rosenthal, L. J. (2015). When hawks attack: animal-borne video studies of goshawk pursuit and prey-evasion strategies. *The Journal of Experimental Biology*, *218*(Pt 2), 212–222. <https://doi.org/10.1242/jeb.108597>
- Kane, S. A., & Zamani, M. (2014). Falcons pursue prey using visual motion cues: new perspectives from animal-borne cameras. *The Journal of Experimental Biology*, *217*(Pt 2), 225–234. <https://doi.org/10.1242/jeb.092403>
- Kappel, P., Hohenbrink, S., & Radespiel, U. (2011). Experimental evidence for olfactory predator recognition in wild mouse lemurs. *American Journal of Primatology*, *73*(9), 928–938. <https://doi.org/10.1002/ajp.20963>
- Keeton, W. T. (1974). The Orientational and Navigational Basis of Homing in Birds. In D. S. Lehrman, J. S. Rosenblatt, R. A. Hinde, & E. Shaw (Eds.), *Advances in the Study of Behavior* (Vol. 5, pp. 47–132). Academic Press. [https://doi.org/10.1016/S0065-3454\(08\)60020-0](https://doi.org/10.1016/S0065-3454(08)60020-0)
- Kepecs, A., Uchida, N., & Mainen, Z. F. (2007). Rapid and precise control of sniffing during olfactory discrimination in rats. *Journal of Neurophysiology*, *98*(1), 205–213. <https://doi.org/10.1152/jn.00071.2007>
- Killian, N. J., Jutras, M. J., & Buffalo, E. A. (2012). A map of visual space in the primate entorhinal cortex. *Nature*, *491*(7426), 761–764. <https://doi.org/10.1038/nature11587>
- Kim, B., Kocsis, B., Hwang, E., Kim, Y., Strecker, R. E., McCarley, R. W., & Choi, J. H. (2017). Differential modulation of global and local neural oscillations in REM sleep by homeostatic sleep regulation. *Proceedings of the National Academy of Sciences of the United States of America*, *114*(9), E1727–E1736. <https://doi.org/10.1073/pnas.1615230114>
- Kim, M., & Maguire, E. A. (2018). 3D grid cells in human entorhinal cortex: Theoretical and methodological considerations and fMRI findings. In *Cold Spring Harbor Laboratory* (p. 282327). <https://doi.org/10.1101/282327>
- Kim, S. S., Rouault, H., Druckmann, S., & Jayaraman, V. (2017). Ring attractor dynamics in the Drosophila central brain. *Science*, *356*(6340), 849–853. <https://doi.org/10.1126/science.aal4835>
- Kjelstrup, K. B., Solstad, T., Brun, V. H., Hafting, T., Leutgeb, S., Witter, M. P., Moser, E. I., & Moser, M.-B. (2008). Finite scale of spatial representation in the hippocampus. *Science*, *321*(5885), 140–143. <https://doi.org/10.1126/science.1157086>
- Kleinfeld, D., Deschênes, M., & Ulanovsky, N. (2016). Whisking, Sniffing, and the Hippocampal  $\theta$ -Rhythm: A Tale of Two Oscillators. *PLoS Biology*, *14*(2), e1002385. <https://doi.org/10.1371/journal.pbio.1002385>
- Klimesch, W. (2003). EEG Theta, Memory, and Sleep. In J. Polich (Ed.), *Detection of Change: Event-Related Potential and fMRI Findings* (pp. 149–165). Springer US. [https://doi.org/10.1007/978-1-4615-0294-4\\_9](https://doi.org/10.1007/978-1-4615-0294-4_9)
- Kohler, M., & Wehner, R. (2005). Idiosyncratic route-based memories in desert ants, *Melophorus bagoti*: how do they interact with path-integration vectors? *Neurobiology of Learning and Memory*, *83*(1), 1–12. <https://doi.org/10.1016/j.nlm.2004.05.011>
- Komisaruk, B. R. (1970). Synchrony between limbic system theta activity and rhythmical behavior in rats. *Journal of Comparative and Physiological Psychology*, *70*(3), 482–492. <https://doi.org/10.1037/h0028709>
- Koutsoumpa, A., & Papatheodoropoulos, C. (2019). Short-term dynamics of input and output of CA1 network greatly differ between the dorsal and ventral rat hippocampus. *BMC Neuroscience*, *20*(1), 35. <https://doi.org/10.1186/s12868-019-0517-5>

- Kouvaros, S., & Papatheodoropoulos, C. (2016). Theta burst stimulation-induced LTP: Differences and similarities between the dorsal and ventral CA1 hippocampal synapses. *Hippocampus*, *26*(12), 1542–1559. <https://doi.org/10.1002/hipo.22655>
- Kraft, P., Evangelista, C., Dacke, M., Labhart, T., & Srinivasan, M. V. (2011). Honeybee navigation: following routes using polarized-light cues. *Philosophical Transactions of the Royal Society of London. Series B, Biological Sciences*, *366*(1565), 703–708. <https://doi.org/10.1098/rstb.2010.0203>
- Kramer, G. (2008). Experiments on bird orientation. *The Ibis*, *94*(2), 265–285. <https://doi.org/10.1111/j.1474-919x.1952.tb01817.x>
- Kropff, E., Carmichael, J. E., Moser, M.-B., & Moser, E. I. (2015). Speed cells in the medial entorhinal cortex. *Nature*, *523*(7561), 419–424. <https://doi.org/10.1038/nature14622>
- Kubie, J. L., & Muller, R. U. (1991). Multiple representations in the hippocampus. *Hippocampus*, *1*(3), 240–242. <https://doi.org/10.1002/hipo.450010305>
- Landfield, P. W., McGaugh, J. L., & Tusa, R. J. (1972). Theta rhythm: a temporal correlate of memory storage processes in the rat. *Science*, *175*(4017), 87–89. <https://doi.org/10.1126/science.175.4017.87>
- Langille, J. J. (2019). Remembering to Forget: A Dual Role for Sleep Oscillations in Memory Consolidation and Forgetting. *Frontiers in Cellular Neuroscience*, *13*, 71. <https://doi.org/10.3389/fncel.2019.00071>
- Languille, S., Blanc, S., Blin, O., Canale, C. I., Dal-Pan, A., Devau, G., Dhenain, M., Dorieux, O., Epelbaum, J., Gomez, D., Hardy, I., Henry, P.-Y., Irving, E. A., Marchal, J., Mestre-Francés, N., Perret, M., Picq, J.-L., Pifferi, F., Rahman, A., ... Aujard, F. (2012). The grey mouse lemur: a non-human primate model for ageing studies. *Ageing Research Reviews*, *11*(1), 150–162. <https://doi.org/10.1016/j.arr.2011.07.001>
- Latuske, P., Kornienko, O., Kohler, L., & Allen, K. (2017). Hippocampal Remapping and Its Entorhinal Origin. *Frontiers in Behavioral Neuroscience*, *11*, 253. <https://doi.org/10.3389/fnbeh.2017.00253>
- Lebhardt, F., Koch, J., & Ronacher, B. (2012). The polarization compass dominates over idiothetic cues in path integration of desert ants. *The Journal of Experimental Biology*, *215*(Pt 3), 526–535. <https://doi.org/10.1242/jeb.060475>
- Lein, E. S., Hawrylycz, M. J., Ao, N., Ayres, M., Bensinger, A., Bernard, A., Boe, A. F., Boguski, M. S., Brockway, K. S., Byrnes, E. J., Chen, L., Chen, L., Chen, T.-M., Chin, M. C., Chong, J., Crook, B. E., Czaplinska, A., Dang, C. N., Datta, S., ... Jones, A. R. (2007). Genome-wide atlas of gene expression in the adult mouse brain. *Nature*, *445*(7124), 168–176. <https://doi.org/10.1038/nature05453>
- Leonardo, E. D., Richardson-Jones, J. W., Sibille, E., Kottman, A., & Hen, R. (2006). Molecular heterogeneity along the dorsal-ventral axis of the murine hippocampal CA1 field: a microarray analysis of gene expression. *Neuroscience*, *137*(1), 177–186. <https://doi.org/10.1016/j.neuroscience.2005.08.082>
- Leonhard, C. L., Stackman, R. W., & Taube, J. S. (1996). Head direction cells recorded from the lateral mammillary nuclei in rats. *Soc Neurosci Abstr*, *22*, 1873.
- Leutgeb, S., Leutgeb, J. K., Barnes, C. A., Moser, E. I., McNaughton, B. L., & Moser, M.-B. (2005). Independent codes for spatial and episodic memory in hippocampal neuronal ensembles. *Science*, *309*(5734), 619–623. <https://doi.org/10.1126/science.1114037>
- Lever, C., Burton, S., Jeewajee, A., O'Keefe, J., & Burgess, N. (2009). Boundary vector cells in the subiculum of the hippocampal formation. *The Journal of Neuroscience: The Official Journal of the Society for Neuroscience*, *29*(31), 9771–9777. <https://doi.org/10.1523/JNEUROSCI.1319-09.2009>
- Li, M., Liu, F., Jiang, H., Lee, T. S., & Tang, S. (2017). Long-Term Two-Photon Imaging in Awake Macaque Monkey. *Neuron*, *93*(5), 1049–1057.e3. <https://doi.org/10.1016/j.neuron.2017.01.027>
- Ludvig, N., Tang, H. M., Gohil, B. C., & Botero, J. M. (2004). Detecting location-specific neuronal firing rate increases in the hippocampus of freely-moving monkeys. *Brain Research*, *1014*(1-2), 97–109. <https://doi.org/10.1016/j.brainres.2004.03.071>
- Macrides, F., Eichenbaum, H. B., & Forbes, W. B. (1982). Temporal relationship between sniffing and the limbic theta rhythm during odor discrimination reversal learning. *The Journal of Neuroscience: The Official Journal of the Society for Neuroscience*, *2*(12), 1705–1717. <https://www.ncbi.nlm.nih.gov/pubmed/7143047>
- Madan, C. R. (2015). Creating 3D visualizations of MRI data: A brief guide. *F1000Research*, *4*, 466. <https://doi.org/10.12688/f1000research.6838.1>
- Maggio, N., & Segal, M. (2007). Striking variations in corticosteroid modulation of long-term potentiation along the septotemporal axis of the hippocampus. *The Journal of Neuroscience: The Official Journal of the Society for Neuroscience*, *27*(21), 5757–5765. <https://doi.org/10.1523/JNEUROSCI.0155-07.2007>
- Malik, R., Dougherty, K. A., Parikh, K., Byrne, C., & Johnston, D. (2016). Mapping the electrophysiological and morphological properties of CA1 pyramidal neurons along the longitudinal hippocampal axis. *Hippocampus*, *26*(3), 341–361. <https://doi.org/10.1002/hipo.22526>
- Maruki, K., Izaki, Y., Nomura, M., & Yamauchi, T. (2001). Differences in paired-pulse facilitation and long-term potentiation between dorsal and ventral CA1 regions in anesthetized rats. *Hippocampus*, *11*(6), 655–661. <https://doi.org/10.1002/hipo.1080>
- Matsumura, N., Nishijo, H., Tamura, R., Eifuku, S., Endo, S., & Ono, T. (1999). Spatial- and task-dependent neuronal responses during real and virtual translocation in the monkey hippocampal formation. *The Journal*

- of *Neuroscience: The Official Journal of the Society for Neuroscience*, 19(6), 2381–2393.  
<https://doi.org/10.1523/JNEUROSCI.19-06-02381.1999>
- Mau, W., Sullivan, D. W., Kinsky, N. R., Hasselmo, M. E., Howard, M. W., & Eichenbaum, H. (2018). The Same Hippocampal CA1 Population Simultaneously Codes Temporal Information over Multiple Timescales. *Current Biology: CB*, 28(10), 1499–1508.e4. <https://doi.org/10.1016/j.cub.2018.03.051>
- Ma, Y.-Y., Ryou, J.-W., Kim, B.-H., & Wilson, F. A. (2004). Spatially directed movement and neuronal activity in freely moving monkey. *Progress in Brain Research*, 143, 513–520.  
[https://doi.org/10.1016/S0079-6123\(03\)43048-3](https://doi.org/10.1016/S0079-6123(03)43048-3)
- McNaughton, B. L., Barnes, C. A., & O’Keefe, J. (1983). The contributions of position, direction, and velocity to single unit activity in the hippocampus of freely-moving rats. *Experimental Brain Research. Experimentelle Hirnforschung. Experimentation Cerebrale*, 52(1), 41–49. <https://doi.org/10.1007/BF00237147>
- Merigan, W. H. (1989). Chromatic and achromatic vision of macaques: role of the P pathway. *The Journal of Neuroscience: The Official Journal of the Society for Neuroscience*, 9(3), 776–783.  
<https://doi.org/10.1523/JNEUROSCI.09-03-00776.1989>
- Milior, G., Di Castro, M. A., Sciarria, L. P., Garofalo, S., Branchi, I., Ragozzino, D., Limatola, C., & Maggi, L. (2016). Electrophysiological Properties of CA1 Pyramidal Neurons along the Longitudinal Axis of the Mouse Hippocampus. *Scientific Reports*, 6, 38242. <https://doi.org/10.1038/srep38242>
- Miller, J. F., Neufang, M., Solway, A., Brandt, A., Trippel, M., Mader, I., Hefft, S., Merkow, M., Polyn, S. M., Jacobs, J., Kahana, M. J., & Schulze-Bonhage, A. (2013). Neural activity in human hippocampal formation reveals the spatial context of retrieved memories. *Science*, 342(6162), 1111–1114.  
<https://doi.org/10.1126/science.1244056>
- Mitchell, S. J., Rawlins, J. N., Steward, O., & Olton, D. S. (1982). Medial septal area lesions disrupt theta rhythm and cholinergic staining in medial entorhinal cortex and produce impaired radial arm maze behavior in rats. *The Journal of Neuroscience: The Official Journal of the Society for Neuroscience*, 2(3), 292–302.  
<https://www.ncbi.nlm.nih.gov/pubmed/7062110>
- Miyashita, Y., Rolls, E. T., Cahusac, P. M., Niki, H., & Feigenbaum, J. D. (1989). Activity of hippocampal formation neurons in the monkey related to a conditional spatial response task. *Journal of Neurophysiology*, 61(3), 669–678. <https://doi.org/10.1152/jn.1989.61.3.669>
- Mizumori, S. J., & Williams, J. D. (1993). Directionally selective mnemonic properties of neurons in the lateral dorsal nucleus of the thalamus of rats. *The Journal of Neuroscience: The Official Journal of the Society for Neuroscience*, 13(9), 4015–4028. <https://www.ncbi.nlm.nih.gov/pubmed/8366357>
- Moser, E. I., Roudi, Y., Witter, M. P., Kentros, C., Bonhoeffer, T., & Moser, M.-B. (2014). Grid cells and cortical representation. *Nature Reviews. Neuroscience*, 15(7), 466–481. <https://doi.org/10.1038/nrn3766>
- Moser, M. B., & Moser, E. I. (1998). Functional differentiation in the hippocampus. *Hippocampus*, 8(6), 608–619.  
[https://doi.org/10.1002/\(SICI\)1098-1063\(1998\)8:6<608::AID-HIPO3>3.0.CO;2-7](https://doi.org/10.1002/(SICI)1098-1063(1998)8:6<608::AID-HIPO3>3.0.CO;2-7)
- Moser, M.-B., Rowland, D. C., & Moser, E. I. (2015). Place cells, grid cells, and memory. *Cold Spring Harbor Perspectives in Biology*, 7(2), a021808. <https://doi.org/10.1101/cshperspect.a021808>
- Müller, M., & Wehner, R. (1988). Path integration in desert ants, *Cataglyphis fortis*. *Proceedings of the National Academy of Sciences of the United States of America*, 85(14), 5287–5290.  
<https://doi.org/10.1073/pnas.85.14.5287>
- Muller, R. U., Bostock, E., Taube, J. S., & Kubie, J. L. (1994). On the directional firing properties of hippocampal place cells. *The Journal of Neuroscience: The Official Journal of the Society for Neuroscience*, 14(12), 7235–7251. <https://www.ncbi.nlm.nih.gov/pubmed/7996172>
- Muller, R. U., & Kubie, J. L. (1987). The effects of changes in the environment on the spatial firing of hippocampal complex-spike cells. *The Journal of Neuroscience: The Official Journal of the Society for Neuroscience*, 7(7), 1951–1968. <https://www.ncbi.nlm.nih.gov/pubmed/3612226>
- Nadkarni, N. A., Bougacha, S., Garin, C., Dhenain, M., & Picq, J.-L. (2019). A 3D population-based brain atlas of the mouse lemur primate with examples of applications in aging studies and comparative anatomy. *NeuroImage*, 185, 85–95. <https://doi.org/10.1016/j.neuroimage.2018.10.010>
- Naudé, J., Didiéne, S., Takillah, S., Prévost-Solié, C., Maskos, U., & Faurej, P. (2018). Acetylcholine-dependent phasic dopamine activity signals exploratory locomotion and choices. In *bioRxiv* (p. 242438).  
<https://doi.org/10.1101/242438>
- Nei, M., Xu, P., & Glazko, G. (2001). Estimation of divergence times from multiprotein sequences for a few mammalian species and several distantly related organisms. *Proceedings of the National Academy of Sciences of the United States of America*, 98(5), 2497–2502. <https://doi.org/10.1073/pnas.051611498>
- Nishijo, H., Ono, T., Eifuku, S., & Tamura, R. (1997). The relationship between monkey hippocampus place-related neural activity and action in space. *Neuroscience Letters*, 226(1), 57–60.  
[https://doi.org/10.1016/s0304-3940\(97\)00255-3](https://doi.org/10.1016/s0304-3940(97)00255-3)
- NITRC. (n.d.). *NITRC*. Retrieved October 3, 2020, from <https://www.nitrc.org/projects/mouselemuratlas>
- Nourizonoz, A., Zimmermann, R., Ho, C. L. A., Pellat, S., Ormen, Y., Prévost-Solié, C., Reymond, G., Pifferi, F., Aujard, F., Herrel, A., & Huber, D. (2020). EthoLoop: automated closed-loop neuroethology in naturalistic

- environments. *Nature Methods*, 17(10), 1052–1059. <https://doi.org/10.1038/s41592-020-0961-2>
- Ognjanovski, N., Broussard, C., Zochowski, M., & Aton, S. J. (2018). Hippocampal Network Oscillations Rescue Memory Consolidation Deficits Caused by Sleep Loss. *Cerebral Cortex*, 28(10), 3711–3723. <https://doi.org/10.1093/cercor/bhy174>
- O'Keefe, J. (1976). Place units in the hippocampus of the freely moving rat. *Experimental Neurology*, 51(1), 78–109. [https://doi.org/10.1016/0014-4886\(76\)90055-8](https://doi.org/10.1016/0014-4886(76)90055-8)
- O'Keefe, J., & Burgess, N. (1996). Geometric determinants of the place fields of hippocampal neurons. *Nature*, 381(6581), 425–428. <https://doi.org/10.1038/381425a0>
- O'Keefe, J., & Conway, D. H. (1978). Hippocampal place units in the freely moving rat: why they fire where they fire. *Experimental Brain Research. Experimentelle Hirnforschung. Experimentation Cerebrale*, 31(4), 573–590. <https://doi.org/10.1007/bf00239813>
- O'Keefe, J., & Dostrovsky, J. (1971). The hippocampus as a spatial map. Preliminary evidence from unit activity in the freely-moving rat. *Brain Research*, 34(1), 171–175. [https://doi.org/10.1016/0006-8993\(71\)90358-1](https://doi.org/10.1016/0006-8993(71)90358-1)
- O'Keefe, J., & Recce, M. L. (1993). Phase relationship between hippocampal place units and the EEG theta rhythm. *Hippocampus*, 3(3), 317–330. <https://doi.org/10.1002/hipo.450030307>
- O'Keefe, J., & Speakman, A. (1987). Single unit activity in the rat hippocampus during a spatial memory task. *Experimental Brain Research. Experimentelle Hirnforschung. Experimentation Cerebrale*, 68(1), 1–27. <https://doi.org/10.1007/bf00255230>
- O'Mara, S. M., Rolls, E. T., Berthoz, A., & Kesner, R. P. (1994). Neurons responding to whole-body motion in the primate hippocampus. *The Journal of Neuroscience: The Official Journal of the Society for Neuroscience*, 14(11 Pt 1), 6511–6523. <https://www.ncbi.nlm.nih.gov/pubmed/7965055>
- Omer, D. B., Maimon, S. R., Las, L., & Ulanovsky, N. (2018). Social place-cells in the bat hippocampus. *Science*, 359(6372), 218–224. <https://doi.org/10.1126/science.aao3474>
- Ono, T., Nakamura, K., Fukuda, M., & Tamura, R. (1991). Place recognition responses of neurons in monkey hippocampus. *Neuroscience Letters*, 121(1-2), 194–198. [https://doi.org/10.1016/0304-3940\(91\)90683-k](https://doi.org/10.1016/0304-3940(91)90683-k)
- Ono, T., Nakamura, K., Nishijo, H., & Eifuku, S. (1993). Monkey hippocampal neurons related to spatial and nonspatial functions. *Journal of Neurophysiology*, 70(4), 1516–1529. <https://doi.org/10.1152/jn.1993.70.4.1516>
- Page, H. J. I., Wilson, J. J., & Jeffery, K. J. (2018). A dual-axis rotation rule for updating the head direction cell reference frame during movement in three dimensions. *Journal of Neurophysiology*, 119(1), 192–208. <https://doi.org/10.1152/jn.00501.2017>
- Papatheodoropoulos, C. (2015). Higher intrinsic network excitability in ventral compared with the dorsal hippocampus is controlled less effectively by GABAB receptors. *BMC Neuroscience*, 16, 75. <https://doi.org/10.1186/s12868-015-0213-z>
- Papatheodoropoulos, C., & Kostopoulos, G. (2000). Decreased ability of rat temporal hippocampal CA1 region to produce long-term potentiation. *Neuroscience Letters*, 279(3), 177–180. [https://doi.org/10.1016/s0304-3940\(99\)01002-2](https://doi.org/10.1016/s0304-3940(99)01002-2)
- Pastalkova, E., Itskov, V., Amarasingham, A., & Buzsáki, G. (2008). Internally generated cell assembly sequences in the rat hippocampus. *Science*, 321(5894), 1322–1327. <https://doi.org/10.1126/science.1159775>
- Patel, J., Fujisawa, S., Berényi, A., Royer, S., & Buzsáki, G. (2012). Traveling theta waves along the entire septotemporal axis of the hippocampus. *Neuron*, 75(3), 410–417. <https://doi.org/10.1016/j.neuron.2012.07.015>
- Pernía-Andrade, A. J., & Jonas, P. (2014). Theta-gamma-modulated synaptic currents in hippocampal granule cells in vivo define a mechanism for network oscillations. *Neuron*, 81(1), 140–152. <https://doi.org/10.1016/j.neuron.2013.09.046>
- Perret, M. (1997). Change in photoperiodic cycle affects life span in a prosimian primate (*Microcebus murinus*). *Journal of Biological Rhythms*, 12(2), 136–145. <https://doi.org/10.1177/074873049701200205>
- Perret, M., & Schilling, A. (1993). Response to short photoperiod and spontaneous sexual recrudescence in the lesser mouse lemur: role of olfactory bulb removal. *The Journal of Endocrinology*, 137(3), 511–518. <https://doi.org/10.1677/joe.0.1370511>
- Petrovich, G. D., Canteras, N. S., & Swanson, L. W. (2001). Combinatorial amygdalar inputs to hippocampal domains and hypothalamic behavior systems. *Brain Research. Brain Research Reviews*, 38(1-2), 247–289. [https://doi.org/10.1016/s0165-0173\(01\)00080-7](https://doi.org/10.1016/s0165-0173(01)00080-7)
- Phillips, J. B. (1996). Magnetic Navigation. *Journal of Theoretical Biology*, 180(4), 309–319. <https://doi.org/10.1006/jtbi.1996.0105>
- Pifferi, F., Epelbaum, J., & Aujard, F. (2019). Strengths and weaknesses of grey mouse lemur (*Microcebus murinus*) to model Alzheimer's disease and neuropsychiatric conditions. *Frontiers in Pharmacology*. <https://www.frontiersin.org/articles/10.3389/fphar.2019.01291/abstract>
- Pifferi, F., Epelbaum, J., & Aujard, F. (2019). Strengths and Weaknesses of the Gray Mouse Lemur (*Microcebus murinus*) as a Model for the Behavioral and Psychological Symptoms and Neuropsychiatric Symptoms of Dementia. *Frontiers in Pharmacology*, 10, 1291. <https://doi.org/10.3389/fphar.2019.01291>

- Quirk, G. J., Muller, R. U., & Kubie, J. L. (1990). The firing of hippocampal place cells in the dark depends on the rat's recent experience. *The Journal of Neuroscience: The Official Journal of the Society for Neuroscience*, 10(6), 2008–2017. <https://www.ncbi.nlm.nih.gov/pubmed/2355262>
- Radespiel, U. (2000). Sociality in the gray mouse lemur (*Microcebus murinus*) in northwestern Madagascar. *American Journal of Primatology*, 51(1), 21–40. [https://doi.org/10.1002/\(SICI\)1098-2345\(200005\)51:1<21::AID-AJP3>3.0.CO;2-C](https://doi.org/10.1002/(SICI)1098-2345(200005)51:1<21::AID-AJP3>3.0.CO;2-C)
- Ravassard, P., Kees, A., Willers, B., Ho, D., Aharoni, D. A., Cushman, J., Aghajan, Z. M., & Mehta, M. R. (2013). Multisensory control of hippocampal spatiotemporal selectivity. *Science*, 340(6138), 1342–1346. <https://doi.org/10.1126/science.1232655>
- Reveley, C., Gruslys, A., Ye, F. Q., Glen, D., Samaha, J., E Russ, B., Saad, Z., K Seth, A., Leopold, D. A., & Saleem, K. S. (2017). Three-Dimensional Digital Template Atlas of the Macaque Brain. *Cerebral Cortex*, 27(9), 4463–4477. <https://doi.org/10.1093/cercor/bhw248>
- Risold, P. Y., Thompson, R. H., & Swanson, L. W. (1997). The structural organization of connections between hypothalamus and cerebral cortex. *Brain Research. Brain Research Reviews*, 24(2-3), 197–254. [https://doi.org/10.1016/s0165-0173\(97\)00007-6](https://doi.org/10.1016/s0165-0173(97)00007-6)
- Roberts, L. (2019). Small, furry and powerful: are mouse lemurs the next big thing in genetics? *Nature*, 570(7760), 151–154. <https://doi.org/10.1038/d41586-019-01789-0>
- Robertson, R. G., Rolls, E. T., Georges-François, P., & Panzeri, S. (1999). Head direction cells in the primate pre-subiculum. *Hippocampus*, 9(3), 206–219. [https://doi.org/10.1002/\(SICI\)1098-1063\(1999\)9:3<206::AID-HIPO2>3.0.CO;2-H](https://doi.org/10.1002/(SICI)1098-1063(1999)9:3<206::AID-HIPO2>3.0.CO;2-H)
- Robertson, R. G., Rolls, E. T., & Georges-François, P. (1998). Spatial view cells in the primate hippocampus: effects of removal of view details. *Journal of Neurophysiology*, 79(3), 1145–1156. <https://doi.org/10.1152/jn.1998.79.3.1145>
- Rodda, G. H., & Phillips, J. B. (1992). Navigational systems develop along similar lines in amphibians, reptiles, and birds. *Ethology Ecology & Evolution*, 4(1), 43–51. <https://doi.org/10.1080/08927014.1992.9525349>
- Rolls, E. T., & O'Mara, S. M. (1995). View-responsive neurons in the primate hippocampal complex. *Hippocampus*, 5(5), 409–424. <https://doi.org/10.1002/hipo.450050504>
- Rolls, E. T., Robertson, R. G., & Georges-François, P. (1997). Spatial view cells in the primate hippocampus. *The European Journal of Neuroscience*, 9(8), 1789–1794. <https://doi.org/10.1111/j.1460-9568.1997.tb01538.x>
- Rolls, E. T., Treves, A., Robertson, R. G., Georges-François, P., & Panzeri, S. (1998). Information about spatial view in an ensemble of primate hippocampal cells. *Journal of Neurophysiology*, 79(4), 1797–1813. <https://doi.org/10.1152/jn.1998.79.4.1797>
- Rolls, E. T., & Xiang, J.-Z. (2005). Reward-spatial view representations and learning in the primate hippocampus. *The Journal of Neuroscience: The Official Journal of the Society for Neuroscience*, 25(26), 6167–6174. <https://doi.org/10.1523/JNEUROSCI.1481-05.2005>
- Royer, S., Zemelman, B. V., Losonczy, A., Kim, J., Chance, F., Magee, J. C., & Buzsáki, G. (2012). Control of timing, rate and bursts of hippocampal place cells by dendritic and somatic inhibition. *Nature Neuroscience*, 15(5), 769–775. <https://doi.org/10.1038/nn.3077>
- Roy, S., & Wang, X. (2012). Wireless multi-channel single unit recording in freely moving and vocalizing primates. *Journal of Neuroscience Methods*, 203(1), 28–40. <https://doi.org/10.1016/j.jneumeth.2011.09.004>
- Rubin, A., Yartsev, M. M., & Ulanovsky, N. (2014). Encoding of head direction by hippocampal place cells in bats. *The Journal of Neuroscience: The Official Journal of the Society for Neuroscience*, 34(3), 1067–1080. <https://doi.org/10.1523/JNEUROSCI.5393-12.2014>
- Sanguinetti-Scheck, J. I., & Brecht, M. (2020). Home, head direction stability, and grid cell distortion. *Journal of Neurophysiology*, 123(4), 1392–1406. <https://doi.org/10.1152/jn.00518.2019>
- Sarasa, M., & Pesini, P. (2009). Natural non-transgenic animal models for research in Alzheimer's disease. *Current Alzheimer Research*, 6(2), 171–178. <https://doi.org/10.2174/156720509787602834>
- Sarel, A., Finkelstein, A., Las, L., & Ulanovsky, N. (2017). Vectorial representation of spatial goals in the hippocampus of bats. *Science*, 355(6321), 176–180. <https://doi.org/10.1126/science.aak9589>
- Sargolini, F., Fyhn, M., Hafting, T., McNaughton, B. L., Witter, M. P., Moser, M.-B., & Moser, E. I. (2006). Conjunctive representation of position, direction, and velocity in entorhinal cortex. *Science*, 312(5774), 758–762. <https://doi.org/10.1126/science.1125572>
- Savelli, F., Yoganarasimha, D., & Knierim, J. J. (2008). Influence of boundary removal on the spatial representations of the medial entorhinal cortex. *Hippocampus*, 18(12), 1270–1282. <https://doi.org/10.1002/hipo.20511>
- Schliehe-Diecks, S., Eberle, M., & Kappeler, P. M. (2012). Walk the line—dispersal movements of gray mouse lemurs (*Microcebus murinus*). *Behavioral Ecology and Sociobiology*, 66(8), 1175–1185. <https://doi.org/10.1007/s00265-012-1371-y>
- Schmid, J., & Kappeler, P. M. (1998). Fluctuating sexual dimorphism and differential hibernation by sex in a primate, the gray mouse lemur (*Microcebus murinus*). *Behavioral Ecology and Sociobiology*, 43(2), 125–132. <https://doi.org/10.1007/s002650050474>
- Schmid, J., & Speakman, J. R. (2000). Daily energy expenditure of the grey mouse lemur (*Microcebus murinus*): a

- small primate that uses torpor. *Journal of Comparative Physiology. B, Biochemical, Systemic, and Environmental Physiology*, 170(8), 633–641. <https://doi.org/10.1007/s003600000146>
- Scholz, J., LaLiberté, C., van Eede, M., Lerch, J. P., & Henkelman, M. (2016). Variability of brain anatomy for three common mouse strains. *NeuroImage*, 142, 656–662. <https://doi.org/10.1016/j.neuroimage.2016.03.069>
- Schultz, C., & Engelhardt, M. (2014). Anatomy of the hippocampal formation. *Frontiers of Neurology and Neuroscience*, 34, 6–17. <https://doi.org/10.1159/000360925>
- Seyfarth, E.-A., Hergenröder, R., Ebbes, H., & Barth, F. G. (1982). Idiothetic orientation of a wandering spider: Compensation of detours and estimates of goal distance. *Behavioral Ecology and Sociobiology*, 11(2), 139–148. <https://doi.org/10.1007/BF00300103>
- Skaggs, W. E., Knierim, J. J., Kudrimoti, H. S., & McNaughton, B. L. (1995). A model of the neural basis of the rat's sense of direction. *Advances in Neural Information Processing Systems*, 7, 173–180. <https://www.ncbi.nlm.nih.gov/pubmed/11539168>
- Skaggs, W. E., McNaughton, B. L., Wilson, M. A., & Barnes, C. A. (1996). Theta phase precession in hippocampal neuronal populations and the compression of temporal sequences. *Hippocampus*, 6(2), 149–172. [https://doi.org/10.1002/\(SICI\)1098-1063\(1996\)6:2<149::AID-HIPO6>3.0.CO;2-K](https://doi.org/10.1002/(SICI)1098-1063(1996)6:2<149::AID-HIPO6>3.0.CO;2-K)
- Skrede, K. K., & Westgaard, R. H. (1971). The transverse hippocampal slice: a well-defined cortical structure maintained in vitro. *Brain Research*, 35(2), 589–593. [https://doi.org/10.1016/0006-8993\(71\)90508-7](https://doi.org/10.1016/0006-8993(71)90508-7)
- Solstad, T., Boccara, C. N., Kropff, E., Moser, M.-B., & Moser, E. I. (2008). Representation of geometric borders in the entorhinal cortex. *Science*, 322(5909), 1865–1868. <https://doi.org/10.1126/science.1166466>
- Sommer, S., & Wehner, R. (2005). Vector navigation in desert ants, *Cataglyphis fortis*: celestial compass cues are essential for the proper use of distance information. *Die Naturwissenschaften*, 92(10), 468–471. <https://doi.org/10.1007/s00114-005-0020-y>
- Spellman, T., Rigotti, M., Ahmari, S. E., Fusi, S., Gogos, J. A., & Gordon, J. A. (2015). Hippocampal-prefrontal input supports spatial encoding in working memory. *Nature*, 522(7556), 309–314. <https://doi.org/10.1038/nature14445>
- Squire, L. R., Stark, C. E. L., & Clark, R. E. (2004). The medial temporal lobe. *Annual Review of Neuroscience*, 27, 279–306. <https://doi.org/10.1146/annurev.neuro.27.070203.144130>
- Stangl, M., Achtzehn, J., Huber, K., Dietrich, C., Tempelmann, C., & Wolbers, T. (2018). Compromised Grid-Cell-like Representations in Old Age as a Key Mechanism to Explain Age-Related Navigational Deficits. *Current Biology: CB*, 28(7), 1108–1115.e6. <https://doi.org/10.1016/j.cub.2018.02.038>
- Starkhammar, J., Moore, P. W., Talmadge, L., & Houser, D. S. (2011). Frequency-dependent variation in the two-dimensional beam pattern of an echolocating dolphin. *Biology Letters*, 7(6), 836–839. <https://doi.org/10.1098/rsbl.2011.0396>
- Stensola, H., Stensola, T., Solstad, T., Frøland, K., Moser, M.-B., & Moser, E. I. (2012). The entorhinal grid map is discretized. *Nature*, 492(7427), 72–78. <https://doi.org/10.1038/nature11649>
- Stensola, T., Stensola, H., Moser, M.-B., & Moser, E. I. (2015). Shearing-induced asymmetry in entorhinal grid cells. *Nature*, 518(7538), 207–212. <https://doi.org/10.1038/nature14151>
- Strange, B. A., Witter, M. P., Lein, E. S., & Moser, E. I. (2014). Functional organization of the hippocampal longitudinal axis. *Nature Reviews. Neuroscience*, 15(10), 655–669. <https://doi.org/10.1038/nrn3785>
- Sündermann, D., Scheumann, M., & Zimmermann, E. (2008). Olfactory predator recognition in predator-naïve gray mouse lemurs (*Microcebus murinus*). *Journal of Comparative Psychology*, 122(2), 146–155. <https://doi.org/10.1037/0735-7036.122.2.146>
- Tamura, R., Ono, T., Fukuda, M., & Nakamura, K. (1990). Recognition of egocentric and allocentric visual and auditory space by neurons in the hippocampus of monkeys. *Neuroscience Letters*, 109(3), 293–298. [https://doi.org/10.1016/0304-3940\(90\)90010-7](https://doi.org/10.1016/0304-3940(90)90010-7)
- Tamura, R., Ono, T., Fukuda, M., & Nakamura, K. (1992). Spatial responsiveness of monkey hippocampal neurons to various visual and auditory stimuli. *Hippocampus*, 2(3), 307–322. <https://doi.org/10.1002/hipo.450020309>
- Taube, J. S. (1995). Head direction cells recorded in the anterior thalamic nuclei of freely moving rats. *The Journal of Neuroscience: The Official Journal of the Society for Neuroscience*, 15(1 Pt 1), 70–86. <https://doi.org/10.1523/JNEUROSCI.15-01-00070.1995>
- Taube, J. S. (2007). The head direction signal: origins and sensory-motor integration. *Annual Review of Neuroscience*, 30, 181–207. <https://doi.org/10.1146/annurev.neuro.29.051605.112854>
- Taube, J. S., Muller, R. U., & Ranck, J. B., Jr. (1990). Head-direction cells recorded from the postsubiculum in freely moving rats. I. Description and quantitative analysis. *The Journal of Neuroscience: The Official Journal of the Society for Neuroscience*, 10(2), 420–435. <https://www.ncbi.nlm.nih.gov/pubmed/2303851>
- Terrazas, A., Krause, M., Lipa, P., Gothard, K. M., Barnes, C. A., & McNaughton, B. L. (2005). Self-motion and the hippocampal spatial metric. *The Journal of Neuroscience: The Official Journal of the Society for Neuroscience*, 25(35), 8085–8096. <https://doi.org/10.1523/JNEUROSCI.0693-05.2005>
- Thomas, P., Pouydebat, E., Brazidec, M. L., Aujard, F., & Herrel, A. (2016). Determinants of pull strength in captive grey mouse lemurs. *Journal of Zoology*, 298(2), 77–81. <https://doi.org/10.1111/jzo.12292>
- Thompson, L. T., & Best, P. J. (1989). Place cells and silent cells in the hippocampus of freely-behaving rats. *The*

- Journal of Neuroscience: The Official Journal of the Society for Neuroscience*, 9(7), 2382–2390.  
<https://www.ncbi.nlm.nih.gov/pubmed/2746333>
- Tolman, E. C. (1948). Cognitive maps in rats and men. *Psychological Review*, 55(4), 189–208.  
<https://doi.org/10.1037/h0061626>
- Toussaint, S., Herrel, A., Ross, C. F., Aujard, F., & Pouydebat, E. (2015). Substrate Diameter and Orientation in the Context of Food Type in the Gray Mouse Lemur, *Microcebus murinus*: Implications for the Origins of Grasping in Primates. *International Journal of Primatology*, 36(3), 583–604.  
<https://doi.org/10.1007/s10764-015-9844-2>
- Ulanovsky, N., & Moss, C. F. (2007). Hippocampal cellular and network activity in freely moving echolocating bats. *Nature Neuroscience*, 10(2), 224–233. <https://doi.org/10.1038/nn1829>
- Ulanovsky, N., & Moss, C. F. (2011). Dynamics of hippocampal spatial representation in echolocating bats. *Hippocampus*, 21(2), 150–161. <https://doi.org/10.1002/hipo.20731>
- Vágó, L., & Ujfalussy, B. B. (2018). Robust and efficient coding with grid cells. *PLoS Computational Biology*, 14(1), e1005922. <https://doi.org/10.1371/journal.pcbi.1005922>
- Vanderwolf, C. H. (1969). Hippocampal electrical activity and voluntary movement in the rat. *Electroencephalography and Clinical Neurophysiology*, 26(4), 407–418.  
[https://doi.org/10.1016/0013-4694\(69\)90092-3](https://doi.org/10.1016/0013-4694(69)90092-3)
- Vazdarjanova, A., & Guzowski, J. F. (2004). Differences in hippocampal neuronal population responses to modifications of an environmental context: evidence for distinct, yet complementary, functions of CA3 and CA1 ensembles. *The Journal of Neuroscience: The Official Journal of the Society for Neuroscience*, 24(29), 6489–6496. <https://doi.org/10.1523/JNEUROSCI.0350-04.2004>
- Villette, V., Malvache, A., Tressard, T., Dupuy, N., & Cossart, R. (2015). Internally Recurring Hippocampal Sequences as a Population Template of Spatiotemporal Information. *Neuron*, 88(2), 357–366.  
<https://doi.org/10.1016/j.neuron.2015.09.052>
- Voigts, J., Newman, J. P., Wilson, M. A., & Harnett, M. T. (2019). An easy-to-assemble, robust, and lightweight drive implant for chronic tetrode recordings in freely moving animals. In *Cold Spring Harbor Laboratory* (p. 746651). <https://doi.org/10.1101/746651>
- Wallraff, H. G. (2004). Avian olfactory navigation: its empirical foundation and conceptual state. *Animal Behaviour*, 67(2), 189–204. <https://doi.org/10.1016/j.anbehav.2003.06.007>
- Wang, Y., Romani, S., Lustig, B., Leonardo, A., & Pastalkova, E. (2015). Theta sequences are essential for internally generated hippocampal firing fields. *Nature Neuroscience*, 18(2), 282–288.  
<https://doi.org/10.1038/nn.3904>
- Warrant, E. J., Kelber, A., Gislén, A., Greiner, B., Ribi, W., & Wcislo, W. T. (2004). Nocturnal vision and landmark orientation in a tropical halictid bee. *Current Biology: CB*, 14(15), 1309–1318.  
<https://doi.org/10.1016/j.cub.2004.07.057>
- Watanabe, T., & Niki, H. (1985). Hippocampal unit activity and delayed response in the monkey. *Brain Research*, 325(1-2), 241–254. [https://doi.org/10.1016/0006-8993\(85\)90320-8](https://doi.org/10.1016/0006-8993(85)90320-8)
- Wiener, S. I. (1993). Spatial and behavioral correlates of striatal neurons in rats performing a self-initiated navigation task. *The Journal of Neuroscience: The Official Journal of the Society for Neuroscience*, 13(9), 3802–3817. <https://www.ncbi.nlm.nih.gov/pubmed/8366346>
- Wikelski, M., Arriero, E., Gagliardo, A., Holland, R. A., Huttunen, M. J., Juvaste, R., Mueller, I., Tertitski, G., Thorup, K., Wild, M., Alanko, M., Bairlein, F., Cherenkov, A., Cameron, A., Flatz, R., Hannila, J., Hüppop, O., Kangasniemi, M., Kranstauber, B., ... Wistbacka, R. (2015). True navigation in migrating gulls requires intact olfactory nerves. *Scientific Reports*, 5, 17061. <https://doi.org/10.1038/srep17061>
- Wikenheiser, A. M., & Redish, A. D. (2015). Hippocampal theta sequences reflect current goals. *Nature Neuroscience*, 18(2), 289–294. <https://doi.org/10.1038/nn.3909>
- Wilson, M. A., & McNaughton, B. L. (1993). Dynamics of the hippocampal ensemble code for space. *Science*, 261(5124), 1055–1058. <https://doi.org/10.1126/science.8351520>
- Wirth, S., Baraduc, P., Planté, A., Pinède, S., & Duhamel, J.-R. (2017). Gaze-informed, task-situated representation of space in primate hippocampus during virtual navigation. *PLoS Biology*, 15(2), e2001045.  
<https://doi.org/10.1371/journal.pbio.2001045>
- Witter, M. P. (2010). Connectivity of the Hippocampus. In V. Cutsuridis, B. Graham, S. Cobb, & I. Vida (Eds.), *Hippocampal Microcircuits: A Computational Modeler's Resource Book* (pp. 5–26). Springer New York.  
[https://doi.org/10.1007/978-1-4419-0996-1\\_1](https://doi.org/10.1007/978-1-4419-0996-1_1)
- Wittlinger, M., Wehner, R., & Wolf, H. (2006). The ant odometer: stepping on stilts and stumps. *Science*, 312(5782), 1965–1967. <https://doi.org/10.1126/science.1126912>
- Wolf, H. (2011). Odometry and insect navigation. *The Journal of Experimental Biology*, 214(Pt 10), 1629–1641.  
<https://doi.org/10.1242/jeb.038570>
- Yartsev, M. M., & Ulanovsky, N. (2013). Representation of three-dimensional space in the hippocampus of flying bats. *Science*, 340(6130), 367–372. <https://doi.org/10.1126/science.1235338>
- Yartsev, M. M., Witter, M. P., & Ulanovsky, N. (2011). Grid cells without theta oscillations in the entorhinal cortex of

- bats. *Nature*, 479(7371), 103–107. <https://doi.org/10.1038/nature10583>
- Yoder, A. D. (2013). The lemur revolution starts now: the genomic coming of age for a non-model organism. *Molecular Phylogenetics and Evolution*, 66(2), 442–452. <https://doi.org/10.1016/j.ympev.2012.08.024>
- Yoder, A. D., & Yang, Z. (2004). Divergence dates for Malagasy lemurs estimated from multiple gene loci: geological and evolutionary context. *Molecular Ecology*, 13(4), 757–773. <https://doi.org/10.1046/j.1365-294x.2004.02106.x>
- Yu, G. J., Bouteiller, J.-M. C., & Berger, T. W. (2020). Topographic Organization of Correlation Along the Longitudinal and Transverse Axes in Rat Hippocampal CA3 Due to Excitatory Afferents. *Frontiers in Computational Neuroscience*, 14, 588881. <https://doi.org/10.3389/fncom.2020.588881>
- Zannoni, N., Wikelski, M., Gagliardo, A., Raza, A., Kramer, S., Seghetti, C., Wang, N., Edtbauer, A., & Williams, J. (2020). Identifying volatile organic compounds used for olfactory navigation by homing pigeons. *Scientific Reports*, 10(1), 15879. <https://doi.org/10.1038/s41598-020-72525-2>
- Ziv, Y., Burns, L. D., Cocker, E. D., Hamel, E. O., Ghosh, K. K., Kitch, L. J., El Gamal, A., & Schnitzer, M. J. (2013). Long-term dynamics of CA1 hippocampal place codes. *Nature Neuroscience*, 16(3), 264–266. <https://doi.org/10.1038/nn.3329>



# EthoLoop: automated closed-loop neuroethology in naturalistic environments

Ali Nourizonoz<sup>1</sup>, Robert Zimmermann<sup>1</sup>, Chun Lum Andy Ho<sup>1</sup>, Sebastien Pellat<sup>1</sup>, Yannick Ormen<sup>1</sup>, Clément Prévost-Solié<sup>1</sup>, Gilles Reymond<sup>1</sup>, Fabien Pifferi<sup>2</sup>, Fabienne Aujard<sup>2</sup>, Anthony Herrel<sup>2</sup> and Daniel Huber<sup>1</sup>✉

**Accurate tracking and analysis of animal behavior is crucial for modern systems neuroscience. However, following freely moving animals in naturalistic, three-dimensional (3D) or nocturnal environments remains a major challenge. Here, we present EthoLoop, a framework for studying the neuroethology of freely roaming animals. Combining real-time optical tracking and behavioral analysis with remote-controlled stimulus-reward boxes, this system allows direct interactions with animals in their habitat. EthoLoop continuously provides close-up views of the tracked individuals and thus allows high-resolution behavioral analysis using deep-learning methods. The behaviors detected on the fly can be automatically reinforced either by classical conditioning or by optogenetic stimulation via wirelessly controlled portable devices. Finally, by combining 3D tracking with wireless neurophysiology we demonstrate the existence of place-cell-like activity in the hippocampus of freely moving primates. Taken together, we show that the EthoLoop framework enables interactive, well-controlled and reproducible neuroethological studies in large-field naturalistic settings.**

A precise quantification of behavior is essential for understanding brain function. Neuroscientists and ethologists have studied animal behavior for decades seeking to identify the underlying neural circuits<sup>1,2</sup>. The quest for linking neuronal activity to specific behaviors in a laboratory setting imposes several constraints on experimental frameworks<sup>3</sup>. Besides the obvious need for tractable variables, the studied behavior should retain most ethologically relevant sensory, motor and cognitive components, while remaining reproducible. The environmental setting in which the animal moves should also be flexible enough to allow probing for multiple parameters involved in the studied behavior. Finally, simultaneous recordings or manipulations of neuronal activity is essential.

One strategy is to partially or fully immobilize the animals in a virtual reality environment<sup>4</sup>. This approach facilitates detailed observation of behavior and allows for accurate closed-loop stimulus control. It can also provide convenient and stable access to the brain for optical<sup>5,6</sup> or electrophysiological recordings<sup>7</sup>. However, important drawbacks exist<sup>8</sup>. In most instances, natural motor output and the related sensory feedback are substantially disrupted, possibly inhibiting normal spatial processing<sup>9</sup> (although see refs. <sup>10,11</sup>). Furthermore, virtual reality is often limited to a single sensory modality, such as vision<sup>4-6,12</sup>, somatosensation<sup>13</sup> or olfaction<sup>14</sup>. Finally, studying typical primate motor patterns such as climbing or jumping and probing behaviors such as social interactions involving multiple animals is more challenging in virtual reality.

An alternative approach is to retain the animal's full sensorimotor experience by studying its behavior while the animal is freely moving in naturalistic environments. This, however, poses challenges regarding behavioral control and quantification. It necessitates knowing where the animal is and what it does, as well as tracking the identity of multiple subjects. Systems for tracking in naturalistic environments have been developed for several animal

species, including insects<sup>15-19</sup>, rodents<sup>20-22</sup>, primates<sup>23,24</sup> or flying bats<sup>25,26</sup>. Multiple subject identification can be achieved based on the recognition of coat color<sup>27</sup>, wearable colored markers<sup>23,28</sup>, electronic markers<sup>29</sup>, Kalman and nearest neighbor filters<sup>17</sup> or deep learning<sup>19,30</sup>. Finally, immersive visual virtual reality for unrestrained animals has also been developed<sup>11,31,32</sup>. However, by projecting a single viewpoint into the arena, these systems are currently restricted to the use with single animals, and provide only nonbinocular views. In general, most tracking systems are limited by small and relatively empty laboratory environments, and require bright and even illumination (although see refs. <sup>23-25</sup>) to extract position and behavior or to provide feedback. Studying animals in more naturalistic environments with noisy or changing backgrounds and poorly lit conditions (for example, in arboreal and nocturnal settings), poses serious challenges to most existing tracking systems.

Finally, interacting with freely roaming and fast-moving animals in a closed-loop manner for behavioral conditioning would require a tracking framework to be extremely fast, robust and to provide sufficient high-resolution information about the tracked animal. However, most current systems for freely moving animals are still designed for offline behavioral analysis (although see refs. <sup>11,19,31-34</sup>) and thus cannot react to behavioral elements in the order of tens of milliseconds. Taken together, there is currently a need for an integrated framework able to carry out the next generation of reproducible neuroethological experiments with freely moving animals in more naturalistic settings.

## Results

**Implementation of the EthoLoop tracking system.** To follow the behavior of freely roaming nocturnal animals, such as mice (*Mus musculus*) or mouse lemurs (*Microcebus murinus*, a small arboreal primate), in naturalistic 3D environments, we developed an ultra-fast, multi-camera closed-loop tracking system capable

<sup>1</sup>University of Geneva, Department of Basic Neurosciences, Geneva, Switzerland. <sup>2</sup>Musée National d'Histoire Naturelle, Adaptive Mechanisms and Evolution, UMR7179—CNRS, Paris, France. ✉e-mail: [daniel.huber@unige.ch](mailto:daniel.huber@unige.ch)

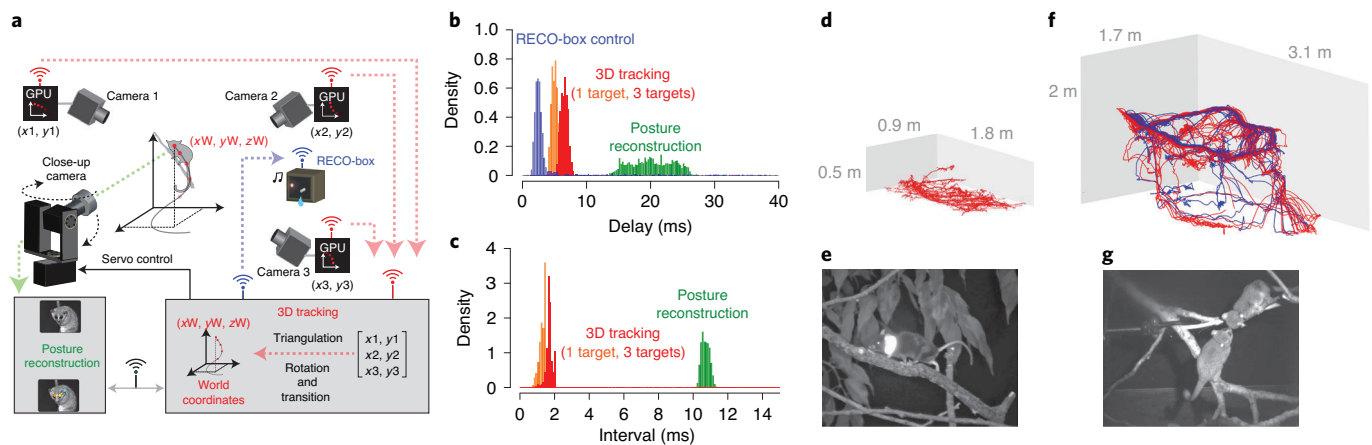


**Fig. 1 | The EthoLoop behavioral tracking system.** **a**, Schematic depiction and spatial arrangement of the different EthoLoop elements. Multiple infrared cameras (cameras 1–3) with dedicated GPUs process images from different viewing angles. The identity and positions of the detected markers are wirelessly transmitted to a central host computer for 3D reconstruction (triangulation, followed by rotation and transition into real-world 3D coordinates). The 3D coordinates are forwarded to control the position and focus of a gimbal-mounted close-up camera. The images from the close-up system are either saved for offline analysis or processed on-the-fly to trigger remote-controlled reward boxes (RECO box). RECO boxes are connected wirelessly and can provide auditory or visual stimuli or liquid rewards. **b**, Latencies for the communication with the RECO box (blue), reconstructing 3D position (1 and 3 targets, orange and red), and the real-time posture analysis (green). **c**, Intervals for consecutive reconstitutions (1 and 3 targets, orange and red) and time for the postural analysis (green) of two subsequent frames. **d**, 3D trajectory of a mouse tracked in a naturalistic environment (red line, 60 min, Supplementary Video 1), in an arena covered with wooden branches (representative example of 26 experiments). The tracking was carried out in the dark and based on a passive retro-reflective marker fixed around the neck. **e**, Still image from the infrared close-up camera following the position of the tracked mouse in **d**. **f**, 30 min of 3D trajectories of two mouse lemurs (red, blue) tracked in an arena filled with tree branches (representative example of 20 experiments). **g**, Infrared close-up image of the two tracked mouse lemurs (from **f**).

of providing simultaneous close-up views and analyses of the ethology of tracked individuals (Fig. 1). We hence termed the system EthoLoop.

Multiple high-speed infrared cameras are installed above a tracking arena, providing views of the freely moving animals from different angles (Fig. 1a). The images from each camera are processed separately to extract the two-dimensional (2D) positions of each animal. The identification and tracking of individuals in the dark is either achieved using retro-reflective passive markers (Fig. 1d and Supplementary Video 1) or, when multiple individuals have to be tracked simultaneously, by spectrally separating the hue of miniature battery-powered infrared light emitting diodes (LEDs) with different wavelengths (Fig. 1f, Supplementary Fig. 1 and Supplementary Video 2). To increase the speed and decrease the processing time, the spatial localization and spectral separation of each camera view is carried out on stand-alone graphical processing units (GPUs) (Fig. 1a). The position of each animal is then transformed into real-world 3D coordinates by geometric triangulation<sup>17,23</sup> from the different camera views (Fig. 1a). We achieved maximal tracking at rates ranging from 785 to 580 Hz (for 1–3 targets, 1 ms exposure time, Fig. 1c), with delays below 8 ms for up to three targets (Fig. 1b and Supplementary Fig. 2). The ideal number of cameras (minimum 2) depends on the complexity of the obstructing structures in the environment. Adding more cameras can also improve the tracking accuracy in larger arenas, if they reduce the minimal distance to the target. Thus, by combining off-the-shelf hardware and open source code, this system can be adapted to spatial scales of 1 m<sup>3</sup> (Fig. 1a and Supplementary Video 1), 10 m<sup>3</sup> (Fig. 1f and Supplementary Videos 2 and 3) and up to 100 m<sup>3</sup> (Supplementary Fig. 3 and Supplementary Video 4). Tracking multiple animals in such large arenas while preserving their respective identity allows detailed study of their social interactions (Supplementary Fig. 4). Finally, to facilitate the installation of additional cameras in large-scale and challenging conditions (trees, branches), all cameras and GPUs can be battery-powered and communicate via wireless network

protocols, thus removing the need for external wiring and facilitating their placement in strategic locations.

Although the GPU-based 3D tracking allows determining the animal's position with high temporal resolution (Fig. 1b,c) and precision (Supplementary Fig. 1i), it does not provide any information about the actual behavior carried out at that location. Inspired by the pioneering work on freely flying and walking insects<sup>15,17</sup>, we therefore added a gimbal-mounted, close-up video camera to the EthoLoop system, providing a focused and magnified view continuously centered on the tracked individual (Fig. 1e,g and Supplementary Video 3). This way, the behavior of a tracked animal can be analyzed in detail, independent of the actual size of the tracked volume in which it navigates. Since jumping primates can reach speeds up to 2 m s<sup>-1</sup> (Supplementary Video 3), the focusing mechanism of the close-up system was driven by a liquid lens capable of changing focus within milliseconds. Although we only used a single close-up view for our experiments, the position of one or multiple animals can be forwarded to multiple close-up systems in parallel. To ensure sufficient illumination of the tracked subject in dark large-scale environments, we mounted an infrared light source in parallel to the camera path (Supplementary Video 4) or on a separate gimbal system. This allowed a targeted and economical illumination independently of any ambient light. In summary, the EthoLoop system combines fast and accurate tracking of animal position even in large, arboreal or nocturnal settings with high-resolution close-up views of their behavior.

**Observation and manipulation of natural foraging behavior using remote-controlled reward sources.** Out of all animal behaviors, foraging is most likely one of the most universal activities<sup>35,36</sup>. It was probably a prominent driver behind main evolutionary specializations of sensory, motor and cognitive capacities in primates and other clades<sup>37</sup>. To study naturalistic foraging in laboratory settings, the distribution of food sources, as well as sensory cues signaling their availability would ideally be controlled by the experimenter

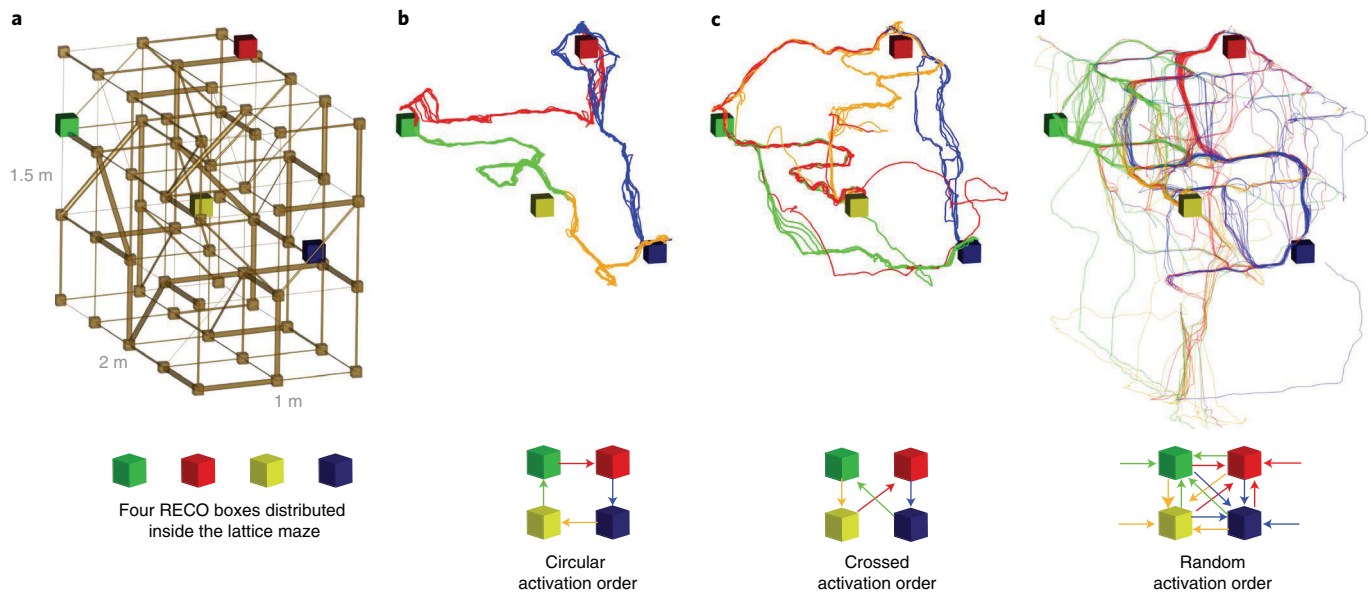


**Fig. 2 | Foraging of a mouse lemur in a 3D lattice maze.** **a**, Four RECO boxes (colored cubes) spatially distributed at different locations of a lattice maze (0.5 m branch length). RECO boxes are shown in different colors and are activated with different sequences. Reward availability was indicated by a 9 kHz tone. The actual reward delivery was made conditional on the animal's arrival at the feeder within 10 s. **b, c**, 10 min of 3D trajectory of the mouse lemur where the RECO boxes are activated in a circular (**b**) or crossed order (**c**). The trajectory color indicates the currently activated RECO box (representative trajectories of eight experiments). **d**, 3D trajectory of a mouse lemur when activation order was random and conditional on the actual position of the animal in the arena (representative trajectory of four experiments).

in real time, taking into account the animal's actual position and behavior. This way, specific situations could be created in a reproducible manner. We therefore integrated small, remote-controlled and interactive reward boxes (RECO box) into the EthoLoop framework. The RECO boxes are able to play sensory cues (auditory or visual) and provide calibrated amounts of liquid rewards (Fig. 1a and Supplementary Fig. 5a,b). Multiple of these battery-powered boxes can be distributed in the environment to mimic the availability and cues associated with natural resources.

To illustrate the range of basic behavioral patterns in freely roaming mouse lemurs, we positioned multiple RECO boxes in the behavioral arena (Fig. 2a and Extended Data Fig. 1a). To cover the volumetric space more evenly and make the experiments more reproducible, we also replaced the naturalistic branches with a parameterizable artificial lattice maze<sup>38,39</sup>. The availability of a liquid reward at a given location was indicated by an auditory cue (9 kHz tone, 1 s intermittent at 0.5 Hz). To mimic a variable degree of predictability of the next food location, we first activated the different boxes sequentially in a fixed order (Fig. 2b,c, Supplementary Video 5 and Extended Data Fig. 1b,c). This type of activation triggered highly stereotypical and most likely memory-guided paths. On the other hand, the random activation of a RECO box (triggered by the specific spatial location of the animal, Fig. 2d) established a situation where the animal could not predict the next reward location, and hence resulted in more variable behavioral patterns (Fig. 2d). The location-triggered random activation allowed us to have the mouse lemurs cover a large part of the 3D lattice maze (Fig. 2b,c). These data illustrate how combining real-time tracking with remotely controlled elements can rapidly shape specific behaviors and force the animals to adopt different foraging strategies.

Other, more global environmental parameters such as illumination also affect behavior in a given environment<sup>36</sup>. To highlight how our system can detect behavioral signs related to such global parameter changes, we reduced the illumination levels from dim (<1 lux, Extended Data Fig. 1d) to complete darkness (Extended Data Fig. 1e and Supplementary Video 6). This triggered a profound change in

the movement parameters including a reduction in the number of jumps (Extended Data Fig. 1f), or the locomotor speed distribution (Extended Data Fig. 1g and Supplementary Video 6).

Taken together, the combination of the EthoLoop tracking system with interactive agents, such as RECO boxes, or changes of global parameters, such as illumination, is ideally suited for exploring different aspects of ethologically relevant parameters within naturalistic settings.

#### Fully automated conditioning of behavior in naturalistic settings.

To explore the possibility of using the EthoLoop system to reinforce specific behaviors by operant conditioning<sup>40</sup>, we combined the principle of clicker training by human experts<sup>41,42</sup> with real-time and automated behavioral analysis. An auditory stimulus (9 kHz tone) followed by a small liquid reward from one of the RECO boxes was triggered on an automated detection of a specific behavior. To test the effectiveness of such automated conditioning procedures, we first conditioned mice to enter an arbitrarily chosen location in a naturalistic environment designed with tree branches (Fig. 3a and Extended Data Figs. 2 and 3). On detecting an entry into a defined location, the tracking system triggered a sound from a single RECO box and a reward was available for the subsequent 10 s in the center of the arena. Mice learned the task (Fig. 3b–d and Extended Data Fig. 2b), and the number of entries into the conditioned area increased compared to the initial rate (Fig. 3d and Extended Data Fig. 2b–f). Similarly, we were able to condition a mouse lemur to climb repeatedly to an experimenter-defined position within the 3D lattice maze (Fig. 3e and Extended Data Fig. 4a). The number of entries increased over a 30 min session (Fig. 3f–h and Extended Data Fig. 4b,c).

Inspired by more sophisticated behavioral conditioning experiments carried out by professional animal trainers with pets or zoo animals<sup>41,42</sup>, we further sought to use the real-time close-up video stream to automatically detect specific postures<sup>43</sup> and reinforce them using the RECO boxes. As a proof of principle, we chose to reinforce rearing behavior, which is observed spontaneously in

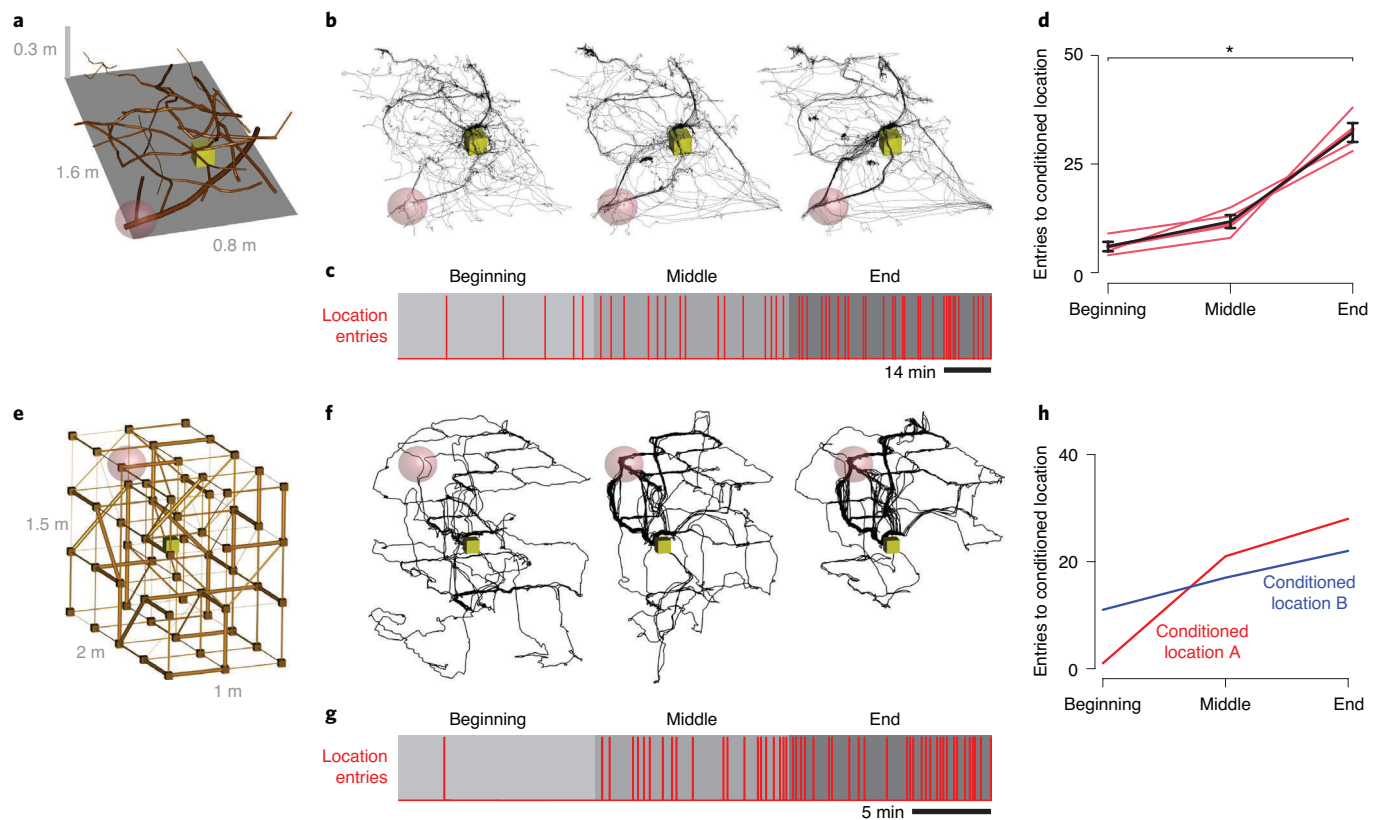


**Fig. 3 | Fully automated place conditioning in 3D environments.** **a**, An arena for freely moving mice covered with tree branches containing a single RECO box. Mice were trained to visit an unmarked location on a branch (red sphere). The reinforced location was changed daily. **b**, Example of a 3D trajectory of a mouse in the beginning, middle and end of a behavioral session (all other trajectories in Extended Data Fig. 2). **c**, Entries to the conditioned place across a behavioral session of **b**. **d**, Number of entries to the conditioned place. Mice entered the conditioned place more frequently ( $N = 4$  mice, third day, one-way repeated measure ANOVA,  $F(2,6) = 46.867$ , main effect  $P = 0.0002$ , pairwise two-sample  $t$ -test, Bonferroni correction for multiple comparison, beginning versus end,  $*P = 0.01$ ). Bars represent standard error of mean. **e**, Place conditioning of mouse lemurs in a 3D lattice maze. The red sphere indicates the conditioned location. **f**, Trajectories of a mouse lemur in the beginning, middle and end of a behavioral session (all other trajectories in Extended Data Fig. 4). **g**, Number of entries to the conditioned place across the behavioral session in **f**. **h**, The number of entries increases for different conditioned places. The two colors represent the conditioning at two different locations for the same mouse lemur (Extended Data Fig. 4).

both mice and mouse lemurs (Fig. 4). To detect rearing, we first trained a deep-learning network (DeepLabCut<sup>44</sup>) to track different body parts in a set of hand-annotated close-up videos (Fig. 4a). In a second step, we adapted DeepLabCut to classify the streamed images and localize the position of the different body parts in real time in the stream of close-up images (Fig. 4a). Using this procedure, we were able to identify body parts at an average rate of 93 Hz (Fig. 1c, green histogram) using a standard commercial computer graphics card. In a third step, the rearing behavior was detected using a set of geometrical rules, taking into account the relative spatial position of body parts. Reinforcing automatically detected rearing with a click (9 kHz), followed by a reward from a nearby RECO box (Fig. 4a), mouse lemurs rapidly increased the number of rearings (red arrows in Fig. 4g,h,i and Supplementary Video 7). In parallel, we also conditioned mice to rear on top of a branch in a naturalistic environment (Fig. 4b and Extended Data Fig. 5) and at a specific location in an open-field arena (Extended Data Fig. 6). Mice increased the number of rearings within the session (Fig. 4c–e and Supplementary Video 8). These experiments illustrate how real-time and automated behavioral classification by the EthoLoop system can be efficiently used to shape or reinforce specific actions in situations that would have been very challenging to do for any trained human observer (due to fast-moving subjects, poor illumination, large arenas or partial occlusions).

**Operant conditioning by optogenetic stimulation of reward circuits.** Using behavior-triggered operant conditioning with actual cues and rewards can become problematic when multiple subjects are present in the vicinity, since the reinforcement should target only one individual. Individualized conditioning can be achieved by optogenetic tools; for example, by the selective activation of dopamine (DA) neurons in the ventral tegmental area (VTA)<sup>45</sup>. We tested whether behaviors detected by the EthoLoop system can also be reinforced by real-time optogenetic stimulation of VTA DA neurons in mice (Fig. 5).

We first conditioned mice to enter a specific location in the arena by optogenetically activating VTA DA neurons either wirelessly through a portable, battery-powered stimulator (Supplementary Fig. 6) in naturalistic environments (Fig. 5b), or tethered via an optical fiber connected to a blue laser in open-field environments. Within single sessions, we successfully conditioned mice to enter a defined place more often (Fig. 5e and Extended Data Fig. 7).

In a second set of experiments, VTA DA neurons were activated on the detection of a predefined behavioral syllable<sup>43</sup>. As before (Fig. 4), we chose to reinforce rearing on the hind limbs (Fig. 5a). On reinforcement with optogenetic VTA stimulation, mice started rearing more within the specified area (Fig. 5g,i, Extended Data Fig. 8 and Supplementary Video 9). These experiments show that the EthoLoop system is well suited to provide precisely timed and

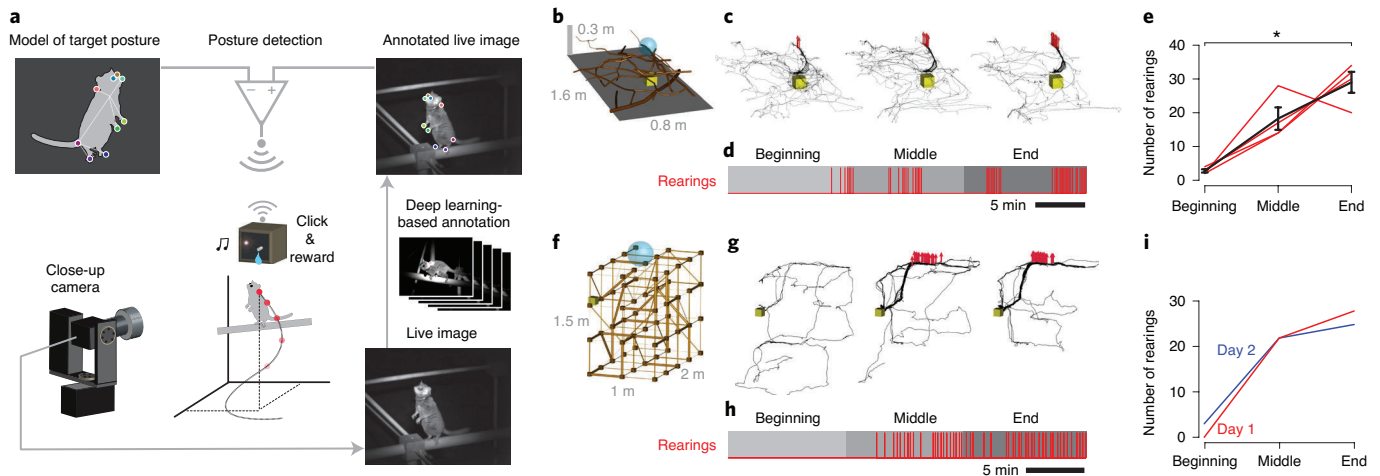


**Fig. 4 | Operant conditioning of automatically detected behavior.** **a**, Schematic representation of the information flow. While the close-up camera provides high-resolution live images of the tracked animal, the body parts are classified in real time by the weights of a pretrained deep-learning network. A match of the annotated live image with a geometric model of the posture to be reinforced, will trigger a sound, followed by a reward in the RECO box. **b**, The naturalistic environment designed with tree branches for mice with a RECO box (yellow cube) and an experimenter-defined area where rearing was conditioned (blue sphere). **c**, Trajectory of a mouse during a conditioning session where the number of rearings increased (all other trajectories in Extended Data Fig. 5). **d**, Rearings detected across the session in **c**. **e**, Summary data of the number of rearings detected across all sessions. The number of rearings increased within a behavioral session ( $N=4$  mice, one-way repeated measure ANOVA,  $F(2,6)=16.618$ , main effect  $P=0.004$ , pairwise two-sample  $t$ -test, Bonferroni adjustment for multiple comparison,  $*P=0.009$ ). Bars represent standard error of mean. **f**, The lattice maze for mouse lemurs with a RECO box (yellow cube) and an experimenter-defined area where rearing was conditioned (blue sphere). **g**, Three-dimensional trajectory of a mouse lemur during a conditioning session (representative trajectory of two experiments). The red arrows indicate rearing. **h**, The number of rearings detected across the session in **g**. **i**, Number of detected rearings across two sessions (days 1 and 2) with the same mouse lemur.

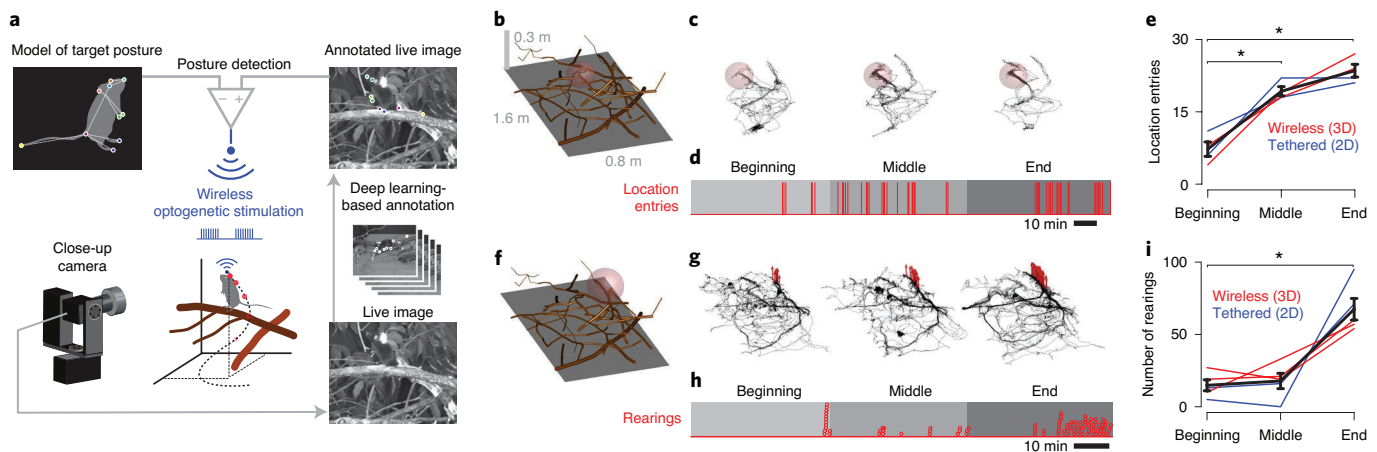


**Fig. 5 | Reinforcing automatically detected behaviors using optogenetic VTA stimulation.** **a**, Schematic representation of the information flow during conditioning by optogenetic activation of VTA DA neurons. The steps are identical to Fig. 4, except that the detection of a behavioral event wirelessly triggered the optogenetic stimulation of VTA DA neurons through a portable, battery-powered stimulator (Supplementary Fig. 6). **b**, Naturalistic environment covered with tree branches for freely moving mice. The red sphere indicates the conditioned location. **c**, Trajectory of a mouse in the beginning, middle and end of a conditioning session with wireless optogenetic stimulation (all other trajectories in Extended Data Fig. 7). **d**, Occurrence of entries to the conditioned location across a session (from **c**). **e**, Summary data for the second day of place conditioning using wireless optogenetic VTA stimulation in naturalistic (3D, red) and tethered stimulation in an open-field arena (blue). The number of entries to the conditioned place increased within a session ( $N=4$  mice, combined 3D and open-field arena, one-way repeated measure ANOVA,  $F(2,6)=29.137$ , main effects  $P=0.0008$ , pairwise two-sample  $t$ -test, Bonferroni correction for multiple comparison, beginning versus end,  $*P=0.023$ , beginning versus middle,  $*P=0.026$ ). **f**, Same arena as in **b** with the red sphere indicating the predefined location where rearing triggered VTA DA stimulation. **g**, Trajectory of a mouse during a session with optogenetic reinforcement of an automatically detected posture (rearing, red arrows; all other trajectories in Extended Data Fig. 8). **h**, Rearings detected across the session in **g** shown in red dots. **i**, Number of rearings detected at the beginning, middle and end of the behavioral session with wireless (red) and tethered (blue) optogenetic stimulations. The number of rearings increased within single sessions ( $N=5$  mice, one-way repeated measure ANOVA,  $F(2,8)=17.73$ , main effect  $P=0.001$ , pairwise two-sample  $t$ -test, Bonferroni correction for multiple comparison,  $*P=0.023$ ). Bars represent standard error of mean in **e** and **i**.

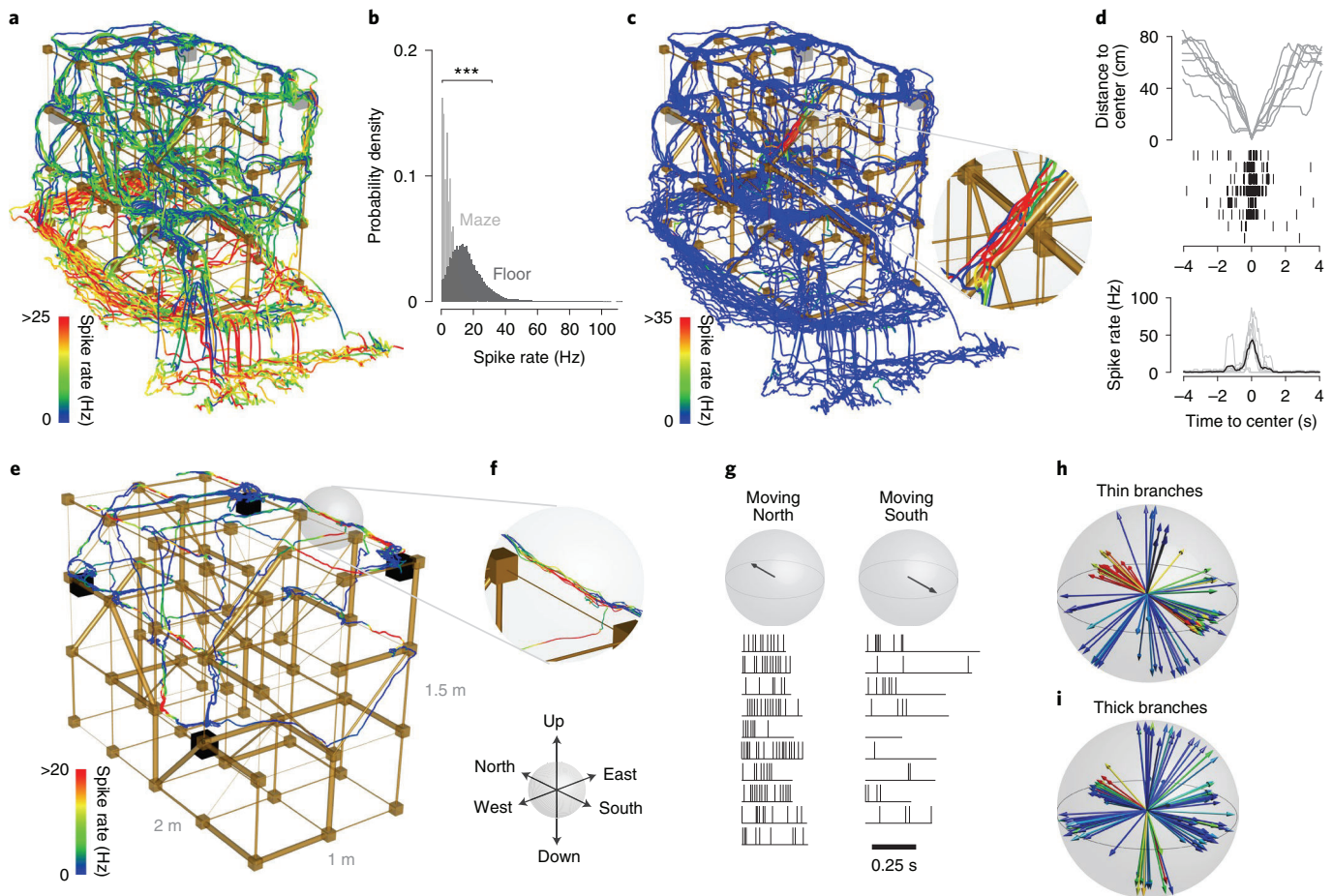


**Fig. 6 | Wireless recordings of neuronal activity in dorsal CA1 during navigation in a 3D lattice maze.** **a**, A neuron in mouse lemur CA1 during foraging in a lattice maze showing increased spike rate when on the floor. **b**, The neuronal activity (over segments of 13 cm) on the floor compared to the activity in the rest of the lattice maze ( $***P < 2.2 \times 10^{-16}$ , two-sample Kolmogorov–Smirnov test). **c**, Spike rates for a CA1 neuron showing increased activity preferentially on a single branch location (same recording session as in **a**). **d**, Distance of the animal to the location with highest average activity (top), action potentials of the recorded neuron (middle) and spike rate of the recorded neuron during individual passages (gray) and their average (black), in relation to the time to reach the center (highest average activity). **e**, **f**, Spike rates of a CA1 neuron showing increased activity on multiple locations in the maze. **g**–**i**, Additional analysis revealed that the neuronal activity was specific to one specific spatial direction (**g**) (north, neuronal data from the location in the gray sphere in **e** and higher when moving north on thin (**h**) compared to thick branches (**i**). The arrows in the sphere indicate the movement directions (13 cm segments), while the color indicates the level of activity.

behaviorally triggered optogenetic stimuli to freely moving animals in a fully automated manner and thus shape specific behavioral elements within single behavioral sessions.

**Combining 3D tracking with wireless neuronal recordings.** The ultimate goal of many neuroethological studies is to link a specific behavior to its underlying neuronal activity. To illustrate the feasibility of simultaneous neuronal recordings in combination with actively controlled foraging (Fig. 2), we set up a miniature wireless electrophysiological recording system for freely moving mouse lemurs. We recorded neurons in the dorsal CA1 of hippocampus (Supplementary Fig. 7), a brain area related to various aspects of spatial navigation<sup>46–48</sup>.

By synchronizing the recorded activity with the 3D position of the mouse lemur (Fig. 6) we found neurons that were responsive to a large region (floor, Fig. 6a,b) or a specific location (single branch, Fig. 6c,d and Extended Data Fig. 9) of the lattice maze, or mainly when moving in one direction on branches with a given diameter (Fig. 6e–i and Extended Data Fig. 10). The EthoLoop system allowed us to induce the specific foraging patterns and thus ensure that the animals either cover large parts of the lattice maze (Fig. 6a,c) or

create multiple reproducible paths across a given location (Fig. 6e). These recordings are to our knowledge among the first examples of 3D place cell-like activity recorded in freely roaming primates and illustrate the vast potential for future experiments when combining the EthoLoop system with wireless electrophysiology.

## Discussion

EthoLoop is a video tracking framework that allows following animal behavior in naturalistic environments. More importantly, it can actively shape behaviors via closed-loop interactions. Such active interaction with the tracked subjects opens possibilities for many types of experiment ranging from automated reinforcement of innate sequences to the learning of complex cognitive tasks.

Furthermore, its scalability as well as its wireless connectivity to battery-powered optogenetic stimulation and electrophysiological recording devices make it a powerful tool for characterizing complex behaviors in large-scale and naturalistic settings. The possibility of using batteries also as a power source for cameras and RECO boxes furthermore opens the door to study the behavior of wild animals in their natural habitats. Adding more tracking and close-up cameras will be necessary, however, if foliage or branches

are too obstructive or if the behavior of multiple animals needs to be characterized simultaneously at high resolution.

We have shown that synchronized optogenetic manipulations and electrophysiological recordings during free navigation are, in principle, feasible. Similar to the pioneering work with freely flying bats<sup>25,26,49</sup> we have chosen data loggers as recording devices. For future closed-loop experiments involving triggering events by neuronal activity, actively transmitting recording systems will be necessary.

Our experiments illustrate that the EthoLoop system is ideally suited to studying behaviors such as foraging<sup>35</sup>. Foraging provides a unique setting where not only the limits of multi-sensory integration, sensory-guided motor control, high level cognition or 3D spatial navigation<sup>25,26,39,49</sup> can be probed in a reproducible manner, but it can also become a powerful tool for dissecting neuronal dynamics underlying decision making and economic choice<sup>35</sup>.

The overall principles of the EthoLoop framework (close-up view, online classification, interaction with RECO boxes) are also applicable to other real-time tracking systems<sup>11,15–18,23,29</sup> and might thus be combined with already existing hardware (as long as the relative position can be updated fast enough). Finally, the recent emergence of markerless methods for tracking multiple subjects<sup>19</sup> or for behavioral analysis going beyond basic postures<sup>43,44,50</sup> can also be combined with this framework. Technically, using wireless sensors, actuators and automated analysis can be considered a particular extension of the ‘Internet of Things’<sup>51</sup>. Hence, hardware and software development from the Internet of Things field will most likely inspire the design of improved devices and enable better behavioral models and analysis methods.

### Online content

Any methods, additional references, Nature Research reporting summaries, source data, extended data, supplementary information, acknowledgements, peer review information; details of author contributions and competing interests; and statements of data and code availability are available at <https://doi.org/10.1038/s41592-020-0961-2>.

Received: 16 September 2019; Accepted: 24 August 2020;  
Published online: 29 September 2020

### References

1. Tinbergen, N *The Study of Instinct* 195 (Clarendon Press, 1951).
2. Krakauer, J. W., Ghazanfar, A. A., Gomez-Marín, A., MacIver, M. A. & Poeppel, D. Neuroscience needs behavior: correcting a reductionist bias. *Neuron* **93**, 480–490 (2017).
3. Huber, F. & Markl, H. (eds) *Neuroethology and Behavioral Physiology: Roots and Growing Points* (Springer, 1983).
4. Hölscher, C., Schnee, A., Dahmen, H., Setia, L. & Mallot, H. A. Rats are able to navigate in virtual environments. *J. Exp. Biol.* **208**, 561–569 (2005).
5. Dombeck, D. A., Harvey, C. D., Tian, L., Looger, L. L. & Tank, D. W. Functional imaging of hippocampal place cells at cellular resolution during virtual navigation. *Nat. Neurosci.* **13**, 1433–1440 (2010).
6. Keller, G. B., Bonhoeffer, T. & Hübener, M. Sensorimotor mismatch signals in primary visual cortex of the behaving mouse. *Neuron* **74**, 809–815 (2012).
7. Harvey, C. D., Collman, F., Dombeck, D. A. & Tank, D. W. Intracellular dynamics of hippocampal place cells during virtual navigation. *Nature* **461**, 941–946 (2009).
8. Minderer, M., Harvey, C. D., Donato, F. & Moser, E. I. Neuroscience: virtual reality explored. *Nature* **533**, 324–325 (2016).
9. Aghajani, Z. M. et al. Impaired spatial selectivity and intact phase precession in two-dimensional virtual reality. *Nat. Neurosci.* **18**, 121–128 (2015).
10. Aronov, D. & Tank, D. W. Engagement of neural circuits underlying 2D spatial navigation in a rodent virtual reality system. *Neuron* **84**, 442–456 (2014).
11. Stowers, J. R. et al. Virtual reality for freely moving animals. *Nat. Methods* **14**, 995–1002 (2017).
12. Dombeck, D. A., Khabbaz, A. N., Collman, F., Adelman, T. L. & Tank, D. W. Imaging large-scale neural activity with cellular resolution in awake, mobile mice. *Neuron* **56**, 43–57 (2007).

13. Sofroniew, N. J., Cohen, J. D., Lee, A. K. & Svoboda, K. Natural whisker-guided behavior by head-fixed mice in tactile virtual reality. *J. Neurosci.* **34**, 9537–9550 (2014).
14. Radvansky, B. A. & Dombeck, D. A. An olfactory virtual reality system for mice. *Nat. Commun.* **9**, 839 (2018).
15. Fry, S. N., Bichsel, M., Müller, P. & Robert, D. Tracking of flying insects using pan-tilt cameras. *J. Neurosci. Methods* **101**, 59–67 (2000).
16. Fry, S. N., Rohrseitz, N., Straw, A. D. & Dickinson, M. H. TrackFly: virtual reality for a behavioral system analysis in free-flying fruit flies. *J. Neurosci. Methods* **171**, 110–117 (2008).
17. Straw, A. D., Branson, K., Neumann, T. R. & Dickinson, M. H. Multi-camera real-time three-dimensional tracking of multiple flying animals. *J. R. Soc. Interface* **8**, 395–409 (2011).
18. Bath, D. E. et al. FlyMAD: rapid thermogenetic control of neuronal activity in freely walking *Drosophila*. *Nat. Methods* **11**, 756–762 (2014).
19. Romero-Ferrero, F., Bergomi, M. G., Hinz, R. C., Heras, F. J. H. & de Polavieja, G. G. idtracker.ai: tracking all individuals in small or large collectives of unmarked animals. *Nat. Methods* **16**, 179–182 (2019).
20. Weissbrod, A. et al. Automated long-term tracking and social behavioural phenotyping of animal colonies within a semi-natural environment. *Nat. Commun.* **4**, 2018 (2013).
21. de Chaumont, F. et al. Computerized video analysis of social interactions in mice. *Nat. Methods* **9**, 410–417 (2012).
22. Matsumoto, J. et al. A 3D-video-based computerized analysis of social and sexual interactions in rats. *PLoS ONE* **8**, e78460 (2013).
23. Ballesta, S., Reymond, G., Pozzobon, M. & Duhamel, J.-R. A real-time 3D video tracking system for monitoring primate groups. *J. Neurosci. Methods* **234**, 147–152 (2014).
24. Khan, Z., Herman, R. A., Wallen, K. & Balch, T. An outdoor 3-D visual tracking system for the study of spatial navigation and memory in rhesus monkeys. *Behav. Res. Methods* **37**, 453–463 (2005).
25. Tsoar, A. et al. Large-scale navigational map in a mammal. *Proc. Natl Acad. Sci. USA* **108**, E718–E724 (2011).
26. Yartsev, M. M. & Ulanovsky, N. Representation of three-dimensional space in the hippocampus of flying bats. *Science* **340**, 367–372 (2013).
27. Hong, W. et al. Automated measurement of mouse social behaviors using depth sensing, video tracking, and machine learning. *Proc. Natl Acad. Sci. USA* **112**, E5351–E5360 (2015).
28. Shemesh, Y. et al. Correction: high-order social interactions in groups of mice. *eLife* **3**, e03602 (2014).
29. De Chaumont, F. et al. Real-time analysis of the behaviour of groups of mice via a depth-sensing camera and machine learning. *Nat. Biomed. Eng.* **3**, 930–942 (2019).
30. Pérez-Escudero, A., Vicente-Page, J., Hinz, R. C., Arganda, S. & de Polavieja, G. G. idTracker: tracking individuals in a group by automatic identification of unmarked animals. *Nat. Methods* **11**, 743–748 (2014).
31. Strauss, R., Schuster, S. & Götz, K. G. Processing of artificial visual feedback in the walking fruit fly *Drosophila melanogaster*. *J. Exp. Biol.* **200**, 1281–1296 (1997).
32. Del Grosso, N. A., Graboski, J. J., Chen, W., Blanco-Hernández, E. & Sirota, A. Virtual reality system for freely-moving rodents. Preprint at *bioRxiv* <https://doi.org/10.1101/161232> (2017).
33. Buccino, A. P. et al. Open source modules for tracking animal behavior and closed-loop stimulation based on Open Ephys and Bonsai. *J. Neural Eng.* **15**, 055002 (2018).
34. Lim, J. & Celikel, T. Real-time contextual feedback for close-loop control of navigation. *J. Neural Eng.* **16**, <https://iopscience.iop.org/article/10.1088/1741-2552/ab2ffa> (2019).
35. Stephens, D. W., Brown, J. S. & Ydenberg, R. C. *Foraging: Behavior and Ecology* (University of Chicago Press, 2008).
36. Krebs, J. R. & Davies, N. B. *Behavioural Ecology: An Evolutionary Approach* (John Wiley & Sons, 2009).
37. Silcox, M. T. & López-Torres, S. Major questions in the study of primate origins. *Ann. Rev. Earth Planet. Sci.* **45**, 113–137 (2017).
38. Grobety, M.-C. & Schenck, F. Spatial learning in a three-dimensional maze. *Anim. Behav.* **43**, 1011–1020 (1992).
39. Jovalekic, A. et al. Horizontal biases in rats’ use of three-dimensional space. *Behav. Brain Res.* **222**, 279–288 (2011).
40. Skinner, B. F. *The Behaviour of Organisms* (D. Appleton and Co., 1938).
41. Breland, K. & Breland, M. A field of applied animal psychology. *Am. Psychol.* **6**, 202–204 (1951).
42. Pryor, K. *Don’t Shoot the Dog! The New Art of Teaching and Training* revised edn (Bantam Books, 1999).
43. Wiltshchko, A. B. et al. Mapping sub-second structure in mouse behavior. *Neuron* **88**, 1121–1135 (2015).
44. Mathis, A. et al. DeepLabCut: markerless pose estimation of user-defined body parts with deep learning. *Nat. Neurosci.* **21**, 1281–1289 (2018).
45. Tsai, H.-C. et al. Phasic firing in dopaminergic neurons is sufficient for behavioral conditioning. *Science* **324**, 1080–1084 (2009).

46. O'Keefe, J. & Nadel, L. *The Hippocampus as a Cognitive Map* (Clarendon Press, 1978).
47. Wilson, M. A. & McNaughton, B. L. Dynamics of the hippocampal ensemble code for space. *Science* **261**, 1055–1058 (1993).
48. Ulanovsky, N. Neuroscience: how is three-dimensional space encoded in the brain? *Curr. Biol.* **21**, R886–R888 (2011).
49. Finkelstein, A. et al. Three-dimensional head-direction coding in the bat brain. *Nature* **517**, 159–164 (2015).
50. Pereira, T. D. et al. Fast animal pose estimation using deep neural networks. *Nat. Methods* **16**, 117–125 (2019).
51. Gershenfeld, N., Krikorian, R. & Cohen, D. The internet of things. *Sci. Am.* **291**, 76–81 (2004).

**Publisher's note** Springer Nature remains neutral with regard to jurisdictional claims in published maps and institutional affiliations.

© The Author(s), under exclusive licence to Springer Nature America, Inc. 2020

## Methods

**Hardware. Infrared real-time video tracking system.** Four to six high-speed USB3 cameras (MQ013CG-ON, XIMEA) were used for tracking. The cameras were equipped with wide-angle lenses (NAVITAR, f4.5 mm, 1.4) and infrared long-pass filters (FGL 665, Thorlabs, or 832 nm Bandpass Filter, Edmund Optics) to eliminate light in the visible range. Each camera was connected via a USB connection to an independent GPU-based microprocessor (Jetson TK1 or TX2, NVIDIA, running Linux4Tegra). The microprocessors communicated via ethernet (TK1) or WIFI (TX2) with a central host machine (Optiplex 9020, Intel Core i7, Dell, running Linux Ubuntu 16.04 LTS) using a wireless router (RT-AC88U, ASUS). An additional USB3 camera (MQCG-ON, XIMEA) was connected to the host machine for continuous monitoring of the experimental room. Cameras and GPU units could either be powered by external power supplies or with 12-V car batteries (44 ampere hours (Ah), Miocar). When tracking with passive reflective markers (see below), the tracking cameras were equipped with a custom illumination ring of 20 LEDs with wavelength of 850 nm (TSHG6400, Vishay Semiconductors).

**Portable passive markers.** Passive reflective markers consisted either of retro-reflective spheres (14 mm, Optitrack), or were custom made with flexible retro-reflective transfer foil (Seritec) in the shape of a neck collar.

**Portable active markers.** To track multiple animals simultaneously, infrared LED light sources of different wavelengths were used (SMC660, SMC750, SMC830, Roithner). These wavelengths are beyond the visible spectrum of mouse lemurs, and therefore do not interfere with their photoperiod<sup>52</sup>. To make the light spot visible from wide angles, the light was diffused using 6-mm opal glass diffuser (no. 46163, Edmund Optics). To hold the light sources on the top of the neck of the mouse lemurs, the animal carried a custom collar around its neck with a miniature rechargeable battery attached below (Lipo 3.7 V, 140 mAh, LP451430). The total weight of the neck collar including the battery was <4 g.

**Close-up imaging system.** The close-up imaging system consisted of a near-infrared enhanced CMOS camera (MQ013RG-E2, XIMEA), mounted on the center of a custom designed two-axis gimbal, actuated by two high-power digital servo motors (MX-64, Dynamixel). The camera was equipped with a high-resolution lens (Xenon, 2.0/50 mm, Schneider or a Rodagon, 4.0/80 mm, Rodenstock) and an electrically tunable lens (EL-16-40-TC, Optotune). According to the manufacturer's specification, the response time of this lens is ~7 ms for a square pulse of 0–250 mA. The central host machine was communicating in real time with the servos via a serial port protocol (USB2Dynamixel). The focus of the electrically tunable lens was simultaneously controlled via ethernet protocol and a dedicated controller (TR-CL180, GIGE Vision). For recordings with mouse lemurs, the close-up camera system was protected with a transparent Plexiglas half-dome (40 cm, L acrylic shop).

**Target illumination system.** To illuminate animals for the close-up imaging system, a high-power infrared LED (H2W5, 850 nm) and reflector (10158, Roithner) or a narrow beam LED (ELJ-650-637, Roithner) was mounted in parallel with the close-up imaging system. Alternatively, the target illumination system was mounted separately on a second two-axis gimbal powered by two digital servo motors (MX-64, Dynamixel) and were controlled via a serial port (USB2, Dynamixel).

**Remote-controlled stimulus and reward boxes (RECO box).** The RECO box is based on a low-power WiFi-enabled microprocessor (MKR-1000, Arduino) powered by a lithium ion battery (3.7 V, 7.8 Ah, Pi-shop) and interacted via a wireless user datagram protocol (UDP) protocol with the host computer. The following parts were packed inside a waterproof plastic box (100 × 100 × 90 mm<sup>3</sup>, RND 455-00123, RND Component) and held in place by a custom 3D-printed insert. An optical lick port with a single lick spout was mounted on the top cover of the plastic box. Auditory stimuli (9 kHz tone) were generated by a piezo speaker (KPEG-126, Kingstate), and loud clicks by a solenoid valve (ZHO-0420L/S, Adafruit) tapping against the plastic side wall. A green LED (565 nm) was activated as a visual cue, whereas an infrared LED (750 nm) was used to localize the position of the RECO box by the tracking system. The liquid reward was stored in a 20-ml glass bottle and delivered to the lick port by a peristaltic pump (OINA). The stepper motor (QSH-2818, Trinamic) of the pump was controlled via a low-voltage stepper driver (DRV8833, Adafruit).

**Software.** EthoLoop software was written in C++ using OpenCV and CUDA libraries. Real-time 3D visualization of data points was done by gnuplot ([www.gnuplot.info](http://www.gnuplot.info)). Dynamixel SDK libraries for C++ were used to control the servos of the close-up system ([www.github.com/ROBOTIS-GIT](http://www.github.com/ROBOTIS-GIT)). RECO boxes were programmed with Arduino software (IDE).

**Animals. Mouse lemurs.** Four adult gray mouse lemurs (*M. murinus*) were used for this study (Supplementary Table 1). All mouse lemurs were born and raised in the 'Mouse Lemur Platform' (authorization number E-91-114-1) of the Museum of Natural History in Brunoy, France, under the supervision of the staff of the UMR CNRS-MNHN 7179-MECADEV. The procedures are in accordance with European

animal welfare regulations and were reviewed by the local ethics committee (Comité d'éthique en expérimentation animale no. 68) in Brunoy, France, by the ethics committee of the University of Geneva, Switzerland, and authorized by the French 'Ministère de l'éducation nationale de l'enseignement supérieur et de la recherche'. All experiments involving mouse lemurs were carried out in Brunoy, France. The behavioral experiments were restricted to the awake period of their circadian cycle (dark). Animals were housed socially (2 or 3 per cage) in cages (50 × 60 × 70 cm<sup>3</sup>) with wooden branches, leaves and wooden nest boxes. Temperature was kept between 24 and 26 °C, relative humidity was approximately 55% and artificial light cycle was 14 h on per day (winter period<sup>53</sup>). Animals had free access to water and food consisting of pieces of fresh apples and bananas, insect larvae and a liquid food mix (condensed milk, egg yolk, cottage cheese, spice bread, baby milk powder diluted in water and homogenized in a kitchen mixer).

**Mouse lemur experimental room.** The experimental room for the mouse lemurs (1.7 × 2 × 3.1 m<sup>3</sup>) was covered with matt black paint to avoid reflections of the infrared light sources. The mouse lemurs were allowed to freely roam in the room. The lighting condition of the room was controlled in respect to the animals' day/night cycles and the temperature was maintained at 25 °C. For initial tracking sessions and social interactions, the experimental room was equipped with tree branches, food platforms and wooden nest boxes (one per animal) (Fig. 1). For closed-loop experiments, the room was equipped with a custom-made 3D lattice maze inspired by ref. <sup>38</sup>. The sides of the lattice cubes (500 mm) were built out of round wood and ranged in diameter from 4 to 24 mm.

During the days of the behavioral experiments, food availability was limited to the behavioral sessions to increase motivation. The weight and overall behavior of the animals was monitored twice a day. The animals were habituated to the RECO boxes in their home cages, where liquid food (described above) was available at random moments (on average every minute). Reward availability was indicated with an auditory cue (9 kHz tone approximately every minute) and delivery was triggered if a lick followed within 30 s. The conditioning experiments were usually stopped after the animals performed ~120 trials (reward size, ~0.02 ml of liquid food mix) or when they showed a drop in motivation (ignoring the task for >5 min). Additional food was supplemented after the experiment to keep the weight stable.

**Mice.** Ten laboratory mice (C57Bl/6J, Jackson Laboratory) were used for the conditioning experiments (six mice for open-field and four mice for the 3D arena). All experiments with mice were carried out in Geneva, Switzerland, and reviewed by the local ethics committee and authorities of the Geneva canton. Animal cages were kept in the animal facility (temperature of 21 °C and humidity of 50%) and each cage was housing a maximum of five mice. During behavioral experiments, access to water was restricted to the behavioral session and limited to 1 ml per day<sup>54</sup>. Mice were monitored daily and additional water was provided if necessary. All the experiments were carried out in the dark period of their circadian cycle. The conditioning experiments were stopped after the animals performed ~100 trials (reward size, ~0.01 ml of water) or when they showed a drop in motivation. Additional water was supplemented after the experiment to keep the weight stable.

**Surgery for optogenetic stimulation.** For optogenetic experiments using DAT-iresCre mice (Slc6a3<sup>tm1.1(cre)Bkmn</sup>/J), called DAT-Cre in the manuscript), the animals were injected with rAAV5-Efla-DIO-hChR2(H134R)-eYFP (Addgene) in the VTA. Mice were anesthetized with a mixture of oxygen (1 l min<sup>-1</sup>) and isoflurane 3% (Baxter) and placed in a stereotaxic frame (Angle One, Leica). The skin was shaved, locally anesthetized with 40–50 µl lidocaine 0.5% and disinfected. The animals were placed in a stereotaxic frame and bilateral craniotomy was made over the VTA at the following stereotaxic coordinates: lateral ±0.5 mm, posterior –3.2 mm, depth –4.20 ± 0.05 mm from Bregma. A total volume of 500 nl was injected. The virus expressed for 3–4 weeks and mice were subsequently implanted with optic fibers (200 µm, Thorlabs, for the tethered experiments) or with a custom fiber-coupled (400 µm, FP400URT, Thorlabs) miniature LED (OV55MBBCR4, TTI) wired to a miniature connector (Millmax). To deliver the light via the optical fibers to the DA neurons, the VTA was targeted with a 10° angle at the following coordinates: lateral ±0.9 mm, posterior –3.2 mm, depth –3.95 ± 0.05 mm from Bregma. The fibers were fixed on the skull with dental acrylic. The placement of the optical fiber and the range of virus infection were confirmed post hoc immunostaining (Supplementary Fig. 7). We used a primary antibody against Tyrosine Hydroxylase (TH, 1/500 dilution) enzyme, followed by secondary antibody donkey anti rabbit alexa fluor 555 (1/500 dilution).

**Experimental procedures. Optical tracking and 3D reconstruction.** The local processing of the images of the tracking cameras on the NVIDIA Jetson TX2 consisted of several steps carried out in multiple parallel threads:

- (1) Adjusting camera parameters: XIMEA camera parameters such as exposure, gain, downsampling, image format and sensor's bit depth were initially adjusted. Setting the exposure level to <1.2 ms, downsampling by 2 × 2 (pixel skipping method, final resolution is 640 × 512), retrieving frames in RAW 8-bit format and enabling ZERO-ROT mode allowed us to achieve a maximum performance of ~780 frames per second. The communication

with the camera for grabbing and retrieving frames is done in parallel central processing units threads to minimize latency and maximize tracking speed (Supplementary Fig. 2).

- (2) Custom color demosaicing: to spectrally separate the hues of different infrared LEDs, we developed a custom demosaicing process using OpenCV and CUDA libraries (Supplementary Fig. 3). The ratio of the different color sensitivity curves (specified by the camera chip, OnSemi PYTHON 1300) were used as a lookup table to produce the false colors. This process resulted in a mapping of 660 nm to visible red, 750 nm to orange and 810 nm to blue.
- (3) 2D target position estimation: the different colors were thresholded by pre-specified values for hue, saturation and value, and the centroid of the target image blob was estimated by a projection barycenter algorithm<sup>23</sup>.
- (4) Communication with the central host computer: The 2D position of the centroids determined by each tracking camera per GPU was sent to the central host computer via the network using the UDP protocol.

The triangulation of the simultaneously received 2D target information was performed in the central host computer by using a projective-invariant method, whereby the 3D target position was chosen to minimize the quadratic distance between its computed 2D projections and the measured 2D targets<sup>23,55,56</sup>. Correct triangulation of a 3D target is theoretically possible when seen by at least two cameras. However, robustness to image noise and visual occlusions increases with the number of available cameras in the setup. In practice, 4–6 cameras were found to be sufficient to cover a 10-m<sup>3</sup> room with branches. The actual spatial resolution of the tracking does not depend on the number of cameras, but is defined primarily by the resolution and optics of the cameras, their position relative to the targets and the quality of the spatial calibration of the system.

**Calibration of the 3D tracking system.** An initial geometric calibration phase of the system was performed by manually moving a single LED target over the entire measurement space. The recorded 2D projections were first used to estimate the 3D position of the first two cameras using the five-point algorithm<sup>57</sup> and RANSAC estimation methods implemented in OpenCV. The 3D target position was then reconstructed using the above-mentioned triangulation algorithm. The position of each additional camera was then estimated with OpenCV's implementation of the perspective-n-point algorithm<sup>57</sup> using the 3D triangulated points. The resulting estimated position of all cameras was then refined, using a bundle adjustment method based on a sparse Levenberg–Marquardt optimization procedure, as implemented in the SSBA software library<sup>58</sup>. As usual for 3D reconstruction algorithms, a final calibration was done to align and scale the resulting data to real-world coordinates, using a reference box object of known dimensions placed in the measurement space.

To illustrate the ability of the EthoLoop system to track fast-moving objects in large-scale environments (>100 m<sup>3</sup>), a commercial drone (Tello by DJI, Ryze Tech) was used (Supplementary Fig. 1 and Supplementary Video 4). The drone was steered around the plants in the room under manual control.

**Calibration of the close-up system.** The liquid lens autofocus of the close-up system was calibrated manually by placing an object at more than four locations in front of the camera while adjusting the necessary current to achieve perfect focus. These settings were used to fit a current–distance curve for the tunable lens.

The spatial parameters of the close-up system were calibrated using a semi-automated procedure. An infrared LED was placed at a random location and the close-up system started to scan the environment by spinning over the axes of both servos while capturing RAW images and thresholding in a specific range of the infrared LED (60 frames per second at full resolution of 1,024 × 1,280). This scanning stopped as soon as the LED was detected by the camera. At this point the close-up system started to move in steps of 0.087° (in both axes of servos) every 500 ms to locate the LED at the center of the frame. The exact 3D position of the LED calculated by the host machine ( $x, y, z$ ), and the final angle of both servos (azimuth  $\alpha$ , elevation  $\beta$ ) were saved. The procedure was repeated several times, and the location  $x_c, y_c, z_c$  of the close-up camera was computed by solving the system of equations:

$$\tan(\beta) = \frac{x - x_c}{y - y_c}$$

$$\tan(\alpha) = \frac{z - z_c}{\sqrt{(x - x_c)^2 + (y - y_c)^2}}$$

Finally, the angles of the servo motors were trigonometrically calculated by the host machine based on the spatial position of the target and respective location of the close-up camera and communicated via the serial port. In parallel, the distance from the target to the close-up camera was calculated and sent via ethernet to the GIGE Vision controller to focus the tunable lens on the object using the above-mentioned calibration curve.

**Evaluation of EthoLoop system performance. 3D tracking and real-time behavior analysis latency.** The latency for 3D tracking was defined by the time between the appearance of a target and the 3D reconstruction. To measure this latency, a microcontroller (Arduino Mega) with an infrared LED (750 nm) was connected

to the host PC and placed in the tracking area. The host program was modified to command the microcontroller to illuminate the LED at repeated intervals, and to measure the time elapsed until reception of the corresponding 3D position measurement of the LED. This procedure was repeated 1,000 times at random intervals. The average value gives a high estimate of the actual latency of the system, considering the added latency of commanding the microcontroller to turn on the infrared LED (Fig. 1b and Supplementary Fig. 2).

The latency of the real-time behavioral analysis was defined by the time evolving between turning on a LED in the field of view of the close-up system, its correct identification by the DeepLabCut software (with pretrained network) and the final receipt by the host computer of the 2D coordinates (position of the LED within the close-up image) and likelihoods of correct identification (Fig. 1b). The procedure for turning on the LED and calculating the time difference was identical to the one described above (tracking latency).

**RECO box communication latency.** The latency to communicate with a RECO box was defined as the time between sending a command (by the host machine) and the reception of that command by the RECO box. For this purpose, 1,000 commands at random intervals were sent to a RECO box to turn on the infrared LED. Once the LED was turned on, the cameras sent the 2D coordinate to the host machine for 3D reconstruction. The time difference between sending of the command and the reconstruction of the LED's 3D position was calculated by the host machine. These measurements were then subtracted from the mean value of 3D reconstruction latency (single target, Fig. 1b, light-red histogram) to obtain communication latency with the RECO box (Fig. 1b, blue histogram).

**Rate of 3D tracking and real-time behavior analysis.** The interval for 3D tracking was defined as the time between two subsequent 3D reconstructions. We recorded the time between reception of subsequent 3D data measurements, repeated over a 60-s tracking session with one, two and three targets (Fig. 1c). Real-time behavior analysis interval was defined as the time between subsequent detection and labeling of body parts. For this purpose, a moving doll was placed in front of the close-up camera. The body parts were labeled with the real-time DeepLabCut (using the pretrained network) and the time between subsequent labeled frames were recorded over 60 s.

**Positional accuracy.** An infrared LED was placed on the edge of a circular turntable (Thorens, TD160) spinning at 33 and 45 rounds per minute. The measurement was carried out in our large >10-m<sup>3</sup> tracking arena. The tracking cameras were therefore >2 m from the target. In this setting (resolution of 640 × 512) one pixel covered roughly 7 × 9 mm<sup>2</sup>. The LED light source consisted of an actual tracking target including the 5-mm flat glass diffuser. The difference between the actual turntable radius and the radius of the circle of the trajectory tracked by the EthoLoop system was reported as the positional error estimated for the tracking system. The tracking error measured (<8 mm) was in the range of the actual target dimensions (Supplementary Fig. 1i).

**Real-time detection of behaviors.** To detect specific behaviors (rearing, Fig. 4) in the stream of close-up images the following steps were carried out:

- (1) Real-time classification of body parts. The close-up images were labeled on-the-fly using a custom-programmed real-time version of DeepLabCut software<sup>44</sup>. Close-up images were initially streamed at full resolution (1,280 × 1,024) to a computer (Dell, Optiplex 990-Intel Core i7, equipped with a GeForce GTX 1080 Ti graphics card), resized to 640 × 512 and saved using OpenCV functions. In parallel, the images were further resized to 320 × 256 (to reduce latency and increase speed) and labeled by the DeepLabCut software. The deep neural network used for the classification was trained with hand-annotated images (<400 frames) from previous recordings carried out under identical lighting conditions. The tracked body parts included: eyes, nose, forelimbs, hind limbs and the base of the tail.
- (2) Once the body parts were labeled in an image, the frame number, the coordinates of the body parts and their likelihood were saved in a single string. This string was transmitted in real-time as a UDP packet to the main host machine. A special thread in a multithreaded tracking program was assigned to receive and parse the string.
- (3) Real-time detection of posture: the spatial relationship of individual real-time labeled body parts was used to define a given posture (Fig. 4a). Specifically, rearing was detected if one of the following conditions were met:
  - (a) Difference between the nose and hind limbs on the  $y$  axis was more than 200 pixels and both lines connecting the nose to the hind limbs made an angle of less than 20° with the  $y$  axis.
  - (b) Difference between one of the eyes and hind limbs in  $y$  axis was more than 200 pixels and both lines connecting one eye to the hind limbs made an angle of less than 20° with the  $y$  axis.
- (a) **Spatial constraints:** in the experiments where the posture had to be carried out at a specific location (Fig. 4b–g), a predefined virtual sphere (200 mm) was placed at a chosen location. The reward was only triggered when the posture was detected within the sphere.

**Real-time control of RECO box.** The RECO box was controlled via a Wifi Arduino. After establishing the connection to the central host computer via the wireless network, the Arduino was waiting for incoming UDP packets. Each received packet was decoded and the corresponding function (reward, noise and so on) was activated. The delay of this process was around ~2.5 ms (Fig. 1b, blue histogram). The RECO boxes were attached to different branches of the lattice maze, and their position was determined by the tracking system using a built-in infrared LED (750 nm). RECO boxes indicated the availability of a reward as a 1-s long sound at 9 kHz repeated at 0.5 Hz. The actual reward was delivered on arrival of the animal within 10 cm of the RECO box.

**Close-loop behavioral experiments. Mouse lemur foraging.** Four to five RECO boxes were distributed at different locations inside the 3D lattice maze (Fig. 2 and Extended Data Fig. 1). Their activation was set in either predefined or random sequences. In experiments with defined sequences, a subsequent RECO box was activated when the animal reached a distance of 20 cm from the previous one. In experiments with random activation, a different RECO box was chosen at random to be activated after a variable delay (0 to 60 s) as soon as the animal reached a distance of 1 m to the previous activated box. In both cases, the animal was given 40 s to collect the reward from the active feeder.

**Mouse lemur 3D place conditioning.** On the entrance of the animal to a 15-cm radius sphere surrounding the selected location (place) a RECO box was activated. The animal was given 20 s to collect the reward from the active RECO box.

**Mouse lemur behavioral conditioning (rearing).** On executing the defined behavior (rearing) at a specified location a RECO box was activated. The animal was given 30 s to collect the reward from the active RECO box.

**Mouse place conditioning.** A RECO box was placed in an arena covered with tree branches (Fig. 3a–d and Extended Data Figs. 2a and 5a) or in an open-field (Extended Data Fig. 3a). The RECO box was localized by the tracking system with an infrared (750 nm) LED. The activation of a feeder was signaled by a click sound, and liquid reward (0.01 ml of 0.1% sucrose in water) was provided on arrival near the RECO box. Initially, the mice were habituated to the RECO box, by providing rewards at random intervals.

**Mouse behavioral conditioning (rearing).** To detect rearing on hind limbs, a threshold on the *z* axis was defined for mice performing the task in a simple 2D environment where they had to rear on an elevated platform (Extended Data Fig. 6). For mice performing the task in naturalistic 3D environment rearing was the same as described in Fig. 4a. Once rearing was detected, a RECO box was activated and the mouse had 10 s to collect the reward. If mice did not spontaneously rear on the defined location, a small bell was suspended by a string from the ceiling (pointing toward the rearing location). Mice rapidly started rearing to explore the new object. The bell was removed after the tenth rearing.

**Wireless mouse optogenetic place and behavioral conditioning.** The wireless optogenetic activation of the VTA in mice in the naturalistic arena was carried out using a portable, remote-controlled stimulation device (Supplementary Fig. 6). The unit was composed of the electronic circuit board (16 × 20 mm<sup>2</sup>) taken from a miniature remote-controlled car (Nano Racer, Carson). The two leads originally powering the DC-motor were connected to the head mounted LED-fiber assembly targeting the VTA (see details above). The unit was powered by a rechargeable 3.7-V lithium ion coin battery (CP 1254 A3, Varta) and attached around the neck of the mouse for the duration of the experiment. The optogenetic stimulation consisted of 8 × 20-ms pulses repeated at 10 Hz. The power output at the end of the fiber was ~5 mW. To control the timing of the pulses, the original remote control was connected to a WiFi-enabled microprocessor (MKR-1000, Arduino) circuit that received the commands wirelessly via a UDP protocol from the host computer.

**Fiber-based mouse optogenetic place and behavioral conditioning.** For the optogenetic conditioning experiments on an open-field arena the mice were connected to a flexible optical fiber (FC/PC 200- $\mu$ m fiber, 2 m, ThorLabs) hanging from the ceiling. The light source was a fiber pig-tailed to a blue laser (473 nm, 50 mW, OBIS, Coherent) controlled via a WiFi-enabled microprocessor (MKR-1000, Arduino) circuit. The maximal power of the fiber output was 20 mW (measured in continuous mode using a power meter (Field Mate, Coherent)). Stimulation consisted of eight pulses of 4-ms duration, repeated at 30 Hz (output ranging from 8–12 mW). During the place conditioning experiment, mice were optogenetically stimulated on entering the defined location (20–25-cm radius). The optogenetic stimulation continued for a maximum of eight consecutive bursts if the mouse remained inside the target area. The place conditioning experiments were stopped after the animals received ~900 burst stimulations. During the behavioral conditioning experiments, mice were optogenetically stimulated on executing the defined behavior (rearing) detected with the real-time DeepLabCut software. The experiments were stopped after the animals received ~450 burst stimulations.

**Mouse lemur electrophysiological recordings. Electrodes and drive.**

Custom-made tetrode wire bundles were produced by twisting and heating four individual 12.7- $\mu$ m Tetrode Nickel-Chrome Wires covered with Easy Bond XTC (Sandvik). Tetrodes were inserted and glued into polyamide tubing (0.14-mm diameter) inside the moving part of a custom designed 3D-printed microdrive. The electrode tips were cut and gold-plated with Sifco 5355 (mixed 1:1 with polyethylene glycol solution and carbon nanotubes, Neuralynx) to lower the impedance. The free end of the tetrode was connected to a miniature connector (Omnetics) via a custom designed interface board. The tetrode array was lowered by turning the M1 screw of the microdrive.

**Electrophysiology setup.** Extracellular recordings were performed using custom wireless data acquisition logger hardware (Spike Gadgets) together with Trodes software (Spike Gadgets). Acquired data were sampled at 20 kHz and broad-band filtered between 0.1 Hz and 10 kHz. Data were further filtered post hoc between 600 Hz and 6 kHz for spike extraction. Spike sorting was carried out with semi-automated SpikingCircus and Kilosort algorithms.

**Surgery.** One day before the surgery the animal was administered antibiotics (Ceftriaxon, 50  $\mu$ g g<sup>-1</sup>, intramuscular) and housed individually without food. Surgeries were carried out under aseptic conditions. Anesthesia was induced in a small Plexiglas box with a continuous flow of a mixture of oxygen with 5% Isoflurane (Vetflurane, Virbac). After induction, the animal was removed from the box and placed in a custom designed stereotaxic frame. Eyes were protected with Lacryvisc cream and whiskers and tongue were covered with Vaseline. Isoflurane was decreased (2.5–1%) while breathing rate and toe pinch reflexes were continuously monitored. The following drugs were administered: buprenorphine (3  $\mu$ g g<sup>-1</sup>, subcutaneous), dexamethasone (0.8  $\mu$ g g<sup>-1</sup> intramuscular), ceftriaxon (50  $\mu$ g g<sup>-1</sup>, intramuscular), carprofen (22  $\mu$ g g<sup>-1</sup>, intramuscular) and rapidocaine (100–150  $\mu$ l, locally injected). The area of the surgical procedure was disinfected sequentially with 70% ethanol, betadine and chlorhexidine 1%. The cranial bones were exposed after skin incision. The periosteum was gently removed with cotton swabs and the skull surface was dried and roughened to improve glue bonding. The area for the craniotomy was located at 0.5 mm anterior and 3 mm lateral from the interaural midpoint and was chosen based on coordinates from atlases of the mouse lemur brain<sup>59–61</sup>. A thin layer of cyanoacrylate (5011, ERGO) was applied on the skull and holes for ground wires and craniotomy for electrodes were made using a dental drill. The microdrive was placed on the skull and fixed with dental acrylic (Lang Dental). The skin was closed with stitches and the animal was placed on a heating blanket for recovery. Animals were monitored daily and administered with buprenorphine (analgesic, 3  $\mu$ g g<sup>-1</sup>, subcutaneous) for the following week and antibiotics (ceftriaxon (50  $\mu$ g g<sup>-1</sup>, intramuscular) for a total of 9 d.

**Synchronization of electrophysiology and tracking.** To synchronize the 3D position from the tracking system and the electrophysiology recording, a signal was sent from the 3D tracking program to a Wifi Arduino (MKR-1000) via the UDP protocol. The timing of this signal was recorded in the tracking software. On arrival of the UDP packet at the Wifi Arduino, a digital pulse was sent to the main control unit of the electrophysiology acquisition system (Spike Gadgets) that synchronizes the recordings in the wireless head-stage via radio frequency pulses. The timings of these pulses were extracted offline and aligned with the 3D tracking.

**Post hoc data analysis.** All the position data, timing and signals (stimulations and rewards) were stored in a text file. All post data analysis was done in R using OpenGL libraries ([www.r-project.org](http://www.r-project.org)).

**Position data filtering.** Image artifacts produced by reflections can cause false detections in the 3D tracking system. These false detections appear as sudden jumps between the actual location of the LED and the reflecting surface. To correct for these artifacts:

- Points that appeared outside the tracking boundary were excluded.
- Sudden jumps (speed > 5 m s<sup>-1</sup>) inside the tracking space were excluded and the trajectories interpolated.
- Finally, the tracking data was smoothed over all three axes using locally weighted regression (LOWESS function in R).

From the filtered position data, velocity and acceleration on each axis at each time point was computed using a moving average over a 60-ms sliding window.

**Movement categorization (ethograms).** Five behavioral types were automatically extracted from the animal's movements using the following mutually exclusive rules:

- 'Short quiet': velocity was below 20 cm s<sup>-1</sup> for less than 2 s.
- 'Long quiet': velocity was below 20 cm s<sup>-1</sup> for more than 2 s.
- 'Running': velocity was above 20 cm s<sup>-1</sup>, and cumulative displacement was over 10 cm otherwise categorized into the above 'quiet' states, depending on duration.

- ‘Jumping’: vertical acceleration equal to Earth’s gravity  $\pm 3 \text{ m s}^{-2}$ .
- ‘Falling’: vertical acceleration equal to Earth’s gravity  $\pm 3 \text{ m s}^{-2}$ , vertical displacement above 20 cm and the average horizontal velocity below  $50 \text{ cm s}^{-1}$ .

**Distance between animals during quiet states.** In tracking sessions with two animals, when both animals were at long quiet state, we computed the 3D distance between them and the amount of time they were at this distance. A histogram of distances binned at 20-cm intervals was plotted where the *y* axis represents the percentage of time spent at each interval.

**State transitions.** State transitions were defined by the event when a lemur changed from one state to another state. The distances between two mouse lemurs were calculated when one of them (lemur A) transitions from ‘long quiet’ to ‘running’ state ( $ST_{Q \rightarrow R}$ ) while the other animal was in ‘running’ state (lemur B). These distances were all binned in 200 mm intervals and the number of  $ST_{Q \rightarrow R}$  at each interval was calculated. At each distance interval, the probability of  $ST_{Q \rightarrow R}$  of lemur A on approaching lemur B was estimated as the number of  $ST_{Q \rightarrow R}$  divided by the total duration where distance between two animals was within the interval. To detect whether lemur B was approaching lemur A or moving away, the distance between them was also calculated 2 s before  $ST_{Q \rightarrow R}$  of lemur A.

**Analysis of closed-loop experiment with RECO box.** In the closed-loop experiments using RECO box (place and behavior conditioning in mice and mouse lemurs) the time until the animals activate the RECO box for the 50th time by entering conditioned location or executing the conditioned behavior was divided into three equal time bins termed beginning, middle and end.

**Analysis of the operant conditioning by optogenetic stimulation.** In the place conditioning sessions, the time until the first 50th entrance to the conditioned place and in the behavioral conditioning session the time until the first 100 rearings was divided into three equal time bins termed beginning, middle and end.

**3D reconstruction of lattice maze.** All 60 cubes connecting different branches of the lattice maze were numbered. Each branch in the lattice maze was defined by its thickness (4, 6, 12 and 24 mm) and the cube numbers connecting them to each other. The 3D coordinate of the first cube was manually measured in the real-world coordinates and set as the base for reconstructing the lattice maze in 3D. The 3D position of all cubes in the lattice maze was reconstructed relative to the base cube (considering the constant 3D distance between neighboring cubes). Finally, the whole lattice maze was reconstructed by adding the branches while knowing their connecting cubes.

**Analysis of electrophysiology.** Spike rates (for the color-coded trajectories in Fig. 6a,c,e) were calculated by averaging the number of spikes during a sliding window (500 ms). The trajectories of the mouse lemurs were divided into bins of 13 cm displacement length. Spike rates were assigned to each bin by counting the number of spikes divided by the time taken to complete the displacements. The floor (Fig. 6b) was defined as the first 30 cm above ground.

For cells with spatially restricted firing, a virtual 10-cm sphere was initially placed at the center of the branch. All passages through the sphere with their respective firing rate were aligned based on their minimum distance to the center of the sphere (time zero is when the minimum distance happens for each passage, Fig. 6d). Iteratively, the sphere was moved along the branch and the firing rate of all trajectories were calculated and aligned. The sphere movement was stopped once the average firing rate of all trajectories reached its maximum value when passing the center of the sphere. This center of the sphere at this location was considered to be the center.

For a more detailed analysis (Fig. 6e–j), the direction of displacement was also added as a factor, creating directional vectors. The vectors were color-coded based on the spike rate and the thickness of branches (4 and 6 mm considered as thin, and 12 and 24 mm considered as thick). To quantify the movement along branches, the area around the connecting cubes (radius of 5 cm) were excluded from this analysis. The nomenclature of the directions (north, south, east, west, up, down) were defined with regards to the *x*, *y* and *z* axis of the lattice maze and independent of the real-world coordinates.

**In vivo estimation of tetrode position in the mouse lemur brain.** The position of the tetrode bundles was determined by the 3D reconstruction of computer tomography scans acquired in the anesthetized animals (isoflurane, as detailed above, scan time, 3 min), which were carried out at the MicroCT platform of Paris Descartes University. The position of the brain areas with respect to the skull and the tetrodes (reconstructed by the computer tomography data) were estimated based on the manual alignment of existing data from high-resolution MRI atlas<sup>61</sup>, Supplementary Fig. 7) using the AMIRA software (Thermo Fisher Scientific).

**Statistics and reproducibility.** All the statistical analysis was carried out using R. A two-sided two-sample Kolmogorov–Smirnov test was used to compare distributions in Extended Data Figs. 1g and 6b. For all one-way repeated measure

analysis of variance (ANOVA) tests, Mauchly’s test was used to test the sphericity assumption and the Shapiro–Wilk test was performed to test the normality assumption (Figs. 3d, 4e and 5e,i and Extended Data Figs. 3b and 7b). A pairwise *t*-test was performed as post hoc analysis with the Bonferroni correction for multiple comparison. For the analysis of the directional-branch related cell (Extended Data Fig. 8) we performed two independent nonparametric one-way ANOVA tests (Kruskal–Wallis test), since both assumptions of normality and homogeneity of variance were not met.

**Reporting Summary.** Further information on research design is available in the Nature Research Reporting Summary linked to this article.

## Data availability

The MRI Atlas for the mouse lemur is available at <https://www.nitrc.org/projects/mouselemurAtlas>. Source data for Figs. 1 and 3–6 as well as source data for Extended Data Figs. 1–3, 6, 7 and 10 are provided. The original raw data containing all 3D trajectories, feedback signals and electrophysiology data is only available upon request due to the large file sizes. Source data are provided with this paper.

## Code availability

All the codes for tracking (GPU units and host machine), RECO boxes and real-time labeling of body parts are available at [www.huberlab.org/EthoLoop/software](http://www.huberlab.org/EthoLoop/software). R codes used for analysis are available upon request.

## References

- Perret, M., Gomez, D., Barbosa, A., Aujard, F. & Théry, M. Increased late night response to light controls the circadian pacemaker in a nocturnal primate. *J. Biol. Rhythms* **25**, 186–196 (2010).
- Perret, M. Change in photoperiodic cycle affects life span in a prosimian primate (*Microcebus murinus*). *J. Biol. Rhythms* **12**, 136–145 (1997).
- Guo, Z. V. et al. Procedures for behavioral experiments in head-fixed mice. *PLoS ONE* **9**, e88678 (2014).
- Hartley, A. & Zisserman, A. *Multiple View Geometry in Computer Vision* (Cambridge Univ. Press, 2006).
- Hartley, R. I. & Sturm, P. Triangulation. *Comput. Vis. Image Underst.* **68**, 146–157 (1997).
- Nistér, D. An efficient solution to the five-point relative pose problem. *IEEE Trans. Pattern Anal. Mach. Intell.* **26**, 756–777 (2004).
- Zach, C. Robust bundle adjustment revisited. In *Proc. Computer Vision – ECCV 2014 772–787* (Springer, 2014).
- Bons, N. A *Stereotaxic Atlas of the Grey Lesser Mouse Lemur Brain* (*Microcebus murinus*) (Elsevier, 1998).
- Dhenain, M., Ruffins, S. W. & Jacobs, R. E. Three-dimensional digital mouse atlas using high-resolution MRI. *Dev. Biol.* **232**, 458–470 (2001).
- Nadkarni, N. A., Bougacha, S., Garin, C., Dhenain, M. & Picq, J.-L. Digital templates and brain atlas dataset for the mouse lemur primate. *Data Brief* **21**, 1178–1185 (2018).

## Acknowledgements

We express our gratitude to the members of the Huber laboratory for their support and discussions. We thank M. Perret and the animal caretakers at the Brunoy facility for their help with mouse lemur breeding, care and handling, and H. Clamouze for constructing the maze. M. Scharter for advice with implementing DeepLabCut. We thank P. Yger for advice on spike sorting, L. Slimani and N. Liaudet for their help with the reconstruction of the electrode position. We thank Varta Microbattery for supplying the CP 1254 A3 coin batteries. We thank M. Prsa, G. Galiñanes and M. Long for their comments on the manuscript. This work was supported by the Vahabzadeh Foundation (A.N.), Human Frontiers Science Program (D.H. and F.P., grant no. RGP0024/2016), the New York Stem Cell Foundation (D.H.), Swiss National Science Foundation/Deutsche Forschungsgemeinschaft (D.H., grant no. 310030E\_190060). D.H. is a New York Stem Cell Foundation–Robertson Investigator.

## Author contributions

A.N. and D.H. conceptualized the EthoLoop system. A.N. and D.H. designed the tracking and close-up hardware. A.N. wrote all software for acquisition, tracking, close-loop control and RECO boxes. A.N. ran all experiments and analyzed all the data. D.H. oversaw data analysis. A.N., D.H. and S.P. designed the RECO box. R.Z. carried out the surgeries and ran the electrophysiological recording experiments. A.H. reconstructed the electrode trajectories. C.P.S. provided the mice and advice for the optogenetic experiments. Y.O. participated in the limb tracking. F.P. and F.A. provided expertise, guidance and resources related to the mouse lemurs. A.H. provided the 3D lattice maze and advice regarding the computer tomography scan. G.R. provided expertise for the tracking software. D.H. and A.N. wrote the manuscript.

## Competing interests

The authors declare no competing interests.

**Additional information**

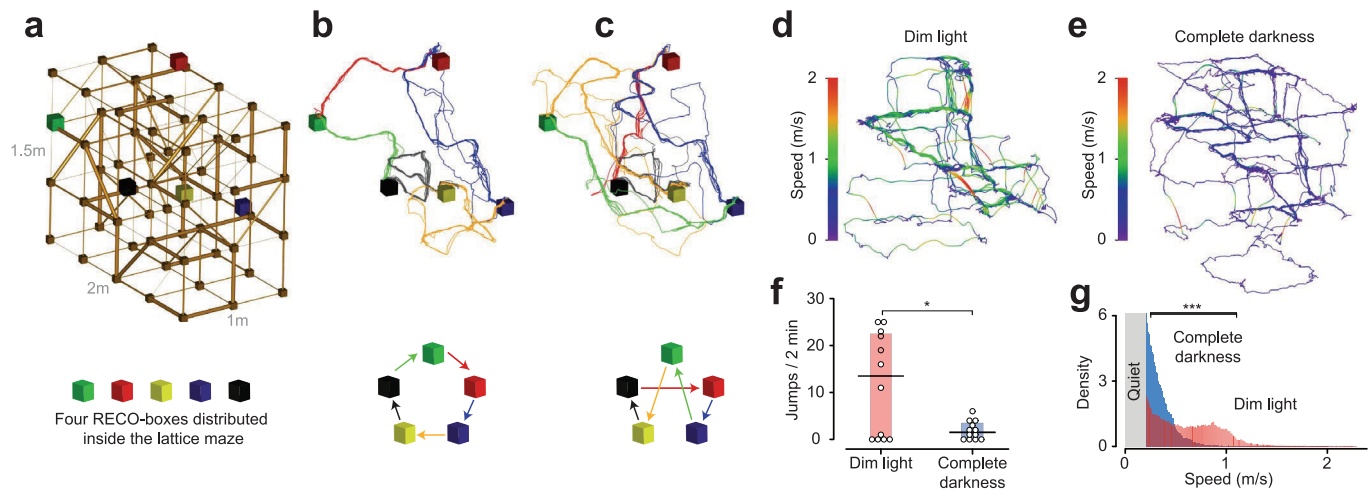
**Extended data** is available for this paper at <https://doi.org/10.1038/s41592-020-0961-2>.

**Supplementary information** is available for this paper at <https://doi.org/10.1038/s41592-020-0961-2>.

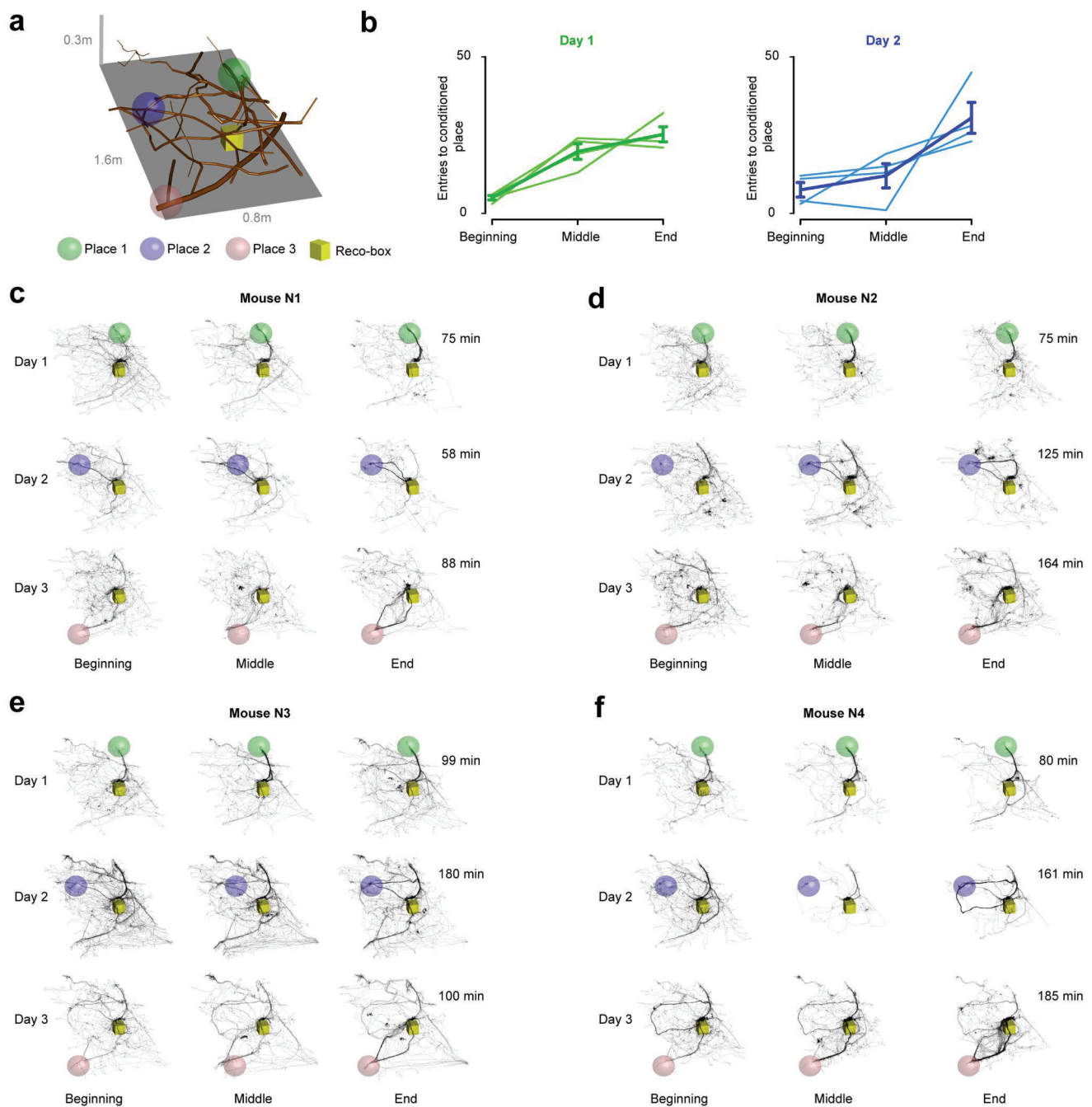
**Correspondence and requests for materials** should be addressed to D.H.

**Peer review information** Nina Vogt was the primary editor on this article and managed its editorial process and peer review in collaboration with the rest of the editorial team.

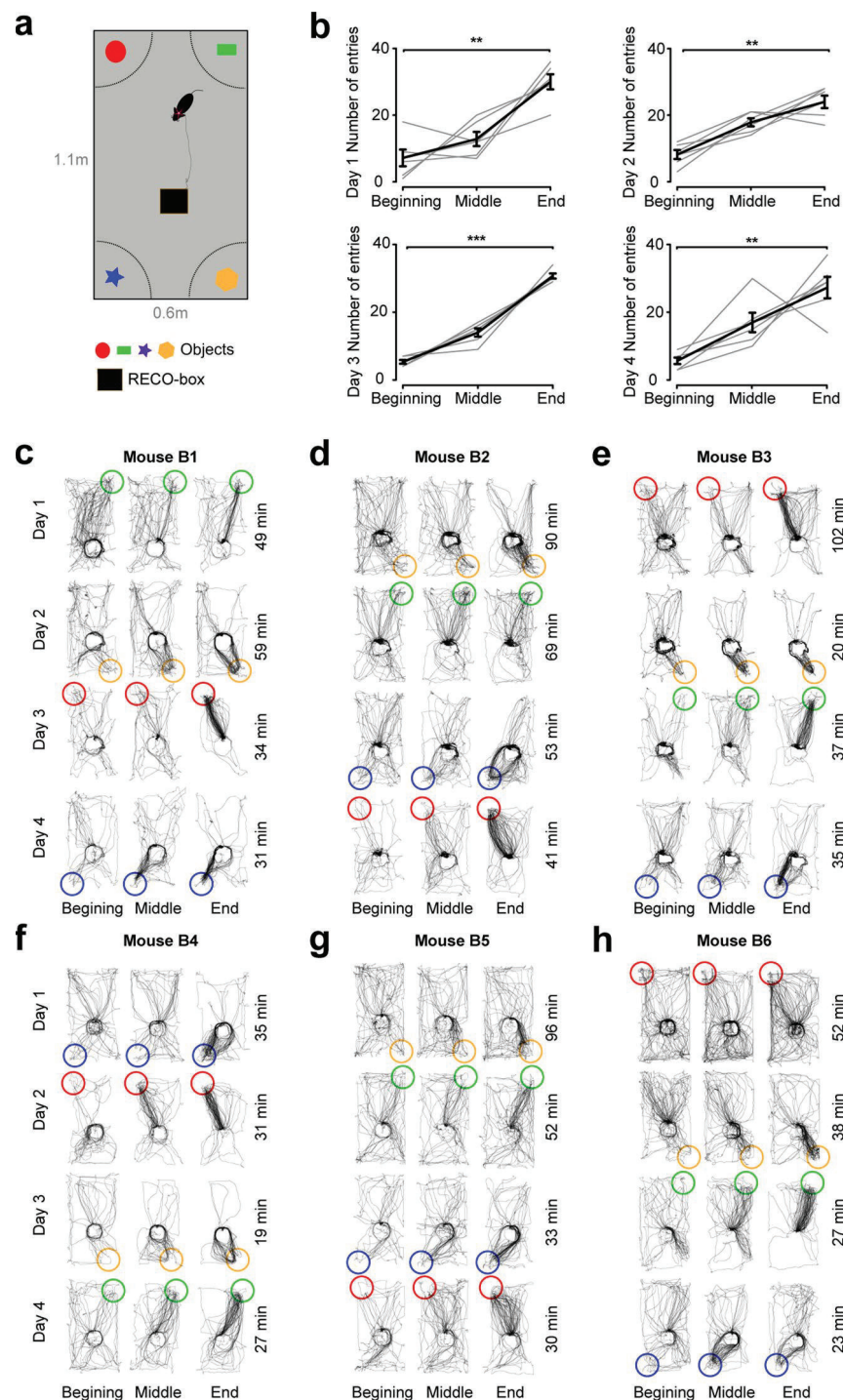
**Reprints and permissions information** is available at [www.nature.com/reprints](http://www.nature.com/reprints).



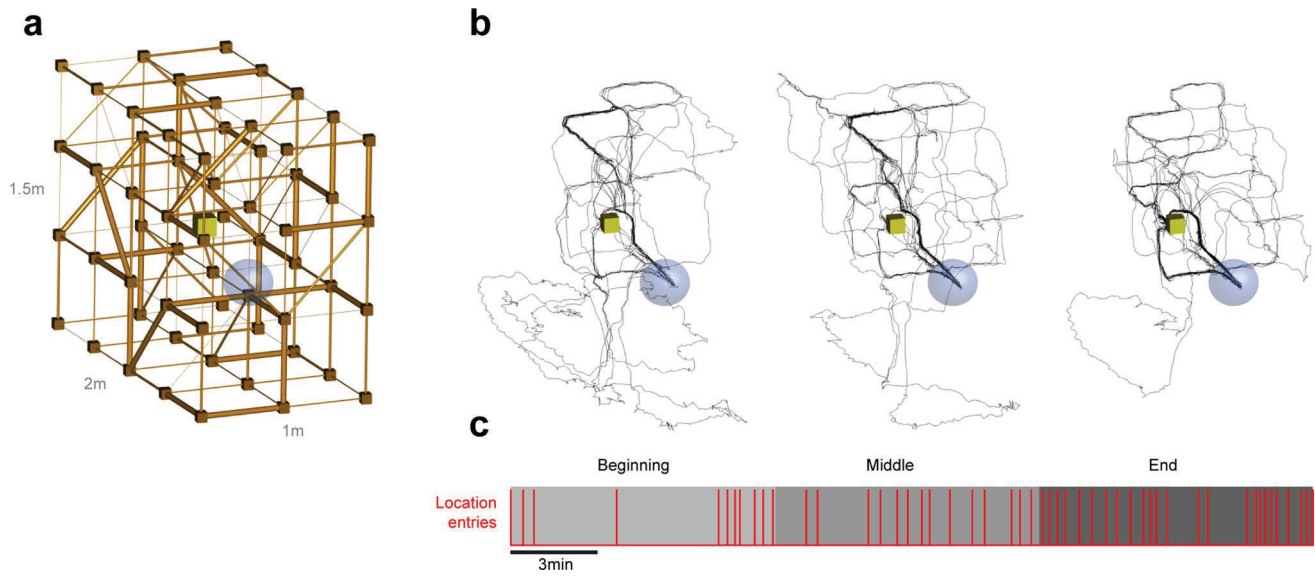
**Extended Data Fig. 1 | Foraging mouse lemur in the lattice maze with 5 RECO-boxes.** **a**, Five RECO-boxes (colored cubes) were spatially distributed at different locations of the lattice maze. RECO-boxes were activated in different sequences. **b,c**, Ten minutes of 3D trajectory of the mouse lemur where the RECO-boxes are activated in a circular (**b**) or non-circular order (**c**). The trajectory color is based on the currently activated RECO-box. **e,f**, Speed of locomotion (color-coded) under dim light (**e**) and complete darkness (**f**). **g,h**, The number of jumps (**g**) (12 time intervals for 1 mouse lemur, two-sided Wilcoxon signed rank test,  $*P=0.0207$ ) as well as the overall speed (**h**) was reduced in the absence of light (blue) compared to the dimly lit condition (red, two-sample Kolmogorov-Smirnov test, two sided,  $***P < 2.210 \cdot 10^{-16}$ ). The boxplot in (**g**) represents the upper and lower quartiles as well as the median.



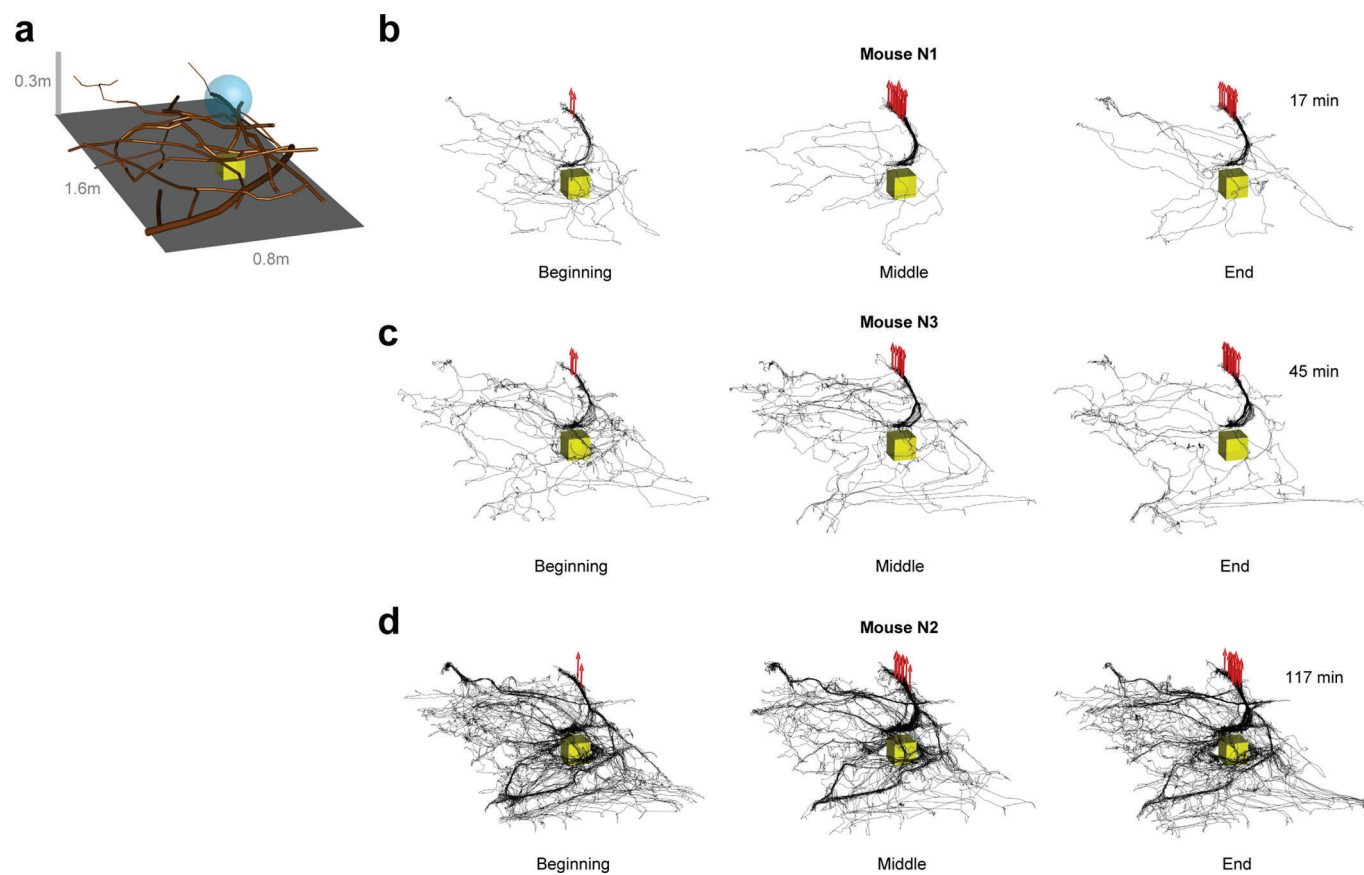
**Extended Data Fig. 2 | Mouse place-conditioning in naturalistic conditions.** **a**, The behavioral arena was filled with tree branches and included a RECO-box (yellow cube). Mice were conditioned to visit one of three unmarked locations (colored spheres). **b**, Number of entries to the conditioned place 1 and 2 during each session for all mice ( $N=4$ ). Bars represent standard error of mean. **c-f**, 3D trajectories of the beginning, middle and end of all sessions for all four mice that underwent 3D place conditioning. Trajectories of Day 3 for Mouse N3 shown in Fig. 3b is repeated here. Three different conditioned locations are shown in green, red and purple spheres. The time to reach the criteria condition (50th entrance to the conditioned place) is noted on the right.



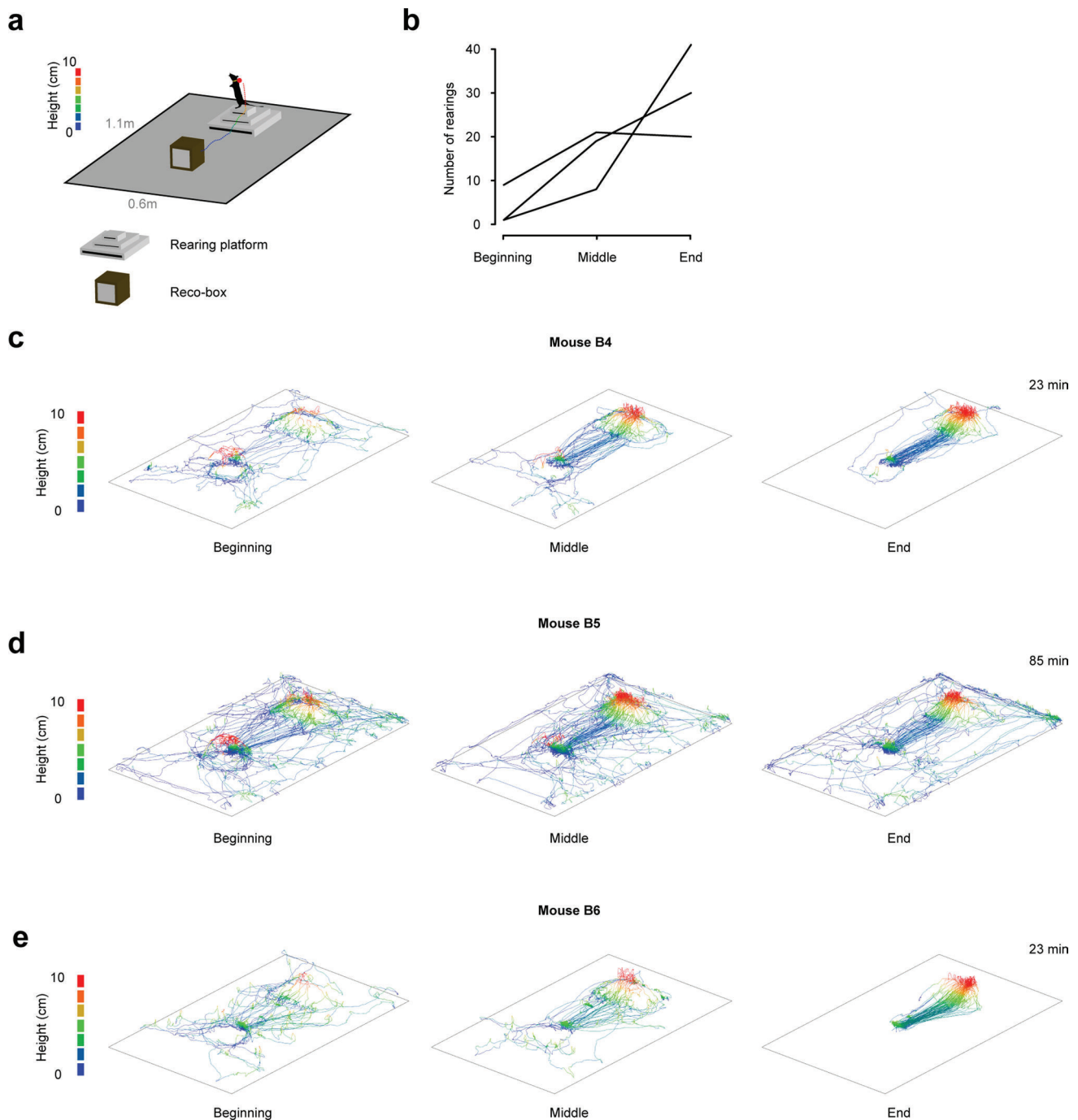
**Extended Data Fig. 3 | Mouse place-conditioning in an open-field arena.** **a**, A flat open-field arena for freely moving mice containing a single RECO-box and differently shaped objects placed at the four corners. The mice were trained to visit one of the four corners of the arena. Every session a different corner was reinforced. **b**, Number of entries to the conditioned place for all four days of training. For all days the mice entered the conditioned place more frequently ( $N=6$  mice; one-way repeated measure ANOVA; Two-sample pairwise t-test; Bonferroni correction for multiple comparison; beginning versus end; Day 1:  $**P=0.009$ , Day 2:  $**P=0.008$ ; Day 3:  $***P=2.910\text{-}7$ ; Day 4:  $P=0.006$ ). Error bars represent SEM. **c-h**, Original tracking traces of the beginning, middle and end of all sessions (four corners - illustrated with colored circles) for all six mice that underwent place conditioning. The time to reach the criteria condition (50th entry) is noted on the right.



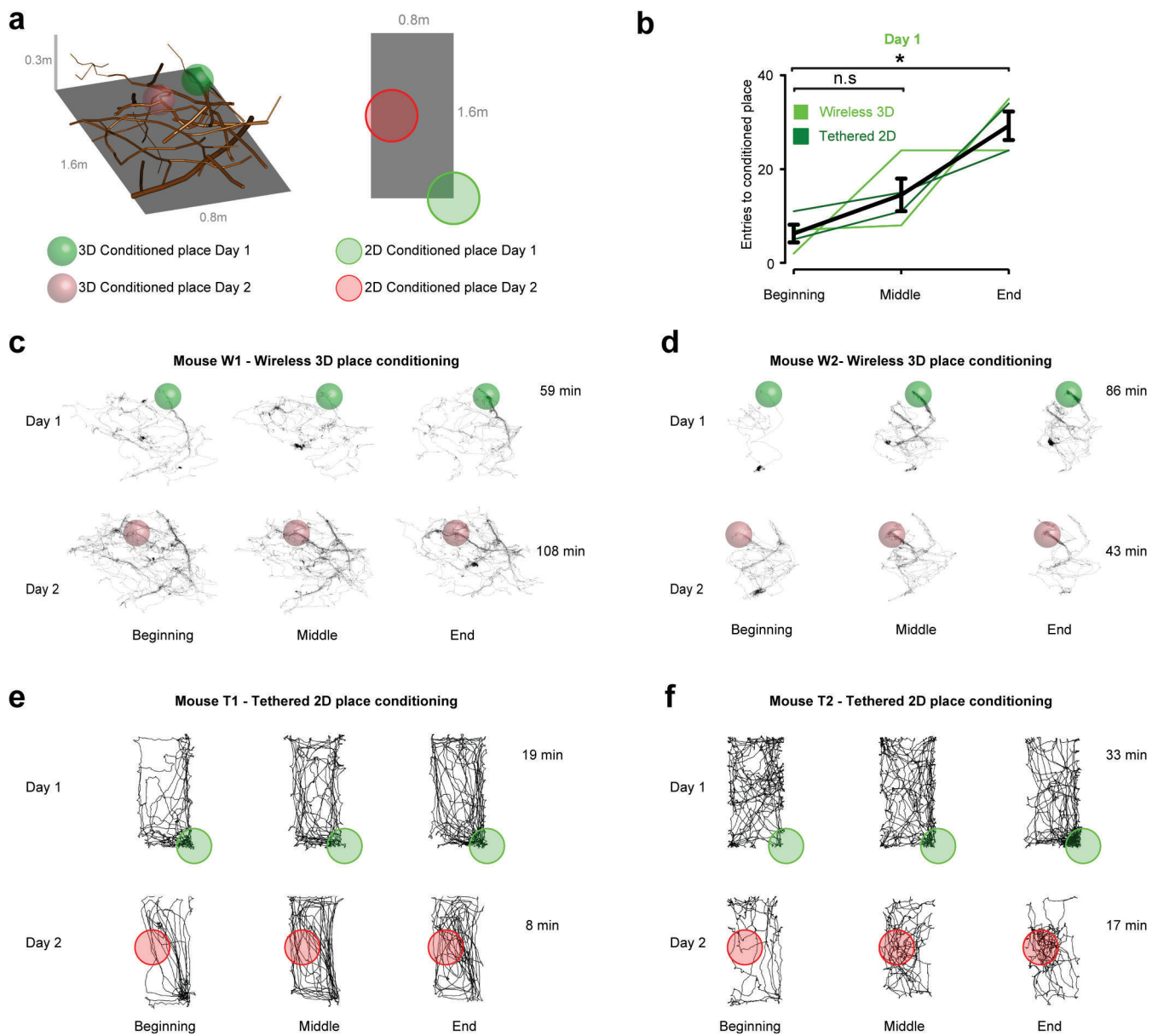
**Extended Data Fig. 4 | Trajectory of a mouse lemur during a place-conditioning experiment in the lattice maze. a**, Traces of a second conditioning experiment of a mouse lemur in the 3D lattice maze at the beginning, middle, and end of a behavioral session. The blue sphere indicates the location which was conditioned. **b**, The number of entries to the conditioned place across a behavioral session. **c**, Entries to the conditioned place across the session.



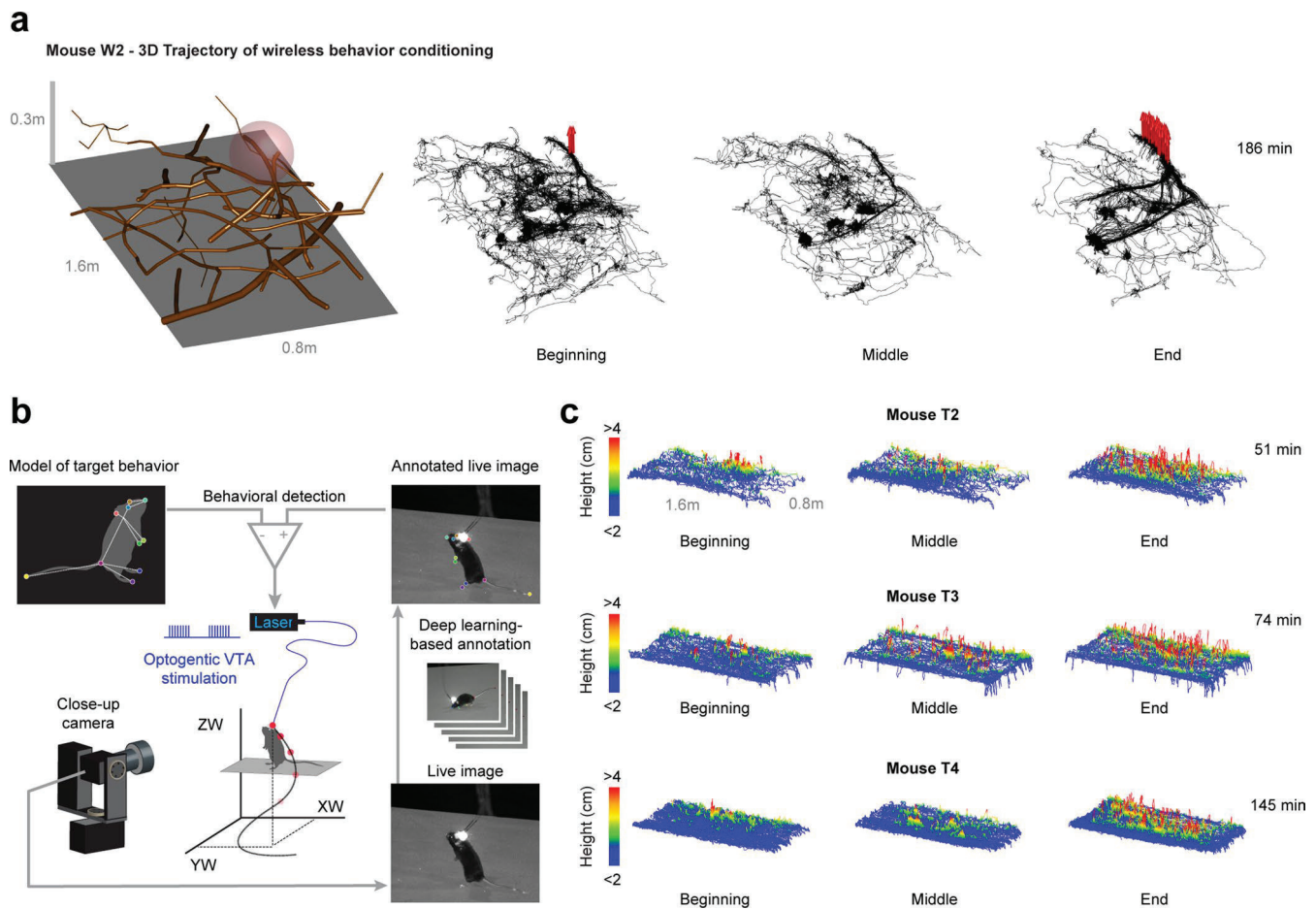
**Extended Data Fig. 5 | Mouse operant-conditioning of automatically detected behavior in naturalistic environments. a–c.** Additional 3D trajectories of three mice during conditioning of automatically detected postures. The time to reach the criteria condition (50th rearing) is noted on the right.



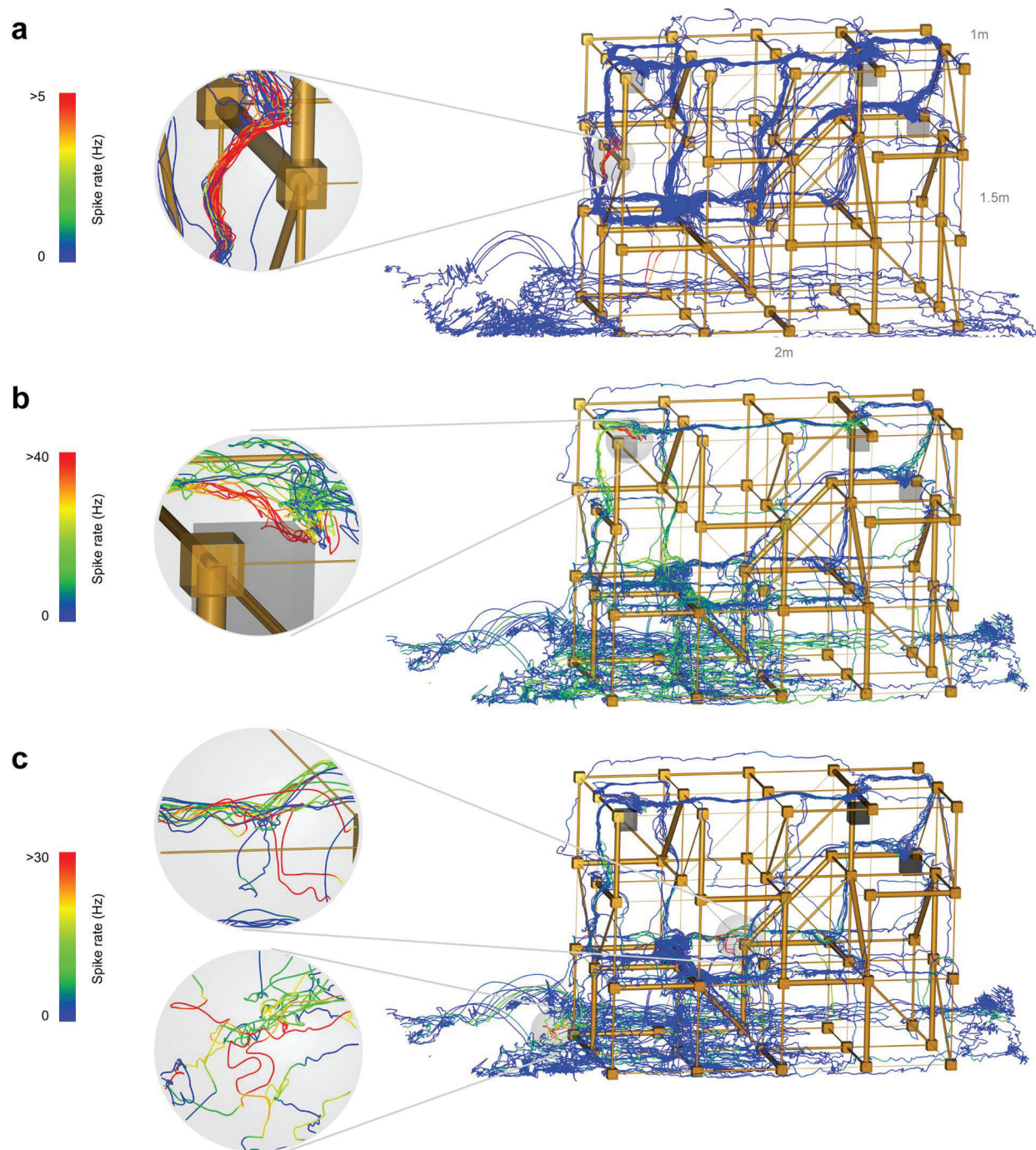
**Extended Data Fig. 6 | Mouse operant-conditioning of automatically detected behavior in an open-field arena.** **a**, Open-field arena for mice with an elevated platform and a RECO-box. The color code indicates the height of the tracked marker on the neck of the mouse. **b**, Summary data from 3 mice across the sessions (N=3 mice). **c-e**, Trajectories of three mice during condition sessions where the number of rearings increased. The time to reach the criteria condition (50th rearing) is noted on the right.



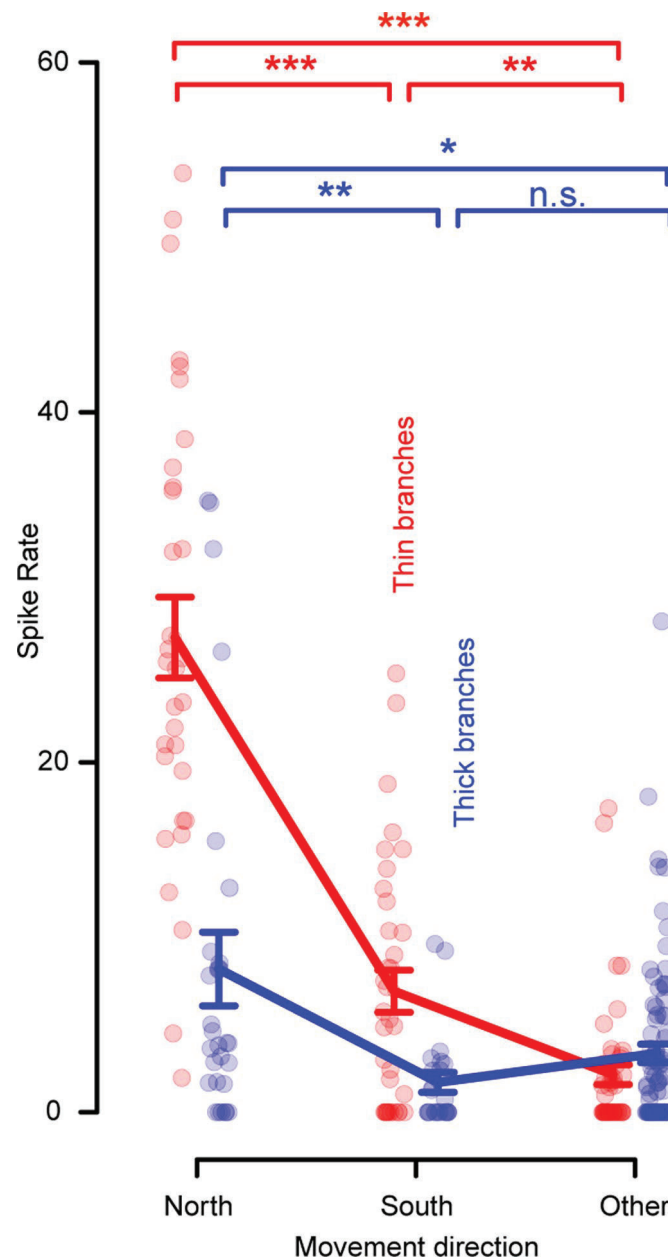
**Extended Data Fig. 7 | Place-conditioning using wireless and tethered optogenetic stimulation of VTA.** **a**, The red and green spheres indicate the conditioning locations in a naturalistic arena for mice using wireless optogenetics. **b**, Summary data of first day place conditioning session using wireless (3D, 2 mice) and tethered (2D, 2 mice) optogenetic VTA stimulation. The data from the wireless and tethered optogenetic were grouped together based on the day the place conditioning experiments were carried out. Mice were naive on the first day. The number of entries to the conditioned place increased within a session ( $N=4$  mice; one-way repeated measure ANOVA;  $F(2,6)=10.916$ ; main effect  $P=0.01$ ; pairwise two-sample  $t$  test; Bonferroni correction for multiple comparison; beginning versus end  $*P=0.025$ ; beginning versus middle;  $P=0.053$ ; n.s is not significant). Error bars represent SEM. **c,d**, Original trajectories of two place-conditioning sessions in 3D environment using wireless optogenetics for two mice (trajectories for Day 2 in **d**) are the same as the one shown in Fig 5.c. The colored spheres (red and green) show the conditioned places. **e,f**, Original trajectories of two place conditioning sessions for two mice in the open-field arena using tethered optogenetics. The colored circles (red and green) show the conditioned locations. The time to reach the criteria condition (50th entrance to the conditioned place) is noted on the right.



**Extended Data Fig. 8 | Automatically reinforcing postures using wireless and tethered optogenetic VTA stimulation. a**, A arena covered with branches for mice with an experimenter-defined area where rearing was conditioned (red sphere). 3D trajectories of an additional mouse during a session with optogenetic reinforcement of an automatically detected behavior syllable (rearing, red arrows). **b**, Schematic representation of the information flow during optogenetic VTA DA neurons stimulation in 2D open-field arena. The steps are identical to Fig. 6a, except that the detection of a behavioral event triggers tethered optogenetic stimulation of VTA DA neurons. **c**, 3D trajectory of three mice during the session of reinforcement of an automatically detected behavior syllable (rearing) using tethered optogenetics in 2D environment. The color code indicates the height of the mouse. The time to reach the criteria condition (100th rearing) is noted on the right.



**Extended Data Fig. 9 | Additional CA1 neurons with spatially restricted activity. a**, CA1 neuron showing increased activity preferentially on a single branch. **b**, CA1 neuron from different session (but same animal) showing increased activity near a feeder (gray square). **c**, CA1 neuron from the same session as (**b**) but showing increased activity at two different locations.



**Extended Data Fig. 10 | Detailed analysis of a directional cell (Fig. 6).** This neuron showed the highest activity when moving on a thin branch towards the north of the maze. Each dot represents the average spike rate during a 13cm segment. Kruskal-Wallis tests; main effect  $P=1.110\text{-}14$  for thin (red) and  $P=0.007$  for thick (blue) branches; Wilcoxon rank sum test for multiple comparison; Holm adjustment; red;  $N=32$ ,  $N=35$  and  $N=46$  for North, South and Rest; North versus South;  $***P < 10^{-8}$ ; North versus Rest;  $***P < 10^{-8}$ ; South versus Rest;  $**P=0.0018$ ; blue;  $N=27$ ,  $N=23$  and  $N=84$  for North, South and Rest; North versus South;  $**P=0.006$ ; North versus Rest;  $*P=0.03$ ; South versus Rest;  $P=0.14$ ; n.s. not significant;). Bars represent the standard error of mean.

## Reporting Summary

Nature Research wishes to improve the reproducibility of the work that we publish. This form provides structure for consistency and transparency in reporting. For further information on Nature Research policies, see [Authors & Referees](#) and the [Editorial Policy Checklist](#).

### Statistics

For all statistical analyses, confirm that the following items are present in the figure legend, table legend, main text, or Methods section.

n/a Confirmed

- The exact sample size ( $n$ ) for each experimental group/condition, given as a discrete number and unit of measurement
- A statement on whether measurements were taken from distinct samples or whether the same sample was measured repeatedly
- The statistical test(s) used AND whether they are one- or two-sided  
*Only common tests should be described solely by name; describe more complex techniques in the Methods section.*
- A description of all covariates tested
- A description of any assumptions or corrections, such as tests of normality and adjustment for multiple comparisons
- A full description of the statistical parameters including central tendency (e.g. means) or other basic estimates (e.g. regression coefficient) AND variation (e.g. standard deviation) or associated estimates of uncertainty (e.g. confidence intervals)
- For null hypothesis testing, the test statistic (e.g.  $F$ ,  $t$ ,  $r$ ) with confidence intervals, effect sizes, degrees of freedom and  $P$  value noted  
*Give  $P$  values as exact values whenever suitable.*
- For Bayesian analysis, information on the choice of priors and Markov chain Monte Carlo settings
- For hierarchical and complex designs, identification of the appropriate level for tests and full reporting of outcomes
- Estimates of effect sizes (e.g. Cohen's  $d$ , Pearson's  $r$ ), indicating how they were calculated

*Our web collection on [statistics for biologists](#) contains articles on many of the points above.*

### Software and code

Policy information about [availability of computer code](#)

Data collection

Custom C & C++ (gcc 5.4.0) code (using OpenCV 3.1) was used for animal tracking and all the closed-loop control. Real-time visualization of 3D trajectories was done using gnuplot (5.2). Real-time behavior analysis was done using a custom programmed (Python 3) real-time version of DeepLabCut (1.0) software (Mathis et al. 2018). Electrophysiology recordings was acquired using Trodes software (1.8.1, SpikeGadgets). Custom Arduino (1.8.5) code was used to program the RECO-boxes.

Data analysis

All the analysis of tracking data, statistics and plots were done using R (3.4.4) software. Spike sorting was done using SpykingCircus (only one version exists). Analysis of tetrode position in the mouse lemur brain was done using Amira software (6.0.0).

For manuscripts utilizing custom algorithms or software that are central to the research but not yet described in published literature, software must be made available to editors/reviewers. We strongly encourage code deposition in a community repository (e.g. GitHub). See the Nature Research [guidelines for submitting code & software](#) for further information.

### Data

Policy information about [availability of data](#)

All manuscripts must include a [data availability statement](#). This statement should provide the following information, where applicable:

- Accession codes, unique identifiers, or web links for publicly available datasets
- A list of figures that have associated raw data
- A description of any restrictions on data availability

All figure data is provided in the Supplementary Data section. The original raw data (videos, electrophysiological recordings, 3D trajectories) is available upon request. The MRI Atlas for mouse lemur is available at: <https://www.nitrc.org/projects/mouselemuratlas>.

## Field-specific reporting

Please select the one below that is the best fit for your research. If you are not sure, read the appropriate sections before making your selection.

Life sciences       Behavioural & social sciences       Ecological, evolutionary & environmental sciences

For a reference copy of the document with all sections, see [nature.com/documents/nr-reporting-summary-flat.pdf](https://www.nature.com/documents/nr-reporting-summary-flat.pdf)

## Life sciences study design

All studies must disclose on these points even when the disclosure is negative.

Sample size	Sample size was not predetermined in this study for both mice and mouse lemurs. We used 4 mice in 3D arena and 6 mice for open-field arena for closed-loop experiments and 5 mice for optogenetics experiments to be able to perform statistical analysis on their performance. For the mouse lemur closed-loop experiments we only used one mouse lemur as a proof of principle that our system can produce same results with primates. For the social behavior analysis of mouse lemurs we used 3 mouse lemurs (2 male and 1 female) and run experiments with male-male and female-male mouse lemurs to be able to compare their social interaction. For the electrophysiology experiments we only recorded neuronal activity from two mouse lemurs.
Data exclusions	We did not exclude any data.
Replication	We repeated experiments with multiple mice for place conditioning (N=4 for 3D arena, N=6 for 2D arena), behavior conditioning (N=4 for 3D arena, N=3 for open field), operant conditioning via wireless optogenetic stimulation (N=2) and tethered optogenetic stimulation (N=2 for place conditioning and N=3 for behavior conditioning) to demonstrate system's ability to reproduce the same data in different experimental conditions (multiple conditioned locations in both the 3D and open-field arena). The replication was successful as reported in Extended Data Figures 2-8 in addition to Figures 3-5. Additionally we performed the same conditioning experiments for one mouse lemur (2 different location for place conditioning and rearing for behavior conditioning) as a proof of principle that we can reproduce the same data with primates. The replication for place conditioning experiment in mouse lemur was successful as reported in Extended Data Fig 4.
Randomization	We did not divide animals into different experimental groups.
Blinding	We did not perform any blinding since all the data acquisition and the pipeline for the analysis was automatically done.

## Reporting for specific materials, systems and methods

We require information from authors about some types of materials, experimental systems and methods used in many studies. Here, indicate whether each material, system or method listed is relevant to your study. If you are not sure if a list item applies to your research, read the appropriate section before selecting a response.

### Materials & experimental systems

n/a	Involved in the study
<input type="checkbox"/>	<input checked="" type="checkbox"/> Antibodies
<input checked="" type="checkbox"/>	<input type="checkbox"/> Eukaryotic cell lines
<input checked="" type="checkbox"/>	<input type="checkbox"/> Palaeontology
<input type="checkbox"/>	<input checked="" type="checkbox"/> Animals and other organisms
<input checked="" type="checkbox"/>	<input type="checkbox"/> Human research participants
<input checked="" type="checkbox"/>	<input type="checkbox"/> Clinical data

### Methods

n/a	Involved in the study
<input checked="" type="checkbox"/>	<input type="checkbox"/> ChIP-seq
<input checked="" type="checkbox"/>	<input type="checkbox"/> Flow cytometry
<input checked="" type="checkbox"/>	<input type="checkbox"/> MRI-based neuroimaging

## Antibodies

Antibodies used	In this study, the following primary antibodies was used: rabbit polyclonal anti-Tyrosine Hydroxylase (1/500 dilution, abcam, ab6211). The following secondary antibodies was used: donkey polyclonal anti-rabbit 555 (Alexa Fluor - 1/500 dilution, abcam-ab150062).
Validation	The antibodies used in the study were commercially available antibodies validated for IHC and WB experiments in rodents. For references of the primary antibody: <a href="https://www.abcam.com/tyrosine-hydroxylase-antibody-ab6211.html">https://www.abcam.com/tyrosine-hydroxylase-antibody-ab6211.html</a> and the secondary antibody: <a href="https://www.abcam.com/donkey-rabbit-igg-hl-alexa-fluor-555-preadsorbed-ab150062.html">https://www.abcam.com/donkey-rabbit-igg-hl-alexa-fluor-555-preadsorbed-ab150062.html</a> under the References section.

## Animals and other organisms

Policy information about [studies involving animals](#); [ARRIVE guidelines](#) recommended for reporting animal research

Laboratory animals	Mice used for all experiments in 3D arena were adult C57Bl/6J (N=4 mice; 2 males and 2 females; mice were 18, 18, 12 and 12
--------------------	---

## Laboratory animals

weeks old during the experiment).

Mice used in the operant conditioning using optogenetic stimulation were adult DAT-iresCre mice (Slc6a3tm1.1(cre)Bkmn/J; tethered optogenetics; N=3 mice; 2 females and 1 male; mice were 13, 13 and 48 weeks old during experiment; wireless optogenetics; N=2 mice; both female; mice were 17 and 27 weeks old during experiment).

Mice used for experiments in open-field arena were adult C57Bl/6J (N=6 mice; 5 females and 1 male; mice were 29, 34, 34, 11, 11 and 26 weeks old during experiment).

4 adult grey mouse lemurs (*Microcebus murinus*) were used for this study. All mouse lemurs were born and raised in the "Mouse Lemur Platform" of the Museum of Natural History in Brunoy, France (N=4 mouse lemurs; 3 males and 1 female; mouse lemurs were 1.5, 3, 2.5 and 3 years old during experiment).

## Wild animals

No wild animals were used for this study.

## Field-collected samples

No field-collected samples were used for this study.

## Ethics oversight

The procedures with mouse lemurs are in accordance with European animal welfare regulations and were reviewed by the local ethics committee ("Comité d'éthique en expérimentation animale No. 68") in Brunoy, France, by the ethics committee of the University of Geneva, Switzerland, and authorized by the French "Ministère de l'éducation nationale de l'enseignement supérieur et de la recherche".

All experiments with mice were carried out in Geneva, Switzerland, and reviewed by the local ethics committee and authorities of the Geneva canton ("Institutional Animal Care and Use Committee of the University of Geneva and Geneva veterinary offices. ").

Note that full information on the approval of the study protocol must also be provided in the manuscript.

# Current Biology

## Pupil Size Coupling to Cortical States Protects the Stability of Deep Sleep via Parasympathetic Modulation

### Highlights

- Infrared back-illumination allows accurate pupillometry in sleeping mice
- Brain activity and pupil diameter are tightly coupled during sleep
- The parasympathetic system is the main driver of pupillary changes during NREM sleep
- Pupillary constrictions might have a protective function to stabilize deep sleep

### Authors

Özge Yüzgeç, Mario Prsa,  
Robert Zimmermann, Daniel Huber

### Correspondence

daniel.huber@unige.ch

### In Brief

Using infrared back-illumination pupillometry in head-fixed sleeping mice, Yüzgeç et al. show that pupil diameter is tightly coupled to cortical states during sleep. Pharmacological and light-stimulation experiments reveal that the pupillary constrictions are parasympathetically driven and might have a protective function to stabilize deep sleep.



# Pupil Size Coupling to Cortical States Protects the Stability of Deep Sleep via Parasympathetic Modulation

Özge Yüzgeç,<sup>1,2</sup> Mario Prsa,<sup>1,2</sup> Robert Zimmermann,<sup>1,2</sup> and Daniel Huber<sup>1,3,\*</sup>

<sup>1</sup>Department of Basic Neurosciences, University of Geneva, Geneva, Switzerland

<sup>2</sup>These authors contributed equally

<sup>3</sup>Lead Contact

\*Correspondence: [daniel.huber@unige.ch](mailto:daniel.huber@unige.ch)

<https://doi.org/10.1016/j.cub.2017.12.049>

## SUMMARY

During wakefulness, pupil diameter can reflect changes in attention, vigilance, and cortical states. How pupil size relates to cortical activity during sleep, however, remains unknown. Pupillometry during natural sleep is inherently challenging since the eyelids are usually closed. Here, we present a novel head-fixed sleep paradigm in combination with infrared back-illumination pupillometry (iBip) allowing robust tracking of pupil diameter in sleeping mice. We found that pupil size can be used as a reliable indicator of sleep states and that cortical activity becomes tightly coupled to pupil size fluctuations during non-rapid eye movement (NREM) sleep. Pharmacological blocking experiments indicate that the observed pupil size changes during sleep are mediated via the parasympathetic system. We furthermore found that constrictions of the pupil during NREM episodes might play a protective role for stability of sleep depth. These findings reveal a fundamental relationship between cortical activity and pupil size, which has so far been hidden behind closed eyelids.

## INTRODUCTION

Fluctuations in cortical states may determine learning efficiency, impact performance, and predict decisions [1–3]. Electrophysiological measurements, such as electrocorticograms (ECoGs), are reliable indicators of different cortical states and have as such been used to determine optimal conditions for sensory processing or cognitive performance [4]. Other physiological measurements, such as pupillometry, can be used as a non-invasive proxy for tracking vigilance states during behavior. Variations in pupil size can predict arousal [5], vigilance levels [6], and emotional responses [7] and reveal choice inclinations [8]. Due to its inexpensive and simple methodology, pupillometry has attracted not only the interest of neuroscientists, but also that of market researchers, athletes, and engineers. It became as such the focus for the development of practical applications, such as drowsiness detection while driving [9], fatigue [10],

and mental health assessments [11] or affective state classification [12].

More recently, studies in rodents and non-human primates have investigated interactions between cortical states and pupil diameter and found a close coupling during quiet wakefulness [13–15]. Follow-up studies combining optical imaging, electrophysiology, and modeling revealed that the link between brain activity and pupil diameter might be modulated by noradrenergic and cholinergic systems [16] and confirmed the occurrence of transient periods for optimal sensory processing.

Given the existing link between pupil size and cortical states during wakefulness, we asked whether a similar relationship persists during sleep. Changes in cortical states are very prominent during different sleep phases, while cognition- and sensory-related processes are strongly reduced. Would the pupil thus still fluctuate and what kind of changes would these fluctuations be related to during sleep? Might the pupil play a specific functional role, disturbance of which might interfere with sleep? In this study, we combined a novel approach allowing pupillometry in head-fixed naturally sleeping mice together with electrophysiology and pharmacology to find the answers to these questions.

## RESULTS

### Head-Fixed Sleeping Paradigm

The main challenge for pupil tracking during natural sleep is that mice often close their eyes, incline their head, or curl up (Figures 1A and 1B). Since pupil tracking is greatly facilitated during head-fixation as compared to freely moving conditions [17], we developed a setting allowing mice to fall asleep under head-fixed conditions. Using X-ray-based posture analysis, we adjusted the head angle and body position to mimic the body's natural position observed during quiet wakefulness and sleep (Figures 1B, 1C, and S1A; STAR Methods). Mice were gradually habituated to sleep in this position within 7 days in sound- and light-isolated boxes. ECoGs and electromyography (EMG; STAR Methods) of the neck muscle were used to monitor and quantify sleep states (Figure 1E). Recordings started while mice were awake and lasted up to 4 hr, most of which was spent in non-rapid eye movement (NREM) sleep with intermittent periods of rapid-eye movement (REM) sleep and wakefulness (awake) (Figure 1E). Similarly to sleeping mice in freely moving conditions [18, 19] (Figures S1B and S1C), awake states were characterized by high-amplitude, continuous EMG activity and high-frequency,



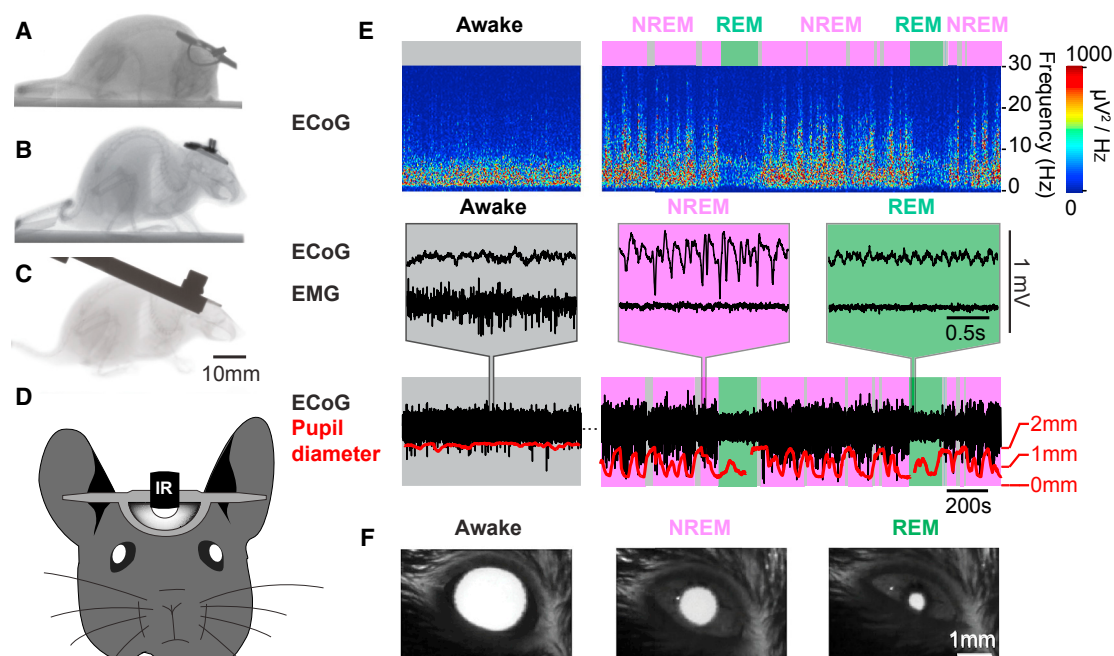


**Figure 1. Head Fixed Sleep and iBip Pupil Tracking**

(A) X-ray images of a naturally sleeping mouse in a curled-up position.

(B) Position of a sitting mouse during natural sleep.

(C) Head-fixed mouse with a head angle of 30 degrees.

(D) Front-view schematics of the infrared back-illumination pupillometry (iBip) pupil-tracking system. The 940 nm infrared light-emitting diode (LED) is placed above the skull, which allows the bright LED light to penetrate the head and back-illuminate the pupils.

(E) Top row: power spectrogram of M1 ECoG signal during awake, non-rapid eye movement (NREM) sleep, and rapid eye movement (REM) sleep states. Second row: a close-up of the ECoG and electromyography (EMG) signals during awake, NREM, and REM states. Third row: ECoG signal and pupil diameter during different cortical states. Data are from a habituated head-fixed mouse. The pupil diameter data are missing due to eye blinks at the beginning or end of REM periods.

(F) Images of pupil with infrared back illumination in awake, NREM and REM states.

See also [Figures S1](#) and [S2](#) and [Movie S1](#).

low-amplitude oscillations in the ECoG signal. NREM sleep was defined by high-amplitude ECoG and low or absent EMG activity. REM sleep was characterized by prominent  $\sim 7$  Hz oscillations in the ECoG signal and complete disappearance of EMG activity (Figure 1E). Surprisingly, we found that head-fixed mice consistently sleep with their eyelids partially or fully open (Figure 1F), which allowed us to have access to the pupil diameter during continuous, natural-like sleep. Thus, we found that mice are able to sleep under head-fixed conditions, showing sleep patterns comparable to natural sleep under freely moving conditions (Figures S1B and S1C), yet with open eyelids [19, 20].

#### High-Contrast Infrared Back-Illumination Pupillometry

To enhance the contrast of the pupil for reliable tracking during head-fixed sleep, we developed infrared back-illumination pupillometry (iBip; see [STAR Methods](#)). For iBip, a 940 nm LED light source was placed on the skull of the mouse above frontal cortex, thereby illuminating the structures inside the head including the brain and the back of the eyes. When we imaged the eyes with infrared video cameras, the pupils appeared brightly illuminated (Figure 1F; [Movie S1](#)) and allowed reliable high-contrast tracking of their diameter and movement dynamics during natural sleep (Figures 1E, S2A, and S2B).

#### Pupil Size as an Identifier of Awake and Sleep Brain States

We first asked whether pupil diameter is qualitatively different during different sleep states. The average distribution of pupil size in darkness revealed that during the awake state, the pupil remains dilated most of the time (Figure 2A). During REM sleep (Figure S2B; [Movie S1](#)), it remains mostly constricted, whereas during NREM sleep, the pupil's diameter continually oscillates between small and large (Figure 2A). Plotting the median diameter versus its distribution width for each session yields three clearly separable clusters of points each corresponding to one of the three brain states (Figure 2A). Indeed, a K-means clustering analysis correctly partitioned 46 out of the 48 points into three sleep state categories.

The latter result implies that pupil size can be used as a reliable signal for brain state identification during sleep. To explicitly test this, we trained a neural network machine learning algorithm by providing the pupil diameter signal to its input layer and the sleep state label, identified based on the characteristics of corresponding ECoG and EMG signals, to the output layer. Each training trial consisted of a 100 s chunk of data, and we trained the neural network separately for each session by including datasets from all sessions but that one. The data of the remaining

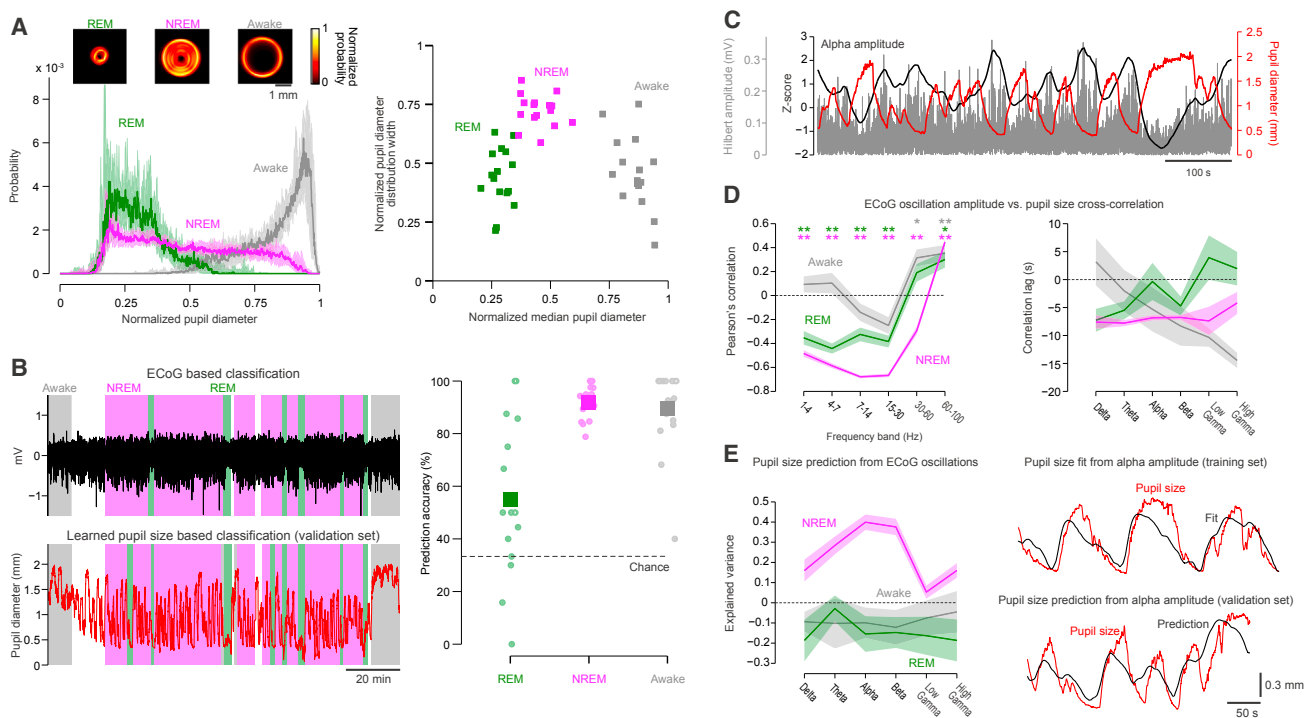


**Figure 2. Pupil Size Fluctuations in Different Sleep States and Its Coupling to Brain Oscillations**

(A) Left: median distribution (shaded regions are quartiles) of pupil diameter during REM, NREM, and awake states ( $n = 16$  sessions). The pupil diameter has been normalized to its maximum recorded value in each experimental session. Insets show the location probability of the pupil's contour in one representative session for each state separately. Right: median pupil diameter versus its distribution width (the middle range containing 95% of the data points) of the 16 sessions. (B) Top: ECoG recording of an example session with the identified sleep states based on delta, theta, and EMG power classification criteria (see STAR Methods for details). Bottom: predicted sleep states based on the pupil diameter recording (red trace) of the same session using a trained neural network algorithm (see STAR Methods for details). Note that the episodes marked in white include mixed NREM and awake bouts shorter than 100 s and were therefore excluded. (C) Example session illustrating co-fluctuations of pupil size (red) and the Hilbert amplitude of ECoG oscillations in the alpha frequency band depicted in gray and its low-passed trace (denoted as alpha amplitude) in black.

(D) Mean ( $\pm$ SEM) Pearson's correlation between ECoG oscillatory magnitude of each frequency band and pupil diameter ( $n = 16$  sessions) and the corresponding correlation lags, where negative values indicate that changes in oscillation size lead changes in pupil size. \* $p < 0.01$ , \*\* $p < 0.001$  (Student's *t* test, Bonferroni corrected).

(E) Left: mean ( $\pm$ SEM) variance accounted for between measured and predicted pupil size based on ECoG oscillations of each frequency band. Right: example session comparing the measured pupil size (red) to the fitted (top) and predicted (bottom) pupil size with a general linear model using alpha amplitude as a regressor.

See also Figure S2 and STAR Methods for details.

session was used to evaluate prediction accuracy. In this manner, the learned classification based on pupil diameter correctly predicted all three sleep states (Figure 2B) more often than expected by chance (REM: 58%, NREM: 96%, awake: 95%; REM:  $p = 0.016$ , NREM:  $p < 0.001$ , awake:  $p < 0.001$ , Wilcoxon signed-rank test). These results reveal that pupil size during natural sleep is a reliable identifier of different sleep states.

### Co-variation of Pupil Size and Brain Oscillations

Temporal changes in pupil size were previously found to be tightly coupled to oscillations in bandlimited EEG power in awake animals [14–16]. We therefore asked whether such coupling is also present during sleep and how it differs between the different brain states. In order to test this, we looked at the correlation between pupillary activity and traditional brain rhythms [21–24]. Striking co-fluctuations of pupil size and amplitudes of bandlimited ECoG oscillations were indeed observed in sleeping mice (Figure 2C). This analysis revealed that the stron-

gest coupling is observed for the alpha (7 to 14 Hz) and beta (15 to 30 Hz) frequency bands (Figure 2D) in the NREM sleep state, where brain oscillations and pupil diameter are inversely correlated. Analysis at finer frequency resolution showed that peak negative correlation occurs in the spindle band (12 to 14 Hz; Figure S2C). Positive correlations were only found in the high-gamma band (60 to 100 Hz) and were similar in all three states. Brain oscillation changes led in time the changes in pupil size as indicated by the negative cross-correlation lags (Figure 2D).

To assess how steady these correlations are throughout a session in the different sleep states, we tested whether the oscillation amplitude can actually be used to predict pupil size ( $n = 5$  mice). For each session, low-pass-filtered ECoG oscillation amplitudes were scaled to fit the pupil signal, and the fitted parameters were cross-validated on separate data of the same session (see STAR Methods). Surprisingly, only magnitude fluctuations of low-frequency oscillations (alpha and beta bands) during NREM sleep could reliably predict changes in pupil diameter

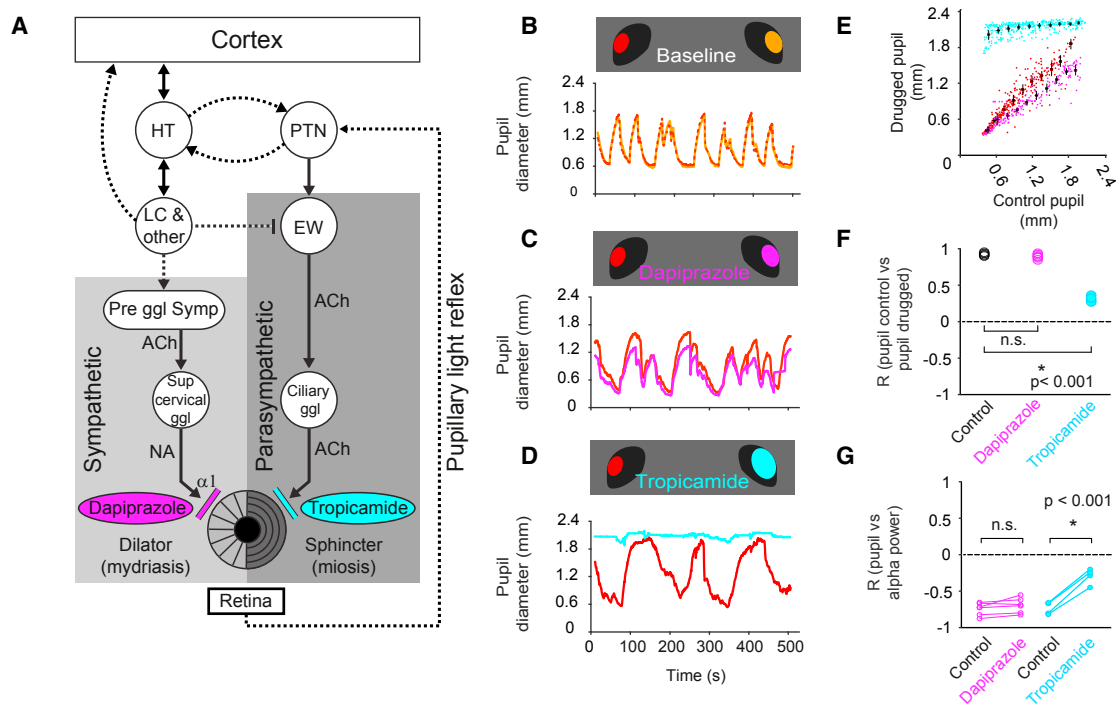


**Figure 3. Mechanisms Underlying Coupling of Pupil Diameter and Brain Activity**

- (A) Schematics of the regulation of pupil size in relation to cortex through sympathetic and parasympathetic pathways (adapted from [28]).  
 (B) Pupillary oscillations in both eyes in baseline condition in NREM sleep.  
 (C) Pupillary oscillations in intact and dapiprazole-instilled eyes in NREM sleep.  
 (D) Pupillary oscillations in intact and tropicamide-instilled eyes in NREM sleep.  
 (E) Pupil size comparison of the eyes in baseline, dapiprazole-instilled, and tropicamide-instilled conditions in NREM sleep. Colored dots correspond to individual NREM bouts, and black dots are means ( $\pm$ SEM) of binned data (ten equally sized bins between the minimum and maximum size of the control pupil).  
 (F) Cross-correlation of the pupil diameters in opposing eyes in NREM sleep in baseline, dapiprazole-instilled, and tropicamide-instilled conditions.  
 (G) Cross-correlation of pupil diameter and the alpha power in the contralateral M1 in control, dapiprazole-instilled, and tropicamide-instilled conditions.  
 See also [Figure S3](#) and [Movie S1](#).

(Figure 2E). Peak prediction accuracy was again observed to occur in the spindle band when the analysis was performed at a finer frequency resolution (Figure S2D). Given the inverse correlation, it follows that during NREM sleep, increases in the size of low-frequency brain oscillations predict pupil constrictions, and decreases predict pupil dilations. These two phenomena seem to reflect the fragile and deep sub-states of NREM sleep [25], respectively. These results also reveal that the covariation of cortical oscillations and pupil diameter is stronger during sleep as compared to the awake condition (Figure 2D) [14–16]. The fluctuations of pupil size and amplitude of ECoG oscillations were found to be periodic, with an infra-slow modulation frequency ranging from 0.01 to 0.02 Hz (Figures S2E–S2G). These infra-slow modulations have been shown to affect not only cortical activity, but also heartbeat [25, 26]. We indeed found that the changes in pupil diameter were positively correlated with changes in heart rate during NREM periods (Figure S3).

### Mechanisms of Pupil Size Control in Sleep

During wakefulness, the pupil diameter is driven by an equilibrium of the sympathetic and parasympathetic systems [27]. Whereas the parasympathetic pathway mediates the constriction of the pupil during relaxation and upon light illumination, pu-

pil dilations during arousal or locomotion are mediated by the sympathetic system. In wakefulness, the sympathetic changes are closely coupled to cortical oscillations and are correlated with fluctuations in noradrenergic and cholinergic afferents [16]. The question therefore arises, is it the parasympathetic or the sympathetic system that mediates the tight coupling between pupil size and cortical states that we found to occur during sleep?

To assess their respective roles, we pharmacologically blocked the action of each of these two pathways at the level of the pupil. The sympathetic pathway was blocked by using an adrenergic  $\alpha$ -1 receptor antagonist (dapiprazole), and the parasympathetic input to the pupil was inhibited by a cholinergic antagonist (tropicamide; Figure 3A). The drugs were applied to a single eye before the beginning of the sleep session, and the other eye was used as simultaneous control. To assess the effect of the drugs, we compared the correlation between ECoG in the alpha power band and pupil size in the NREM sleep state, which was found to be the most prominent co-fluctuation that exists between brain oscillations and pupil dynamics (Figure 2).

Under natural conditions, the pupils of the two eyes co-varied and were both correlated with the ECoG alpha power (Figures 3B, 3E, and 3G). Blocking the sympathetic afferents by

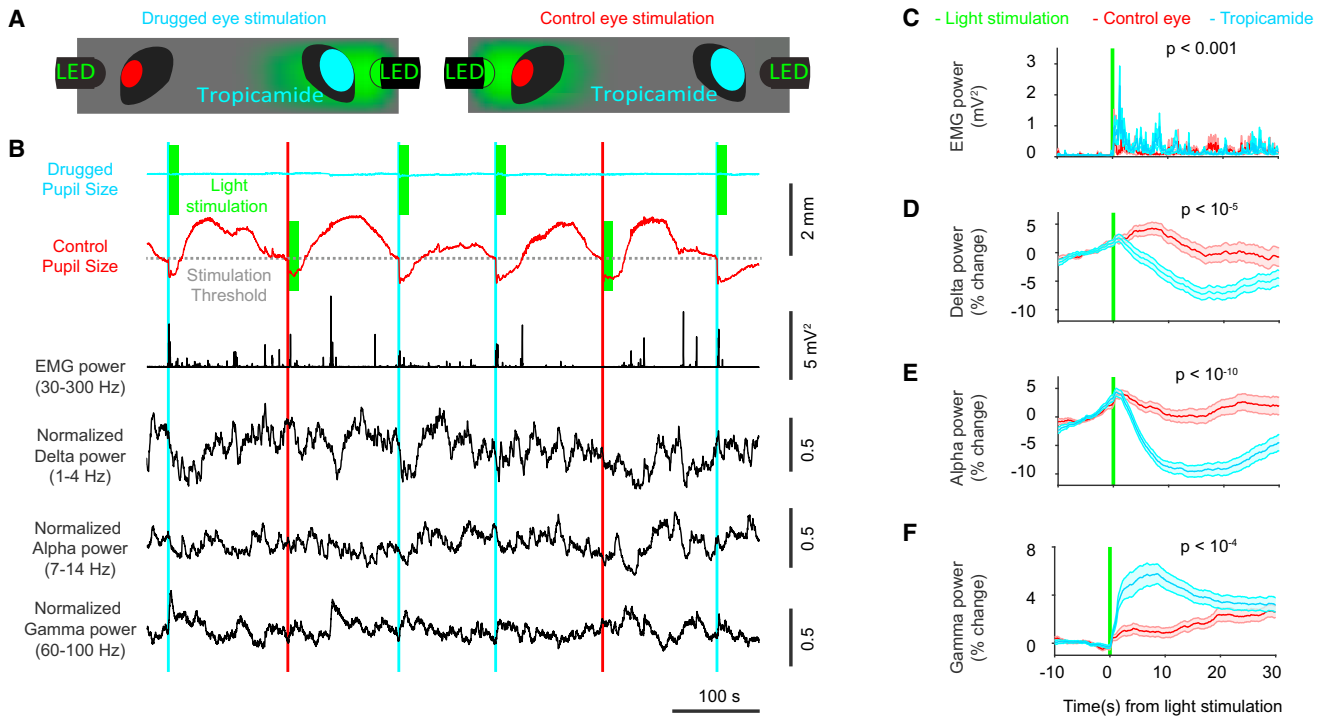


**Figure 4. Potential Role of Pupillary Constrictions during NREM Sleep**

(A) Schematics of the light-stimulation experiment.

(B) Pupil size traces of the drugged and control eyes with EMG and bandlimited ECoG power signals in a typical stimulation experiment. 1-s-long light stimulations are marked with green vertical bars on the pupil diameter traces.

(C) EMG activity at the time of light stimulation (two animals, 11 sessions, 196 control and 207 drugged-eye stimulation trials, mean  $\pm$  SEM) in C–F.

(D–F) Delta (D), alpha (E), and gamma (F) power change at the time of light stimulation.

application of dapiprazole led to a reduction of the maximum pupil diameter (Figures 3C–3F;  $p < 10^{-10}$ , Student's *t* test) but did not significantly change the correlation with the control eye pupil size (Figure 3F;  $p = 0.61$ , Student's *t* test) or with the power of alpha oscillations (Figure 3G;  $p = 0.41$ ). In contrast, blocking the parasympathetic drive by tropicamide application dilated the pupil and removed its prominent fluctuations during NREM sleep (Figures 3D and 3F;  $p < 10^{-6}$ ). More importantly, tropicamide treatment abolished the coupling that existed between pupil size and cortical activity (Figure 3G;  $p < 0.001$ ). These results suggest that fluctuations in pupil diameter during sleep are mainly driven by the parasympathetic pathway.

As an independent measurement of the parasympathetic drive, we also monitored the heart rate (extracted from the EMG signal; see STAR Methods). We found that pupil diameter and heart rate are positively correlated during NREM sleep (Figure S3). These findings complement previous reports showing that heart rate is correlated with parasympathetic modulation and also with cortical activity during NREM sleep [25, 26, 29].

#### Potential Function of Pupil Size Changes during Sleep

Might the observed pupil size fluctuations be playing a functional role during sleep? For instance, could pupil constriction be acting as a protector from visual stimuli in order to preserve the stability of deep sleep? In order to investigate the potential protective function of pupil constrictions, we artificially dilated

one pupil with tropicamide, while leaving the other pupil intact as a control. The control pupil also allowed us to monitor the depth of NREM sleep (Figure 2). We then stimulated either the eye with the dilated pupil or the control eye with 1-s-long flashes of light (510 nm, 90  $\mu$ W) at the moment of putative deepest NREM sleep (i.e., at local minima of control pupil diameter and high alpha and delta power; see STAR Methods) [25] (Figure 4A). We simultaneously monitored the pupil diameters of both eyes, as well as EMG and ECoG activity (Figure 4B).

As expected, we found that briefly illuminating the control pupil caused a pupillary light reflex (Figure 4B), yet it only had a minor effect on the sleep state (Figures 4B–4F, red trace). In contrast, when the dilated pupil was illuminated with equal amounts of light, the animals showed robust signs of change in sleep states (Figures 4B–4F, blue trace). Besides the expected light-reflex-related constriction of the contra-lateral control pupil, the light stimulus triggered a sharp decrease in ECoG delta (Figure 4D;  $p < 10^{-5}$ , Student's *t* test) and alpha (Figure 4E,  $p < 10^{-10}$ ) power, whereas it provoked significant increases in power in the high-gamma range (Figure 4F;  $p < 10^{-4}$ ) and EMG activity (Figure 4C;  $p < 0.001$ , Wilcoxon rank-sum test). Given that high power in alpha and delta oscillations are associated with NREM sleep whereas high gamma power is associated with arousal [21], we conclude that light stimulation resulted in an arousal-like state change. These changes are reminiscent of state transitions toward arousal induced by brief optogenetic

manipulations [20, 30, 31]. Taken together, these results indicate that sleep states are altered differently upon sudden illumination depending on pupil size. We thus suggest that sustained pupil constrictions during deep sleep might have a protective role preventing light-induced wake-up.

## DISCUSSION

Our study reveals that pupil size is dynamic during sleep and tightly coupled to the different sleep states. The deeper the sleep, the more the pupil constricts. This coupling is primarily mediated via the parasympathetic system and might provide a protective function by blocking visual input during deep sleep.

Pupil diameter and cortical states have been shown to be coupled to various degrees during wakefulness [13–15]. In our study, we show that cortico-pupillary coupling is enhanced during NREM compared to awake or REM states (Figure 2). We find that this correlation is strongest and negative in the alpha band (7 to 14 Hz, with a peak in the spindle band) and positive at higher frequencies (60 to 100 Hz) of cortical activity. This is consistent with previous reports during awake states in which the low alpha band (2 to 10 Hz) best predicted the decrease in sensory discrimination performance [15]. It is also reminiscent of recent reports in which slow fluctuations in the sigma range (10 to 15 Hz) were identified to best predict the depth and stability of NREM sleep [25, 32]. In the context of sleep versus wakefulness, this might also explain a higher correlation in our study compared to previous findings. We speculate that this tight coupling during sleep is not only due to the absence of external stimuli or locomotion, but is also related to the strong cyclical fluctuations of various neuronal and physiological parameters during NREM sleep, imposing a broad synchronicity on many processes.

The slow fluctuations in the  $\sim 0.01$  to 0.02 Hz range found to pattern the alpha rhythm and pupil diameter during NREM sleep have previously been described across several species and brain regions. These infra-slow oscillations have been termed “cyclic alternating patterns” in humans [33], but they have also been found modulating the 10 to 15 Hz power in mice [25], the hippocampal EEG rhythms [34, 35], and activity in locus coeruleus neurons during sleep in mice [36]. Similar fluctuations and coupling with the pupil diameter have been reported during urethane anesthesia in rats [37]. Due to its ease of implementation and cost efficiency, monitoring pupil diameter with iBip thus provides a non-invasive and reliable handle (Figures 2A, 2B, and S2A) to this ultra-slow rhythm, facilitating the identification of sleep stages or fragility periods during natural sleep.

One of the potential origins of such infra-slow oscillations might be the suprachiasmatic nucleus (SCN) of the hypothalamus. The SCN shows prominent  $\sim 0.01$  to 0.02 Hz oscillations [38, 39] and is connected to the main modulatory systems [40], which might alter cortical activity [16]. The SCN also has a direct and reciprocal connection with the pretectal nucleus (PTN) [41, 42], where the infra-slow oscillations are also observed [41–44] (Figure 3A). This pathway would provide a direct link to the parasympathetic modulation of the pupil via the Edinger-Westphal and the ciliary ganglion (Figure 3A). Alternatively, the thalamus has been suggested to modulate not only slow oscillations [45], but also alpha- and spindle-range activity in the cortex [46, 47]. Thalamic nuclei have been shown to oscillate at an infra-

slow rate [48] and to take part in maintaining the oscillations in SCN-PTN loop that impact pupillary constrictions [43]. Moreover, cholinergic activation of thalamic nuclei is reported to induce alpha rhythms [49]. Further experiments including subcortical recordings during sleep could reveal more about the role of different structures in generating infra-slow rhythms in the cortex and pupil size.

Blocking the sympathetic pathway with dapiprazole (an alpha adrenergic receptor antagonist) did not abolish the fluctuations or the correlation with ECoG oscillations (Figures 3C, 3F, and 3G). In contrast, tropicamide, a cholinergic blocker inhibiting the parasympathetic pathway to the pupil, significantly reduced the pupillary fluctuations and uncoupled them from the ECoG activity (Figures 3C, 3F, and 3G). Furthermore, we show that changes in the parasympathetically modulated heart rate [29] correlate positively to the pupillary oscillations in NREM sleep. These findings suggest that the observed dynamics of pupil diameter are not mediated by a decrease in sympathetic tone in the dilator muscle, but rather are mediated by an increase in the parasympathetic drive, causing an active pupil constriction during periods of deep sleep. Whether the cholinergic modulation of the pupil during NREM sleep is local or whether similar afferents can also affect other circuits, including the cortex, will have to be addressed in future experiments. The cholinergic tone in the brain is believed to be increase mostly during awake and REM states, yet there are reports of basal forebrain activity also in NREM sleep [50, 51].

How well these findings are applicable to other species, including humans, is not yet clear. Coupling of cortical activity and heart rhythm during sleep has been shown to be different in mice and humans [25, 26]. Also, blocking the parasympathetic input to the pupil was not sufficient to maintain complete dilations during sleep in children [52]. We can speculate that these inter-species differences might be due to differences in the balance of parasympathetic versus sympathetic drive during sleep or to different levels of baseline activity in autonomously regulated effector organs. The exact mechanism of how opposing autonomous systems act during sleep in both species remains an intriguing question for future sleep research.

This study was made possible by the fact that head-fixed mice can show an incomplete closure of their eyelids during natural sleep (nocturnal lagophthalmos). In humans, lagophthalmos can be caused by various conditions, including facial palsy (damage of the seventh nerve [53]). The reasons and mechanisms why this occurs in head-fixed sleeping mice are currently unclear. Anecdotally, we observed that the lagophthalmos decreased over weeks of repeated sleep sessions in some mice and might therefore be related to the habituation of the imposed body position. To reliably measure the pupil diameter during partial eyelid closure, we developed iBip. This technique was inspired by pupil tracking during *in vivo* two-photon calcium imaging, where the infrared light from the Ti Sapphire laser used for fluorophore excitation illuminates the back of the eyes [54]. The simplicity and low cost of iBip will most likely facilitate reliable pupil tracking in future studies during sleep and awake conditions. If used with higher frame rate ( $>60$  Hz), iBip is ideally suited to track the eye movement dynamics during REM sleep (Figure S2B; Movie S1). Eye movements during tonic and phasic REM periods have been shown to have neural and muscular

correlates in adult and developing mammals [55–57]. Currently, the state-of-the-art rodent eye-tracking systems include implanted coils or electrodes around the eye area [57, 58]. Our technique would therefore provide a simple and noninvasive alternative for REM sleep studies.

Finally, we provide the first evidence for the protective role of pupil constrictions during sleep. Although eyelids have primarily a protective function, they still transmit light sufficiently [59] to cause changes in cortical states [60]. Light stimulus into the pharmacologically dilated eye during NREM sleep resulted in a change in ECoG and EMG signals that were similar to state transitions toward arousal induced by brief optogenetic manipulations [20, 30, 31] (Figures 4D–4F). In contrast, light stimulation to the control eye had only a minor effect on sleep states. Until recently, one of the primary mechanisms for regulating cortex and sensory stimuli interaction during sleep was thought to be the thalamic gating hypothesis [61] (but see [60, 62]). Our study provides an additional, periphery-dependent gating mechanism for protecting the brain from waking up during phases of deep sleep. We hypothesize that pupillary constriction might ensure the continuity of NREM sleep periods [25], which is considered to be critical for memory consolidation [20, 63].

## STAR★METHODS

Detailed methods are provided in the online version of this paper and include the following:

- KEY RESOURCES TABLE
- CONTACT FOR REAGENT AND RESOURCE SHARING
- EXPERIMENTAL MODEL AND SUBJECT DETAILS
- METHOD DETAILS
  - Surgeries
  - Handling and sleep training
  - X-Ray imaging
  - Electrophysiology
  - Heart beat detection
  - Pupil tracking with iBip
  - Pharmacology and light stimulation experiments
- QUANTIFICATION AND STATISTICAL ANALYSIS
  - Sleep state classification
  - Pupil diameter detection
  - Pupil-based sleep state classification
  - Relating ECoG oscillations to pupil size fluctuations
  - Changes in ECoG signals with light stimulation

## SUPPLEMENTAL INFORMATION

Supplemental Information includes three figures and one movie and can be found with this article online at <https://doi.org/10.1016/j.cub.2017.12.049>.

## ACKNOWLEDGMENTS

We thank Gregorio Galifianes for insightful discussions, Anita Lüthi and Antoine Adamantidis for their advice and comments on the manuscript, and all members of the Huber lab for their support. This research was supported by the Swiss National Science Foundation (PP00P3\_133710), European Research Council (OPTOMOT), New York Stem Cell Foundation, and International Foundation for Paraplegia Research. D.H. is a New York Stem Cell Foundation-Robertson Investigator.

## AUTHOR CONTRIBUTIONS

O.Y., R.Z., and D.H. conceived the study. R.Z. developed the head-fixed sleep paradigm, conducted pilot head-fixed sleep experiments including the X-ray analysis, and discovered the coupling between pupil diameter and cortical activity. O.Y. conducted all experiments described in this paper including the design of pharmacology and stimulation experiments. O.Y. and R.Z. manually scored the data. O.Y. and M.P. analyzed the data. M.P. developed the video-acquisition and pupil-size-tracking systems. O.Y., M.P., and D.H. wrote the paper.

## DECLARATION OF INTEREST

The authors declare no competing interests.

Received: October 4, 2017

Revised: December 1, 2017

Accepted: December 21, 2017

Published: January 18, 2018

## REFERENCES

1. Eldar, E., Cohen, J.D., and Niv, Y. (2013). The effects of neural gain on attention and learning. *Nat. Neurosci.* *16*, 1146–1153.
2. Hesselmann, G., Kell, C.A., Eger, E., and Kleinschmidt, A. (2008). Spontaneous local variations in ongoing neural activity bias perceptual decisions. *Proc. Natl. Acad. Sci. USA* *105*, 10984–10989.
3. Cohen, M.R., and Maunsell, J.H.R. (2010). A neuronal population measure of attention predicts behavioral performance on individual trials. *J. Neurosci.* *30*, 15241–15253.
4. Aston-Jones, G., and Cohen, J.D. (2005). An integrative theory of locus coeruleus-norepinephrine function: adaptive gain and optimal performance. *Annu. Rev. Neurosci.* *28*, 403–450.
5. Bradley, M.M., Miccoli, L., Escrig, M.A., and Lang, P.J. (2008). The pupil as a measure of emotional arousal and autonomic activation. *Psychophysiology* *45*, 602–607.
6. Ebitz, R.B., Pearson, J.M., and Platt, M.L. (2014). Pupil size and social vigilance in rhesus macaques. *Front. Neurosci.* *8*, 100.
7. Partala, T., and Surakka, V. (2003). Pupil size variation as an indication of affective processing. *Int. J. Hum. Comput. Stud.* *59*, 185–198.
8. de Gee, J.W., Knapen, T., and Donner, T.H. (2014). Decision-related pupil dilation reflects upcoming choice and individual bias. *Proc. Natl. Acad. Sci. USA* *111*, E618–E625.
9. Nishiyama, J., Tanida, K., Kusumi, M., and Hirata, Y. (2007). The pupil as a possible premonitor of drowsiness. *Conf. Proc. IEEE Eng. Med. Biol. Soc.* *2007*, 1586–1589.
10. Morad, Y., Lemberg, H., Yofe, N., and Dagan, Y. (2000). Pupillography as an objective indicator of fatigue. *Curr. Eye Res.* *21*, 535–542.
11. Steidtmann, D., Ingram, R.E., and Siegle, G.J. (2010). Pupil response to negative emotional information in individuals at risk for depression. *Cogn. Emotion* *24*, 480–496.
12. Onorati, F., Barbieri, R., Mauri, M., Russo, V., and Mainardi, L. (2013). Characterization of affective states by pupillary dynamics and autonomic correlates. *Front. Neuroeng.* *6*, 9.
13. Reimer, J., Froudarakis, E., Cadwell, C.R., Yatsenko, D., Denfield, G.H., and Tolias, A.S. (2014). Pupil fluctuations track fast switching of cortical states during quiet wakefulness. *Neuron* *84*, 355–362.
14. Vinck, M., Batista-Brito, R., Knoblich, U., and Cardin, J.A. (2015). Arousal and locomotion make distinct contributions to cortical activity patterns and visual encoding. *Neuron* *86*, 740–754.
15. McGinley, M.J., David, S.V., and McCormick, D.A. (2015). Cortical Membrane Potential Signature of Optimal States for Sensory Signal Detection. *Neuron* *87*, 179–192.

16. Reimer, J., McGinley, M.J., Liu, Y., Rodenkirch, C., Wang, Q., McCormick, D.A., and Tolia, A.S. (2016). Pupil fluctuations track rapid changes in adrenergic and cholinergic activity in cortex. *Nat. Commun.* **7**, 13289.
17. Wallace, D.J., Greenberg, D.S., Sawinski, J., Rulla, S., Notaro, G., and Kerr, J.N. (2013). Rats maintain an overhead binocular field at the expense of constant fusion. *Nature* **498**, 65–69.
18. Weber, F., and Dan, Y. (2016). Circuit-based interrogation of sleep control. *Nature* **538**, 51–59.
19. Franken, P., Malafosse, A., and Tafti, M. (1999). Genetic determinants of sleep regulation in inbred mice. *Sleep* **22**, 155–169.
20. Rolls, A., Colas, D., Adamantidis, A., Carter, M., Lanre-Amos, T., Heller, H.C., and de Lecea, L. (2011). Optogenetic disruption of sleep continuity impairs memory consolidation. *Proc. Natl. Acad. Sci. USA* **108**, 13305–13310.
21. Buzsáki, G., and Draguhn, A. (2004). Neuronal oscillations in cortical networks. *Science* **304**, 1926–1929.
22. Steriade, M. (2006). Grouping of brain rhythms in corticothalamic systems. *Neuroscience* **137**, 1087–1106.
23. da Silva, F.H., van Lierop, T.H.M.T., Schrijer, C.F., and van Leeuwen, W.S. (1973). Organization of thalamic and cortical alpha rhythms: spectra and coherences. *Electroencephalogr. Clin. Neurophysiol.* **35**, 627–639.
24. Csicsvari, J., Jamieson, B., Wise, K.D., and Buzsáki, G. (2003). Mechanisms of gamma oscillations in the hippocampus of the behaving rat. *Neuron* **37**, 311–322.
25. Lecci, S., Fernandez, L.M.J., Weber, F.D., Cardis, R., Chatton, J.-Y., Born, J., and Lüthi, A. (2017). Coordinated infraslow neural and cardiac oscillations mark fragility and offline periods in mammalian sleep. *Sci. Adv.* **3**, e1602026.
26. Mensen, A., Zhang, Z., Qi, M., and Khatami, R. (2016). The occurrence of individual slow waves in sleep is predicted by heart rate. *Sci. Rep.* **6**, 29671.
27. Loewenfeld, I., and Lowenstein, O. (1999). *The Pupil: Anatomy, Physiology, and Clinical Applications* (Butterworth-Heinemann).
28. Hou, R.H., Samuels, E.R., Langley, R.W., Szabadi, E., and Bradshaw, C.M. (2007). Arousal and the pupil: why diazepam-induced sedation is not accompanied by miosis. *Psychopharmacology (Berl.)* **195**, 41–59.
29. Boudreau, P., Yeh, W.-H., Dumont, G.A., and Boivin, D.B. (2013). Circadian variation of heart rate variability across sleep stages. *Sleep* **36**, 1919–1928.
30. Adamantidis, A.R., Zhang, F., Aravanis, A.M., Deisseroth, K., and de Lecea, L. (2007). Neural substrates of awakening probed with optogenetic control of hypocretin neurons. *Nature* **450**, 420–424.
31. Herrera, C.G., Cadavieco, M.C., Jago, S., Ponomarenko, A., Korotkova, T., and Adamantidis, A. (2016). Hypothalamic feedforward inhibition of thalamocortical network controls arousal and consciousness. *Nat. Neurosci.* **19**, 290–298.
32. McKinney, S.M., Dang-Vu, T.T., Buxton, O.M., Solet, J.M., and Ellenbogen, J.M. (2011). Covert waking brain activity reveals instantaneous sleep depth. *PLoS ONE* **6**, e17351.
33. Parrino, L., Ferri, R., Bruni, O., and Terzano, M.G. (2012). Cyclic alternating pattern (CAP): the marker of sleep instability. *Sleep Med. Rev.* **16**, 27–45.
34. Buzsáki, G. (1986). Hippocampal sharp waves: their origin and significance. *Brain Res.* **398**, 242–252.
35. Penttonen, M., Nurminen, N., Miettinen, R., Sirviö, J., Henze, D.A., Csicsvári, J., and Buzsáki, G. (1999). Ultra-slow oscillation (0.025 Hz) triggers hippocampal afterdischarges in Wistar rats. *Neuroscience* **94**, 735–743.
36. Takahashi, K., Kayama, Y., Lin, J.S., and Sakai, K. (2010). Locus coeruleus neuronal activity during the sleep-waking cycle in mice. *Neuroscience* **169**, 1115–1126.
37. Blasiak, T., Zawadzki, A., and Lewandowski, M.H. (2013). Infra-slow oscillation (ISO) of the pupil size of urethane-anaesthetised rats. *PLoS ONE* **8**, e62430.
38. Miller, J.D., and Fuller, C.A. (1992). Isoperiodic neuronal activity in suprachiasmatic nucleus of the rat. *Am. J. Physiol.* **263**, R51–R58.
39. Aggelopoulos, N.C., and Meissl, H. (2000). Responses of neurones of the rat suprachiasmatic nucleus to retinal illumination under photopic and scotopic conditions. *J. Physiol.* **523**, 211–222.
40. Aston-Jones, G., Chen, S., Zhu, Y., and Oshinsky, M.L. (2001). A neural circuit for circadian regulation of arousal. *Nat. Neurosci.* **4**, 732–738.
41. Moga, M.M., and Moore, R.Y. (1997). Organization of neural inputs to the suprachiasmatic nucleus in the rat. *J. Comp. Neurol.* **389**, 508–534.
42. Krout, K.E., Kawano, J., Mettenleiter, T.C., and Loewy, A.D. (2002). CNS inputs to the suprachiasmatic nucleus of the rat. *Neuroscience* **110**, 73–92.
43. Szkudlarek, H.J., Herdizina, O., and Lewandowski, M.H. (2008). Ultra-slow oscillatory neuronal activity in the rat olivary pretectal nucleus: comparison with oscillations within the intergeniculate leaflet. *Eur. J. Neurosci.* **27**, 2657–2664.
44. Szkudlarek, H.J., Orlowska, P., and Lewandowski, M.H. (2012). Light-induced responses of slow oscillatory neurons of the rat olivary pretectal nucleus. *PLoS ONE* **7**, e33083.
45. Crunelli, V., and Hughes, S.W. (2010). The slow (<1 Hz) rhythm of non-REM sleep: a dialogue between three cardinal oscillators. *Nat. Neurosci.* **13**, 9–17.
46. De Gennaro, L., and Ferrara, M. (2003). Sleep spindles: an overview. *Sleep Med. Rev.* **7**, 423–440.
47. Lorincz, M.L., Kékesi, K.A., Juhász, G., Crunelli, V., and Hughes, S.W. (2009). Temporal framing of thalamic relay-mode firing by phasic inhibition during the alpha rhythm. *Neuron* **63**, 683–696.
48. Hughes, S.W., Lőrincz, M.L., Parri, H.R., and Crunelli, V. (2011). Infraslow (<0.1 Hz) oscillations in thalamic relay nuclei basic mechanisms and significance to health and disease states. *Prog. Brain Res.* **193**, 145–162.
49. Lőrincz, M.L., Crunelli, V., and Hughes, S.W. (2008). Cellular dynamics of cholinergically induced alpha (8–13 Hz) rhythms in sensory thalamic nuclei in vitro. *J. Neurosci.* **28**, 660–671.
50. Lőrincz, M.L., Gunner, D., Bao, Y., Connelly, W.M., Isaac, J.T.R., Hughes, S.W., and Crunelli, V. (2015). A distinct class of slow (~0.2–2 Hz) intrinsically bursting layer 5 pyramidal neurons determines UP/DOWN state dynamics in the neocortex. *J. Neurosci.* **35**, 5442–5458.
51. Hangya, B., Ranade, S.P., Lorenc, M., and Kepecs, A. (2015). Central cholinergic neurons are rapidly recruited by reinforcement feedback. *Cell* **162**, 1155–1168.
52. Krastel, H., Alexandridis, E., and Rating, D. (1996). [Sleep modifies anticholinergic mydriasis]. *Ophthalmologie* **93**, 476–478.
53. Pereira, M.V., and Glória, A.L. (2010). Lagophthalmos. *Semin. Ophthalmol.* **25**, 72–78.
54. Garcia-Junco-Clemente, P., Ikrar, T., Tring, E., Xu, X., Ringach, D.L., and Trachtenberg, J.T. (2017). An inhibitory pull-push circuit in frontal cortex. *Nat. Neurosci.* **20**, 389–392.
55. Brooks, P.L., and Peever, J. (2016). A Temporally Controlled Inhibitory Drive Coordinates Twitch Movements during REM Sleep. *Curr. Biol.* **26**, 1177–1182.
56. Stahl, J.S. (2004). Using eye movements to assess brain function in mice. *Vision Res.* **44**, 3401–3410.
57. Sánchez-López, A., and Escudero, M. (2011). Tonic and phasic components of eye movements during REM sleep in the rat. *Eur. J. Neurosci.* **33**, 2129–2138.
58. Fulda, S., Romanowski, C.P., Becker, A., Wetter, T.C., Kimura, M., and Fenzel, T. (2011). Rapid eye movements during sleep in mice: high trait-like stability qualifies rapid eye movement density for characterization of phenotypic variation in sleep patterns of rodents. *BMC Neurosci.* **12**, 110.
59. Bierman, A., Figueiro, M.G., and Rea, M.S. (2011). Measuring and predicting eyelid spectral transmittance. *J. Biomed. Opt.* **16**, 067011.

60. Sharon, O., and Nir, Y. (2017). Attenuated fast steady-state visual evoked potentials during human sleep. *Cereb. Cortex*. Published online February 25, 2017. <https://doi.org/10.1093/cercor/bhx043>.
61. McCormick, D.A., and Bal, T. (1994). Sensory gating mechanisms of the thalamus. *Curr. Opin. Neurobiol.* *4*, 550–556.
62. Sela, Y., Vyazovskiy, V.V., Cirelli, C., Tononi, G., and Nir, Y. (2016). Responses in Rat Core Auditory Cortex are Preserved during Sleep Spindle Oscillations. *Sleep* *39*, 1069–1082.
63. Walker, M.P., and Stickgold, R. (2004). Sleep-dependent learning and memory consolidation. *Neuron* *44*, 121–133.
64. Jacobs, G.H., Williams, G.A., and Fenwick, J.A. (2004). Influence of cone pigment coexpression on spectral sensitivity and color vision in the mouse. *Vision Res.* *44*, 1615–1622.
65. Xu, M., Chung, S., Zhang, S., Zhong, P., Ma, C., Chang, W.C., Weissbourd, B., Sakai, N., Luo, L., Nishino, S., and Dan, Y. (2015). Basal forebrain circuit for sleep-wake control. *Nat. Neurosci.* *18*, 1641–1647.

## STAR★METHODS

### KEY RESOURCES TABLE

REAGENT or RESOURCE	SOURCE	IDENTIFIER
Chemicals, Peptides, and Recombinant Proteins		
Tropicamidum, % 0.5	Thea Pharma	Tropicamide 0.5% SDU Faure
Dapiprazole, % 0.5	Angelini	Glamidolo
Experimental Models: Organisms/Strains		
Mouse: C57BL/6	Charles River Laboratories	C57BL/6J
Software and Algorithms		
Electrophysiology acquisition interface	Open-ephys.org	Open Ephys GUI
Other		
USB camera, 0.3MP Mono Firefly MV USB	Point Grey Research	FMVU-03MTM
Micro-video lens, 25.0 mm FL, No IR-Cut Filter, f/2.5	Edmund Optics	#56-776
LED, 940 nm 5mm T-1 3/4	Everlight Electronics	IR323
Electrophysiology acquisition board	Open-ephys.org	Acquisition board
Headstage, 32 channels	Intan Technologies	RHD2132/RHD2216
ECoG wires, 75 $\mu$ m	Science Products	AU-3T
EMG wires, 75 $\mu$ m	Science Products	SS-2T/HH

### CONTACT FOR REAGENT AND RESOURCE SHARING

Further information and requests for resources and reagents should be directed to and will be fulfilled by the Lead Contact, Daniel Huber ([daniel.huber@unige.ch](mailto:daniel.huber@unige.ch)).

### EXPERIMENTAL MODEL AND SUBJECT DETAILS

Seven wild-type (C57BL/6, 10 to 11 week old) male mice were used for this study. Animals were caged individually, kept at 12 hr dark/light cycle and were placed under a water restriction regime (1 mL/day). The habituation sessions and experiments were performed in the second tierce of the light period. All procedures were reviewed and approved by the local ethics committee and the authorities of the Canton Geneva.

### METHOD DETAILS

#### Surgeries

To implant the titanium frame for head-fixation, mice were anesthetized with 2% isoflurane-oxygen mix and kept warm on a heating pad (T/PUMP, TP500C). Injections of carprofen (Rimadyl, 50 mg/mL, 1:20 dilution in NaCl, 50  $\mu$ L sub-cutaneous), buprenorphine (Temgesic, 0.3 mg/mL 1:2 dilution in NaCl 25  $\mu$ L intramuscular) and dexamethasone (Mephamesone-4, 4 mg/mL, 20  $\mu$ L intramuscular) were given. The eyes were covered with Vaseline. Local anesthetic lidocaine (Rapidocain 10 mg/mL, 50  $\mu$ L subcutaneous) was applied to the scalp before removal. A titanium head bar was glued to the dried skull with cyanoacrylic glue (ergo 5300 elastomer). Small craniotomies for the ECoG electrodes were drilled over primary motor cortex (in right hemisphere 1.5 mm lateral (L), 1.5 mm rostral (R) of bregma) and cerebellum (all animals, midline 6 mm R). Custom electrodes for ECoG recordings were made from Teflon coated gold wires (75  $\mu$ m, AU-3T, Science Products). The electrodes were soldered to a miniature connector (Millmax). For EMG recordings, custom electrodes were fabricated with twisted Teflon coated half hard stainless steel wires (75  $\mu$ m, SS-2T/HH, Science Products). The coating of the EMG electrodes was stripped off with sharp tweezers and used as bipolar electrodes. These wires were guided into the neck muscles with a 24 G needle and immobilized in the muscle by bending the ends to a hook. Finally, the electrodes and the titanium frame were covered with transparent dental acrylic (Lang Dental Ortho-Jet Powder B1320). The animals were taken off the anesthesia, left to recover in a clean cage placed on a heating pad for 2 hr. Recordings started after an additional recovery period of 7 to 10 days.

#### Handling and sleep training

Animals were handled for 10 min per day for 6 consecutive days. To habituate the mice to sleep under head-fixed condition, their body was placed in a small plastic box (80x80x50 mm) which was filled with cotton bedding to comfortably accommodate the

animal's body. The head of the animals was kept at a 30° angle to imitate the natural sleep position in during head fixation (Figure 1C). During habituation and recordings the mice were held in a sound and light isolated Faraday cage. Through the first three sessions the mice were kept head-fixed for 10, 20 and 30 min and were delivered random water rewards through a lick port. In later sessions water delivery period remained 30 min while the duration of the head fixation increased by 20 to 30 min reaching to ~4 h in 10 to 12 sessions. The state of the mouse was continuously monitored with an IR USB camera (Point Grey Firefly MV USB FMVU-03MTM).

### X-Ray imaging

X-Ray imaging to determine the body position during different head-fixed conditions was conducted using a custom lead shielded BV-25 (Philips) X-Ray machine equipped with a 120 × 70 mm CMOS detector (1207, Dexela). The X-Ray source was run at 52 kV. The effective dose in the path was determined with a RadeEye B20 Geiger counter (Thermo Scientific) and the cumulative dose during the lifetime was kept below 10mSv per animal. Images were acquired and analyzed using custom MATLAB code. During the X-Ray imaging the mice were continuously monitored with an IR USB camera (Point Grey Firefly MV).

### Electrophysiology

ECoG and EMG data were acquired at 1 kHz using a 16 (for natural sleep recordings in the home cage) or 32 channel head stage (for head-fixed recordings) (RHD2132/RHD2216 Amplifier Board, OpenEphys). The signals from the ECoG electrode were referenced to the cerebellar electrode and the bipolar EMG channels were subtracted from each other. Signals were high-pass filtered at 0.1 Hz and a Fast Fourier Transform (FFT) was used to calculate the power spectrum of the ECoG and EMG signals with a 2 s sliding window sequentially shifted in 0.1 s increments. Each 2 s interval of data was first multiplied by an equal length Hamming window before applying the FFT. For the analysis of natural sleep recordings cortical electrodes were referenced to their contralateral counterparts to eliminate movement artifacts on the ECoG signal.

### Heart beat detection

Heart rate was extracted from the EMG signal by detecting the prominent biphasic pulses ( $\approx 10$  ms duration) occurring rhythmically. For this purpose, the EMG signal was filtered between 30 and 300 Hz and heart pulses were detected with the *findpeaks* MATLAB function applied to the squared absolute values of the filtered signal. Heart rate was computed by binning the pulse times into 1 s bins and calculating the mean of the inter-pulse-interval inverse values for each bin. Heart rate was up-sampled to the time base of pupil size by linear interpolation before calculating the cross-correlation between their Z-scored values.

### Pupil tracking with iBip

Pupils of both eyes were monitored with two separate digital USB cameras (Point Grey Research 0.3MP Mono Firefly MV USB FMVU-03MTM) and acquired and saved at 10 frames/s (240×376 pixels 8-bit greyscale images) with a custom video acquisition system written in MATLAB. The timestamp of each frame relative to a digital trigger were saved in the image headers and used for post hoc alignment of pupil and electrophysiology data. To obtain high contrast images of the pupil we used infrared back-illumination pupillometry (iBip). iBip consists of a 940 nm LED (Everlight Electronics, 3 mW, 40 mA, 1.2 V) positioned on the skull above frontal cortex. Light reached the head through the polished dental acrylic of the head-cap. Light emission to the side of the LED was blocked with black tape shielding. The LED at this intensity level did not produce any additional heating of the illuminated area (measured by Peaktech 5140 digital thermometer).

### Pharmacology and light stimulation experiments

Before the start of the recording session, one eye of the mouse was instilled with a drop of cholinergic receptor antagonist Tropicamide (Tropicamide, Thea Pharma,  $\sim 100$   $\mu$ L, 0.5%) or the alpha receptor antagonist Dapiprazole (Glamidolo, Angelini,  $\sim 100$   $\mu$ L, 0.5%), while the other eye was left intact ( $n = 7$  mice). Animals were given 1 to 2 days of break in between pharmacological experiments. The side of the drugged eye was switched every session. For the light stimulation experiments a LED light source (510 nm, 90  $\mu$ W) was positioned 20 mm in front of each eye ( $n = 2$  mice). 510 nm wavelength was chosen as the center of the mouse green cone spectrum [64] and the 90  $\mu$ W were found to be sufficient to induce changes in the ECoG bands (as determined in pilot experiments). The LEDs were mounted in 5 mm wide black tubes to restrict illumination to the targeted eye only. Light pulses (1 s) were triggered manually during NREM sleep when the control pupil diameter was in a decreasing phase and reached  $\sim 0.5$  mm.

## QUANTIFICATION AND STATISTICAL ANALYSIS

### Sleep state classification

Sleep classification was carried out semi-automatically in several consecutive steps. First, delta and theta power signals were calculated by summing the ECoG power in the 1 to 4 Hz, and 6 to 10 Hz frequency ranges, respectively. The EMG power was summed in the ranges between 30 and 300 Hz. NREM sleep was identified by 50 s uninterrupted periods where delta power was two standard deviations larger than its mean and EMG power smaller than its mean (similar to [65]). A state was marked as REM sleep when the theta/delta ratio was two standard deviations larger than its mean and EMG power was two standard deviations smaller than its mean. Everything else was marked as awake. All sleep stages were proof read and corrected by two experienced observers. Micro

awakenings during NREM were identified manually and marked as awake. NREM bouts that were interrupted by micro awakenings were considered continuous. All analysis was carried out with custom MATLAB scripts.

### Pupil diameter detection

To extract the pupil diameter, single frame images were first centered on and cropped around the pupil (90x90 pixels). The greyscale pixel values of the cropped image were classified into 2 clusters (dark and bright pixels) using K-means clustering. A binary image, obtained by setting the dark pixels to 0 and the bright pixels to 1, was used to find connected components (bwconncomp function in MATLAB) and the largest component was deemed to correspond to the pupil. An ellipse was fit to the component's contour (linear least-squares fitting) and its major axis was defined to be the pupil diameter. Eye blinks and periods with closed eyelids were manually detected and excluded from analysis. The pupil diameter traces were upsampled to 1 kHz by linear interpolation to match the ECoG signal sampling and low pass filtered at 2 Hz (except for light stimulation experiments). Converting pupil size to mm was done by calibrating the images to a video recording of 1 mm square graph paper.

### Pupil-based sleep state classification

A neural network with one hidden layer was used to classify sleep states based on pupil diameter. For each sleep session classification, the network was first trained on data from all other sessions ( $n = 5$  mice). Training trials consisted of 100 s pupil diameter traces (sampled at 10 Hz) at the input layer and the corresponding sleep state label at the output layer (awake, REM or NREM). Sleep bouts that were shorter than 100 s were omitted in this analysis. The hidden layer size was set to 30 nodes. The trained network coefficients were then used to predict sleep states of the session not used for training. Prediction accuracy was calculated as the % of the 100 s trials correctly classified in each session and separately for each of the three sleep states.

### Relating ECoG oscillations to pupil size fluctuations

The recorded ECoG signals of each session were bandpass filtered into the traditional delta (1 to 4 Hz), theta (4 to 7 Hz), alpha (7 to 14 Hz), beta (15 to 30 Hz), low (30 to 60 Hz) and high gamma (60 to 100 Hz) frequency bands using a bidirectional second order Butterworth filter, thus eliminating possible phase shifts introduced by filtering. The frequency definitions correspond to cut-off values at  $-3$  dB attenuation. The instantaneous amplitude of each bandlimited oscillation was obtained by computing the magnitude of its Hilbert transform. To assess how the magnitude of cortical oscillations changes relative to fluctuations in pupil size, Pearson's correlation ( $R$ ) was calculated between the low-pass filtered (bidirectional single pole IIR filter, i.e., exponential decay impulse response) Hilbert amplitude signals and pupil diameter. For each frequency band, the time constant of the low pass filter that maximized  $|R|$  was evaluated for each sleep state separately (fminsearch function in MATLAB,  $n = 5$  mice).

We used general linear modeling (GLM) to assess the extent to which ECoG oscillations of each band can be used to model changes in pupil diameter. The GLM consisted of two regressors: the filtered ECoG oscillatory amplitude and a constant term. The former trace was first standardized by taking its z-score. The low pass filter time constant and the two GLM coefficients that minimized the sum of squared errors between the fitted and actual pupil diameter were evaluated on half of the data in each session. The other half of the data, not used for parameter fitting, was used to validate the prediction by computing the explained variance as  $1 - \text{var}(p_m - p_{pr}) / \text{var}(p_m)$  where  $p_m$  is the measured and  $p_{pr}$  the predicted pupil diameter and  $\text{var}()$  symbolizes the signal's variance.

The spectral content, in the infra-slow frequency range, of pupil fluctuations and bandlimited ECoG oscillation amplitude changes during NREM sleep (Figures S2E–S2G) was obtained using the Fast Fourier Transform (FFT). Hilbert transforms of the bandpass filtered ECoG signals or the pupil diameter trace were first normalized to their respective mean values for each NREM bout separately and then multiplied by an equal length Hamming window. The traces were padded with zeros for the number of FFT points to be equal to a higher power of 2. The obtained absolute FFT values were first interpolated at a 0.001 Hz frequency resolution and then averaged across all NREM bouts of an experimental session.

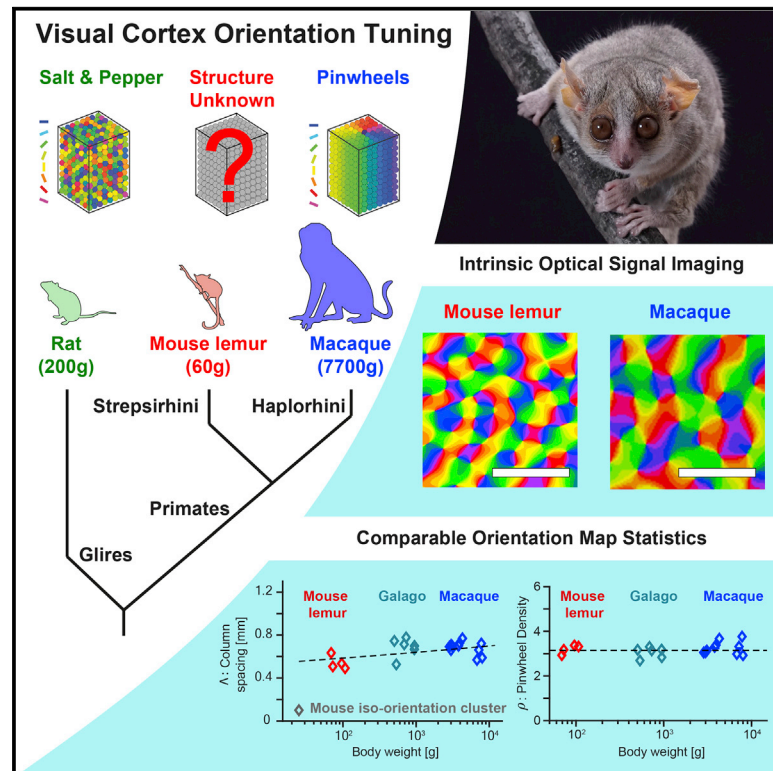
### Changes in ECoG signals with light stimulation

For light stimulation experiments, % change was calculated with respect to a 10 s baseline preceding stimulus onset. Drug and control conditions were compared (red and blue traces in Figures 4C–4F) based on mean values of a 20 s post stimulation period.

# Current Biology

## Orientation Preference Maps in *Microcebus murinus* Reveal Size-Invariant Design Principles in Primate Visual Cortex

### Graphical Abstract



### Authors

Chun Lum Andy Ho,  
Robert Zimmermann,  
Juan Daniel Flórez Weidinger, ...,  
Alessandra Angelucci, Fred Wolf,  
Daniel Huber

### Correspondence

daniel.huber@unige.ch

### In Brief

Orientation preference maps are a hallmark of V1 organization in all primates studied thus far, yet they are absent in rodents. It is uncertain whether these structures scale with body or brain size. Using intrinsic signal imaging, Ho et al. reveal the presence of such maps in the V1 of the world's smallest primate, the mouse lemur (*Microcebus murinus*).

### Highlights

- Mouse lemur V1 possesses orientation preference maps with pinwheel arrangement
- The size and statistics of mouse lemur V1 pinwheels are comparable to the macaque
- Orientation preference columns only weakly scale with body size in primates



## Article

# Orientation Preference Maps in *Microcebus murinus* Reveal Size-Invariant Design Principles in Primate Visual Cortex

Chun Lum Andy Ho,<sup>1,11</sup> Robert Zimmermann,<sup>1,11</sup> Juan Daniel Flórez Weidinger,<sup>2</sup> Mario Prsa,<sup>1</sup> Manuel Schottdorf,<sup>2</sup> Sam Merlin,<sup>3</sup> Tsuyoshi Okamoto,<sup>4</sup> Koji Ikezoe,<sup>5</sup> Fabien Pifferi,<sup>6</sup> Fabienne Aujard,<sup>6</sup> Alessandra Angelucci,<sup>3</sup> Fred Wolf,<sup>2,7,8,9,10</sup> and Daniel Huber<sup>1,12,\*</sup>

<sup>1</sup>University of Geneva, Department of Basic Neurosciences, Rue Michel Servet 1, Geneva 1211, Switzerland

<sup>2</sup>Max Planck Institute for Dynamics and Self-Organization, Am Faßberg 17, Göttingen 37077, Germany

<sup>3</sup>Moran Eye Center, University of Utah, Department of Ophthalmology and Visual Science, 65 Mario Capecchi Drive, Salt Lake City, UT 84132, USA

<sup>4</sup>Kyushu University, Faculty of Arts and Science, 744 Motooka Nishi-ku, Fukuoka 819-0395, Japan

<sup>5</sup>Center for Information and Neural Networks, Osaka University and National Institute of Information and Communications Technology, Graduate School of Frontier Biosciences, 1-3 Yamadaoka Suita, Osaka 565-0871, Japan

<sup>6</sup>UMR CNRS/MNHN 7179, Mécanismes Adaptatifs et Evolution, 1 Avenue du Petit Chateau, Brunoy 91800, France

<sup>7</sup>Campus Institute for Dynamics of Biological Networks, Hermann-Rein-Straße 3, Göttingen 37075, Germany

<sup>8</sup>Bernstein Center for Computational Neuroscience, Hermann-Rein-Straße 3, Göttingen 37075, Germany

<sup>9</sup>Max Planck Institute of Experimental Medicine, Hermann-Rein-Straße 3, Göttingen 37075, Germany

<sup>10</sup>Institute for Dynamics of Complex Systems, Georg-August University, Friedrich-Hund-Platz 1, Göttingen 37073, Germany

<sup>11</sup>These authors contributed equally

<sup>12</sup>Lead Contact

\*Correspondence: [daniel.huber@unige.ch](mailto:daniel.huber@unige.ch)  
<https://doi.org/10.1016/j.cub.2020.11.027>

## SUMMARY

Orientation preference maps (OPMs) are a prominent feature of primary visual cortex (V1) organization in many primates and carnivores. In rodents, neurons are not organized in OPMs but are instead interspersed in a “salt and pepper” fashion, although clusters of orientation-selective neurons have been reported. Does this fundamental difference reflect the existence of a lower size limit for orientation columns (OCs) below which they cannot be scaled down with decreasing V1 size? To address this question, we examined V1 of one of the smallest living primates, the 60-g prosimian mouse lemur (*Microcebus murinus*). Using chronic intrinsic signal imaging, we found that mouse lemur V1 contains robust OCs, which are arranged in a pinwheel-like fashion. OC size in mouse lemurs was found to be only marginally smaller compared to the macaque, suggesting that these circuit elements are nearly incompressible. The spatial arrangement of pinwheels is well described by a common mathematical design of primate V1 circuit organization. In order to accommodate OPMs, we found that the mouse lemur V1 covers one-fifth of the cortical surface, which is one of the largest V1-to-cortex ratios found in primates. These results indicate that the primate-type visual cortical circuit organization is constrained by a size limitation and raises the possibility that its emergence might have evolved by disruptive innovation rather than gradual change.

## INTRODUCTION

Primates and rodents are closely related. The two lineages probably evolved from a common ancestor between the late Cretaceous and the early Eocene<sup>1,2</sup> (Figure 1A). In contrast to most rodents, primates developed into highly encephalized and visual animals, which entailed substantial transformations of their cortical visual system.<sup>3</sup> These transformations specifically affected the functional architecture of the primary visual cortex (V1). Orientation-tuned neurons in primate V1 (as well as in carnivores and ungulates) are clustered into functional orientation columns<sup>4–6</sup> and arranged in a pinwheel-like manner. Such an organization can minimize wiring length,

economizing the volume, building, and maintenance cost of V1.<sup>7</sup> Adjacent columns with the same preferred orientation exhibit a typical spacing,  $\Delta$ . A V1 subregion of area of  $\Delta^2$ , termed hypercolumn area, will typically contain the full set of orientation preferences.<sup>8–10</sup> In contrast to primates, tuned neurons are randomly interspersed in all rodents studied so far<sup>11</sup> (but see Ringach et al.<sup>12</sup>; Figure 1A). Since this “salt and pepper” organization is considered the most likely ancestral state,<sup>5,13–15</sup> a fundamental transformation of V1 circuitry leading to the emergence of functional cortical columns must have marked the course of brain evolution in the primate lineage. Assuming a fixed minimal size of functional cortical columns, the total area of the cortex and the size of V1 are



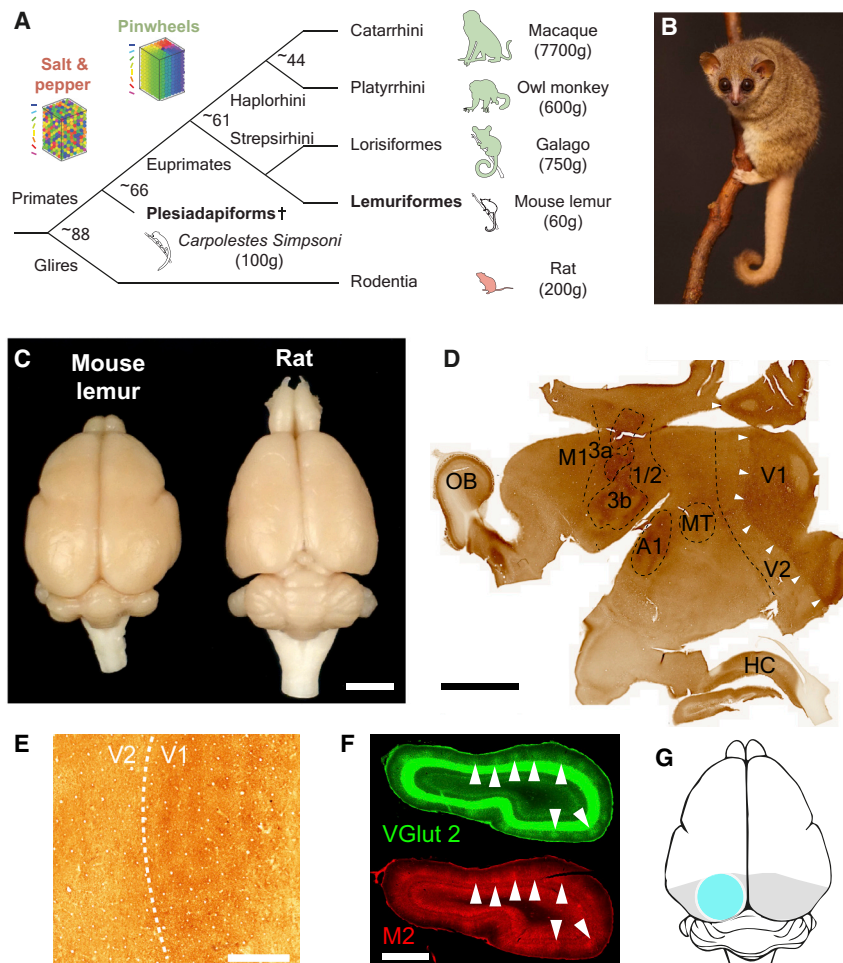


**Figure 1. Mouse Lemur (*Microcebus murinus*)**

(A) Schematic tree of rodent and primate evolution. Species where V1 pinwheels have been reported are labeled in green; species with salt and pepper organization are in red. Numbers at the bifurcation points are approximate ages in millions of years (from Seiffert et al.,<sup>17</sup> however, see also O’Leary et al. and Zhang et al.<sup>2,18</sup> Primate-glires split date taken from Huchon et al.<sup>19</sup>).

(B) A mouse lemur climbing on a branch.

(C) Size comparison of a mouse lemur brain (left) and a rat brain (right; scale bar, 5 mm).

(D) Cytochrome oxidase (CO) staining of a flat-mounted mouse lemur cortex. The visual cortex is clearly delineated (white arrows) by the dark and patchy appearance of the CO staining. OB: olfactory bulb; M1: primary motor cortex; 3a, 3b, 1/2: areas of the primary somatosensory cortex; A1: auditory cortex; MT: medial temporal cortex; V1, V2: primary secondary visual cortex; HC: hippocampus. Scale bar, 5 mm.

(E) High-resolution view of a CO staining in a flat mount with a patch-like pattern in the V1. Scale bar, 1 mm.

(F) Two adjacent coronal sections through V1 with immunolabeling for vesicular glutamate transporter 2 (VGlut2) and the muscarinic receptor 2 (M2). The arrows indicate overlapping patches of dense fiber labeling in supra-granular layers. Representative example for n = 2 animals. Scale bar, 1 mm.

(G) Schematic top view of the mouse lemur brain with V1 outlined in gray and the location of the chronic imaging window in light blue.

predicted to be critical variables in this transformation: below a certain V1 size, the reduced visual field coverage might outweigh the potential benefit of a columnar organization, thus favoring the salt and pepper organization.<sup>14,16</sup> But could cortical orientation columns perhaps be miniaturized? Recently, clusters of orientation-selective neurons were described in mouse V1, which might represent micro-scale precursors of full-fledge orientation columns.<sup>12,15</sup> We therefore asked whether V1 of the smallest living primate, the mouse lemur (Figures 1B and 1C), contains primate-type functional orientation columns and whether they may be miniaturized in such a small brain.

## RESULTS

### Mouse Lemur Visual Cortex Anatomy

We first determined the location and boundaries of the mouse lemur visual cortex. We performed cytochrome oxidase (CO) labeling on cortical flat mounts of three brains. We found that V1 is clearly delineated by a zone containing regularly spaced patterns of darker-stained CO patches, also known as CO blobs (Figures 1D and 1E). The patches were, on average, 269  $\mu\text{m}$  (SD = 78.7  $\mu\text{m}$ ; n = 2 animals; 31 patches) wide and spaced by 485  $\mu\text{m}$  (SD = 70.5  $\mu\text{m}$ ). This is similar to histological results in

other primates,<sup>5,20</sup> yet it is markedly different from the homogeneous CO labeling found in rodents with equally sized or larger brains such as the agouti<sup>21</sup> or the gray squirrel.<sup>22</sup> In addition, we labeled coronal brain sections with antibodies against the vesicular glutamate transporter 2 (VGlut2) and the muscarinic receptor 2 (M2, Figure 1F). VGlut2 staining reveals the boundaries of V1 by dense labeling of the zone of thalamic afferents into the cortical layer IV<sup>23</sup> (L4). Similar to the CO staining, the supra-granular layers contained regularly spaced patches of VGlut2, confirming previous reports,<sup>23</sup> as well as overlapping M2 labeling (white arrows in Figure 1F). Taken together, our characterization of the mouse lemur V1 confirmed that it contains key anatomical hallmarks of primate V1 organization.

### Orientation Preference Maps in the Mouse Lemur

Next, we asked whether V1 also contains functional orientation maps similar to the ones found in larger primates.<sup>24,25</sup> Initial electrode recordings by Cooper and colleagues<sup>26</sup> have already revealed a retinotopic organization of mouse lemur V1. We performed intrinsic signal imaging through a chronic cranial window positioned over V1 (Figure 1G; STAR Methods). Visual stimuli consisting of moving gratings oriented in eight different directions were presented to lightly anesthetized mouse lemurs on a computer screen. Intrinsic optical signals were quantified

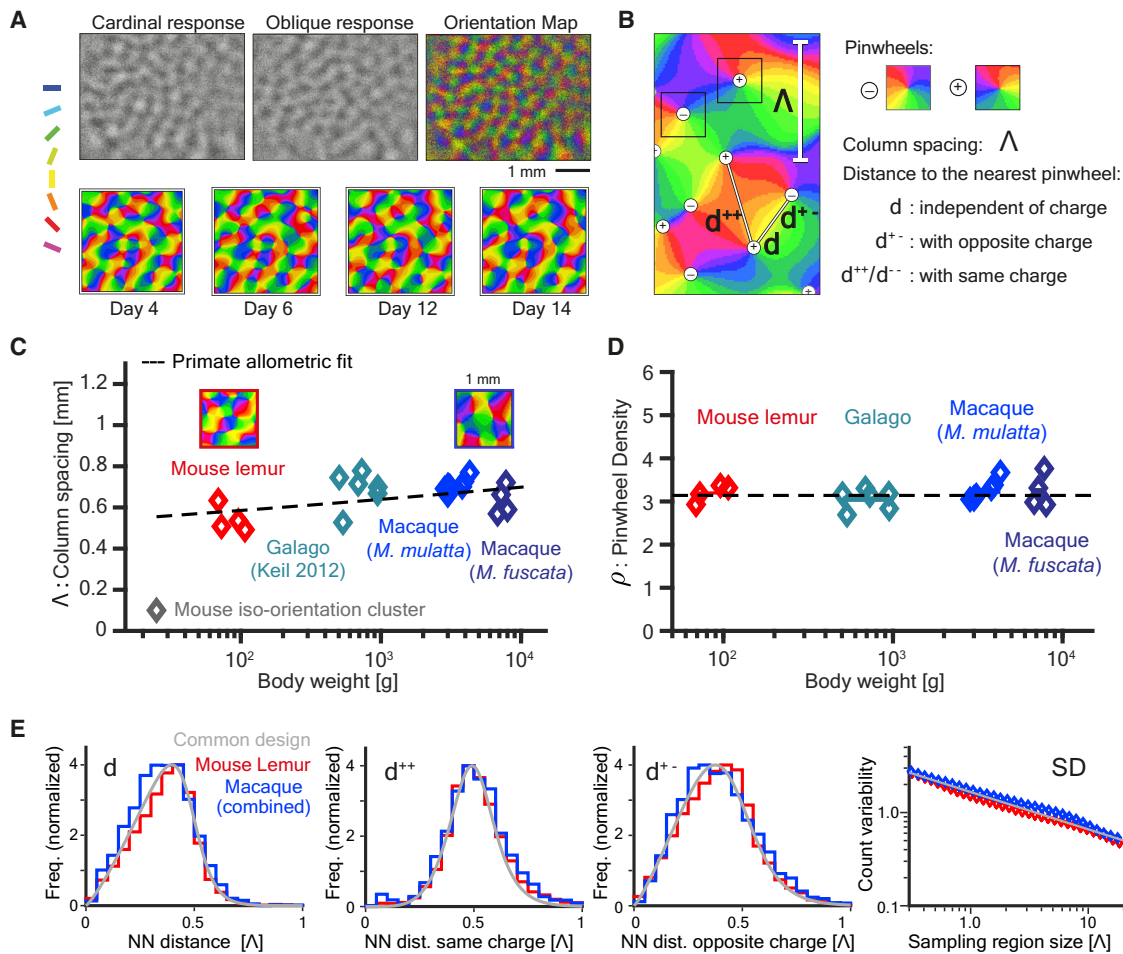


**Figure 2. Orientation Preference Maps and Map Statistics**

(A) Intrinsic signal imaging responses obtained by subtracting responses to the two cardinal and two oblique directions, respectively, displayed as a color-coded orientation map. The responses were stable for up to 14 days of chronic imaging (bottom row; see also Figure S1).  
 (B) Graphical depiction of the definitions of column spacing and pinwheel distances. Pinwheels can assume one of two discrete “charges” —positive or negative—depending on the topological arrangement of orientation preference around the pinwheel center. The nearest neighbor (NN) distance is the shortest distance between pinwheels, dependent or independent of charge.  
 (C) Column spacing of the mouse lemur and macaques (*Macaca fuscata* and *Macaca mulatta*) among the primates (adapted from Keil et al.<sup>14</sup>). Primate allometric fit to species means to guide the eye:  $y = 0.4903x^{0.03842}$  (See also Figure S2A).  
 (D) Pinwheel density of the mouse lemur and macaque among the primates (data from Schottdorf et al.<sup>28</sup> symbol size proportional to the area of measured region in units of  $\Lambda^2$ ; see also Figure S2B).  
 (E) Characteristics of the mouse lemur pinwheels (red) in comparison with the macaque (both species pooled) and the common design model<sup>13</sup> (gray).

by comparing a baseline period with signals evoked during stimulus presentation. The subtraction of orthogonal directions revealed patterned responses of different intensities (Figures 2A and S2A). Angle maps of orientation preference demonstrate orientation domains arranged in a circular fashion, like a pinwheel, around center singularities.<sup>27</sup> The maps were stable across days of repeated imaging (Figures 2A, S1B, and S1C).

Next, we analyzed the spatial arrangement of the orientation domains. The spacing between fields responding to the same orientation, termed column spacing ( $\Lambda$ )<sup>4,13</sup> (Figure 2B), was, on average, 0.54 mm (mean; 95% confidence interval [CI]: [lower 0.5077, upper 0.6342];  $n = 4$  animals; Figure 2C). This is similar to the column spacing found in larger primate species such as the Galago<sup>13</sup> (mean 0.687 mm; CI: [0.5337, 0.7619]) and

Macaque (two species: *Macaca mulatta*  $n = 7$ , *Macaca fuscata*  $n = 4$ ; combined for analysis: mean 0.695 mm, CI: [0.5900, 0.7343]; Figure 2C), which is surprising considering the difference in brain and body size of up to two orders of magnitude.<sup>29</sup> These results indicate that orientation domain size only weakly scales with body or brain size in primates. This weak scaling also appears distinct from carnivore V1, for which substantial interspecies differences in column spacing  $\Lambda$  suggest a much stronger scaling with body and brain size (Figure S4). Our observations quantitatively exclude the possibility that the 50- $\mu$ m iso-orientation clusters observed in mouse V1<sup>12,15</sup> represent allometrically scaled primate orientation domains. Primate V1 orientation domains appear only to weakly scale with body size and hence cannot be arbitrarily miniaturized.

### Universal Pinwheel Arrangement across Primates

Even with an invariant column spacing, the typical size of individual orientation columns could be decreased in small brains by increasing the number of orientation pinwheels per hypercolumn area  $\Lambda^2$ , termed pinwheel density ( $\rho$ , average number of pinwheels per region of size  $\Lambda^2$ ). It has been demonstrated previously that pinwheel density is predicted to be close to the mathematical constant  $\pi$  in models for the joint formation of the system of orientation domains and intracortical circuitry.<sup>30</sup> While this prediction has been confirmed across several mammalian species,<sup>13,14,28</sup> it remained unknown whether it applied to primate V1 in general. We thus examined the spatial organization of orientation domains and pinwheels in the mouse lemur and compared it to other primates and to mathematical models predicting a universal invariant pinwheel density. Are orientation domains and pinwheels arranged distinctly in mouse lemur visual cortex, or do they adhere to general design principles that universally apply to larger primates? To answer this question, we first calculated pinwheel density. Pinwheel density ( $\rho$ ) was found to be indistinguishable between mouse lemur (mean 3.156; CI: [2.850, 3.376]) and other species including the galago (mean 3.332; CI: [2.698, 3.760]), a larger strepsirhine.<sup>31</sup> We also measured the pinwheel density in macaques (both species combined, mean 3.2447, CI: [2.850, 3.672]), which are simiiform primates. We found that in all these primate species spanning over two orders of magnitude in body size, the mean pinwheel density appeared invariant and matched the mathematical constant  $\pi$  (Figure 2D), the value predicted by models of large-scale circuit self-organization.<sup>30,31</sup> This analysis thus further corroborated that both V1 orientation domains and pinwheels cannot be arbitrarily miniaturized across primates.

To critically test the apparent universality of pinwheel arrangement across primates, we quantified further features of the arrangement of pinwheels across V1. We assessed their relative positioning within orientation hypercolumns by nearest neighbor distance distributions (same, opposite or independent of topological charge) for the mouse lemur and compared them to those of the macaque and the predictions of the universal design model<sup>13</sup> (Figure 2E). This analysis revealed that the means of the distributions were similar (mouse lemur mean values:  $d = 0.357$ , CI: [0.343, 0.371]; macaque  $d = 0.349$ , predicted  $d = 0.359$ ; mouse lemur  $d^{+/+} = 0.518$ , CI: [0.502, 0.535]; macaque  $d^{+/+} = 0.511$ , predicted  $d^{+/+} = 0.525$ ; mouse lemur  $d^{+/-} = 0.389$ , CI: [0.372, 0.408], macaque  $d^{+/-} = 0.396$ , predicted  $d^{+/-} = 0.396$ ). We also calculated pinwheel count fluctuations in subregions of V1 ranging from small regions up to subregions of  $20 \Lambda^2$  area (Figure 2E). Taken together, orientation maps in mouse lemur V1 were statistically indistinguishable from the macaque and closely adhered to universal design model predictions (Figure 2E).

### Absence of Ocular Dominance Columns in Mouse Lemur

While the design of orientation domains and pinwheel arrangement in the mouse lemur was indistinguishable from other primates, including the macaque, their visual system might show qualitative differences in the integration of information from both eyes. Neurons driven by inputs from the left and right eye can be segregated in highly variable patterns<sup>32</sup> across primates, and in the macaque, such ocular dominance maps are arranged

in alternating bands.<sup>33</sup> We therefore compared orientation-selective responses evoked by presenting visual gratings selectively to either the left or the right eye in the mouse lemur, but could not find any evidence for the occurrence of ocular dominance maps ( $n = 3$  animals). Repeated observations across subsequent days yielded only weak and highly variable signals, probably due to random fluctuations (Figure S3). These observations expand the overall picture of a highly variable expression of ocular dominance across, but also within, some primate species<sup>34</sup> and might suggest a tendency to fuse left and right eye streams at the earliest cortical stage in the small mouse lemur brain. However, intrinsic signal imaging procedures may not be sufficiently sensitive to reveal ocular dominance maps. It may be needed to use more invasive methods, such as anatomical tract tracing or experiments involving monocular deprivations, to further probe this aspect of cortical architecture.

### Mouse Lemur Visual Acuity

It has been hypothesized that the total number of processing modules such as pinwheels or orientation hypercolumns in V1 limits an animal's visual capabilities.<sup>10,35</sup> The small mouse lemur brain appears ideal to critically test this hypothesis. We thus estimated the visual acuity of the mouse lemur (Figure 3). We first quantified the optokinetic reflex (OKR) response. To evoke the OKR, horizontally moving vertical gratings of different spatial frequencies and contrasts were presented to the lightly anesthetized animal while tracking eye movements (Figure 3A; STAR Methods). The absolute contrast sensitivity was high, as expected for a nocturnal forager and hunter, and peaked at  $\sim 0.5$  cpd (cycles per degree; Figure 3B). Since the optical performance under lightly anesthetized condition is not comparable to awake states, we also determined the visual acuity of mouse lemurs in a visual discrimination task (Figure 3C; STAR Methods; Video S1). We found that they could maximally resolve  $\sim 3$  cpd at maximum contrast (Figure 3D, black line). The behavioral task measurements revealed slightly higher sensitivity compared to the OKR (Figures 3B and 3D, dotted line), yet probably still only represent the lower bound of the actual acuity. Taken together, these results suggest that the mouse lemur possesses a visual acuity similar to other arboreal, but diurnal, species such as tree shrews or gray squirrels (Figure 3D, adapted from da Silva Souza et al.<sup>36</sup>).

### Large Relative V1 Size in the Mouse Lemur

We next assessed how the mouse lemur's visual acuity is related to V1 size (Figure 4). In a small primate brain, the large size of orientation domains (and estimated number of neurons per hypercolumn; Figure 4A) might limit the total number of pinwheels in V1 and hence directly affect the visual acuity. Srinivasan and colleagues<sup>35</sup> proposed that, across primate species, the total pinwheel number and visual acuity are proportional to each other (although not taking into account regional specializations such as the fovea). Given the mouse lemur's behavioral visual acuity of probably  $>3$  cpd (Figure 3), their scaling relation predicts V1 to possess  $\sim 600$  pinwheels per hemisphere. Fitting this number of pinwheels would require V1 to be exceptionally large in comparison to the rest of the cortex. Measuring the size of the mouse lemur V1 as identified by CO staining (Figures 1D and 1E), we found that it covers, on average,  $\sim 21\%$  or  $\sim 48.9 \text{ mm}^2$  ( $\pm 3.91$ ;

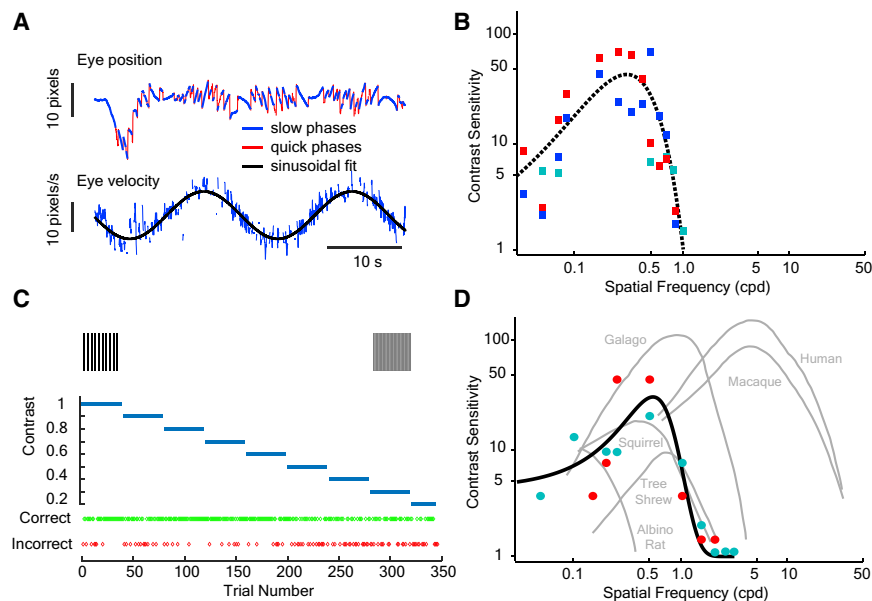


**Figure 3. Visual Acuity of the Mouse Lemur**

(A) Visual reflex threshold estimation using the optokinetic reflex (OKR) response. Example data from eye movements evoked by two 0.05-Hz rotation cycles of a virtual drum consisting of vertical black and white stripes (spatial frequency = 0.1678 and contrast = 1). The velocity trace of the OKR slow phases was fit with a 0.05-Hz sinusoidal function.

(B) Averaged contrast sensitivity threshold (dotted line) based on the OKR of three animals (colored points).

(C) Example session with the behavioral performance of an animal (red points in B and D) at 1.5 cpd and various contrasts. Gratings in the inset are not drawn to scale (see also Video S1).

(D) Contrast sensitivity curve was fitted to the combined and averaged behavioral contrast sensitivity thresholds of two mouse lemurs. The colors of the individual animals correspond to the same identity as in (B).

$n = 6$  [3 animals, both hemispheres]; Figure 4B) of the 227.6-mm<sup>2</sup> cortical surface per hemisphere ( $\pm 22.11$ ;  $n = 6$ ), which is in line with previously published data.<sup>29</sup> Comparable measurements in macaques and humans showed that V1 covers only 10% or 3% of the cortex surface, respectively (Figure 4B, based on literature values<sup>29,37</sup>). This decrease of relative V1 size toward larger primates stands in stark contrast to rodent data where relative V1 size increases monotonically with neocortex size (Figure S4B). Calculating the number of pinwheels in the mouse lemur based on its V1 size, column spacing, and pinwheel density leads to an estimated number of  $\sim 550$  pinwheels per hemisphere. This is close to the  $\sim 600$  pinwheels predicted from visual acuity<sup>35</sup>. It also demonstrates that the mouse lemur V1 is not simply a scaled-down version of the macaque (Figure S4C). Instead, it covers a considerably larger fraction of the cortex compared to all other primates (Figure 4B) or equally sized rodents (Figure S4B) of similar visual acuity (Figure 3D).

## DISCUSSION

In this work, we show that the mouse lemur brain contains robust orientation domains and pinwheels, despite possessing a brain size similar to that of rats. Although mouse lemur orientation domains are the smallest observed so far in any mammal, their weak scaling with body size suggests that primate orientation domains are nearly incompressible. Among primates, mouse lemurs exhibit one of the biggest V1-to-cortex ratios in line with the view that even the most basal primates are visual specialists. The finding that the different features of the orientation maps in the mouse lemur (which lack ocular dominance maps) are indistinguishable from other primates such as the macaque provides strong evidence for an invariant universal design of the orientation system across primates. This invariance contrasts with classical dimension reduction models,<sup>38</sup> which predict that the pinwheel densities would be substantially larger in the presence of strong ocular dominance<sup>39,40</sup> as well as with the highly variable layout and expression of ocular dominance columns across primates.<sup>32</sup>

## A Lower Size Limit for Orientation Columns

What factors could set a lower size limit to orientation domains such that they cannot be scaled down with brain size arbitrarily? On the one hand, anatomical variables such as the typical range of dendrites and axons of cortical pyramidal cells or of connectivity with other cell types might set a spatial scale for the formation of cooperative cell populations.<sup>41</sup> In this case, cell morphology may imply a limit size below which functional columns are not easily formed. Alternatively, computational models of V1 function indicate that local circuit operations are collective in nature and may thus require a minimum number of neurons for reliable function.<sup>42–45</sup> Intriguingly, estimating the number of neurons (based on the species-specific density; see STAR Methods) contained within an orientation hypercolumn ( $\Delta^2$  area<sup>8,13</sup>) across primate species converges on a near invariant count of about  $8 \times 10^4$  (Figure 4A). Smaller primates are reported to have smaller neuron soma size<sup>46</sup> and higher neuronal density.<sup>47,48</sup> This relationship may account for the slightly smaller hypercolumn size observed in our data (Figure 2C). Interindividual variation in the size of orientation columns is under partial genetic control.<sup>10</sup> It is therefore conceivable that natural selection may have driven orientation columns in primates toward an optimized size. Future work should histologically confirm the actual number of neurons per hypercolumn, addressing how this number emerges and whether it satisfies a computational constraint imposed by information processing demands.

## Unifying Accounts for V1 Architecture

Our results have multiple theoretical implications for V1 functional architecture, circuit organization, and its evolutionary emergence. First, our analysis revealed that the geometry of OPMs and pinwheel arrangements in the mouse lemur, the galago, and the macaque follow an extension of the “common design” framework.<sup>13</sup> It has been proposed that orientation columns and their universal organizing principles emerged independently in primates, their closest relatives, and in carnivores.<sup>13</sup> Notably, the common design framework is independent of the

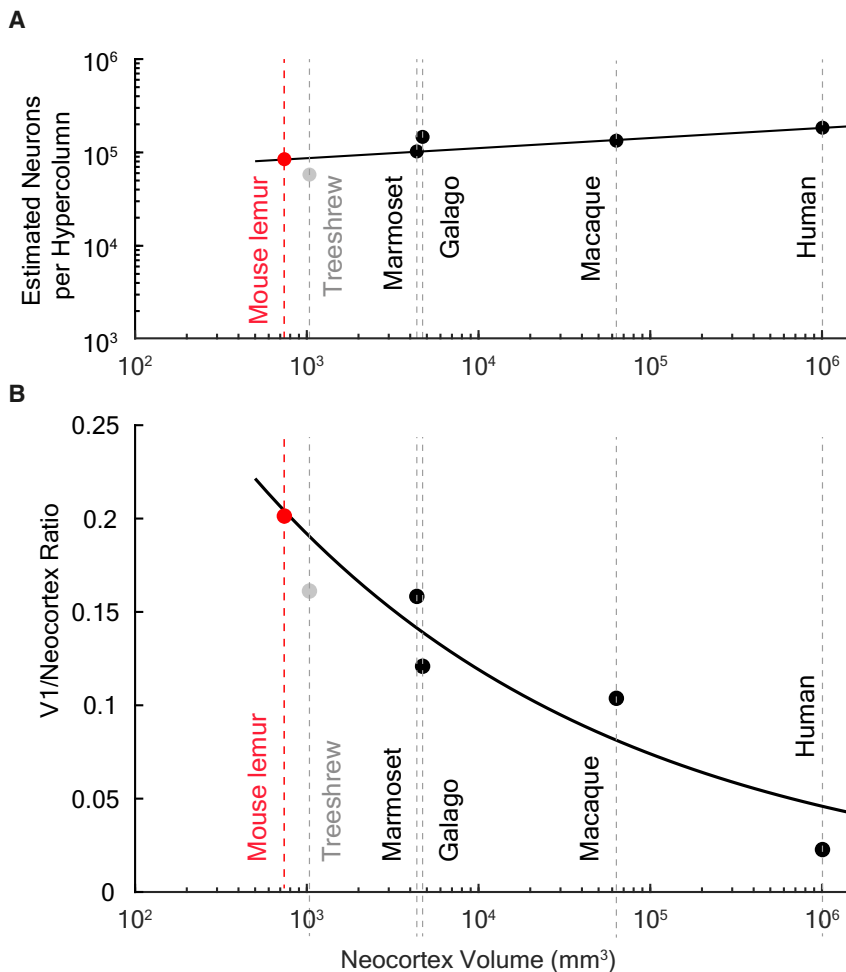


**Figure 4. Estimated Neurons per Hypercolumn and V1-to-Neocortex Ratio**

(A) Estimated number of neurons per hypercolumn for the mouse lemur in relation to other primates and the tree shrew (see STAR Methods for details and references). Fitted line  $y = 4.1 \cdot 10^4 x^{0.1081}$ . (B) V1-to-cortex ratio of primates (fitted line  $y = 0.801x^{-0.2069}$ ) and tree shrew for comparison (see also Figure S4).

precise origins of orientation selectivity within cortical circuits, which are distinct in different lineages. A number of recent studies confirmed for various non-primates that orientation<sup>49,50</sup> and direction selectivity<sup>51</sup> emerge already in V1's input layer IV and originate from the selective convergence of thalamic inputs. In primates, however, orientation selectivity is generated via an intracortical circuit, with input from orientation-unselective layer IV thalamo-recipient neurons.<sup>52</sup> Upper layer neurons then acquire orientation preference by selective convergence of inputs from layer IV.<sup>53</sup> Our finding of the weak scaling of orientation column size across primates and an apparently stronger scaling in carnivores further highlights that orientation columns in these two clades might be distinct structures that independently evolved to adhere to the same organizing principles. Second, a recent study proposed that the retino-cortical mapping ratio can separate species with OPMs from those without.<sup>54</sup> Given the mouse lemur V1 area (48 mm<sup>2</sup>) measured in our study and the retinal area (130 mm<sup>2</sup>) measured from flat mounts,<sup>55</sup> the hypothesis proposed by Jang et al. actually predicts the absence of OPMs in the mouse lemur, which is not supported by our data (Figure 2). Notably, the mouse lemur possesses a neocortex similar in size to the rat and a V1 size smaller than that of the squirrel and agouti (Figure S4A). These results suggest that additional factors apart from V1 size and retino-cortical mapping ratio

govern the presence or absence of OPMs in the mammalian brain.

For instance, the functional implications of orientation columns versus salt and pepper have been frequently envisioned as a balance between minimizing wire length and maximizing coverage.<sup>7,8</sup> It has been argued that the presence of orientation columns impairs the coverage of the visual field compared to salt and pepper. Orientation maps may represent an optimal solution in the case of large V1 in which columns and pinwheels are numerous and the cost of compromising feature coverage is low. Given a fixed minimal size of orientation columns, this impairment in general will be the more severe the smaller the V1 and is predicted to become prohibitive for very small areas<sup>14,16,56</sup> such as the 2-mm<sup>2</sup> V1 of the tenrec or the even smaller V1 of mesozoic stem eutherians.<sup>14,57</sup> Our finding that orientation columns and pinwheels cannot be scaled down arbitrarily strengthens this

prediction. Future tests of the existence of a lower limit to the size of columnar visual cortices will need to focus on miniature mammalian brains outside the primate order.

### Resolving the Evolutionary Origins of Primate Visual Cortex

The small size and basal phylogenetic position of mouse lemurs, and the many similarities of their biology, lifestyle, and habitat to the reconstructed euprimate ancestor, make them a promising model for studying V1 circuit evolution and the origins of primate vision in general.<sup>3,58</sup> Our observations increase the probability that the evolutionary emergence of primate-type V1 functional architecture occurred during a fundamental grade shift that overturned the euarchonta ancestral state in an all-or-nothing transition of becoming a visual specialist. If functional circuit structures intermediate in size between mouse iso-orientation clusters and primate-type orientation domains could be formed and maintained, the brain of the tiny mouse lemur would be a promising place to search for them. Instead, we found a full-fledged system of orientation domains and pinwheels practically indistinguishable from that of the macaque. Recently, Silcox and coworkers argued that the final steps in the evolution of stem primates must have consisted of a substantial encephalization burst that had no analog in rodents<sup>59</sup> and that was coupled to

the frontal repositioning of the primate eye.<sup>58</sup> It would be parsimonious to assume that the primate-typical large and columnar V1 emerged during this vision-related encephalization burst. Given that pinwheels cannot be arbitrarily miniaturized and the close relation between pinwheel number and visual acuity, it is tempting to conjecture that selection for visual performance drove a massive size expansion of V1 near the origin of primates.

### Mouse Lemurs as a Primate Model for Systems Neuroscience

As a primate model for systems neuroscience, the mouse lemur has many advantages, including that most experimental tools developed for mice are potentially transferable. Indeed, our results illustrate that optical methods, such as intrinsic signal imaging through chronic cranial windows can be easily adapted. This is a promising first step toward analyzing single-cell responses within primate cortical circuits using high-density electrophysiology or chronic two-photon calcium imaging.<sup>60</sup> Such experiments will potentially allow us to gain a better understanding of how V1 processing differs between rodents and primates at the single-cell level. Notably, mouse lemurs are so far the only primate species in which fitness proximal traits can be correlated with individual cognitive capabilities in the wild.<sup>61</sup> The ease of breeding in captivity,<sup>62</sup> as well as short gestation (2 months) and quick maturation (1 year<sup>63</sup>), allows studying mouse lemurs in controlled laboratory settings without compromising the wild population. Understanding the circuit basis of ecologically relevant mouse lemur behaviors may thus potentially reveal the adaptive value of primate-specific neuronal information processing principles. For us to learn these lessons, it will however remain critical to protect the integrity of the threatened ecosystems that sustain them in the wild.<sup>64</sup>

### STAR★METHODS

Detailed methods are provided in the online version of this paper and include the following:

- KEY RESOURCES TABLE
- RESOURCE AVAILABILITY
  - Lead Contact
  - Materials Availability
  - Data and Code Availability
- EXPERIMENTAL MODEL AND SUBJECT DETAILS
- METHOD DETAILS
  - Behavioral contrast sensitivity
  - Optokinetic reflex
  - Histology
  - Intrinsic signal imaging (ISI)
  - ISI experimental setup
  - Data Inclusion and Exclusion
- QUANTIFICATION AND STATISTICAL ANALYSIS
  - Determining visual acuity from behavior contrast sensitivity
  - Determining visual acuity from optokinetic reflex
  - VGlut2 and M2 overlay
  - CO patch nearest neighbor distances
  - ISI raw data pre-processing
  - Orientation map design statistics

- Pinwheel statistics calculation
- Calculation of the V1/Neocortex ratio and volumes

### SUPPLEMENTAL INFORMATION

Supplemental Information can be found online at <https://doi.org/10.1016/j.cub.2020.11.027>.

### ACKNOWLEDGMENTS

We would like to thank Siegrid Löwel and Matthias Kaschube for their advice and guidance on V1 intrinsic signal imaging, and Leonard White, Kevan Martin, and Mary Silcox for their comments on the manuscript. We would like to express our gratitude to Martine Perret and the animal caretakers at the Brunoy facility for their help with mouse lemur handling and breeding, and the members of the Huber lab for their support and discussions.

This work was supported by the Human Frontiers Science Program (D.H. and F.P., RGP0024/2016), the New York Stem Cell Foundation (D.H.), the German Research Foundation (F.W., CRC 889; F.W. and D.H., PP2205), the Volkswagen Foundation (F.W., ZN2632), the Ministry for Science and Culture of Lower Saxony, and Max Planck Society (F.W.). D.H. is a New York Stem Cell Foundation-Robertson Investigator.

### AUTHOR CONTRIBUTIONS

D.H. conceptualized the study. D.H., C.L.A.H., R.Z., and M.P. designed the experiments. C.L.A.H. and R.Z. ran the experiments. F.W. and J.D.F.W. designed models and cross-species comparative analyses. C.L.A.H., J.D.F.W., M.S., and M.P. analyzed the data. F.W. and D.H. oversaw data analysis. S.M., K.I., T.O., and A.A. provided the macaque data. F.P. and F.A. provided expertise, guidance, and resources related to the mouse lemurs. D.H., C.L.A.H., and F.W. wrote the manuscript.

### DECLARATION OF INTERESTS

The authors declare no competing interests.

Received: July 19, 2020

Revised: October 8, 2020

Accepted: November 11, 2020

Published: December 3, 2020

### REFERENCES

1. Churakov, G., Sadasivuni, M.K., Rosenbloom, K.R., Huchon, D., Brosius, J., and Schmitz, J. (2010). Rodent evolution: back to the root. *Mol. Biol. Evol.* 27, 1315–1326.
2. O’Leary, M.A., Bloch, J.I., Flynn, J.J., Gaudin, T.J., Giallombardo, A., Giannini, N.P., Goldberg, S.L., Kraatz, B.P., Luo, Z.X., Meng, J., et al. (2013). The placental mammal ancestor and the post-K-Pg radiation of placentals. *Science* 339, 662–667.
3. Kaas, J.H. (2013). The evolution of the visual system in primates. In *The New Visual Neurosciences*, A.L.C.J. Werner, ed. (MIT Press), pp. 1233–1246.
4. Hubel, D.H., and Wiesel, T.N. (1974). Sequence regularity and geometry of orientation columns in the monkey striate cortex. *J. Comp. Neurol.* 158, 267–293.
5. Kaas, J.H. (2012). Evolution of columns, modules, and domains in the neocortex of primates. *Proc. Natl. Acad. Sci. USA* 109 (Suppl 1), 10655–10660.
6. Ohki, K., Chung, S., Ch’ng, Y.H., Kara, P., and Reid, R.C. (2005). Functional imaging with cellular resolution reveals precise micro-architecture in visual cortex. *Nature* 433, 597–603.
7. Koulakov, A.A., and Chklovskii, D.B. (2001). Orientation preference patterns in mammalian visual cortex: a wire length minimization approach. *Neuron* 29, 519–527.

8. Hubel, D.H., and Wiesel, T.N. (1977). Ferrier lecture. Functional architecture of macaque monkey visual cortex. *Proc. R. Soc. Lond. B Biol. Sci.* **198**, 1–59.
9. Hubel, D.H., and Wiesel, T.N. (1974). Uniformity of monkey striate cortex: a parallel relationship between field size, scatter, and magnification factor. *J. Comp. Neurol.* **158**, 295–305.
10. Kaschube, M., Wolf, F., Geisel, T., and Löwel, S. (2002). Genetic influence on quantitative features of neocortical architecture. *J. Neurosci.* **22**, 7206–7217.
11. Ohki, K., and Reid, R.C. (2007). Specificity and randomness in the visual cortex. *Curr. Opin. Neurobiol.* **17**, 401–407.
12. Ringach, D.L., Mineault, P.J., Tring, E., Olivas, N.D., Garcia-Junco-Clemente, P., and Trachtenberg, J.T. (2016). Spatial clustering of tuning in mouse primary visual cortex. *Nat. Commun.* **7**, 12270.
13. Kaschube, M., Schnabel, M., Löwel, S., Coppola, D.M., White, L.E., and Wolf, F. (2010). Universality in the evolution of orientation columns in the visual cortex. *Science* **330**, 1113–1116.
14. Keil, W., Kaschube, M., Schnabel, M., Kisvarday, Z.F., Löwel, S., Coppola, D.M., White, L.E., and Wolf, F. (2012). Response to Comment on “Universality in the Evolution of Orientation Columns in the Visual Cortex”. *Science* **336**, 413–413.
15. Kondo, S., Yoshida, T., and Ohki, K. (2016). Mixed functional microarchitectures for orientation selectivity in the mouse primary visual cortex. *Nat. Commun.* **7**, 13210.
16. Kaschube, M. (2014). Neural maps versus salt-and-pepper organization in visual cortex. *Curr. Opin. Neurobiol.* **24**, 95–102.
17. Seiffert, E.R., Tejedor, M.F., Fleagle, J.G., Novo, N.M., Cornejo, F.M., Bond, M., de Vries, D., and Campbell, K.E., Jr. (2020). A parapatheic stem anthropoid of African origin in the Paleogene of South America. *Science* **368**, 194–197.
18. Zhang, M.-L., Li, M.-L., Ayoola, A.O., Murphy, R.W., Wu, D.-D., and Shao, Y. (2019). Conserved sequences identify the closest living relatives of primates. *Zool. Res.* **40**, 532–540.
19. Huchon, D., Chevret, P., Jordan, U., Kilpatrick, C.W., Ranwez, V., Jenkins, P.D., Brosius, J., and Schmitz, J. (2007). Multiple molecular evidences for a living mammalian fossil. *Proc. Natl. Acad. Sci. USA* **104**, 7495–7499.
20. Preuss, T.M., Qi, H., and Kaas, J.H. (1999). Distinctive compartmental organization of human primary visual cortex. *Proc. Natl. Acad. Sci. USA* **96**, 11601–11606.
21. Dias, I.A., Bahia, C.P., Franca, J.G., Houzel, J.C., Lent, R., Mayer, A.O., Santiago, L.F., Silveira, L.C.L., Picanço-Diniz, C.W., and Pereira, A. (2014). Topography and architecture of visual and somatosensory areas of the agouti. *J. Comp. Neurol.* **522**, 2576–2593.
22. Wong, P., and Kaas, J.H. (2008). Architectonic subdivisions of neocortex in the gray squirrel (*Sciurus carolinensis*). *Anat. Rec. (Hoboken)* **291**, 1301–1333.
23. Saraf, M.P., Balam, P., Pifferi, F., Gămănuț, R., Kennedy, H., and Kaas, J.H. (2019). Architectonic features and relative locations of primary sensory and related areas of neocortex in mouse lemurs. *J. Comp. Neurol.* **527**, 625–639.
24. Grinvald, A., Frostig, R.D., Siegel, R.M., and Bartfeld, E. (1991). High-resolution optical imaging of functional brain architecture in the awake monkey. *Proc. Natl. Acad. Sci. USA* **88**, 11559–11563.
25. Hubel, D.H., and Wiesel, T.N. (1968). Receptive fields and functional architecture of monkey striate cortex. *J. Physiol.* **195**, 215–243.
26. Cooper, H.M., Kennedy, H., Magnin, M., and Vital-Durand, F. (1979). Thalamic projections to area 17 in a prosimian primate, *Microcebus murinus*. *J. Comp. Neurol.* **187**, 145–167.
27. Bonhoeffer, T., and Grinvald, A. (1991). Iso-orientation domains in cat visual cortex are arranged in pinwheel-like patterns. *Nature* **353**, 429–431.
28. Schottdorf, M., Keil, W., Coppola, D., White, L.E., and Wolf, F. (2015). Random Wiring, Ganglion Cell Mosaics, and the Functional Architecture of the Visual Cortex. *PLoS Comput. Biol.* **11**, e1004602.
29. Stephan, H., Frahm, H., and Baron, G. (1981). New and revised data on volumes of brain structures in insectivores and primates. *Folia Primatol. (Basel)* **35**, 1–29.
30. Wolf, F. (2005). Symmetry, multistability, and long-range interactions in brain development. *Phys. Rev. Lett.* **95**, 208701.
31. Kaschube, M., Schnabel, M., Wolf, F., and Löwel, S. (2009). Interareal coordination of columnar architectures during visual cortical development. *Proc. Natl. Acad. Sci. USA* **106**, 17205–17210.
32. Horton, J.C., and Adams, D.L. (2005). The cortical column: a structure without a function. *Philos. Trans. R. Soc. Lond. B Biol. Sci.* **360**, 837–862.
33. Hubel, D.H., and Wiesel, T.N. (1969). Anatomical demonstration of columns in the monkey striate cortex. *Nature* **221**, 747–750.
34. Adams, D.L., and Horton, J.C. (2003). Capricious expression of cortical columns in the primate brain. *Nat. Neurosci.* **6**, 113–114.
35. Srinivasan, S., Carlo, C.N., and Stevens, C.F. (2015). Predicting visual acuity from the structure of visual cortex. *Proc. Natl. Acad. Sci. USA* **112**, 7815–7820.
36. da Silva Souza, G., Gomes, B.D., and Silveira, L.C.L. (2011). Comparative neurophysiology of spatial luminance contrast sensitivity. *Psychol. Neurosci.* **4**, 29–48.
37. Yacoub, E., Harel, N., and Ugurbil, K. (2008). High-field fMRI unveils orientation columns in humans. *Proc. Natl. Acad. Sci. USA* **105**, 10607–10612.
38. Durbin, R., and Mitchison, G. (1990). A dimension reduction framework for understanding cortical maps. *Nature* **343**, 644–647.
39. Wolf, F., and Geisel, T. (1998). Spontaneous pinwheel annihilation during visual development. *Nature* **395**, 73–78.
40. Keil, W., and Wolf, F. (2011). Coverage, continuity, and visual cortical architecture. *Neural Syst. Circuits* **1**, 17.
41. da Costa, N.M., and Martin, K.A.C. (2010). Whose Cortical Column Would that Be? *Front. Neuroanat.* **4**, 16.
42. Ben-Yishai, R., Bar-Or, R.L., and Sompolinsky, H. (1995). Theory of orientation tuning in visual cortex. *Proc. Natl. Acad. Sci. USA* **92**, 3844–3848.
43. Douglas, R.J., Koch, C., Mahowald, M., Martin, K.A., and Suarez, H.H. (1995). Recurrent excitation in neocortical circuits. *Science* **269**, 981–985.
44. Murphy, B.K., and Miller, K.D. (2009). Balanced amplification: a new mechanism of selective amplification of neural activity patterns. *Neuron* **61**, 635–648.
45. Paradiso, M.A. (1988). A theory for the use of visual orientation information which exploits the columnar structure of striate cortex. *Biol. Cybern.* **58**, 35–49.
46. Haug, H. (1987). Brain sizes, surfaces, and neuronal sizes of the cortex cerebri: a stereological investigation of man and his variability and a comparison with some mammals (primates, whales, marsupials, insectivores, and one elephant). *Am. J. Anat.* **180**, 126–142.
47. Gabi, M., Collins, C.E., Wong, P., Torres, L.B., Kaas, J.H., and Herculano-Houzel, S. (2010). Cellular scaling rules for the brains of an extended number of primate species. *Brain, Behavior and Evolution* **76**, 32–44.
48. Herculano-Houzel, S., Manger, P.R., and Kaas, J.H. (2014). Brain scaling in mammalian evolution as a consequence of concerted and mosaic changes in numbers of neurons and average neuronal cell size. *Front. Neuroanat.* **8**, 77.
49. Kremkow, J., Jin, J., Wang, Y., and Alonso, J.M. (2016). Principles underlying sensory map topography in primary visual cortex. *Nature* **533**, 52–57.
50. Lee, K.-S., Huang, X., and Fitzpatrick, D. (2016). Topology of ON and OFF inputs in visual cortex enables an invariant columnar architecture. *Nature* **533**, 90–94.
51. Lien, A.D., and Scanziani, M. (2018). Cortical direction selectivity emerges at convergence of thalamic synapses. *Nature* **558**, 80–86.
52. Blasdel, G.G., and Fitzpatrick, D. (1984). Physiological organization of layer 4 in macaque striate cortex. *J. Neurosci.* **4**, 880–895.
53. Livingstone, M., and Hubel, D. (1988). Segregation of form, color, movement, and depth: anatomy, physiology, and perception. *Science* **240**, 740–749.

54. Jang, J., Song, M., and Paik, S.-B. (2020). Retino-Cortical Mapping Ratio Predicts Columnar and Salt-and-Pepper Organization in Mammalian Visual Cortex. *Cell Rep.* *30*, 3270–3279.e3.
55. Dkhissi-Benyahya, O., Szel, A., Degrip, W.J., and Cooper, H.M. (2001). Short and mid-wavelength cone distribution in a nocturnal Strepsirrhine primate (*Microcebus murinus*). *J. Comp. Neurol.* *438*, 490–504.
56. Harris, K.D., and Mrsic-Flogel, T.D. (2013). Cortical connectivity and sensory coding. *Nature* *503*, 51–58.
57. Kaas, J.H. (2007). 3.03 - Reconstructing the Organization of Neocortex of the First Mammals and Subsequent Modifications. In *Evolution of Nervous Systems*, J.H. Kaas, ed. (Oxford: Academic Press), pp. 27–48.
58. Silcox, M.T., and López-Torres, S. (2017). Major Questions in the Study of Primate Origins. *Annu. Rev. Earth Planet. Sci.* *45*, 113–137.
59. Bertrand, O.C., Amador-Mughal, F., and Silcox, M.T. (2016). Virtual endocasts of Eocene Paramys (Paramyinae): oldest endocranial record for Rodentia and early brain evolution in Euarchontoglires. *Proc. Biol. Sci.* *283*, 20152316, 10.1098/rspb.2015.2316.
60. Li, M., Liu, F., Jiang, H., Lee, T.S., and Tang, S. (2017). Long-Term Two-Photon Imaging in Awake Macaque Monkey. *Neuron* *93*, 1049–1057.e3.
61. Huebner, F., Fichtel, C., and Kappeler, P.M. (2018). Linking cognition with fitness in a wild primate: fitness correlates of problem-solving performance and spatial learning ability. *Philos. Trans. R. Soc. Lond. B Biol. Sci.* *373*, 20170295, 10.1098/rstb.2017.0295.
62. Perret, M. (2005). Relationship between urinary estrogen levels before conception and sex ratio at birth in a primate, the gray mouse lemur. *Hum. Reprod.* *20*, 1504–1510.
63. Languille, S., Blanc, S., Blin, O., Canale, C.I., Dal-Pan, A., Devau, G., Dhenain, M., Dorieux, O., Epelbaum, J., Gomez, D., et al. (2012). The grey mouse lemur: a non-human primate model for ageing studies. *Ageing Res. Rev.* *11*, 150–162.
64. Jones, J.P.G., Ratsimbazafy, J., Ratsifandrihamanana, A.N., Watson, J.E.M., Andrianandrasana, H.T., Cabeza, M., Cinner, J.E., Goodman, S.M., Hawkins, F., Mittermeier, R.A., et al. (2019). Madagascar: Crime threatens biodiversity. *Science* *363*, 825.
65. Schneider, C.A., Rasband, W.S., and Eliceiri, K.W. (2012). NIH Image to ImageJ: 25 years of image analysis. *Nat. Methods* *9*, 671–675.
66. Mathis, A., Mamidanna, P., Cury, K.M., Abe, T., Murthy, V.N., Mathis, M.W., and Bethge, M. (2018). DeepLabCut: markerless pose estimation of user-defined body parts with deep learning. *Nat. Neurosci.* *21*, 1281–1289.
67. Suter, B.A., O'Connor, T., Iyer, V., Petreanu, L.T., Hooks, B.M., Kiritani, T., Svoboda, K., and Shepherd, G.M.G. (2010). Ephus: multipurpose data acquisition software for neuroscience experiments. *Front. Neural Circuits* *4*, 100.
68. Kaschube, M., Wolf, F., Puhlmann, M., Rathjen, S., Schmidt, K.-F., Geisel, T., and Löwel, S. (2003). The pattern of ocular dominance columns in cat primary visual cortex: intra- and interindividual variability of column spacing and its dependence on genetic background. *Eur. J. Neurosci.* *18*, 3251–3266.
69. Languille, S., Aujard, F., and Pifferi, F. (2012). Effect of dietary fish oil supplementation on the exploratory activity, emotional status and spatial memory of the aged mouse lemur, a non-human primate. *Behav. Brain Res.* *235*, 280–286.
70. Sincich, L.C., Adams, D.L., and Horton, J.C. (2003). Complete flatmounting of the macaque cerebral cortex. *Vis. Neurosci.* *20*, 663–686.
71. Wong-Riley, M. (1979). Changes in the visual system of monocularly sutured or enucleated cats demonstrable with cytochrome oxidase histochemistry. *Brain Res.* *171*, 11–28.
72. Huber, D., Gutnisky, D.A., Peron, S., O'Connor, D.H., Wiegert, J.S., Tian, L., Oertner, T.G., Looger, L.L., and Svoboda, K. (2012). Multiple dynamic representations in the motor cortex during sensorimotor learning. *Nature* *484*, 473–478.
73. Okamoto, T., Ikezoe, K., Tamura, H., Watanabe, M., Aihara, K., and Fujita, I. (2011). Predicted contextual modulation varies with distance from pinwheel centers in the orientation preference map. *Sci. Rep.* *1*, 114.
74. Ratzlaff, E.H., and Grinvald, A. (1991). A tandem-lens epifluorescence microscope: hundred-fold brightness advantage for wide-field imaging. *J. Neurosci. Methods* *36*, 127–137.
75. Yokoo, T., Knight, B.W., and Sirovich, L. (2001). An optimization approach to signal extraction from noisy multivariate data. *Neuroimage* *14*, 1309–1326.
76. Fekete, T., Omer, D.B., Naaman, S., and Grinvald, A. (2009). Removal of spatial biological artifacts in functional maps by local similarity minimization. *J. Neurosci. Methods* *178*, 31–39.
77. Herculano-Houzel, S., Watson, C., and Paxinos, G. (2013). Distribution of neurons in functional areas of the mouse cerebral cortex reveals quantitatively different cortical zones. *Front. Neuroanat.* *7*, 35.
78. Mengler, L., Khmelinskii, A., Diedenhofen, M., Po, C., Staring, M., Lelieveldt, B.P.F., and Hoehn, M. (2014). Brain maturation of the adolescent rat cortex and striatum: changes in volume and myelination. *Neuroimage* *84*, 35–44.
79. Krubitzer, L., Campi, K.L., and Cooke, D.F. (2011). All rodents are not the same: a modern synthesis of cortical organization. *Brain, Behavior and Evolution* *78*, 51–93.
80. Keeley, R.J., Burger, D.K., Saucier, D.M., and Iwaniuk, A.N. (2015). The size of non-hippocampal brain regions varies by season and sex in Richardson's ground squirrel. *Neuroscience* *289*, 194–206.
81. Santiago, L.F., Freire, M.A.M., Picanço-Diniz, C.W., Franca, J.G., and Pereira, A. (2019). The Organization and Connections of Second Somatosensory Cortex in the Agouti. *Front. Neuroanat.* *12*, 118.
82. Campos, G.B., and Welker, W.I. (1976). Comparisons between brains of a large and a small hystricomorph rodent: capybara, *Hydrochoerus* and guinea pig, *Cavia*; neocortical projection regions and measurements of brain subdivisions. *Brain Behav. Evol.* *13*, 243–266.
83. Lewitus, E., Hof, P.R., and Sherwood, C.C. (2012). Phylogenetic comparison of neuron and glia densities in the primary visual cortex and hippocampus of carnivores and primates. *Evolution* *66*, 2551–2563.
84. Rockel, A.J., Hiorns, R.W., and Powell, T.P. (1980). The basic uniformity in structure of the neocortex. *Brain* *103*, 221–244.
85. McLoughlin, N., and Schiessl, I. (2006). Orientation selectivity in the common marmoset (*Callithrix jacchus*): the periodicity of orientation columns in V1 and V2. *Neuroimage* *31*, 76–85.

## STAR★METHODS

### KEY RESOURCES TABLE

REAGENT or RESOURCE	SOURCE	IDENTIFIER
<b>Antibodies</b>		
Guinea pig Anti-VGLUT2, Unconjugated antibody	Millipore	Cat# AB2251; RRID:AB_1587626
Anti-Muscarinic Acetylcholine Receptor m2, clone M2-2-B3 antibody	Millipore	Cat# MAB367; RRID:AB_94952
Rabbit Anti-VGluT2, polyclonal	Synaptic Systems	SySy135403; RRID:AB_887883
<b>Chemicals, Peptides, and Recombinant Proteins</b>		
Cytochrome c from equine heart	Sigma Aldrich	C2506 CAS# 9007-43-6
3,3 $\epsilon$ -Diaminobenzidine	Sigma Aldrich	D4293 MDL# MFCD00007725
<b>Experimental Models: Organisms/Strains</b>		
<i>Microcebus murinus</i>	<a href="https://micmu.cnrs.fr/">https://micmu.cnrs.fr/</a>	NCBI:txid30608
<i>Macaca fuscata</i>		NCBI:txid9542
<i>Macaca mulatta</i>		NCBI:txid9544
<b>Software and Algorithms</b>		
ImageJ	Schneider et al. <sup>65</sup>	<a href="https://imagej.nih.gov/ij/">https://imagej.nih.gov/ij/</a>
MATLAB	MathWorks	MATLAB 2003; 2015
DeepLabCut	Mathis et al. <sup>66</sup>	<a href="https://github.com/DeepLabCut/DeepLabCut">https://github.com/DeepLabCut/DeepLabCut</a>
Ephus	Suter et al. <sup>67</sup>	<a href="http://scanimage.org">scanimage.org</a>
Code for column spacing estimation	Kaschube et al. <sup>68</sup>	N/A
Code for pinwheel statistics analysis	Schottdorf et al. <sup>28</sup>	N/A
Code for mouse lemur visual acuity	This paper	<a href="https://doi:10.26037/yareta:n2u7jm3wf5he7p6xpecta4gktm">https://doi:10.26037/yareta:n2u7jm3wf5he7p6xpecta4gktm</a>

### RESOURCE AVAILABILITY

#### Lead Contact

Further information and requests for resources and reagents should be directed to and will be fulfilled by the Lead Contact, Daniel Huber ([daniel.huber@unige.ch](mailto:daniel.huber@unige.ch))

#### Materials Availability

This study did not generate new unique reagents

#### Data and Code Availability

Datasets generated and codes used in this study are available in the research data repository of the University of Geneva: <https://yareta.unige.ch/> <https://doi.org/10.26037/yareta:n2u7jm3wf5he7p6xpecta4gktm>

### EXPERIMENTAL MODEL AND SUBJECT DETAILS

Adult mouse lemurs (8 males and 4 females) between the ages 1–2.5 years were used in this study. All experiments were carried out with individuals bred and raised in the “Mouse Lemur Platform” (authorization number E-91-114-1) of the “Museum National d’Histoire Naturelle” in Brunoy, France (UMR MECADEV CNRS/MNHN 7179.). Animals sacrificed for this study were specifically bred for

biomedical research purposes and did not affect the overall breeding and conservation programs of the facility. Whenever possible, the animals were returned to the colony after the experiments. All experimental procedures were in accordance with European animal welfare regulations and were reviewed by the local ethics committee (“Comité d’éthique en expérimentation animale No. 68”) in Brunoy, France, by the ethics committee of the University of Geneva, Switzerland and authorized by the French “Ministère de l’éducation nationale de l’enseignement supérieur et de la recherche.”

## METHOD DETAILS

### Behavioral contrast sensitivity

To behaviorally determine the contrast sensitivity of mouse lemurs, we trained two young adult males (see Table S1) in a left/right discrimination task. Stimuli consisted of stationary vertical gratings of various contrasts (1 to 0.01) presented in blocks of 40 trials and spanned half the screen (Dell P2414H, 1920x1080,60Hz), either on the right or left side in a pseudo-random order. The other half of the screen was set at a gray level with matched luminance. The correct choice would consist of entering the lick port on the side where the grating was presented. Each session consisted of blocks from one single spatial frequency (between 0.25 and 3 cycles per degree). Contrasts were converted into contrast sensitivity values via the equation:  $1/((I_{max}-I_{min})/(I_{max}+I_{min}))$ , where  $I_{max}$  and  $I_{min}$  are the maximum and minimum luminance of the stimuli as measured by a lux meter, which was fitted by a power function. One day before and during the days of the experiments, food availability was restricted to the rewards obtained during the session. Animals were allowed to perform until satiated or until they stopped engaging in the task. If their weight dropped below 60 gr, animals were supplemented with additional food until they reached 60 gr. The standard liquid diet<sup>69</sup> was used as rewards and food supplements.

A custom made behavior box with three lick-ports (Sanworks) was used for the experiment. The animals viewed visual stimuli on a computer screen (Dell P2414H, 1920x1080, 60Hz, set at 50% brightness, distance 30 cm) through a transparent Plexiglas window on which the three lick-ports were mounted. There was no additional light provided. The animals were trained to initiate visual stimulus presentation by a nose poke at the center port for 300 ms. They were rewarded with liquid food by poking into the left or right lick-port according to the stimulus presented.

### Optokinetic reflex

To assess the optokinetic reflex response we used the visual rotations of a virtual drum. The visual stimulus consisted of vertical black and white stripes of different spatial frequencies and contrasts. The stimulus was generated using the PsychoPy python library on the 27 inch monitor (ASUS PG278QR, 165 Hz refresh rate, 2560 by 1440 pixel, 1 ms response time) placed at a 45 cm viewing distance. Before transmission to the display, each frame was virtually projected to a cylindrical surface giving the impression of a rotating drum centered on the animal’s viewpoint. For each tested pair of spatial frequency and contrast values, the velocity profile of the drum motion consisted of two sinusoidal cycles at 0.05 Hz and always covered the same angular amplitude. Animals ( $n = 3$ ) were administered with buprenorphine (0.3ug/g) and briefly anaesthetised with isoflurane. They were subsequently positioned in a body harness in front of the screen and allowed to wake up from isoflurane anesthesia. Buprenorphine sufficiently sedated the animals to gain stable recordings. The eyes were recorded with a 1/3” CMOS camera (Firefly MV FMVU-03MTM, Point Grey Research). Custom video acquisition software programmed in MATLAB (Mathworks) saved 8-bit greyscale images (376 x 240 pixels) to disk at a variable rate with mean  $\gg 60$  frames/s. The time stamps relative to trial onset of each frame were saved in the image headers. We used the Deep-LabCut toolbox<sup>66</sup> to track the position of the upper and lower extremities of the lemur’s left eye pupil and took their average as an estimate of eye position in video frame coordinates (i.e., pixel units). The eye position trace was up-sampled for analysis to a fixed 100 Hz sampling rate using linear interpolation. We identified the quick phases of ocular nystagmus (or spontaneous saccades) based on an eye acceleration threshold (1000 pixels/s<sup>2</sup>). The start and end of each quick phase was subsequently identified using a velocity threshold (10 pixels/s). The quick phase (and saccade) periods were removed from the eye position trace and the remaining slow phases low-pass filtered with a Savitzky-Golay filter (degree = 1, window = 10 samples). To estimate the size of the evoked optokinetic reflex, we fitted the slow phase velocity trace with a sinusoidal function with the frequency parameter fixed at 0.05 Hz (i.e., the stimulus frequency) and amplitude and phase as the free parameters using the method of non-linear least-squares. The fitted amplitude parameter was taken as a measure of the optokinetic reflex size.

### Histology

Anesthesia was induced with 5% isoflurane in oxygen, followed by an intraperitoneal (IP) injection of pentobarbital (150mg/kg). The animals were transcardially perfused with approximately 60ml 1X Phosphate Buffer Saline (PBS) followed by 60ml of paraformaldehyde (PFA, 1% for flatmounts, 4% for coronal sections) in 1X PBS. For flatmounted sections, the cortex was isolated and flattened based on a modified protocol originally for the macaque brain<sup>70</sup> immediately after perfusion. To isolate the cortex, the brain was first partitioned into its two hemispheres by cutting along the midline with a scalpel. The brainstem and cerebellum were removed by carefully inserting a rounded spatula between the cortex and the cerebellum. The midbrain structures are pried apart and peeled away from the cortex at the level of the corpus callosum. White matter tracts holding the posterior pole in shape are removed to allow unfolding of the occipital lobe. Next the temporal lobe was unfolded while removing the white matter tracts beneath. White matter surrounding the sylvian sulcus was removed as much as possible and a cut was made along the sulcus and the whole cortex was unfolded. The unfolded cortex was then transferred and sandwiched between two glass slides and covered with 4% PFA. A steady

pressure was applied on the top glass slide for approximately 20 s. All specimens were post-fixed in 4% PFA overnight at 4°C and cryo-protected by sinking in 20% sucrose in 0.1M phosphate buffer (PB) or 1X PBS prior to sectioning. Coronal sections were cut at 50 $\mu$ m. Flat-mounted sections were embedded in OCT compound (Cell Path; KMA-0100-00A) and cut at 80-100 $\mu$ m with a freezing sliding microtome (Microm, HM430). Coronal sections were collected into 10 separate series spanning the whole brain at 500 $\mu$ m intervals between sections within a series.

### Immunofluorescence

After initial rounds of 3  $\times$  10 min washes in a base buffer containing 0.3% Triton X-100 in 0.1M PB, specimen slices were first treated with 3% bovine serum albumin (Sigma A3059) in base buffer for 1 h at room temperature. After blocking, they were incubated in with the primary antibody at 4°C. For muscarinic receptor 2, monoclonal IgG2a rat  $\alpha$ -m2 AchR (1:500; Millipore MA367 1mg/mL) antibodies was used for overnight incubation. Following rinsing for 3 rounds of 10 min in base buffer, the slices were incubated with goat  $\alpha$ -rat linked with Alexa Fluor 594 (1:250; Invitrogen A11007) and 1.5% BSA in base buffer for 2.5 h at room temperature in the dark. For vesicular glutamate receptor 2 (VGlut2), incubation with the primary antibody polyclonal guinea pig  $\alpha$ -VGlut2 (1:2000; Millipore AB2251 1mg/mL) or polyclonal rabbit  $\alpha$ -VGlut2 (1:1000; Synaptic System, SySy135403 1mg/mL) with 1.5% BSA in base buffer took 24 h at 4°C. Subsequent to 3 rounds of 10 min rinsing, the slices were incubated with goat  $\alpha$ -guinea pig Alexa Fluor 594 (1:200; Invitrogen A11076) or goat  $\alpha$ -rabbit Alexa Fluor 488 (1:200; Invitrogen A11034) in base buffer for 2 h at room temperature in the dark. Slices were then washed in base buffer for 3 times 10 min each before subsequently counter-stained with DAPI (Thermo Fisher D1306) in the dark and mounted on glass slides with fluoromount (Sigma Aldrich F4650). Sequential brain slices were taken for VGlut2 and M2 immunofluorescence.

Double immunofluorescence against VGlut2 and M2 were carried out using a primary antibody mix of rabbit  $\alpha$ -VGlut2 (1:1000; Synaptic System, SySy135403 1mg/mL) and  $\alpha$ -m2 AchR (1:500; Millipore MA367 1mg/mL) in 1.5% BSA in base buffer at 4°C for 24 h. For the secondary antibody incubation, slices were incubated in a mixture of goat  $\alpha$ -rat Alexa Fluor 594 and goat  $\alpha$ -rabbit Alexa Fluor 488 (both 1:250) and 1.5% BSA in base buffer at 4°C for 12 h in the dark.

### Cytochrome oxidase histochemistry

Cytochrome oxidase (CO) histochemistry was carried out based on a standard protocol.<sup>71</sup> After three rounds of washing in 0.1M PB for 5 min, slices were bathed in a cocktail of cytochrome c (0.4mg/mL; Sigma-Aldrich C2506), sucrose (0.1g/mL), diaminobenzidine (0.7mg/mL; SigmaFast D4293) dissolved in 0.1M PB solution, for around 12 to 18 h at 4°C or until the desired staining intensity was reached. The slices were allowed to dry on glass slides covered by a Petri dish overnight for dry mounting. All widefield and fluorescence imaging were carried out on a Zeiss Axioscan.Z1 slide scanner. Image processing was first performed in ImageJ before determining regions or points of interest. Data was subsequently imported to MATLAB 2018a for quantitative analysis.

### Intrinsic signal imaging (ISI)

For the mouse lemur, four adults (three males and one female) between 1.5-2.5 years old, underwent surgical procedures to implant a cranial window. All surgical procedures were performed under strict sterile conditions and according to European and Swiss animal welfare regulations. Anesthesia was induced by subcutaneous Buprenorphine injection and followed by ~5% Isoflurane (in oxygen). Dexamethasone, Carprofen and Ceftriaxone were administered intramuscularly prior to the surgery. Animal was placed in a custom made stereotaxic frame. The eyes were protected with Lacryvisc and the tongue was covered with a thin layer of Vaseline. The area for the surgical procedure was shaved and was subsequently disinfected with 70% Ethanol, Betadine and Chlorhexidine 1%. Lidocaine was administered subcutaneously. During the surgery breathing rate and reflexes were continuously monitored and the anesthesia levels were adjusted accordingly. The skull was exposed and a titanium bar was attached to the dried bone with cyanoacrylate glue (ERGO 5011). ECoG electrodes were implanted over frontal and visual cortex contralateral to the craniotomy (to determine anesthesia levels during the experiments). A craniotomy of 6mm diameter was performed over the visual cortex and a double layered glass window was inserted to replace the bone.<sup>72</sup> Finally, the window and titanium frame were sealed with transparent dental acrylic (Lang Dental). The animal was administered analgesic treatment (Buprenorphine, 0.1mg/kg) for the following week and antibiotics (Ceftriaxone, 20ul of 1g in 5ml Lidocaine) for 9 days. For the *Macaca fuscata*, the method for performing ISI has been described in detail in a previous publication.<sup>73</sup>

### ISI experimental setup

To perform intrinsic signal imaging the animals were lightly anaesthetized. Anesthesia was induced by subcutaneous buprenorphine injection and followed by ~5% isoflurane. The animal was positioned 20-25 cm from the LCD screen (Dell P2414H, 1920x1080, 60Hz) where full-screen gratings were shown. The head was stabilized by tightly clamping the titanium bar on both sides. The body temperature was controlled using a homeothermic blanket system (Harvard Apparatus). The cranial window was illuminated initially by green 515 nm LED in order to acquire the blood vessel map and followed by 620 nm red LED illumination for the rest of the experiment. Light anesthesia was kept at 0.2%–1.5% isoflurane (in oxygen) based on ECoG signal which was monitored during the entire experiment. Buprenorphine induction at the start of the experiment allowed isoflurane anesthesia to be more stable and at lighter levels. Spontaneous blinking and sporadic eye closures were sufficient to keep the eyes moist. Pre-amplified ECoG was further amplified by Cornerstone Dagan EX4-400 (differential, 500x, 0.3 highpass and 300Hz lowpass filtered). Online ECoG was monitored with a Rigol DS1074 oscilloscope. LED's were powered by a stabilized PeakTech laboratory power supply (6080) at 3.6V at 0.2-0.6mA. The animal and stimulation settings were continuously monitored using three infrared video cameras (Firefly MV FMVU-03MTM, Point Grey Research). Luminosity of the visual stimulus screen was continuously measured with a photodiode (ThorLabs

PDA 100A-EC). A National Instruments NI USB-6341 data acquisition board was used to generate pulses in order to synchronously trigger all cameras and data acquisition.

Visual stimuli consisted of black and white bars of 0.16 cycles per visual degree. Drifting bars in eight different directions were presented in a pseudo-random order (four orientations, each in two directions at 4 cycles per second). Each trial was composed of a 2 s pre-stimulus period, a 4 s stimulus and a 4 s post-stimulus period. During pre- and post-stimulus period animal were exposed to a gray screen which was adjusted in brightness to match the brightness of the stimulus. One experimental session contained up to 10 blocks of 40 trials. After the experiment the animal was handled until it fully recovered from anesthesia and it was returned to the home cage. The repeated chronic imaging allowed us not only to gain more accurate data, but also reduce the total number of animals used (see [Table S1](#)).

ISI data was acquired using a Retiga Ex monochrome 12-bit camera (QImaging). Data output in the form of RAW frames was acquired at 10Hz, 800x600 pixels resolution and spatial binning factor of 2 using EPHUS software. In order to achieve optimal focus and zoom on the cranial window, the camera is equipped with a double lens system ( $f = 105\text{mm}$ ,  $f 2.5$  and  $f = 55\text{mm}$ ,  $f 3.5$ , both Nikon.<sup>74</sup>

### Data Inclusion and Exclusion

All experimental animals were included in the analysis. Intrinsic imaging sessions with high movement artifacts or low signal-to-noise were excluded from analysis. Stimulus conditions in the behavioral task with less than 35 trials pooled across all sessions were excluded from analysis due to low number of repeats. One CO-stained flatmount was excluded from calculation of CO blob nearest neighbor distances due to lower quality of the tissue, containing numerous micro-fractures, which prevented precise localization of the centers of CO blobs.

## QUANTIFICATION AND STATISTICAL ANALYSIS

### Determining visual acuity from behavior contrast sensitivity

Data for each animal were pooled across sessions. The criterion performance was calculated based on a binomial distribution ( $p(\text{success}) = 0.5$ , one tailed) to determine threshold contrasts for each spatial frequency. Threshold contrasts across spatial frequencies were averaged across the two animals tested and a Gaussian fit to the  $\log(\text{contrast sensitivity})$  against spatial frequency was made to obtain an averaged contrast sensitivity curve ([Figure 1](#)).

### Determining visual acuity from optokinetic reflex

Statistical significance was assessed using a bootstrapping method, as follows. For each trial, 1999 datasets each comprising a random sample of half of the eye velocity data points were used for fitting and the sets comprising the other half for cross-validation. The fraction of the 1999 estimates of explained variance with cross-validation sets that were more extreme than zero was defined as the p value. An optokinetic reflex response was deemed to be significant at the  $p < 0.01$  level. For each spatial frequency, the size of the optokinetic reflex (i.e., the fitted amplitude parameter) was plotted as a function of the logarithm of contrast and fitted with an exponential function. At a given spatial frequency, the contrast value at which the exponential fit exceeded the average of the non-significant sizes by a factor of two was defined as the contrast threshold. Contrast values were converted to contrast sensitivity in the same manner as the behavioral contrast sensitivity, a power function was applied to convert contrast to contrast sensitivity. Visual acuity was defined as the contrast sensitivity at the contrast threshold.

### VGlut2 and M2 overlay

Consecutive sections were aligned by rigid transformation using patterns of blood vessels identified in both sections and the resulting alignment was verified by eye. To assess patch colocalization between VGlut2 and M2, rectangular regions of interest of fixed size were drawn over VGlut2 patches tangent to L4. Pixel intensities were first normalized via dividing by the mean intensity across the region of interest. An intensity profile was obtained by averaging across normalized pixel intensities in a line perpendicular to the tangent. The corresponding intensity profile for the same region of interest in the M2 channel or for the consecutively aligned M2 stained slices was similarly obtained. A mean intensity profile was calculated by averaging over all regions of interest for each staining. These mean profile plots were subsequently compared.

### CO patch nearest neighbor distances

For the CO histochemistry preparation, the patches and their centers were identified by eye after adjusting contrast. The nearest neighbor distances were calculated for the visually identified centers. Kruskal-Wallis analysis of variance for non-parametric data was performed to compare nearest neighbor distances across animals. No significant differences were found between animals, hence the data were pooled across animals and the mean and standard deviation computed.

### ISI raw data pre-processing

#### Data extraction

For each experiment session around 60 normalized response images to each stimulus condition were extracted together with 60 blank response images. The images were obtained as follows:

**B - response to blank stimulus:** Blank response images were extracted by averaging 10 frames (1 s) before stimulus onset for each presentation.

**So - baseline signal:** The blank response images corresponding to each full set of stimuli (e.g., 8 drift directions) were averaged to calculate the baseline  $S_o$ . This baseline was calculated separately for each new full set of stimuli presentations.

**S - response signal:** For each stimulus presentation 4 response images were obtained by averaging 10 frames (1 s) each starting two seconds after stimulus onset and continuing until 2 s after stimulus conclusion.

**D - normalized response signal:** The extracted data was calculated using  $D = -(S - S_o)/S_o$ . The minus sign came because in intrinsic signal imaging an increase in neural activity results in a decrease in signal, measured as an increase in blood oxygenation (following a short initial decrease in oxygenation) which absorbs more light.

### Image registration across sessions

**Manual alignment:** The initial alignment was obtained by manually selecting matching reference points between the sessions from the image of the blood vessels. With the points an affine transform matrix was calculated which was constrained to scaling, rotation and translation. The blood vessels image was obtained performing a PCA of the blank responses and selecting the component where the vessels are more visible.

**Automated refinement.** To refine the manual alignment the next steps were based on the structure of the orientation map itself. The procedure to calculate the orientation map from the data of the session is detailed further below:

The first automated method calculated the affine transform that minimizes the distance between corresponding pinwheels in a pair of sessions, again only allowing global translation, rotation and scaling. Pinwheels were marked at the intersection of the zero contours of the real and imaginary components of the complex valued orientation map (see below). Matching pinwheels between the sessions were calculated based on their distance and sign (clockwise or anti-clockwise increase of orientation preference around the center, i.e., topological charge). To increase the possible displacement radius of the pinwheels, the initial and final maps were linearly interpolated and the pinwheels matched iteratively.

The second automated method calculated the affine transform that minimized the dissimilarity of the spatial structure of the orientation maps. The cost function to minimize was the average of the absolute orientation difference between the pixels of the sessions.

### Region of interest (ROI) definition

The ROI was manually defined based on the following reference images:

- 1) A high-pass filtered orientation map, indicating visually responsive areas.
- 2) The sum of the normalized cardinal and oblique responses (real and imaginary part of the complex valued orientation map). This image clearly displayed response modularity and helped to determine activity boundaries.
- 3) The image of the vasculature, as obtained in the alignment procedure. This was used to avoid areas that could potentially suffer from blood vessel artifacts.
- 4) The pixel-wise coefficient of variation (CV) of the orientation map, which helps to identify areas with low signal to noise ratio. The variance of the orientation map for the CV was calculated from the difference of the measured map and 100 bootstrap samples of the data (see below).

### Band-pass filter cutoff settings

**Manual definition:** To define the high-pass cutoff and an initial low-pass cutoff frequencies the radial profile of the 2D power spectrum of the orientation map was calculated, where the x axis was inverted to show the scale in millimeter instead of the wavenumber  $k$ . When the map was of good quality, the power was low for small scales, rapidly increased around 0.4-0.8 mm to a few large peaks corresponding to the typical scale of the map, decreased afterward and started fluctuating depending on the larger structures of the layout. The initial low-pass cutoff was set where the first peak starts raising. The high-pass cutoff was set where the first peaks had dropped and before the power rises again. Both settings were selected using the information of all sessions and are unique to each animal.

**Automated refinement:** To further refine the low-pass cutoff, the setting was selected for which the number of pinwheels and their location was minimally changing when its value was perturbed. To get this value for each pixel a curve is measured of how the local pinwheel density (pinwheel count inside the local hypercolumn size) decreased as the low-pass cutoff was increased. For most pixels this decrease was linear except at a constant plateau in a given cutoff range, representing the settings where locally the map was minimally changing. First the plateau range was extracted for each pixel by piecewise fitting. Then the low-pass cutoff that was included in the majority of the pixel's plateaus was selected. As with the manual definition, the refined low-pass used the information of all sessions combined and is unique to each animal.

### Orientation map calculation

The orientation maps from the normalized response data  $D$  (see data extraction) were calculated by first averaging the images of the responses across stimulus repetitions such that a single image for each condition was obtained. The images were then combined in a circular average, where each image was multiplied by a complex number  $\exp(i\theta)$ , with  $\theta$  twice the orientation of the corresponding drifting grating. The obtained map was normalized by subtracting the mean and dividing by the standard deviation of the pixels inside the defined region of interest. The resulting orientation map was complex valued, where the phase defines twice the preferred orientation and the magnitude of the orientation selectivity.

## Filtering

The resulting orientation map was band-pass filtered in Fourier space. The 2D Fourier transform of the complex orientation map was multiplied by a combination of logistic functions that switch radially at the defined frequency cutoffs between 0 and 1. The steepness parameter of the functions was set to 5% of the respective cutoff frequencies. To account for potential boundary effects, the filtered map was normalized by the result of applying the same filter to the region of interest.

## Bootstrap samples

For each bootstrap sample the normalized response images *D* were re-sampled with replacement for each stimulus condition independently until the same number of images as the original data were gathered. The resampled data was combined to generate a bootstrap sample of the orientation map and is processed as described above.

## Denoising

To increase the signal to noise ratio of the orientation maps, an implementation of the ‘Generalized Indicator Functions’ method was used.<sup>75</sup> The method gets as input the normalized response, data *D* and returns a family of images that simultaneously maximized variations between stimulus conditions and minimized variations inside each stimulus condition. Projections of the data to this family of images with signal to noise ratio above a given threshold were returned and further used to generate orientation maps as described above. This procedure was not used when variations between the bootstrap samples of the data are calculated, since resampling leads to repetitions of the same images in the input data and therefore virtually the same output. In those cases an implementation of the ‘Local Similarity Minimization’ method was used.<sup>76</sup> The method uses a set of images representing potential artifacts as templates and minimizes the neighborhood similarity from the normalized response data *D*. The templates are obtained from a PCA of the blank response images.

## Ocular dominance calculation

To extract potential ocular dominance maps, recordings to ipsilateral and contralateral monocular stimulations were combined. First each recording was processed separately as described above, obtaining two sets of normalized response data *D*<sub>ipsi</sub> and *D*<sub>contra</sub> (see data extraction). For each set the response to the different stimulus conditions in each trial were averaged, obtaining a single cocktail blank image per trial. The set of cocktail blanks for ipsi and contralateral stimulation were passed through the ‘Generalized Indicator Functions’ algorithm,<sup>75</sup> (see Denoising above), maximizing the separation of the monocular response signals. The ocular dominance response was then obtained by averaging the resulting projection for each condition and then subtracting each other.

This procedure was tested successfully in intrinsic signal imaging datasets of cats, ferrets and macaques coming from different imaging experiments. In those datasets this approach showed to be more reliable and obtain better results than subtracting the orientation selectivities of the ipsilateral and contralateral stimulated orientation maps or variations thereof.

## Orientation map design statistics

### Column spacing estimation

To calculate a 2D map of the local column spacing the wavelet method introduced previously was used.<sup>68</sup> Morlet wavelets with 16 orientations and varying spatial sizes were generated and convolved with the real and imaginary part of the complex orientation map separately. These correspond to maps obtained from the subtraction of single response patterns, i.e., (horizontal: 0deg - 90deg) and (oblique: 45deg - 135deg). The so called difference maps have no pinwheels, but show the periodicity measured in orientation maps. For each wavelet size, which varied between 0.3 mm to 1.1 mm in steps of 0.05 mm, the magnitude of the resulting convolution was averaged over the wavelet orientations. With this information, for each pixel a curve of wavelet size versus averaged convolution magnitude was obtained. This curve was interpolated to increase its resolution. The pixel’s column spacing was determined by finding the value where the curve is at its maximum. The results of using the real and the imaginary part of the orientation map were averaged to get the final local column spacing and the average spacing was obtained by averaging the values inside the region of interest.

### Pinwheel statistics calculation

To estimate the pinwheel density and other pinwheel layout parameters a fully automated procedure proposed in a study by Kaschube and colleagues<sup>13</sup> was used. We refer to the Supplemental Material of that paper for further details. MATLAB code to run this analysis is published in the Supplemental Material of Schottdorf’s study.<sup>28</sup>

Confidence intervals for the column spacing and pinwheel density were calculated via bootstrapping as parametric tests were inappropriate since normality of the distribution and similarity of the variances cannot be assumed (due to the low number of animals and cross species comparison). As such, for each animal, a vector of column spacing for each pixel was created, which was bootstrapped 100 times, and the mean calculated. The sampled mean for all animals in a species were combined with the 95% confidence interval obtained from the resulting distribution. For the macaques, the two species *Macaca mulatta* and *Macaca fuscata*, were combined in order to sample from a larger number of animals.

### Calculation of the V1/Neocortex ratio and volumes

The V1:Neocortex ratio was calculated based on area estimates from VGluT2 labeled coronal sections taken throughout the brain of 3 animals for both hemispheres. In two animals, the interslice distance was 250µm while in the third one the interslice distance was 500µm. The length of cortical L4 was measured for each slice and the area of was interpolated between adjacent slides using the trapezium method. Cortical L4 was chosen as V1 could be delineated with ease due to the VGluT2 labeling described above. The

area of V1 was divided by the area of the cortex to derive the ratio. The area V1/Neocortex ratio from the mouse lemur from the current study corresponded well with the volume ratio in Stephan et al.<sup>29</sup> For better comparison, the V1/Neocortex ratio of primates in Figure 3C were calculated from volume measures from Stephan et al. which were given for the whole brain (ie. both hemispheres).<sup>29</sup> For rodents, the values were less readily available from the literature. The mouse neocortex volume, V1 volume and ratio data were taken from a study from Herculano-Houzel et al.<sup>77</sup> Note that these volume values are for one hemisphere. From literature the values for the rat neocortex volume<sup>78</sup> and the ratio<sup>79</sup> were obtained. Similarly, the squirrel neocortex volume<sup>80</sup> and the ratio<sup>79</sup> sourced from previous literature. Neocortex volume of the agouti was calculated by multiplying the cortical flat-mount area<sup>81</sup> with cortical thickness.<sup>21</sup> The agouti V1/Neocortex ratio was measured from a published cortical flat-mount.<sup>81</sup> The capybara neocortex volume was taken from a study by Campos and Welker<sup>82</sup> and the ratio was measured from a schematic diagram found in the same study. Note that the diagram was not of a flat-mount, but more akin to the dorsal view and does not take into account the gyrification found in the capybara cortex. In addition, extrastriate areas were likely to be included in the visual area of the capybara, since visual cortex was determined by electrophysiological response to brief light flashes. Hence the ratio is likely an overestimate and less reliable compared to the values of better studied species. It was nonetheless included for comparison as the capybara is the largest rodent in the world.

#### **Number of neurons per hypercolumn**

The number of neurons per hypercolumn calculated by: number of neurons = (surface neuronal density) x (column spacing).<sup>2</sup> Surface neuronal density: Mouse lemur calculated by multiplying neuronal density (neurons per mm<sup>3</sup>)<sup>83</sup> by V1 volume<sup>29</sup> and dividing by V1 area (this study: 48.9mm<sup>3</sup>). All others from.<sup>84</sup> Note the surface density for the binocular region of the treeshrew was used for calculation. Column spacing: human,<sup>37</sup> marmoset,<sup>85</sup> galago,<sup>13</sup> tree shrew.<sup>13</sup>

#### **Number of pinwheels and hypercolumns in V1**

The number of pinwheels in V1 was estimated by: number of pinwheels = V1 area x pinwheel density / column spacing 2.

The number of hypercolumns in V1 was related to number of pinwheels by: number of hypercolumns = number of pinwheels / pinwheel density

### Prepare or check in advance:

- 1 Prepare drive
- 2 Prepare absorbent points and sterilize
- 3
- 4 Check anesthetics, analgesics and antibiotics (Lidocaine, Buprenorphine, Dexamethason, Carprofen Ceftriaxon)
- 5
- 6 Check availability of cotton swabs (sterile and non-sterile)
- 7 Check surgical instruments
- 8 Check cyano acrylic glue, dental cement and mixing pots
- 9 Check disinfection solutions (Betadine, Ethanol 70%)
- 10 Check Lacrisc/vaseline
- 11 Check sterile saline
- 12 Check edding marker
- 13 Skull screws



### Just before KO

- 1 Check gas and isoflurane levels on anesthesia machine
- 2 Pre-heat stereotactic frame (37°C) and water bath for agar (40°C ~ 45°C)
- 3 Prepare 10ml of 1.5% Agar in 0.9% saline. Dissolve in microwave and keep at 45°C just until using
- 4 Prepare a tube with sterile Saline
- 5 Clean and sterilize Skull screws REAL WELL!!!
- 6 Load syringes with anesthetic and analgesic and antibiotic drugs
- 7 Check the suction system
- 8 Clean the surgery area with 70% ethanol and sterilize tools in hot bead sterilizer @ 200°C
- 9 Sterilize all tools

DATE // POST SURG. DAY	WEIGHT	FUR	EYE	ACTIVITY	POSTURE	BLEED	INFLA- MMATION	NEW VESSELS	DURA THICKENING	BONE REGROWTH					

**KO LEMUR**

Time: \_\_\_\_\_ Weight: \_\_\_\_\_ EOS Time: \_\_\_\_\_

Steps	Check	Comments
1		KO lemur in Plexiglas box.
2		Fix lemur in the stereotaxic frame
3		Protect eyes and tongue with Lacryvisc and whiskers with Vaseline
4		Inject analgesic and antibiotic drugs
4.		Clean skin with 70 EtOH and Betadine
5		Inject lidocaine sub-cutaneous under the head. Cut the skin to expose the skull and hold skin on sides with bulldog clips
6		Remove hairs and periosteum if any and gently push muscles aside
7		Cover muscles with agar, mark intraural line and then cross coordinates
8		Scrape surface of the skull with back of the scalpel, use scalpel blade 11 for grooving the skull in all 4 orientations
9		With flat head oval drill make 3 holes on the muscle attachment edge of bone for screws, predrill craniotomy
10		Plup the screws in, cover skull with cyano acrylic (try not to put superglue on the pre-drawn craniotomy)
11		Drill craniotomy for tetrodes, bath the skull with saline and remove the bone island cover with agar
12		Position the drive above the craniotomy and dip in.
13		Cover the trodes with Vaseline
14		Use very liquid dental acrylic to fix the drive
15		Exchange one screw with the grounded screw
16		Drill cerebellar hole for second ground
17		Fix the grounds that they can't move!!!
18		Cover rest with acrylic let dry and stitch.

Notes

---

---

---

---

---

---

---

---

---

### Surgery:

1. **KO LEMUR:** Animal is anesthetized with ~5% Isoflurane in Plexiglas box During the surgery the anesthesia levels are adjusted to 1-2% isoflurane according to breathing rate and reflexes (checked by toe pinch)
2. **Shaving and Fixing Animal:** Don't shave the animal, just mount animal on stereotactic frame.
3. **Protect eyes and whiskers with Lacryvisc and Vaseline:** apply Lacryvisc over the eyes and Vaseline over the whiskers using a cotton swab.
4. **Inject analgesic and anti-inflammatory drugs:** Dexamethasone (0.8ul/1g) IM in the leg (anti-inflammatory), Buprenorphine (1ul/1g) Subcuta (opioid analgesic), Ceftriaxone (antibiotic) IM (50mg/kg (diluted in 4ml Rapidocaine 25ul for 100g animal)), Lidocaine subcutaneous in the skull (local anesthetic)
5. **Clean skin with EtOH and Betadine:** With a cotton swab clean the skin with ethanol to break the superficial tension of the hair. With a cotton swab disinfect the skin with betadine solution. Be generous. Free the midline by moving hair laterally.
6. **Cut the skin:** Use the scalpel to cut along the midline. If cut insufficient lift up scalp and use scissors to finish with a single cut along the midline.
7. **Remove hairs and periosteum:** Take picture of the skull before skull gets dry, this way you will see where the veins are. From now on work sterile! Remaining gelatinous periosteum and any protruding hairs are cut with small scissors and removed. Bone area is cleaned and dried with sterile cotton swabs spreading the skin to the edge of the skull.
8. **Keep skin on side:** Attach bulldog clips to the skin ant frontal medial and posterior position.
9. **Push muscles away:** Try to fit the fake drive. Gently push muscles which are too close to the drive in the skull with spatula. Once they are aside pour agarose on them so they don't dry.
10. **Scrape the skull surface:** To allow a stronger bonding of the glue and the bone use the drill or the scalpel to make a series of stripes in the surface of the bone. These stripes will increase the surface contact between the bone and cyano acrylic glue and will make the bone rough enough for the glue to work. Scrape and stripe also bone below the muscles.
11. **Mark ROIs:** Mark with Edding marker midline with dots of 2 mm distances, position of the screws, ground electrodes and center of the craniotomy.
12. **Cover the skull with cyano acrylic glue:** The cleaned bone area (if possible, avoid the area where the craniotomy will be done) and an additional 1mm of skin is covered with a thin layer of cyano-acrylic glue as primer. Make sure the whole area is dry as the cyano acrylic glue polymerizes in water and it is not what you want to happen.
13. **Implant skull screws:** Drill tiny holes for the skull screws and screw them in just a bit.

14. **Draw the window and start craniotomy:** Using the Edding marker draw a putative window. Add sterile saline to soften the bone, make it transparent and keep the brain cool to prevent damage during the drilling process. Drill the bone with round bur. Bone debris can be cleaned with wet gel foam and the suction system. Customarily check that the dimension of the drilled area is adequate. Also, determine the 'degree of detachment', of the bone island by gently pressing on the island at different points of it; if it moves relative to the rest of the skull, it is detached. Detachment generally is non-uniform; drill until it is fairly uniform without damaging the dura.
15. **Bath the skull with saline and remove the bone island:** To remove the island of cranial bone soak the whole area with sterile saline (to prevent damage due to negative pressure) and lift it up with sharp tweezers. Any blood is immediately removed using the perfusion system, gel foam or sterile absorbent points. Make sure there are no remains of bone left in the area of the window. Be extremely careful because you are touching the dura. Use gel foam and plenty of saline to clear the area of bone debris. At this stage bleeding from the bones or from the dura can be expected.
16. **Replace dummy drive for real one and position it:** Exchange fake drive for real one and position it with tetrodes above the craniotomy. Once set move it away by sliding whole holder to the back.
17. **Remove dura.** With prefabricated needle hook carefully lift the dura and cut from the center to the edges. Make 3-4 cuts and flip dura outward.
18. **Soak brain surface with dexamethasone.** Add a few droplets of dexamethasone.
19. **Move back the drive and once on place start dipping.** During dipping tetrodes are retracted, however if they have a hard time to penetrate and they create dimple extract them as much as necessary. Count the turns and once dimple overcome retract them to initial position. Be sure that individual tetrodes are entering brain by individual paths, they tend to stick together so there is need to spread them sometimes. At the end inject little bit of Vaseline around the trodes.
20. **Cover with dental cement.** Smoother a drop of superglue to the contact of the drive and the brain and add dental acrylic to cement the head-drive. Remove the bulldog clamps.
21. **Ground it.** Remove one of the screws and replace it with the grounded screw. Drill cerebellar hole for the ground wire. De-insulate the end and stick it in. Cover with super-glue. After, cover whole area with dental acrylate.
22. **Stitch it up.** Once dental acrylate hardened, stitch the skin around the drive.
23. **End of Surgery:** Gently remove the excess of Vaseline and remove the animal from the stereotactic frame and transfer to the recovery cage (temperature controlled).